I-3964

MASTER

DOE/ET/20279-159

A FLYWHEEL ENERGY-STORAGE-AND-CONVERSION SYSTEM FOR PHOTOVOLTAIC APPLICATIONS — FINAL REPORT

March 1982

Philip O. Jarvinen

Massachusetts Institute of Technology
Lincoln Laboratory
Lexington, Massachusetts 02173-0073

Prepared for
THE U.S. DEPARTMENT OF ENERGY
UNDER CONTRACT NO. DE-AC02-76ET20279

DISTRIBUTION OF THIS DOCUMENT IS UNLIMITED

DISCLAIMER

This report was prepared as an account of work sponsored by an agency of the United States Government. Neither the United States Government nor any agency thereof, nor any of their employees, makes any warranty, express or implied, or assumes any legal liability or responsibility for the accuracy, completeness, or usefulness of any information, apparatus, product, or process disclosed, or represents that its use would not infringe privately owned rights. Reference herein to any specific commercial product, process, or service by trade name, trademark, manufacturer, or otherwise does not necessarily constitute or imply its endorsement, recommendation, or favoring by the United States Government or any agency thereof. The views and opinions of authors expressed herein do not necessarily state or reflect those of the United States Government or any agency thereof.

DISCLAIMER

Portions of this document may be illegible in electronic image products. Images are produced from the best available original document.

This book was prepared as an account of work sponsored by an agency of the United States Government. Neither the United States Government nor any agency thereof, nor any of their employees, makes any warranty, express or implied, or assumes any legal liability or responsibility for the accuracy, completeness, or usefulness of any information, apparatus, product, or process disclosed, or represents that its use would not infringe privately owned rights. Reference herein to any specific commercial product, process, or service by trade name, trademark, manufacturer, or otherwise, does not necessarily constitute or imply its endorsement, recommendation, or favoring by the United States Government or any agency thereof. The views and opinions of authors expressed herein do not necessarily state or reflect those of the United States Government or any agency thereof.

Additional copies available from the National Technical Information Service, U.S. Department of Commerce, Springfield, Virginia 22161.

Price: Paper Copy $18.50
Microfiche $ 3.00

DOE/ET/20279-159

DOE/ET/20279--159

DE82 017128

Distribution Category UC 63, a, d
UC 94, b

A FLYWHEEL ENERGY-STORAGE-AND-CONVERSION SYSTEM FOR PHOTOVOLTAIC APPLICATIONS — FINAL REPORT

March 1982

Philip O. Jarvinen

Massachusetts Institute of Technology
Lincoln Laboratory
Lexington, Massachusetts 02173-0073

Prepared for
THE U.S. DEPARTMENT OF ENERGY
UNDER CONTRACT NO. DE-AC02-76ET20279

AIR FORCE JUNE 10, 1982--400

DISTRIBUTION OF THIS DOCUMENT IS UNLIMITED

ABSTRACT

This report discusses efforts to develop a magnetically suspended solar photovoltaic flywheel energy storage unit for residential applications and covers the period from initiation of the project on 1 October 1978 to its completion on 1 October 1981. During FY-79 and FY-80, a 1/10-scale prototype flywheel unit, which stores 1 kWh of energy in a 400-pound, 15-inch-diameter steel rotor at a maximum of 15,000 RPM, was designed, constructed and tested. The 1/10-scale prototype unit was based on a full-scale, 40-kWh residential flywheel design and was a total system in that it included all the electrical features needed for a complete interface between a photovoltaic array and a residential or utility load. Design features of the unit, such as its magnetic bearing, motor-generator, rotor and output power-conditioning equipment, are described and test results are presented. In the utility-interactive mode, a round-trip electrical storage efficiency of 82% was measured, while in the stand-alone cycloconverter mode, 67% efficiency was achieved. Total spindown losses were measured to be less than 4 watts at 15,000 RPM. Manufacturing cost studies of the full-scale, 40-kWh residential flywheel system are reported along with user worth studies of flywheel systems in the Northeast and Southwest.

In FY-81, the 1/10-scale prototype test setup was modified into an advanced prototype flywheel test unit. The advanced prototype unit consisted of a simplified, two-element magnetic bearing, to reduce projected manufacturing costs, and an available GFE advanced composite rotor, originally fabricated for a DOE vehicular application, of 24-inch diameter and 123-pound weight and storing 1-kWh at 15,000 RPM. An objective of this work was to gain experience in the use of such advanced rotors on magnetic suspension. The structural flexibility inherent in the GFE composite rotor was found to require redesign of the axial servo loop control system to obtain magnetic levitation. The magnetically suspended, advanced composite rotor was then spin tested at rotational speeds up to 12,000 RPM. Dynamic interactions between the rotor and control system precluded tests at speeds above

12,000 RPM. A new full-scale design for a 20-kWh, two-element, advanced flywheel system was prepared. Simulation studies of utility-interactive residential flywheel systems are reported which were carried out using actual data taken on a six-minute basis over a month-long period for the photovoltaic array electrical output and monitored house loads. Significant reductions in peak power demand were found possible when a flywheel storage unit was added to a photovoltaic residence.

ACKNOWLEDGMENT

The results described in this report represent the combined contributions of a number of MIT Lincoln Laboratory personnel, including B. L. Brench, R. D. Hay, G. W. Hart, J. T. Kelly, J. Mabey, N. E. Rasmussen, T. Stephens, and I. Wigdor. Special thanks to C. Sullivan for mechanical design aspects of both the prototype and advanced prototype systems. Professor L. L. Bucciarelli of Massachusetts Institute of Technology and A. R. Millner and A. Rangarajan formerly of Lincoln Laboratory and now of TriSolarCorp, Bedford, Massachusetts, are thanked for their technical contributions. Dr. Millner initiated this project and was Principal Investigator until March 1979. At that time, Philip O. Jarvinen became Principal Investigator and directed efforts until completion of the project in October 1981. Mr. Jarvinen also wrote this final report.

Preparation of the final manuscript by Sharon Howland is very much appreciated.

This work is supported by the U.S. Department of Energy, jointly by the Divisions of Energy Storage and Photovoltaic Energy Systems.

TABLE OF CONTENTS

Table of Contents (con'd)

Table of Contents (con'd)

Table of Contents (con'd)

LIST OF FIGURES

List of Figures (con'd)

List of Figures (con'd)

List of Figures (con'd)

List of Figures (con'd)

List of Figures (con'd)

List of Figures (con'd)

List of Figures (con'd)

LIST OF TABLES

LIST OF APPENDICES

1.0 SUMMARY

This report describes progress made during the period 1 October 1978 to 1 October 1981 in the development of a solar photovoltaic flywheel energy storage and conversion system for residential and load center applications. The flywheel energy storage unit acts as a complete interface between a solar photovoltaic array and an ac load. Key elements in the approach include the use of extremely low-loss magnetic bearings, maximum power tracking of the photovoltaic array, integrated motor-generator and output power-conditioning of the stand-alone cycloconverter or utility-interactive inverter type, and selection of a configuration tolerant to rotor imbalances by suspending the rotor from a flexible quill.

During FY-79, designs for full-size, 40-kWh residential flywheel storage systems were developed, manufacturing cost studies of these residential designs were prepared by three industrial contractors, and flywheel energy storage economics were studied in a system-worth analysis by the MIT Energy Laboratory. Each of these studies is discussed herein. Flywheel energy storage systems are shown to be technically and economically competitive with battery inverter systems for the same application.

During FY-79 and FY-80, a fully operational 1/10-scale prototype flywheel energy storage unit was built which is capable of operating either in a stand-alone mode or in a utility-interactive mode. The report describes in detail the mechanical and electrical design features of the prototype. Magnetic bearing design, dynamic analysis of the magnetically suspended flywheel and preliminary test results are also discussed. The prototype flywheel unit was operated over its complete operational speed range from 7,500 RPM to 15,000 RPM with a 400-pound magnetically levitated steel rotor.

In FY-81, a series of careful measurements were made on the 1/10-scale prototype flwheel unit to determine the overall in-out electrical storage efficiency and the component power-transfer efficiencies when the unit was operating in either a utility-interactive mode or a stand-alone mode. A measurement accuracy of $\pm 0.5\%$ was achieved through the use of calibrated power meters and by conducting the tests in a hard vacuum of 10^{-6} to 10^{-7} torr

to eliminate rotor aerodynamic friction drag effects and associated data corrections. The measured in-out storage efficiency of the utility-interactive inverter flywheel unit is 82% for a storage time of one hour and 80% for a 10-hour storage time. The stand-alone, cycloconverter-equipped flywheel unit has comparable efficiencies of 67% for a one-hour storage time and 65% for 10-hour storage time. Battery-inverter systems for the same application have storage efficiencies of 67%.

Also during FY-81, an advanced prototype flywheel storage unit with a simplified two-element magnetic bearing to reduce costs and a GFE advanced composite rotor was designed, fabricated and tested. Structural flexibility inherent in the GFE advanced composite rotor required redesign of the axial servo loop control system to obtain magnetic levitation. Implementation and testing of the new control system are described. Operational tests of the magnetically suspended, advanced composite rotor to 12,000 RPM are reported, the tests being the first known tests of an advanced composite rotor on magnetic suspension. Tests at higher rotational speeds up to 15,000 RPM were precluded by dynamic interactions in the system.

An improved, full-scale 20-kWh flywheel system was designed in FY-81 based on the experience gained during the previous two years of the flywheel project. A smaller storage capacity of 20 kWh was chosen for the new design because solar photovoltaic residential prototypes constructed as part of the Lincoln Laboratory Residential Experiment Stations at Concord, Massachusetts, and Las Cruces, New Mexico, had demonstrated that the trend in photovoltaic-powered homes of the future would be toward energy efficient, passive designs with reduced electrical loads and reduced electrical storage requirements. Simulation modeling of a residential flywheel energy storage unit over a period of a month was accomplished using electrical load data from a lived-in monitored home and photovoltaic array electrical output data from a real array on a residential prototype. It was found that the peak power demand normally seen by the utility was diminished by over 75% with residential flywheel energy storage.

2.0 INTRODUCTION

The goal of the project is to develop a flywheel system to store the electrical output from a solar photovoltaic array, to convert it to regulated 60-Hz ac for use in residences or load centers, and to establish its performance, worth and cost.

The project includes the following major tasks:

- o Design and conduct system studies of a full-scale residential magnetically supported solar photovoltaic flywheel storage system.
- o Perform economic manufacturing cost studies and user worth studies of residential and 100-kW load center units.
- o Build and test a 1/10-scale working residential system capable of operating in either a stand-alone or utility-interactive mode, and experimentally evaluate its performance and efficiency.
- o Test the 1/10-scale system over a range of residential loads and off-design conditions; modify the test setup to include an advanced composite rotor.

The first three tasks listed above were accomplished in FY-79 and FY-80. The fourth task, the testing of the 1/10-scale system over a range of residential loads and the construction and testing of an advanced prototype flywheel unit with a composite rotor, was completed in FY-81. The flywheel economic manufacturing cost studies discussed herein were prepared by three industrial firms, Theodore Barry Associates, Kelsey-Hayes Research, and Garrett AiResearch; the user worth analysis was prepared by the MIT Energy Laboratory. Both of these study elements were performed under subcontract to MIT Lincoln Laboratory. The flywheel system being developed is also ideally suited to other storage applications for wind, load-leveling and peak shifting systems.

The report which follows first describes the flywheel storage concept being developed by MIT Lincoln Laboratory. Then the characteristics of the experimental 1/10-scale prototype flywheel storage unit and its mechanical, electrical and magnetic elements are discussed. The Lincoln Laboratory

prototype flywheel test setup is described and measured component and system efficiency measurements are reviewed. Next, a full-scale, 40-kWh residential flywheel storage unit design is presented along with estimates by industrial firms of manufacturing costs to produce such storage units and a comparison of those costs with the user worth analysis. The design and testing of an improved 1/10-scale prototype flywheel unit equipped with a GFE advanced composite rotor is described. Modifications of the axial magnetic bearing servo system to accomplish these tests are reviewed. Design features of an improved 20-kWh flywheel storage unit are discussed. Finally, digital simulations of flywheel energy storage units in conjunction with a residence are offered.

3.0 FLYWHEEL STORAGE CONCEPT

For the past three years, MIT Lincoln Laboratory has been working on a flywheel storage system for solar photovoltaic (PV) applications with the following major components:

Magnetic bearings
Maximum-power-point tracker
Motor-generator
Low-cost rotor (not part of this project)
Integrated power-conditioning electronics
Vacuum housing.

The unit is intended to be a complete interface between a solar PV array and an ac load and to be used in residential or load-center applications. The residential system concept is shown in the artist's sketch in Fig. 3-1 and its major components are depicted schematically in Fig. 3-2.

C74-1899

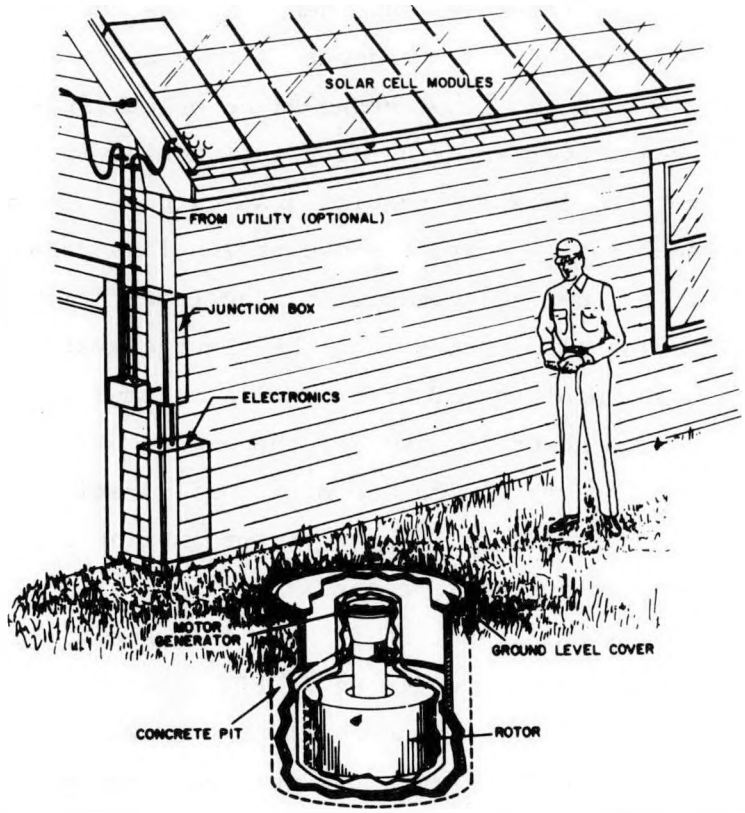

Figure 3-1. Residential photovoltaic flywheel system.

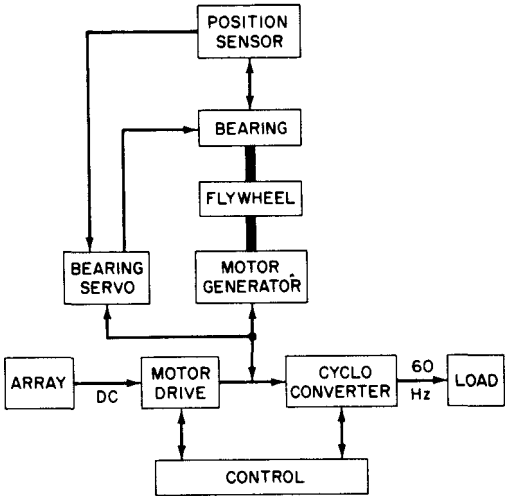

Figure 3-2. Flywheel system schematic.

During the day, the system stores electricity in the flywheel from PV modules on the roof of the residence and then converts the rotational mechanical energy back to electricity, as needed to supply electrical loads. The flywheel system may operate in either stand-alone or utility-interactive modes with a stand-alone cycloconverter or utility-interactive inverter being used, respectively, to convert DC input to regulated AC output. The key elements in the present flywheel approach are the use of low-loss magnetic suspension bearings with long life and high reliability, the integration of motoring and output power-conditioning electronics into the storage system to minimize system cost, the operation of the PV array at its maximum power point with the maximum-power-point tracker to maximize the amount of electricity stored in the flywheel system, and the selection of a configuration (rotor suspended from a flexible quill) which is tolerant to rotor imbalances expected in early-generation, advanced composite rotors.

Flywheel storage system parameters for a 1/10-scale, residential and 100-kW load center applications are listed in Fig. 3-3. The 40-kWh, full-scale residential unit is rated for 8-kW, steady-state ac power delivered to a load. The parameters for the 1/10-scale prototype unit were selected based on flywheel scaling laws previously reported in reference 3-1. The 1/10-scale

prototype is designed to store 1 to 4 kWh of energy; 1 kWh with a steel rotor and 4 kWh with an advanced composite rotor. Its maximum rotational speed is 15,000 RPM with an operational range from 7,500 RPM to 15,000 RPM. The input and output power rating of the prototype unit is 0.625 kW.

C74-1571

PARAMETERS	UNIT	SUBSCALE	40-kWh RESIDENCE	500-kWh LOAD CENTER
ENERGY STORED	kWh	1 TO 4	40	500
ROTOR WEIGHT	lbs	350	2,700	33,000
ENERGY AVAILABLE	kWh	0.75TO 3.0	25	325
MAXIMUM SPEED	krpm	15	12	6.5
POWER INPUT	kW	0.50	8	100
POWER OUTPUT				
STEADY STATE	kW	0.50	8	100
PEAK	kW	0.625	10	100
INPUT O.C. VOLTAGE MAXIMUM	VOLTS DC	400	400	800
INPUT S.C. CURRENT MAXIMUM	AMPS DC	2.5	40	260
INPUT VOLTAGE RANGE	VOLTS DC	220-330	220-330	440-660
INPUT CURRENT MAXIMUM	AMPS DC	2.3	35	230
OUTPUT VOLTAGE	RMS VOLTS DC	110	220 C.T.	440
MAXIMUM OUTPUT CURRENT	RMS AMPS PER PHASE	5.6	45	130
PHASES	NO.	1	1	3

Figure 3-3. Flywheel system parameters.

As noted in Fig. 3-3, the maximum rotor spin speed of the flywheel unit is reduced as the system is scaled from 1/10-scale to full-scale residential and then to 500-kWh load center size. This results[3-1] from the fact that rotor speed is limited by material stresses. These stresses are set by rotor diameter and spin speed. For a fixed material stress level and fixed shape factor, the energy stored is proportional to total weight and volume. Stress is given by:

$$S_r \sim L_r^2 w^2 \quad (1)$$

where L_r = diameter of the rotor

ω = rotor spin speed, rad/sec.

Energy scales for constant shape factor as:

$$E \sim M_r L_r^2 \omega^2 \sim L_r^{5\ 2} \quad (2)$$

where M_r = mass of the rotor.

Therefore, for constant stress, as a function of energy:

$$L_r \sim E^{+\ 1/3}, \quad (3)$$

and

$$\omega \sim E^{-\ 1/3}. \quad (4)$$

Equation 3 shows that rotor mass (and therefore cost) is proportional to the energy stored. Equation 4 indicates that for constant rotor stress, the rotor spin speed decreases as the energy stored increases.

Solar PV power systems presently being developed have invariably used electric storage batteries when on-site storage is required. Moreover, studies of future PV power systems assume continued use of batteries for on-site storage, albeit with more advanced, efficient and inexpensive battery designs. This predominance of batteries is due at least in part to the generally held conviction that no other on-site storage system can compete on an efficiency and economic basis with batteries for PV usage. However, studies performed during the past year at MIT Lincoln Laboratory and discussed later in this report show that flywheel energy storage can be technically and economically competitive with either present-day or advanced storage batteries. This conclusion was reached after comparing battery and flywheel storage in a PV system context. The overall in-out storage efficiency of the flywheel system was found to be several points higher than that of a battery system, when battery storage subsystem efficiencies for the maximum-power-point tracker and inverter are included in addition to the battery storage efficiency. PV flywheel systems were also found to be cost competitive with battery systems

when battery associated costs for inverter, battery charger, microprocessor controller, battery room and environmental control requirements are included in the determination of the total cost for a battery storage system.

4.0 1/10-SCALE PROTOTYPE FLYWHEEL STORAGE UNIT

4.1 Preliminary Design Studies - 40-kWh Residential Unit

The flywheel storage program was initiated in FY-79 by developing preliminary design layouts for a number of 40-kWh flywheel system concepts using magnetic bearings. The designs were based on earlier experience at MIT Lincoln Laboratory in the development of energy storage and control flywheel systems with magnetic bearings for satellite use.[4-1,4-2] Two generic flywheel configurations were considered: a flywheel rotor underslung on a thin quill beneath the magnetic bearings versus the conventional technique of supporting the rotor between magnetic bearings above and below. Five configurations of each generic type were considered. Each configuration explored the relative merits of various physical placements of the various components: magnetic bearing system, permanent magnet motor-generator, flywheel rotor, and rotor support shaft assembly.

The 40-kWh residential flywheel energy storage configuration shown in Fig. 4-1 was selected from these design configurations as the most promising approach for further detailed study. In this preferred approach, a six-element, magnetic bearing unit supports the flywheel rotor with three of the magnetic bearings clustered at the top and three magnetic bearings clustered at the bottom of the bearing shaft. The spacing between bearing clusters is provided to ensure static pendulum stability of the magnetically suspended flywheel rotor. The motor-generator unit is attached to the top of the bearing shaft where it is easily accessible for maintenance or repair. The rotor is supported by a thin flexible quill attached rigidly to the top of the bearing shaft. The quill telescopes through the hollow interior of the bearing shaft assembly to minimize the overall height of the flywheel unit. Mechanical touchdown bearings are provided to support the rotor in the unlikely event that magnetic suspension is lost. The flywheel system is enclosed in a vacuum container to eliminate aerodynamic drag effects on the spinning rotor. An axially active, radially passive, permanent magnet suspension system is used. An axial position feedback control loop with auxiliary electromagnetic control coils is provided to ensure axial position stability.

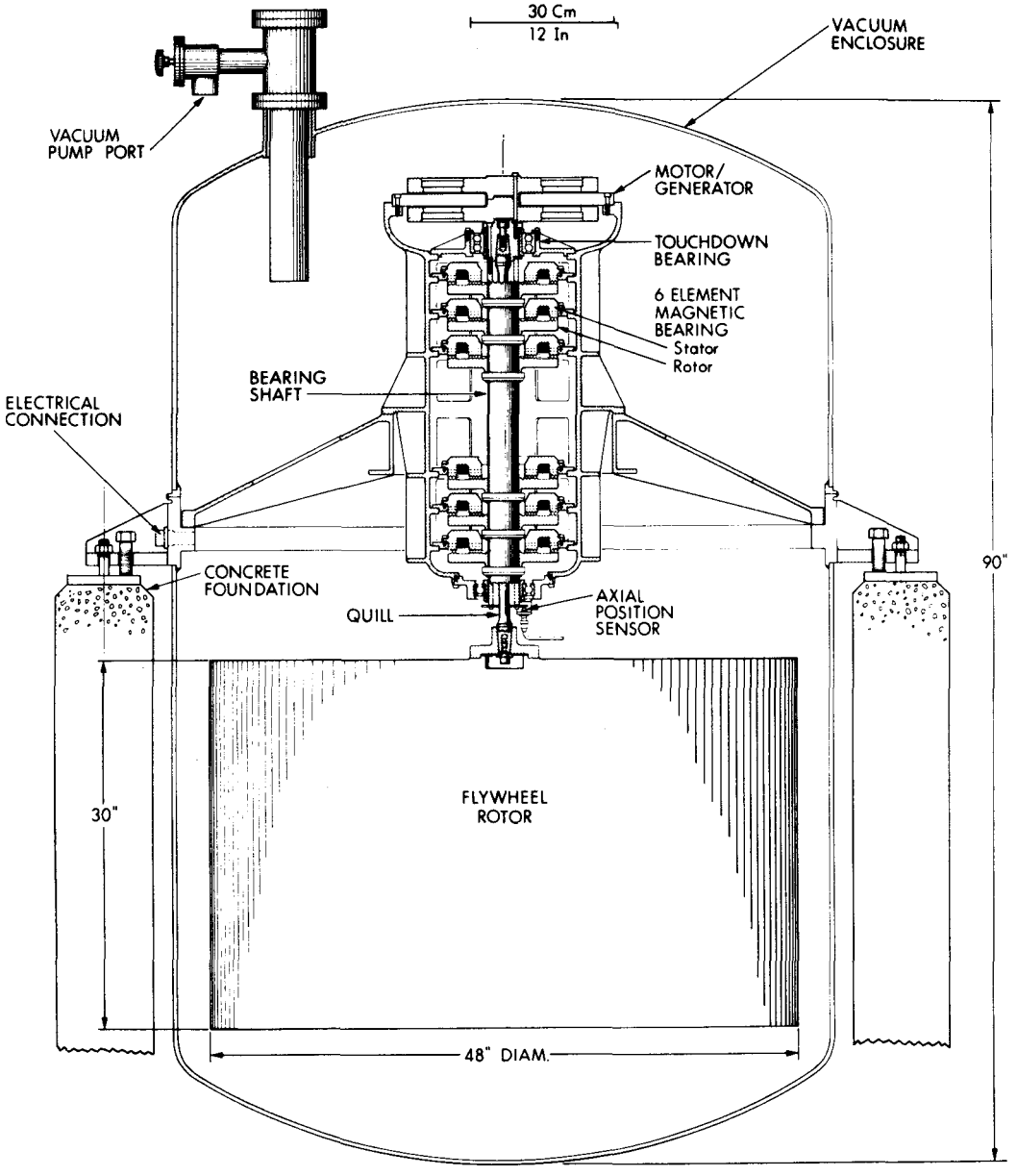

Figure 4-1. 40-kWh residential flywheel energy storage unit.

The overriding reasons for the selection of the configuration shown in Fig. 4-1 include the simple one-sided interface between the rotor and the bearing shaft/quill support system, ease of access to the motor-generator, natural pendulum stability of the magnetic bearing/rotor assembly, a telescoped design to minimize the vertical height of the flywheel system and a flexible quill which is tolerant to rotor imbalances. The simple rotor-shaft interface allows rotors to be exchanged easily, so that new technological developments in rotors can be incorporated in the storage system, and facilitates the testing of advanced composite rotors in conjunction with the magnetic bearing suspension, a major program goal. The use of a flexible quill to offset rotor imbalance effects was demonstrated analytically using dynamic analysis computer programs. These computer programs were developed concurrently with the mechanical design of the system.

4.2 Mechanical Description of the 1/10-Scale Prototype

A 1/10-scale prototype of the full-scale residential flywheel system was designed, fabricated and tested. The elements of the subscale system are drawn in design layout in Fig. 4-2 and a photograph of the completed unit is shown in Fig. 4-3. The subscale unit is identical to the full-scale unit with the exceptions that the quill is not telescoped inside the bearing shaft and the motor-generator is mounted below the magnetic bearing. These design changes were instituted to obtain extra separation between components for ease of testing. However, system dynamics and component configuration and function were deliberately kept similar. The prototype flywheel rotor is a series of seven steel discs pressed onto a steel hub. The rotor with quill shaft, motor-generator rotors and magnetic bearing shaft and rotors weigh a total of 400 pounds and store 1 kWh of energy at 15,000 RPM. The use of the steel rotor allowed testing of the system concept before introducing the uncertainties of an advanced composite rotor design. For testing purposes, the 1/10-scale unit was installed in an existing vacuum test chamber at Lincoln Laboratory, Fig. 4-4. A cross-sectional view of the flywheel and containment system inside the existing vacuum tank is shown in Fig. 4-5.

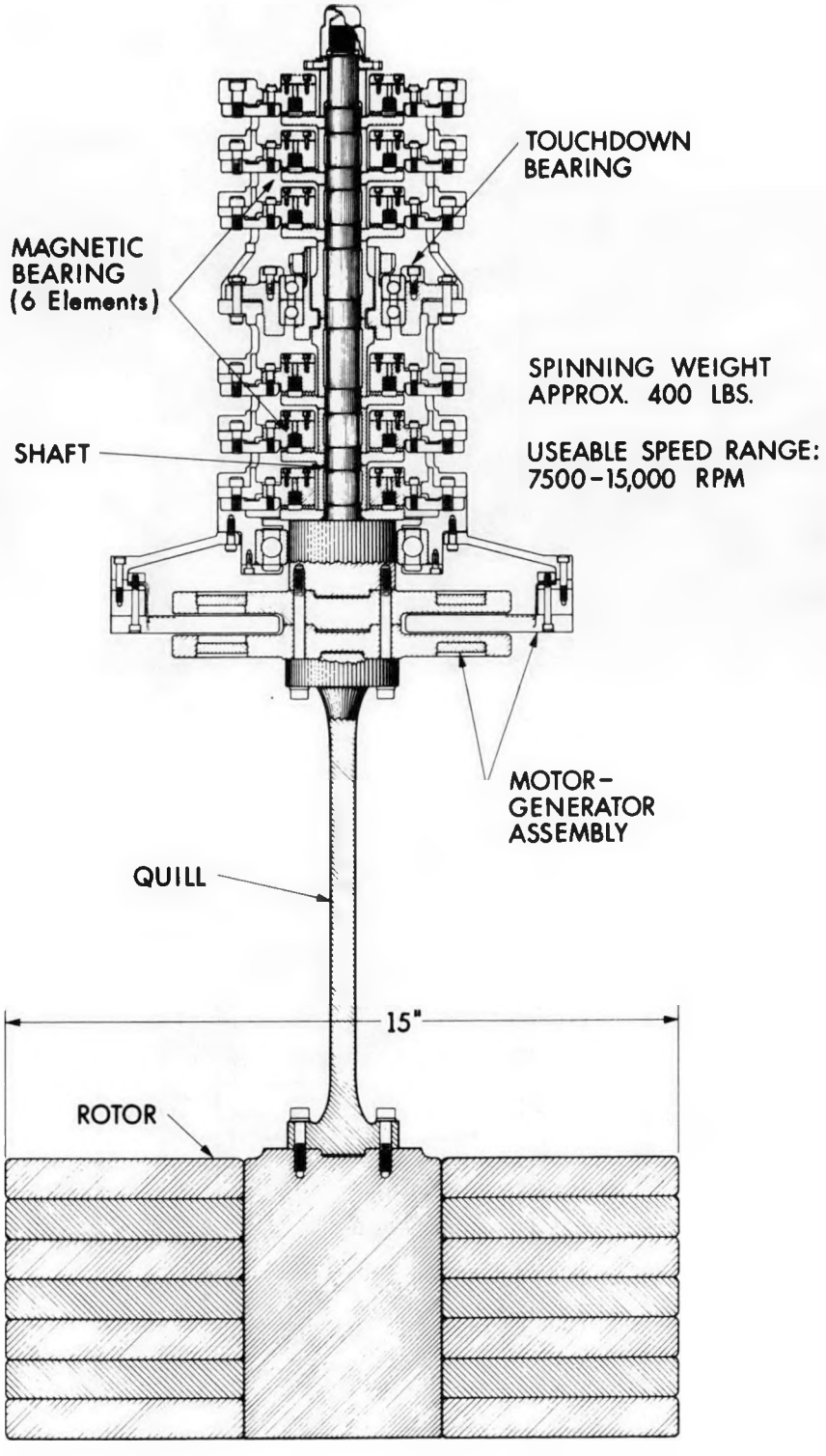

Figure 4-2. 1/10-scale experimental flywheel.

CP267-5403

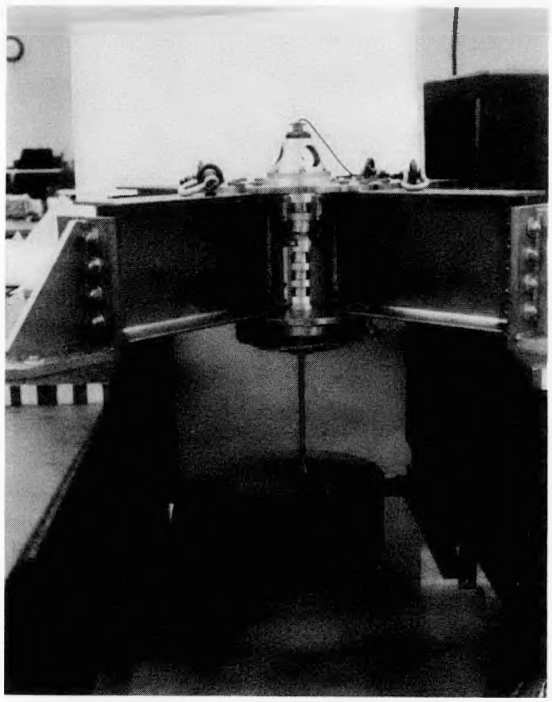

Figure 4-3. Photograph of the 1/10-scale prototype unit.

CP267-6931

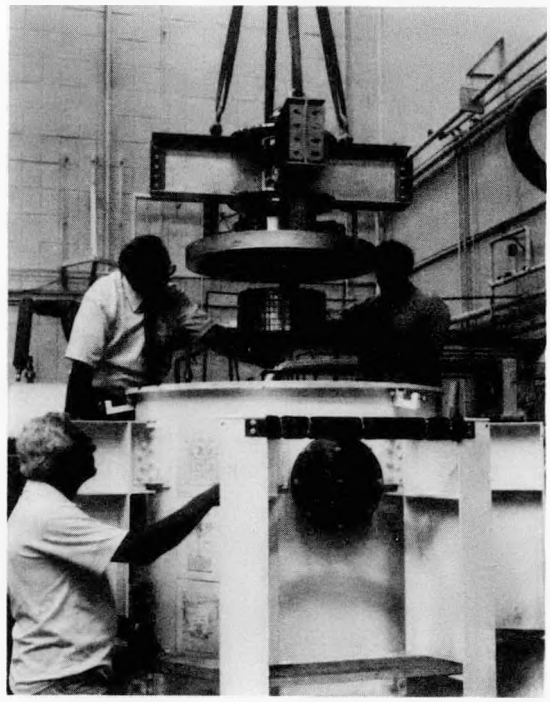

Figure 4-4. Installation of 1/10-scale flywheel system in existing vacuum tank.

C71-1019

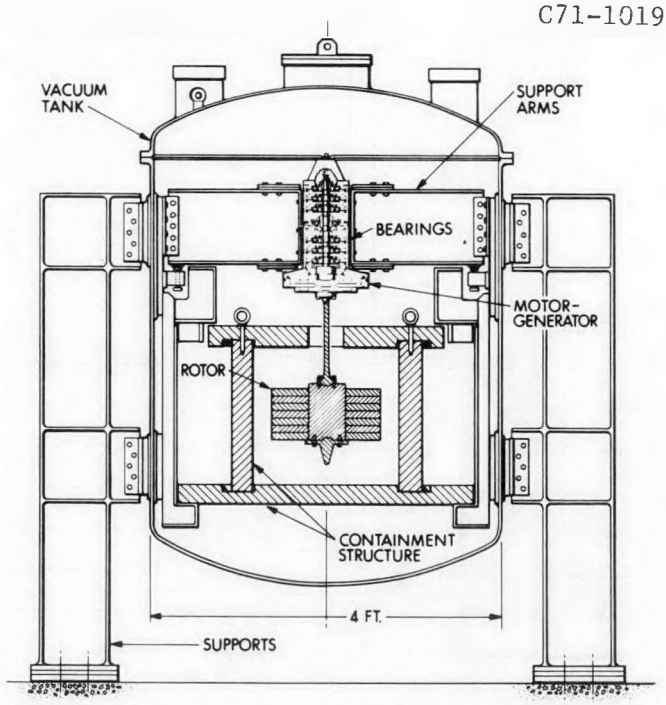

Figure 4-5. Subscale flywheel test chamber.

The flywheel system was designed for continuous operation to speeds of 15,000 RPM in a vacuum. The motor-generator rotor and flywheel rotor were proof tested to 16,500 RPM before installation in the vacuum tank. Individual elements of the flywheel system were designed to have a first modal frequency above the maximum operating speed of 250 Hz (15,000 RPM). The I-beam support system between the flywheel system and the vacuum enclosure was also designed to have its first modal frequency above 250 Hz. The elements of the rotating system were balanced separately except for the motor-generator rotor. For the motor-generator, a tandem set of motor-generator rotors was balanced as a unit to minimize balance errors due to magnetic forces. A more detailed description of the 1/10-scale flywheel, including magnetic bearings, motor-generator and flywheel rotor, is provided below.

4.2.1 Magnetic Bearings

A magnetic bearing assembly was used to support a rotating element weighing 400 pounds and the magnetic bearing concept is shown in Fig. 4-6 and Fig. 4-7. Six identical bearings are used to support the rotating system weight and to provide transverse moment stiffness. The lifting force is based on a magnetic pressure of 14 psi. The lifting area is equally divided between the inner and outer fringe ring areas. Fringe rings in the magnetic bearings focus the magnetic flux in concentric circles and provide the transverse stiffness of the magnetic bearing by generating a passive restoring force as a function of fringing eccentricity. The axial degree of freedom is actively controlled along the spin direction by the magnetic bearing servo control system. The six magnetic bearings are densely clustered into two groups to provide maximum transverse moment stiffness and to leave the area between the two groups available for the upper touchdown ball bearings.

C74-374

C74-1567

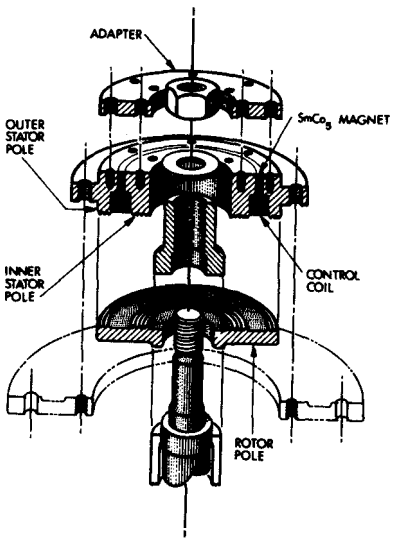

Figure 4-6. Magnetic bearing.

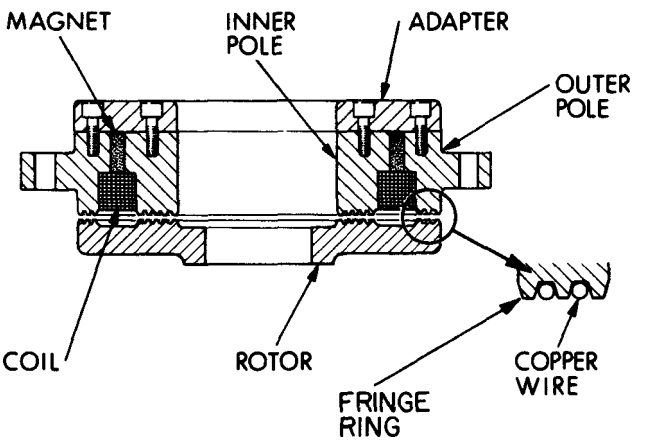

Figure 4-7. Magnetic bearing details.

The materials for the magnetic bearing stator were selected based on their magnetic properties. The inner and outer pole pieces were chosen to have a high permeability and the adapter was non-magnetic. The material selection for these items is given in Table 4-1.

Table 4-1

MAGNETIC BEARING STATOR MATERIALS

Outer Pole	High Silicon Steel
Inner Pole	High Silicon Steel
Adapter	303SS
Magnet	SMC05
Coil	100 Turns #22 Magnetic Wire

The fringe rings have an 18-mil land and are separated by grooves which are 57-mils wide and 57-mils deep, with a circular cross section at the bottom. This provides a space-to-land ratio of 3.0.

The nominal magnetic bearing gap in the axial direction between the fringe ring rotator and stator is 10 mils. Stringent manufacturing and assembly tolerance control were maintained for each part in the magnetic bearing system. Dimensional tolerance was limited to 1 mil and concentricity to a fraction of a mil. Accumulative errors in the axial direction for both position and parallelism of all six bearings were limited to 1 mil by machining the magnetic bearing adapter mounting plate based on assembly measurements. A partially completed assembly of the magnetic bearings is shown in Fig. 4-8. Measurements of each bearing stage were made with respect to a reference surface and compared to the corresponding measurements on the magnetic bearing stator support housing. The adapter plate was then machined to obtain the 10-mil bearing gap. The completed magnetic bearing assembly is shown in Fig. 4-9.

CP267-5307

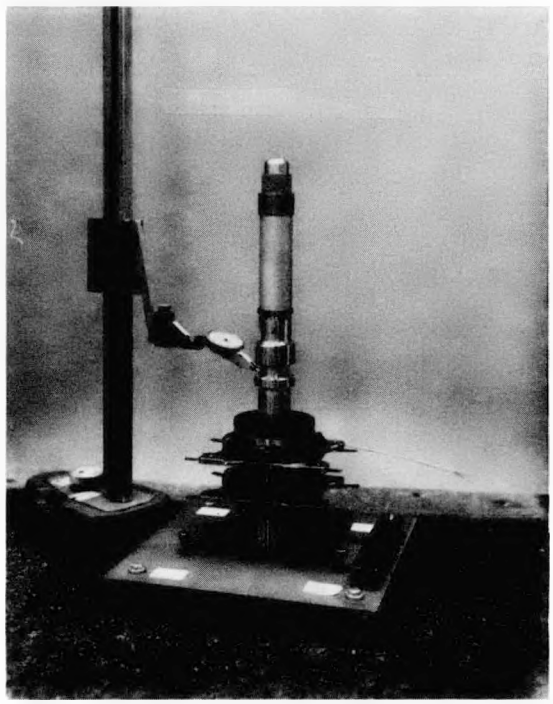

Figure 4-8. Magnetic bearing partial assembly.

CP267-5346

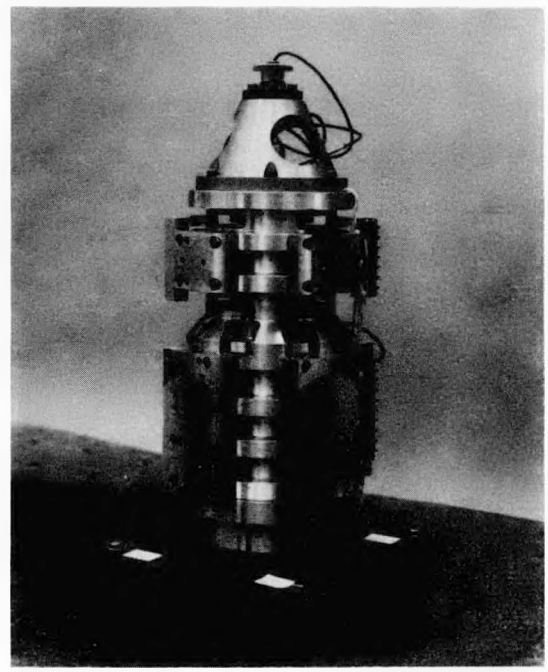

Figure 4-9. Magnetic bearing - shaft and support housing assembly.

4.2.2 Magnetic Bearing Shaft Assembly

The shaft assembly consists of six magnetic bearing rotors mounted to a shaft and positioned by spacers as shown in Fig. 4-10. The assembly is retained by a threaded nut at the top end of the shaft. The rotors are mounted to the shaft with a 0.2-mil interference fit and the sleeves are a slip fit. The OD of the lower flanged end of the shaft provides the lower mechanical touchdown bearing radial restraint. The grooved sleeves in the center of the shaft provide both radial and longitudinal restraint for the upper mechanical touchdown bearing. Parallelism of the rotors and sleeves was tightly controlled to minimize accumulated errors. Dimensional control of these elements in the axial direction was not critical since the 10-mil magnetic bearing gap was controlled by machining the adapter mounting plate at assembly, as mentioned previously.

C74-1221

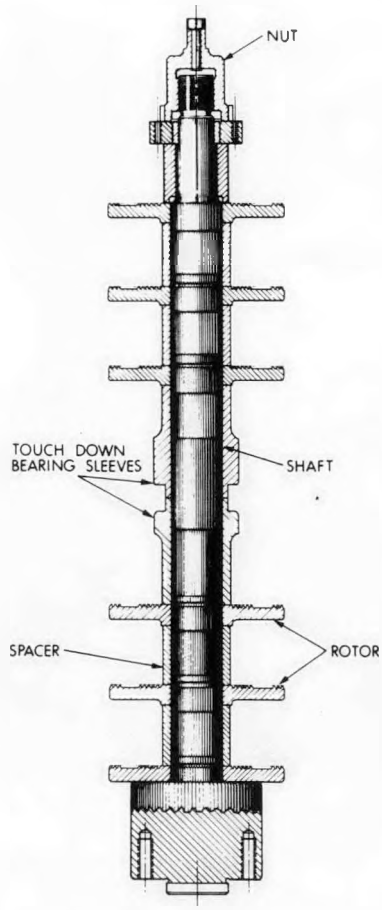

Figure 4-10. Shaft assembly.

4.2.3 Stator Support Housing

The stator support housing, Fig. 4-9, is a split aluminum housing that supports the six magnetic bearing stator assemblies, the upper and lower mechanical touchdown bearing assemblies, the motor-generator stator, the axial control sensor, and test instrumentation including three transverse shaft sensors which monitor shaft position. Adapter blocks are mounted to the housing to provide the interface for the beam supports that adapt the flywheel system to the vacuum chamber. Figure 4-11 is a photograph of the actual components during assembly.

CP267-5400

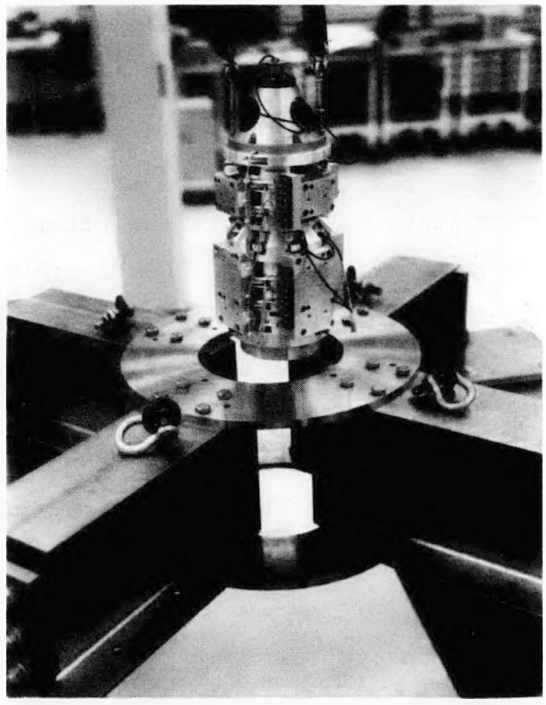

Figure 4-11. Assembly of magnetic bearing and support structure.

4.2.4 Motor-Generator

The essential characteristics of the motor-generator rotor are given in Table 4-2.

Table 4-2

MOTOR-GENERATOR ROTOR CHARACTERISTICS

	Housing	Return Path	Magnet
Material	Titanium 6AL4V	416SS	SMC05
Magnetic Property	Nonmagnetic	Magnetic	Magnet
Fit	---	Interference	---
Balance		Assembly only	
Tensile Stress	138,000	75,000	42,700 (compression)
Working Stress PSI	38,000	21,000	7,000
Factor of Safety	3.6	3.6	6.0

The motor-generator consists of two rotating permanent magnet disc assemblies and a fixed armature, Fig. 4-12. The titanium discs contain a washer-shaped magnetic return path ring and ten $SmCo_5$ magnets, Fig. 4-13. Assembly of the return path ring and the magnets was accomplished without the use of fasteners. The ring inside diameter is mounted to the disc with a 6-mil interference fit and the magnets are held to the disc by magnetic attraction. The magnets are seated to the disc in the radial direction by centrifugal force. The magnets are positioned in place by mounting them in pockets in the disc, as shown in Fig. 4-14. A one-mil Mylar tape provides a compliant interface between the magnets and the disc to eliminate local stresses from surface asperities of either element. The basic strategy in this design concept was to support the magnet in pure compression with minimum restraint. The magnet is supported in the direction parallel to the spin axis by a 100g force magnetically induced and in the radial direction by approximately 20,000 gs induced by centrifugal loading. The concept was verified by proof testing the motor-generator rotors at 16,500 RPM.

C71-994

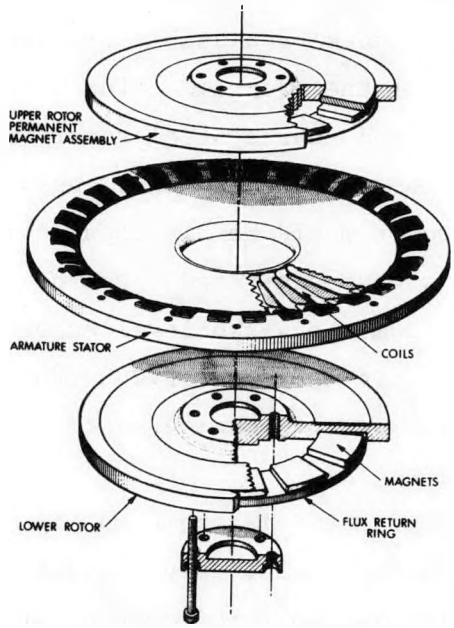

Figure 4-12. Motor-generator.

C74-1217

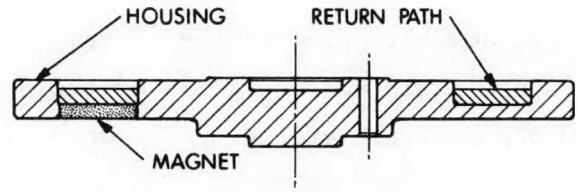

Figure 4-13. Cross section of motor-generator rotor.

C74-1218

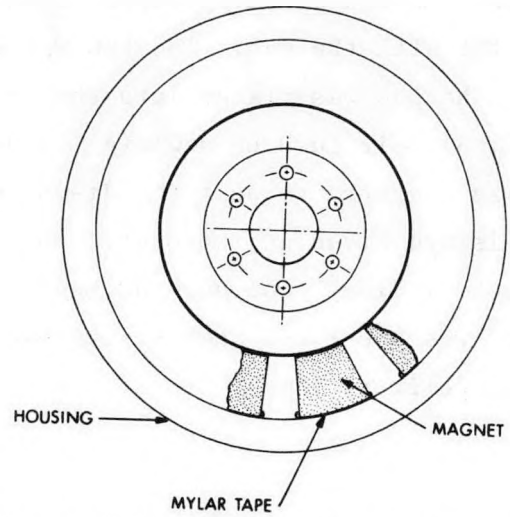

Figure 4-14. Motor-generator rotor.

4.2.5 Flywheel Rotor

The main goal of the flywheel program was to develop a usable flywheel system within the time and monetary constraints of the program. Since system aspects were to be emphasized, it was decided that a steel rotor would suffice to demonstrate the magnetic bearing system concept and that replacement of the steel rotor with an advanced composite rotor would be implemented after the complete magnetic bearing flywheel concept was demonstrated. Use of a steel rotor did diminish the energy storage capacity from the 4-kWh level expected with a composite rotor to the 1-kWh level, at a spin speed of 15,000 RPM. This temporary sacrifice of energy storage capability was not considered critical to the demonstration of the overall concept.

The basic configuration of the steel flywheel rotor is shown in Fig. 4-2 and a photograph of the actual wheel is shown in Fig. 4-15. Seven discs are mounted to a central hub. The containment system design requirements were lowered by constructing the rotor from seven thin discs rather than a single thick disc. The hub is five inches in diameter and seven-inches long and the discs are fifteen inches in diameter and one-inch thick. The hub is tapered (1° half angle) and the discs have a matching taper dimensionally controlled for a 20-mil interference fit with the hub. The hub was assembled with a 1000-ton hydraulic press. The hub was placed into the seven discs with a free fit and then pressed the final half inch to achieve the desired interference fit. A load of 600 tons was required to seat the discs as shown in Fig. 4-16. Candidate flywheel materials are given in Table 4-3. Mandrel-forged 4340Rc50 steel was used for the flywheel disc. The hub was made from Matrix II Rc60. Although the maraging steel was the first choice, its use was prohibited by material cost and quoted delivery time.

CP267-811

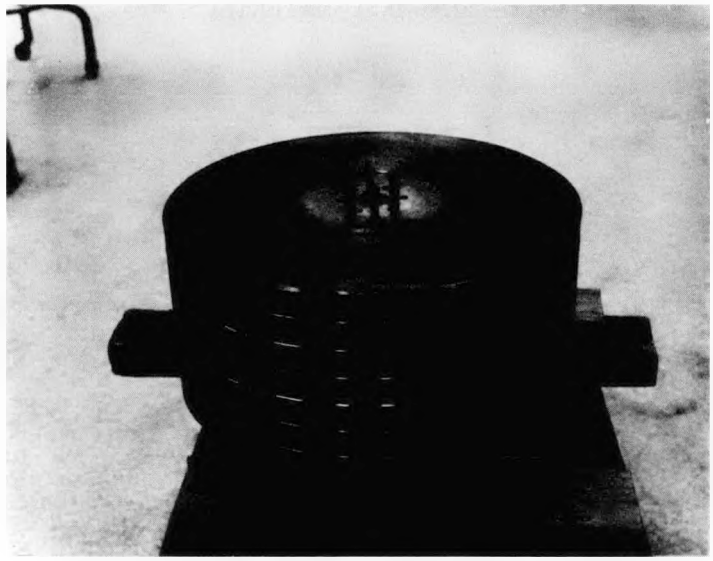

Figure 4-15. Flywheel rotor assembly.

C74-1216

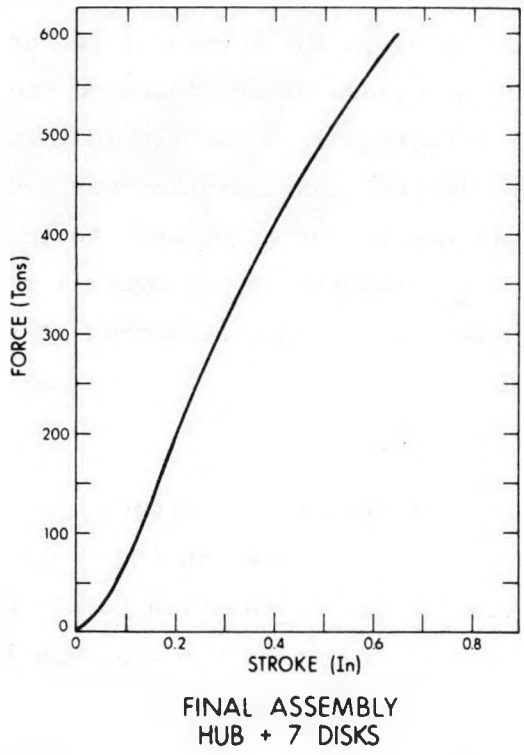

Figure 4-16. Loading in press.

Table 4-3

CANDIDATE FLYWHEEL MATERIALS

	4340 Steel	Vascomax 300 Maraging Steel
Tensile Ultimate (PSI)	260,000	294,000
Tensile Yield (PSI)	217,000	290,000
Fatigue Strength (PSI) 10^8 Cycles	-	125,000
Density $lb/in.^3$	.283	.289
Poisson's Ratio	. 32	. 30
$E \times 10^6$ (Modulus of Elasticity)	29	26.5

The variation of the total stress in a flywheel disc as a function of rotor speed is shown in Fig. 4-17. The stress component due to the interference fit decreases with increasing spin and reaches zero at about 17,500 RPM. Safety was a major consideration in the design of the steel flywheel rotor for the 1/10-scale prototype because of its intended use in an existing, above-ground vacuum system with personnel in close proximity to the test unit. The choice of a multiple-disc flywheel configuration was made to reduce the size (height) and mass of any fragment that might have to be contained by the containment system from that of a segment of the overall rotor to a fragment with the thickness of an individual disc. A description of the containment system may be found in Section 4.2.8.

4.2.6 Rotor-Quill Shaft

The quill shaft is a flexible support between the magnetic bearing/motor-generator and the flywheel rotor, as shown in Fig. 4-18. The quill is flanged at both ends to interface with a bolted connection to its mating components. The straight portion of the quill is eight-inches long and 7/16 inches in diameter and these dimensions were selected to comply with dynamic requirements of the system. The cylindrical portion is elliptically flared into the flanged ends

C74-1219

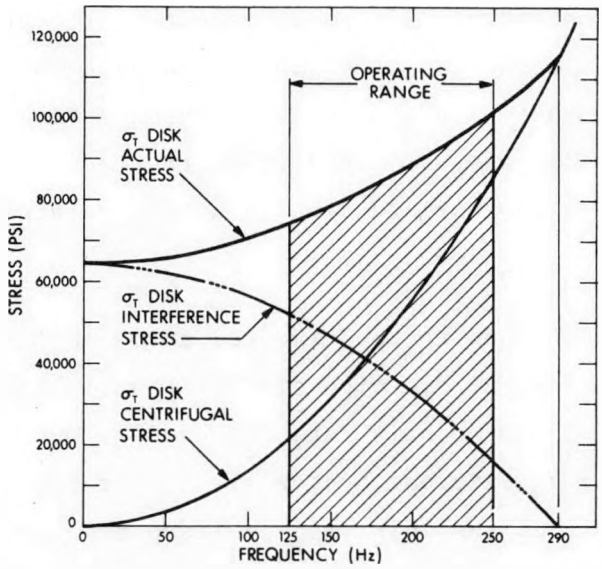

Figure 4-17. Flywheel disc stress - solid hub.

C74-1215

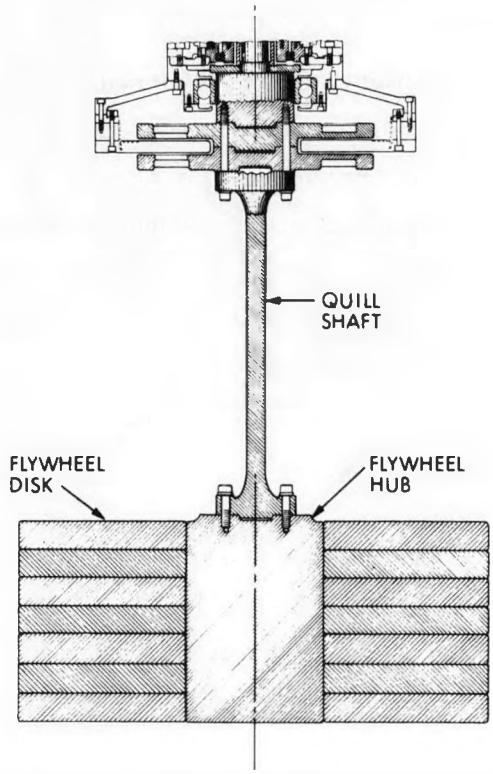

Figure 4-18. Details of rotor/quill shaft.

to minimize stress concentration. It was anticipated that the quill shaft would undergo approximately 5×10^9 stress cycles per year and should be made from a steel with a high fatigue strength. A maraging steel Vascomax 250 was chosen for the quill shaft. It was learned subsequently that the number of stress cycles was grossly overestimated since they only occur at non-synchronous whirl and with appropriate damping should be negligible.

4.2.7 Whirl Damper

A whirl damper was added to the flywheel system after initial flywheel system tests discovered a buildup with time of the amplitude of a low-frequency, 2-Hz whirl mode when the rotor spin rate exceeded 11,000 RPM. As discussed in Sections 4.5.8 and 4.5.9, internal hysteresis in the rotating assembly was identified as the cause of the whirl mode buildup and external damping was identified as the cure. The addition of the mechanical damper completely eliminated the low-frequency whirl mode and the flywheel system with damper now operates consistently at its maximum design speed of 15,000 RPM without problems.

Several options for implementing an external damper were considered. These included electromagnetic dampers and mechanical dampers at locations varying from the bottom of the flywheel rotor to the top of the magnetic bearing shaft. In the interest of a timely demonstration of the external damping cure to the whirl mode problem, a mechanical molded polyurethane damper was designed and fabricated, Fig. 4-19. The three-legged damper was installed at the top of the magnetic bearing shaft as shown in Fig. 4-20; a location selected because of ease of access and as a result of dynamic analyses. A photograph of the completed assembly is shown in Fig. 4-21.

CP267-5957

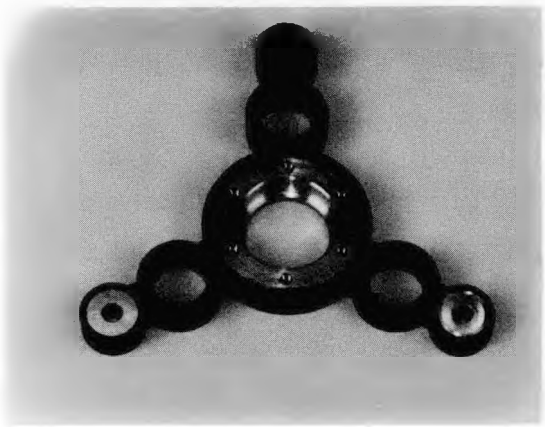

Figure 4-19. Molded polyurethane mechanical damper.

C74-1186

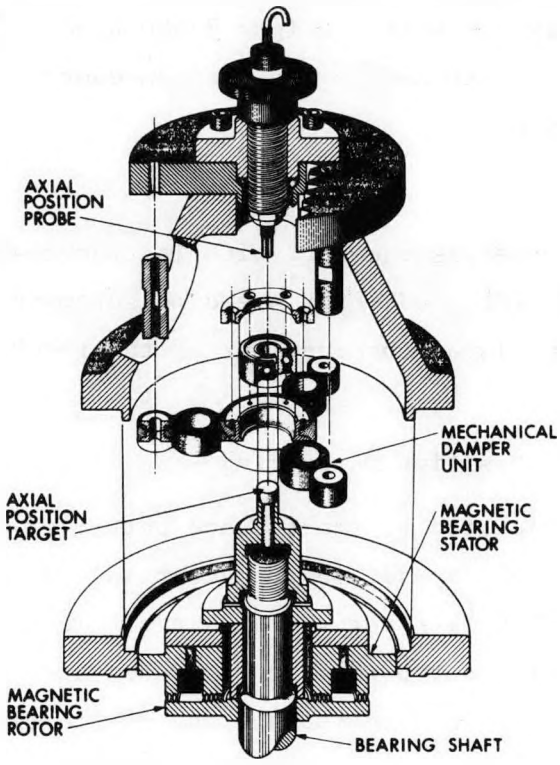

Figure 4-20. Exploded view of mechanical damper installation.

CP267-1096

Figure 4-21. Photograph of mechanical damper assembly.

4.2.8 Vacuum Test Chamber and Safety Containment System

The cylindrical test chamber with standard heads is four feet in diameter and is approximately five feet tall. An existing stainless steel chamber was modified by adding eight 10-inch, WF steel I-beam column supports, as shown in Fig. 4-5. Corresponding stainless steel stiffeners were added internally and served to support the safety containment system and to support arms at four points. The support arms were also fabricated from 10-inch, WF I-beams to meet the stiffness requirements. The entire system was designed to have a first modal frequency above the maximum operating speed of 250 Hz. The safety containment cylinder has a 20-inch ID and is three-inches thick. The flywheel is 15 inches in diameter which leaves a nominal 2.5-inch radial clearance with the ID of the containment cylinder. The top and bottom covers are fabricated from 2-3/4-inch steel and the entire containment system is fabricated from 1020 steel. The containment system and the flywheel support arms were nickel plated for protection. The containment system weighs 2,500 pounds and is freely supported, without fasteners, to accommodate the maximum energy transfer in the event of a flywheel failure.

4.2.9 Instrumentation

The 1/10-scale prototype flywheel system is equipped with instrumentation for magnetic bearing shaft position monitoring and rotor speed measurements and an optical view port is provided to allow visual observations of the flywheel rotor hub during system operation.

4.2.9.1 Magnetic Bearing Shaft Position Monitoring

Non-contacting inductive probes are located at the top and bottom of the magnetic bearing shaft to measure shaft radial position changes resulting from vibrational whirl in the magnetic bearing/quill rotor system. A single probe is mounted at the top of the bearing shaft and two additional probes are mounted at the bottom of the shaft. The single probe at the top and one of the two probes below are mounted in-line at the same azimuth location. These two probes permit measurement of the shaft centerline position including displacement from true center and gimbal rotation. The two probes at the bottom

are mounted in the same horizontal plane but at azimuthal angles separated by 65 degrees from each other. Physical constraints in the 1/10-scale magnetic bearing did not allow the probes to be separated in azimuth angle by 90 degrees. With use of a phase-shifting network, the outputs of the two probes are combined to generate the trajectory of the magnetic shaft in the horizontal plane. The shaft trajectory is then displayed on an oscilloscope. The shaft whirl direction and magnitude may be determined from this display. The inductive probe system employed is Kaman Sciences KD2300 series, using sensor probe 1 SU which is linear to a gap of 0.040 inch. The probe installation provided a position resolution of approximately 0.0002 inch with an absolute accuracy of about 0.001 inch.

4.2.9.2 Rotor Shaft Speed Measurement

Flywheel speed is determined by measuring the frequency of the generator output using a Data Precision Corporation digital frequency counter.

4.2.9.3 Test Chamber Vacuum Pressure

Vacuum pressure in the volume surrounding the rotor is measured with a standard thermocouple gauge for pressures down to 10^{-3} torr and with a VRC ionization gauge for pressures to less than 10^{-6} torr.

4.2.9.4 Optical Port for Visual Observations

The test vacuum tank is equipped with a viewing port and an internal mirror system which permits visual observations of the rotor/quill attachment hub and upper rotor surface during experimental tests, Figs. 4-22 and 4-23. A stroboscope was used through the optical viewing port to illuminate the hub and "stop" its rotation.

CP267-1088

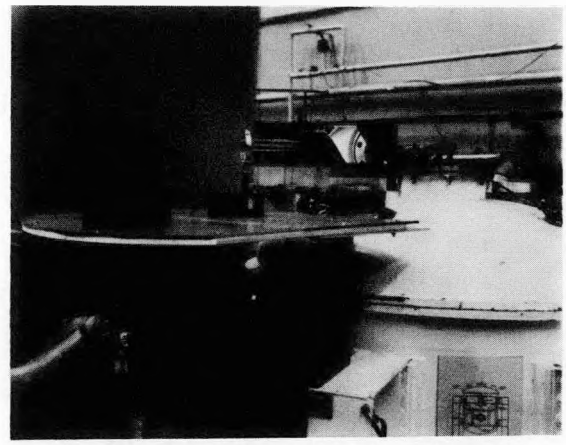

Figure 4-22. Viewing port optical system.

P267-1089

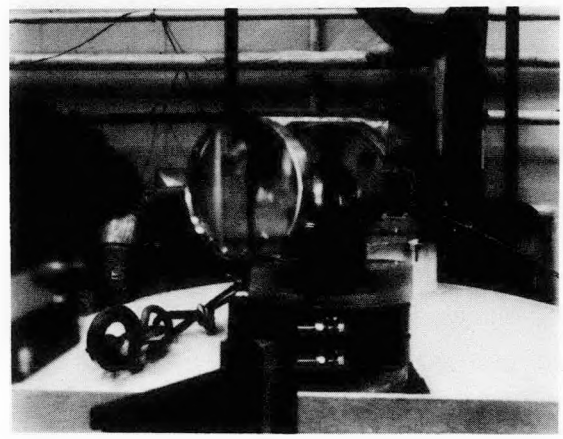

Figure 4-23. View of the rotor/quill attachment hub.

4.2.10 Moments of Inertia

The rotational and transverse moments of inertia of the flywheel system have been calculated as shown in Table 4-4. This calculation is based on component dimensional data and component weights measured during system fabrication, Fig. 4-24. The rotational moment of inertia of the complete flywheel system, including flywheel rotor, quill, motor-generator and magnetic bearing shaft assembly, is calculated to be I_{g_2} = 9958 LB-IN.^{2} while the transverse moment of inertia is I_T = 221, 518 LB-IN^2. These calculated moment of inertia are accurate to within one percent. The rotational and transverse moments of inertia of the 350-pound flywheel rotor component of the flywheel system are calculated to be Ig_{rotor} = 9852 LB-IN.^{2} and I_{rotor} = 6356 LB-IN^2. Thus the inertia ratio (Ig/I) of the flywheel rotor is:

$$\frac{Ig}{I}_{rotor} = \frac{9851.9}{6356.3} = 1.55.$$

The 350-pound flywheel rotor represents 99% of the rotational inertia of the flywheel system.

TABLE 4-4

1/10-SCALE EXPERIMENTAL FLYWHEEL MASS PROPERTIES

Item	Wt/Lb	Spin Axis Ig Lb-In.^{2}	Spin Axis Ig KG-m^2	Weight Kilograms
Shaft	4.08	.759	.0002	1.85
Shaft Hub	2.27	1.567	.0005	1.03
Fringe Rings (6)	2.93	3.532	.001	1.33
M/G	12.55	76.282	.0223	5.69
Bolts	.34	.299	.0001	.15
Quill Shaft	2.85	1.842	.0005	1.29
Bolts	.2	.176	.0001	.09
Flywheel Rotor	350.29	9851.906	2.8826	158.86
Bolts	.39	1.194	.0003	.18
Balance Hub	5.6	20.427	.006	2.54
Total	381.5	9958.0	2.9136	173.02
		Transverse Axis		
Total	381.5	221517.95	2.9136	173.02
Flywheel Ratio of Inertia:		$\frac{9851.906}{6356.3} = 1.55$		

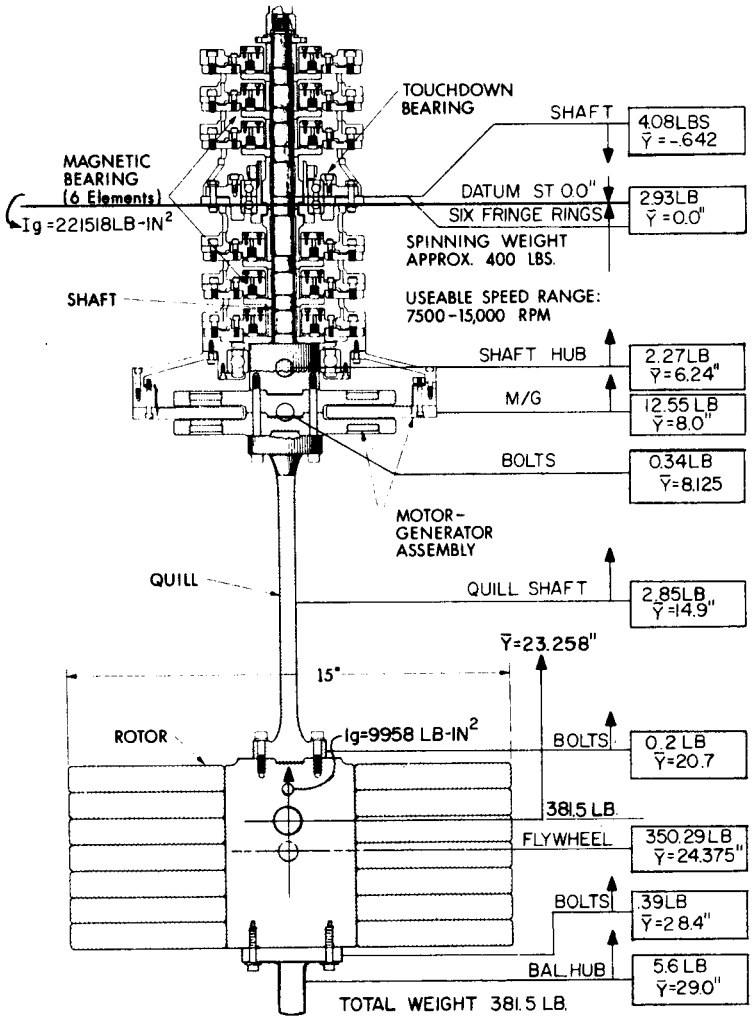

Figure 4-24. Dimensions and weights of moment of inertia calculations.

4.3 Flywheel Electrical System

The flywheel electrical system consists of four major elements: the magnetic bearing feedback control servo system, the motor drive system, the motor-generator system and the power conversion system. The power conversion system is either of the utility-interactive inverter type for utility interface applications or of the cycloconverter type for stand-alone applications. Both forms of power conversion equipment were developed and tested in the course of the present program. The flywheel electrical test setup is shown in Fig. 4-25.

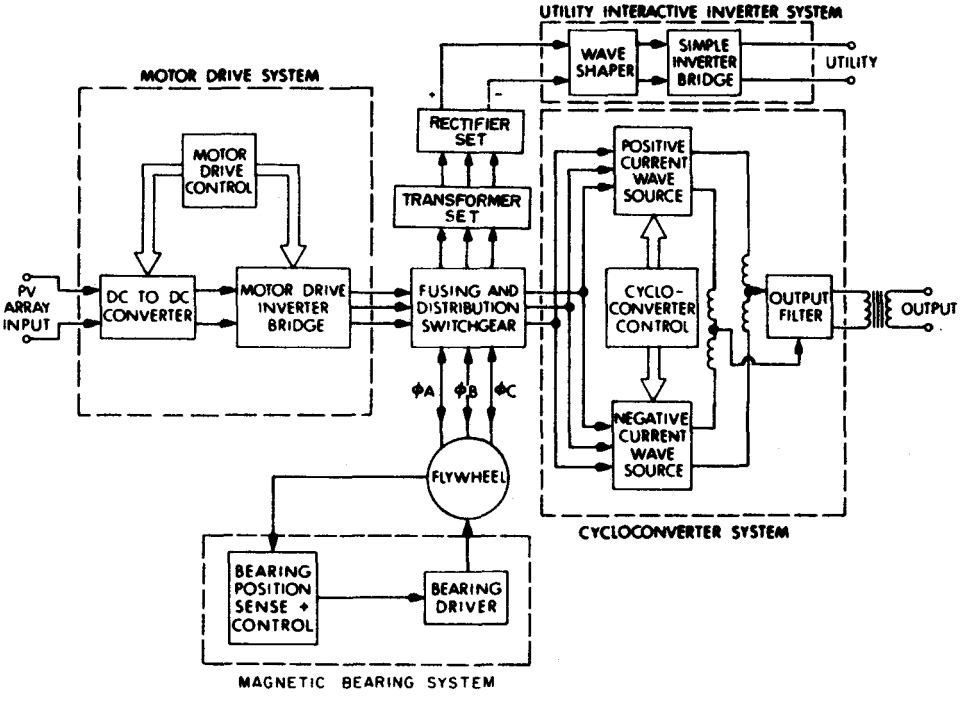

Figure 4-25. Flywheel electronic test setup.

4.3.1 The Magnetic Bearing Control System

The permanent magnet axial suspension system used in the prototype flywheel system behaves as a mass (rotor) suspended from a spring (bearing). Since the spring constant is in this case negative, the system is naturally unstable and the suspended mass will therefore come to rest upon the upper or lower vertical position limit stops. One vertically unstable equilibrium position exists between the upper and lower limit stops, for which the downward pull of gravity is exactly balanced by the upward magnetic force of the bearing. The purpose of the magnetic bearing servo control system, which is described in this section, is to maintain the flywheel actively at this vertical equilibrium position. In the prototype system, electromagnets are used as controllable vertical force sources which supply the restoring forces required to cancel the natural magnetic destabilizing forces. A nonconducting vertical position sensing probe is used to measure the axial position of the rotating shaft, and a signal proportional to the difference between the measured

and desired position is derived. This signal, with appropriate phase, magnitude and nonlinearity compensation, drives the vertical force sourcing electromagnets through the magnetic bearing driver amplifier. In this way, the rotating assembly is maintained at a constant vertical position, hovering between the upper and lower vertical limit stops. The block diagram for this feedback control system is shown in Fig. 4-26. The purpose of the remainder of this section is to describe the control characteristics and requirements for the elements of the servo system, which are:

1) The magnetic bearing
2) The axial position probe
3) The magnetic bearing driver amplifier
4) The axial servo control electronics.

C74-1240

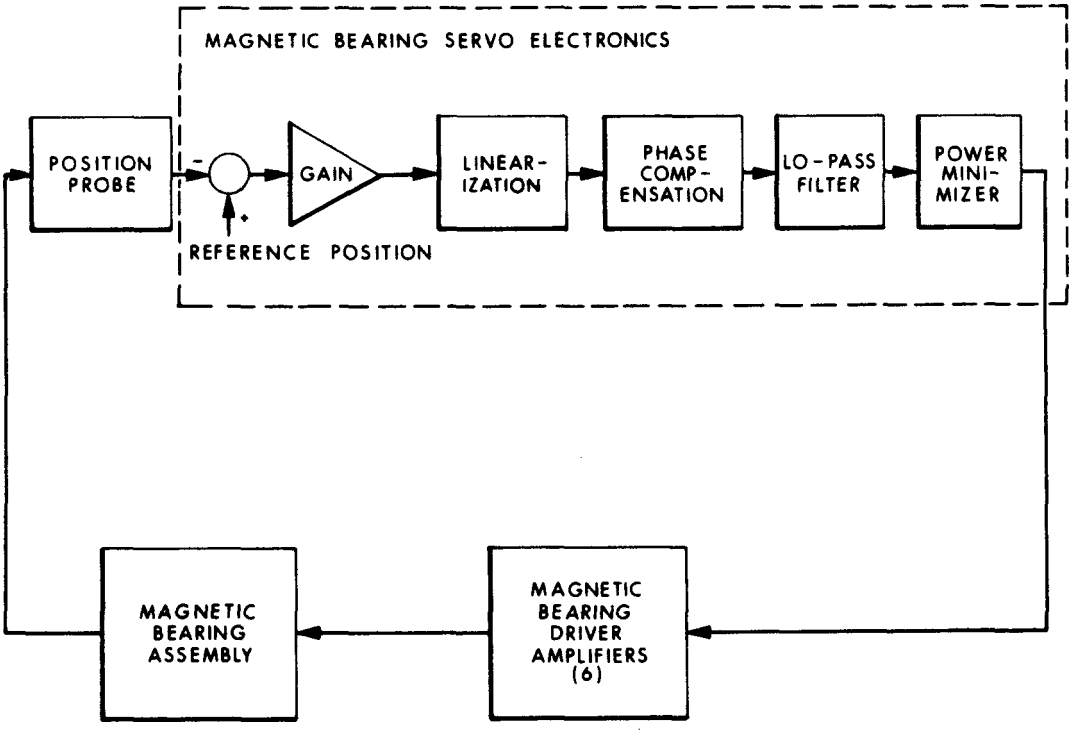

Figure 4-26. Block diagram of axial magnetic bearing feedback control loop.

4.3.1.1 Magnetic Bearing

The axially active magnetic bearing has an unstable equilibrium due to the presence of permanent magnets. This may be expressed as a transfer function from rotor vertical force to rotor displacement of:

$$\frac{1/m}{s^2 - a^2}$$

where m is the mass of the rotor, and a^2 represents the ratio of bearing negative spring constant to mass. This pole-zero plot is shown in Fig. 4-27a along with the associated Bode plot representation. The idealization has been made that the rotor behaves as a single mass, that the displacement and force are measured relative to an infinitely stiff reference, and that the bearing force is linear. To stabilize such an equilibrium, the vertical displacement is measured and a correcting force applied to the rotor. The conventional method of stabilizing the loop is to utilize lead-lag compensation in the servo. This produces a real zero in the left half plane (lead) accompanied by a pole at some higher frequency, as shown in Fig. 4-27b. As the gain is increased, the right half plane pole is brought over to the left of the origin and the system is stable. If the gain is too high, the high-frequency poles will travel into the right half plane and instability results. In the Bode plot representation, the lead-lag compensation results in a range of frequencies over which less than 180° phase lag exists in the loop transfer function. The gain must then be adjusted to create unity-gain crossover at a frequency in this range.

The biggest practical problem in doing this comes from the mechanical resonances in a nonideal system. If these are of very high Q factor (low damping), the result is a large peak in the servo gain at some frequency outside the region of positive phase margin, accompanied by a 180° phase shift. If this is high enough to cross unity gain, an oscillation will result. The Bode plot of the actual transfer characteristic of the prototype axial magnetic bearing is shown in Fig. 4-28. The transfer function magnitude exhibits the

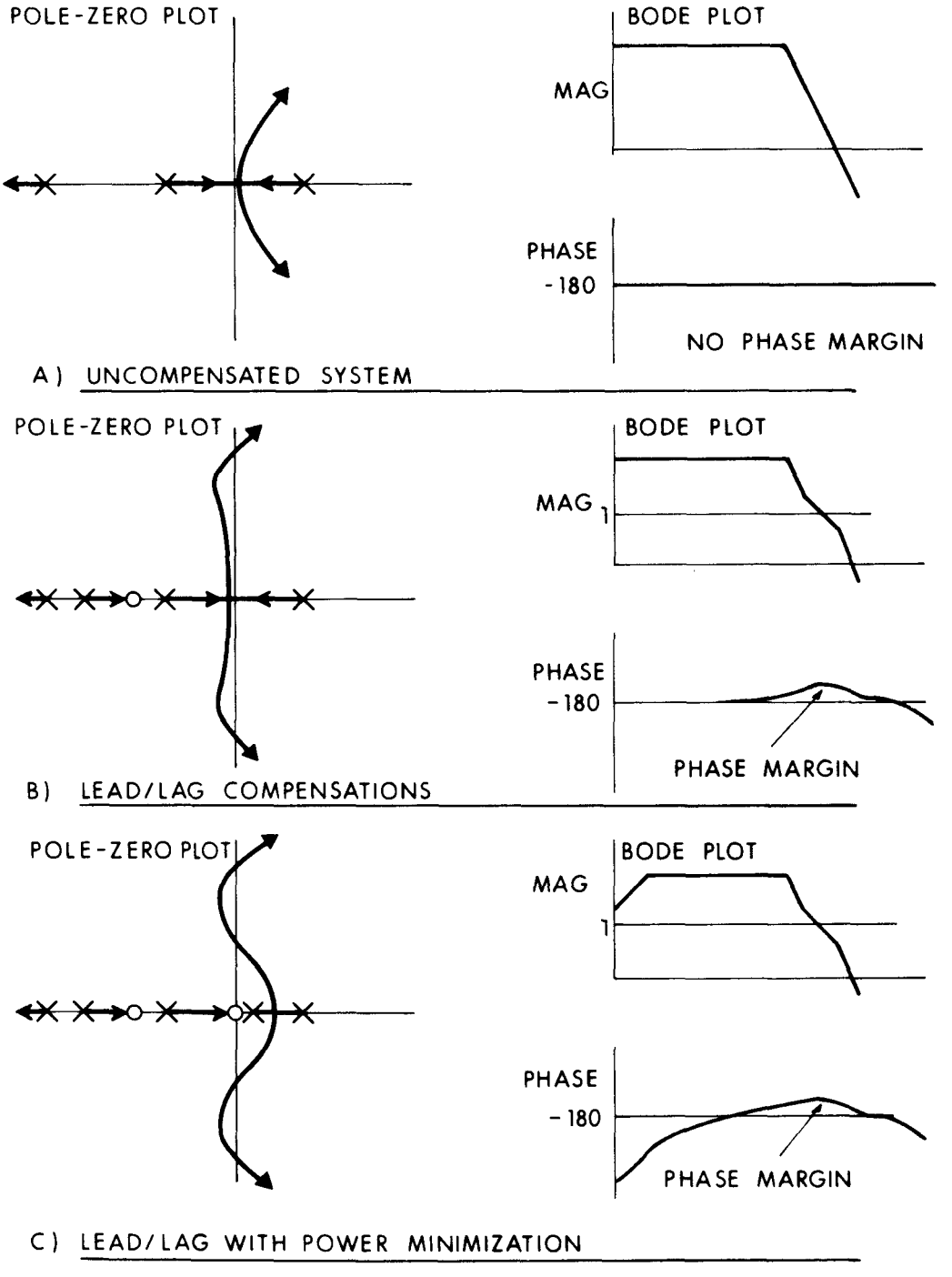

Figure 4-27. Bearing servo system-frequency domain models.

expected two-pole rolloff at 22 Hz, with additional singularities at 90 Hz and 416 Hz. Based on this measurement, the simple mass/spring model of the bearing can be refined to include the following elements:

1) A spring between the bearing stator and earth;
2) The bearing stator and some fraction of the stator assembly is considered to be a lumped mass which is attached to the side of the spring which is not connected to earth.

The schematic diagrams of the bearing model with and without the refinements are shown in Fig. 4-29. The values of the additional mass and spring, which are given in the figure, are determined using the constraints of the measured locations of the complex zero and pole pairs. From Fig. 4-28, it is apparent that the resonant peak at 416 Hz is a potential source of closed-loop oscillations, and that one of the following three steps must be taken to guarantee stability in the region of 416 Hz.

1) The transfer function of the bearing can be modified by mechanically damping the 416-Hz resonance or stiffening the support structure to raise the resonant frequency.
2) The magnitude of the loop transfer functions can be attenuated in the 416-Hz region through the use of electronic notch filters or elliptic-type low-pass filters.
3) The open loop phase shift can be controlled in the 416-Hz region so that an adequate phase margin is maintained despite the -180° phase swing associated with the 416-Hz complex pole pair.

Option 1 requires that the containment structure be redesigned and was therefore only considered as a last resort. The success of option 2 depends on tuning high Q electronic filters to match the exact mechanical resonant frequency. Although it is possible to design filters of exceptionally low drift, the natural variations of the mechnical resonant frequency with age and temperature may give rise to a stability-threatening frequency mismatch. Low Q filters avoid attenuation over a wide band but are unacceptable over a wide band because of their excessive phase shift.

C74-1238

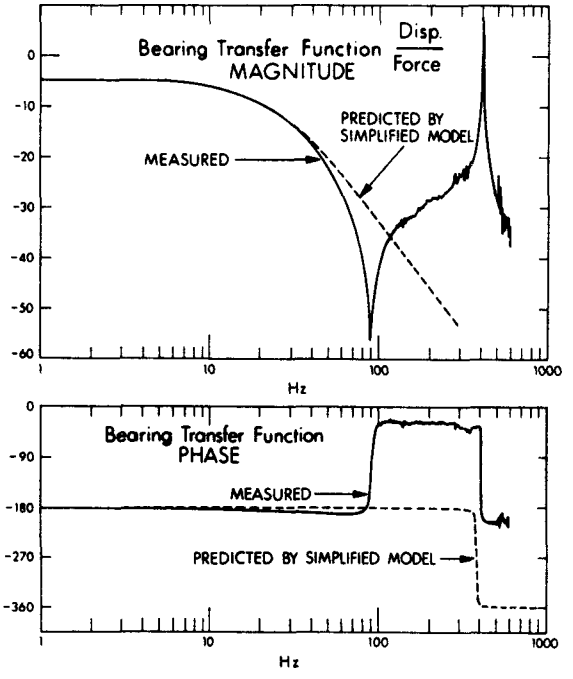

Figure 4-28. Magnetic bearing transfer function.

C74-1322

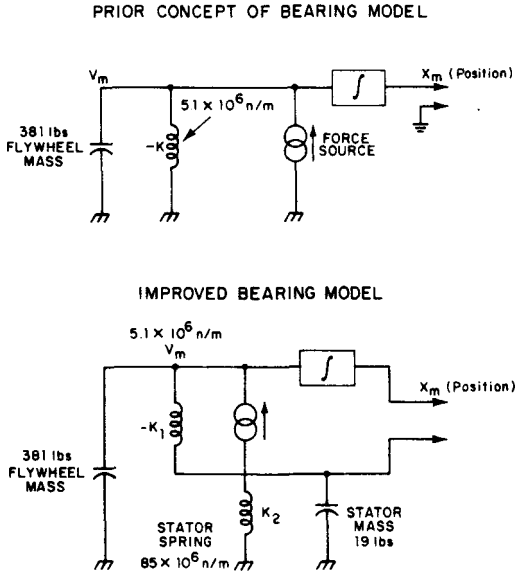

Figure 4-29. Lumped element models for dynamic analysis of axial magnetic bearing.

The control of the loop phase as described in option 3 was chosen for this application as the most practical means to achieve stability. The stability requirement is that the phase shift must not be an odd multiple of 180° over the frequency interval around 416 Hz in which the open loop gain is greater than or equal to one. This condition must be met despite the 180° phase swing which occurs within this interval at exactly 416 Hz as a result of the complex pole pair. In this system, a low Q 3rd-order filter at 200 Hz was used to control the open loop phase shift so that the phase at 416 Hz swings from 240° to 420°, safely centered between the 180° and 540° danger zones.

4.3.1.2 Position Probe

The axial position probe is a noncontacting Kaman Sciences KD2300 series probe which was selected based on its ability to measure accurately the distance to a conductive surface over the range of 5 to 20 mils. In addition, the probe has wide bandwidth and low drift. The output of the probe is a signal proportional to the vertical rotor position with a scale factor of 20 millivolts per vertical mil.

4.3.1.3 Servo Electronics

The servo electronics perform the functions of feedback loop linearization, filtering and phase compensation while at the same time automatically minimizing the bearing electric power consumption. The block diagram of the servo electronics systems is shown in Fig. 4-26.

The gain and phase characteristics of the servo electronics are chosen in a three-part process. First, a third-order low-pass filter is designed which gives the required 240° open loop phase shift at the 416-Hz mechanical resonance. Next, the feedback loop is lead-lag compensated using an RC network; the selected zero and pole locations give a maximum phase margin at approximately 40 Hz. Finally, the loop gain is selected to give a primary crossover frequency at the 40-Hz frequency of maximum phase margin. This condition is satisfied by selecting a loop gain of 6 db for those frequencies less than the unstable mechanical resonant frequency of 22 Hz.

The next nonideal aspect to consider is linearization. For most bearing systems, the effective air gap (including magnet reluctance) changes only $\pm$ 20%, so that effects on this nonlinearity can be tolerated. However, the total magnetizing current (including permanent magnet coercive force) changes over a wider range and is worth linearizing. After the desired net force is derived from the displacement by the servo transfer function, the resulting required total magnetic force is linearly related by adding the gravitational force on the rotor. This is square rooted to get the total magnetizing current. Then the permanent magnet coercive force is subtracted to get the net electromagnet current.

The scheme above requires a perfectly trimmed-out equilibrium point if no average current is to be drawn from the battery. However, thermal drift in the position sensor and slow changes in magnet strength or other parameters will make such close trimming difficult or impossible. To avoid a dc current in the bearing, a zero must be placed at the origin of the s-plane. This requires for stability that a second pole be placed in the right half plane as shown in Fig. 4-27c, resulting in the Bode plot also shown in Fig. 4-27c. This counterintuitive approach implies that the output current is measured and integrated and added to the loop with positive feedback. If the current is positive (up), moving farther in the position (up) direction will result in an equilibrium. The time constant of the pole can be very slow. However, the integrator amplitude must be limited. Otherwise when initial lift-off is attempted, the rotor will be pushed the wrong way. Switching circuitry has been installed within the servo electronics. The circuitry is used to delay attempted bearing lift-off until control circuitry is stabilized; in this way a clean lift-off can be insured when control power is first applied.

The features described above are incorporated in the servo control circuitry. The measured loop gain and phase for the complete suspension system are given in Fig. 4-30 and are well predicted by theory. Figure 4-31 shows the lift-off (step) response of the closed loop from both the upper and lower limit stops. Bearing lift-off is very clean, exhibiting a well-damped second-order response as expected.

C74-1237

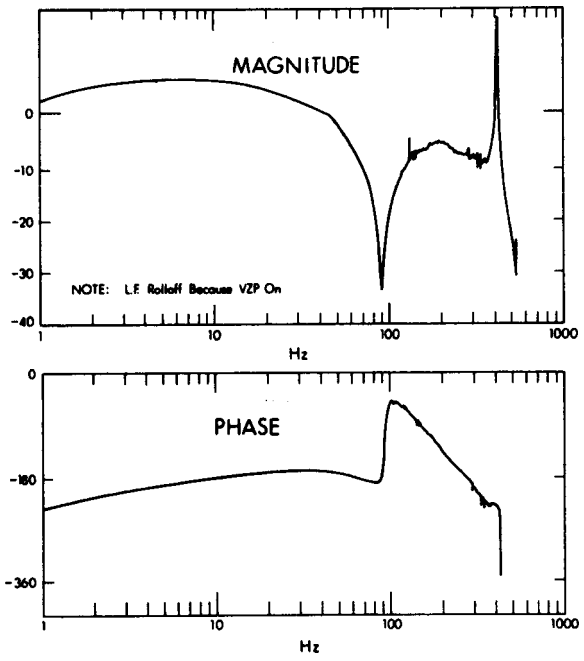

Figure 4-30. Magnetic bearing loop transmission.

C74-1236

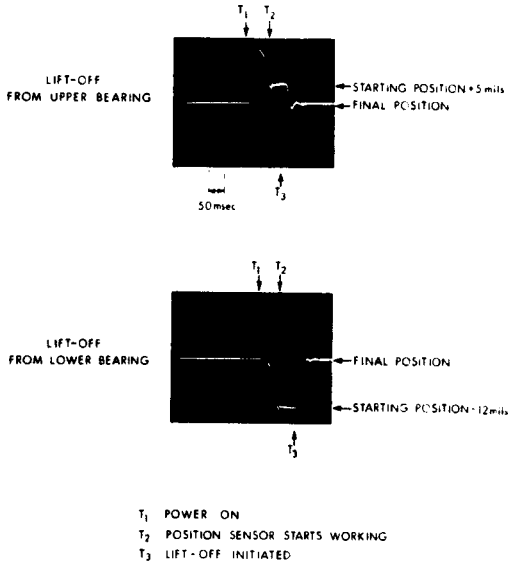

Figure 4-31. Magnetic bearing liftoff response.

4.3.1.4 Magnetic Bearing Driver Amplifiers

The magnetic bearing drivers are linear feedback class D current sourcing amplifiers used to regulate the bearing coil current to the value commanded by the axial suspension servo loop. It is best to avoid the dynamics of the bearing inductance in the loop, since this gives undesirable phase lag. To do so, a current driver can be built with its own internal feedback loop to wide bandwidths. In this system, six separate drive amplifiers were used to energize the six magnetic bearings instead of the simpler arrangement in which a single amplifier drives six series-connected bearings. The multi-driver system was chosen because of:

1. The existence of a single-bearing-sized drive design of known reliability. Amplifiers built to this design have been used to suspend a small flywheel for over 20,000 hours.

2. The redundancy of a multiamplifier connection which allows the flywheel to remain floating despite the simultaneous failure of up to three of the six driver amplifiers.

The bearing amplifier is a standard fixed frequency pulsewidth modulated design using output current feedback. The key design parameter in this amplifier is the large-signal bandwidth which is set by the output current slew rate. The large signal bandwidth must be great enough so that the overall open loop phase margin of the axial position control loop will not be reduced under large signal conditions. Due to the relatively high pulsewidth modulation (PWM) clock rate, the primary mechanism for slew rate limiting in this design is the amplifier output voltage limit. The slew rate is given by

$$SR = \frac{V_{supply}}{L} = \frac{11 \text{ volts}}{2.9 \text{ mH}} = \frac{3797 \text{ amps}}{\text{sec}}$$

where L is the load inductance. The resulting undistorted large signal bandwidth is given by

$$F = \frac{SR}{2\ I_{peak}} = \frac{3793 \text{ A/sec}}{2\ I_{peak}} = \frac{603.6}{I_{peak}}$$

where I_{peak} is the peak value of the sinusoidal output current. Limiting the input signal to ≤ 5 volts corresponding to an output current of ≤ 5 amps gives a large signal bandwidth of 121 Hz which is safely larger than the open loop gain crossover frequency of 40 Hz.

4.3.2 The Motor-Drive System

The motor-drive system contains a maximum-power-point tracking, dc-to-dc down converter section and a motor-drive inverter bridge section, Fig. 4-32. Each of these sections is discussed in further detail below.

4.3.2.1 Maximum-Power-Point Tracking, DC-to-DC Converter

The dc-to-dc converter functions as a variable matching network or "dc transformer" to allow the PV array to be operated at the maximum-power-point

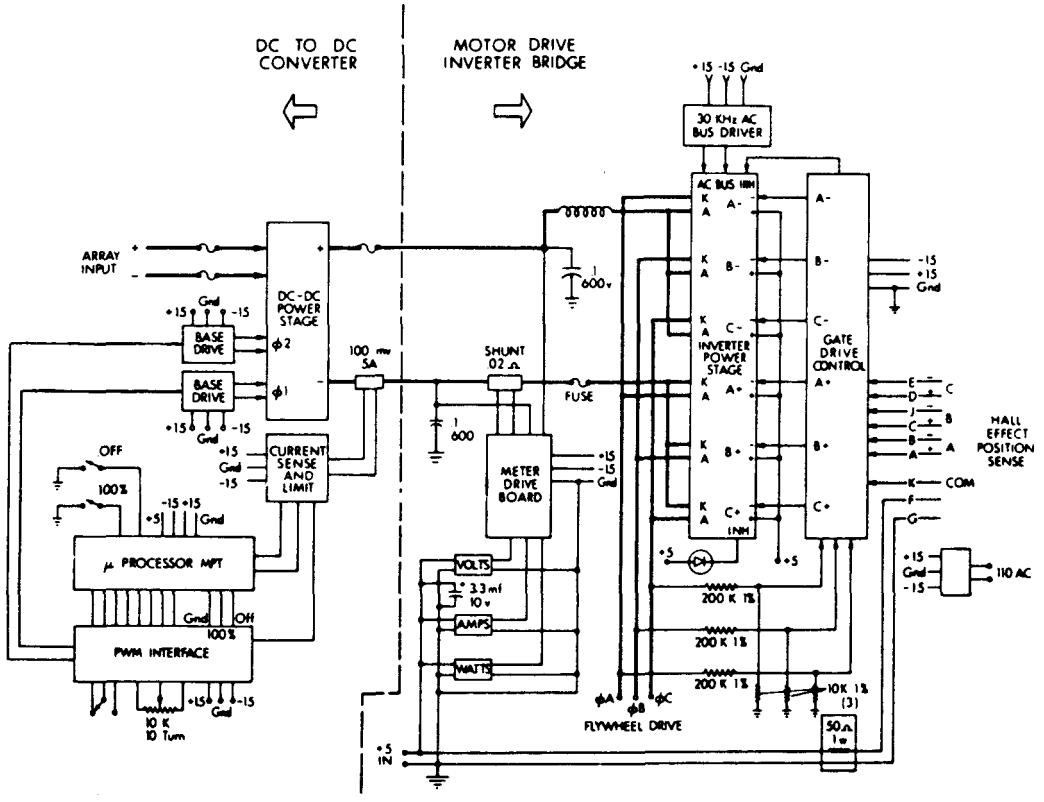

Figure 4-32. The motor-drive system.

voltage despite the wide dynamic variations of the flywheel motor-drive bridge input voltage. The converter consists of three parts: the dc-to-dc converter power stage, the maximum-power-point tracking computer, and the PWM interface, Fig. 4-32. The selection of the optimum transformation ratio at each instant is accomplished by the microprocessor-based, maximum-power-point tracking circuit through adjustment of the PWM switch-drive signal.

The dc-to-dc converter power handling stage is a PWM controlled "buck"-type switching regulator operating with a 20-kHz clock frequency. The converter utilizes a number of features that result in high performance, including regenerative current feedback base drive and a lossless turnoff snubber. The power-stage topology is such that the converter output-to-input voltage ratio is equal to the PWM factor, which can be varied between zero and one. This PWM signal is generated by the PWM interface circuit under the control

of the maximum-power-point tracking computer. The PWM interface circuit converts a computer-generated control word representing the PWM factor into the actual PWM 20-kHz signal. The heart of this circuit is a Motorola 3420 PWM generator integrated circuit. The 3420 is connected in the feedback loop of an operational amplifier in order to guarantee a precise relationship between the commanded and actual PWM signal. A photograph of the dc-to-dc converter hardware is shown in Fig. 4-33.

CP267-5502

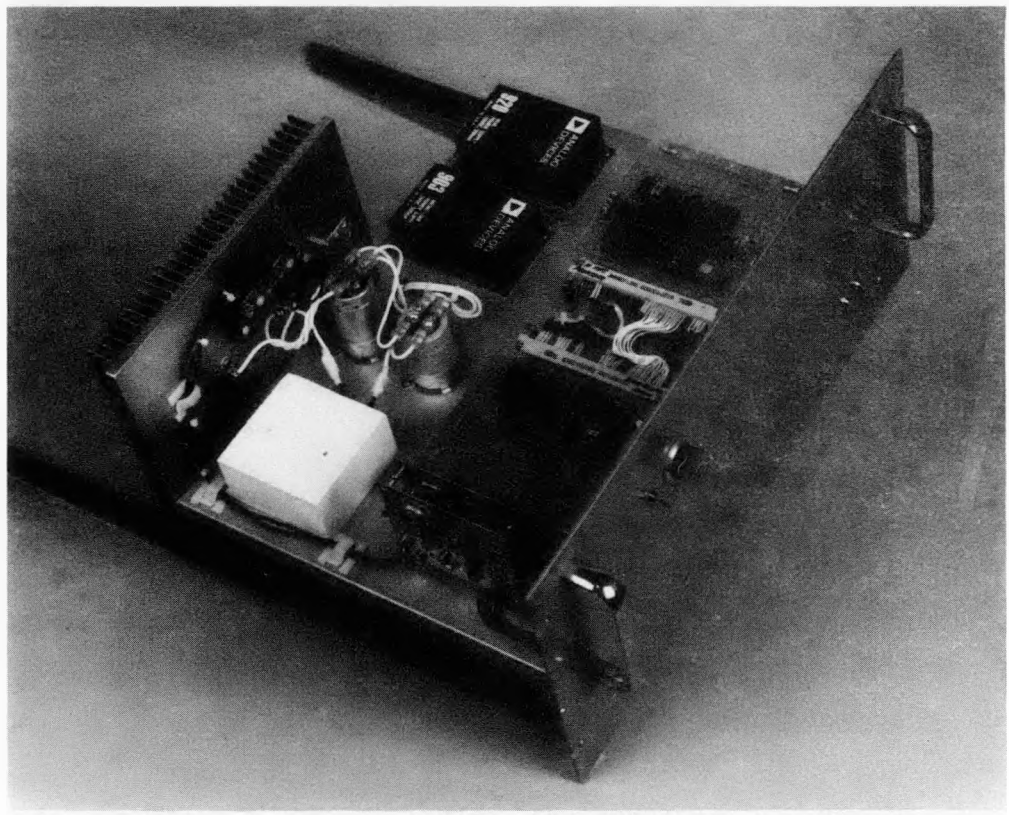

Figure 4-33. Photograph of the dc-to-dc converter hardware.

The maximum-power-point tracking computer measures the switching regulator output current and sets the PWM factor control word using a "hill-climbing" optimization algorithm. The PWM factor control word is updated two times per second by the 8085-type microprocessor; after each update of the control word, the down converter output current is measured. This current is converted to a voltage by a current shunt and then supplied to the microcomputer by a AD571 analog-to-digital converter. The decision to increment or decrement the control word is based on the two latest measurements of the down converter output current as follows:

1. If the control word was incremented at the last update and the last two measurements were larger, then the control word will be incremented.
2. If the control word was incremented at the last update and the first of the last two measurements was larger, then the control word will be decremented.
3. If the control word was decremented at the last update and the second of the last two measurements was larger, then the control word will be decremented.
4. If the control word was decremented at the last update and the first of the last two measurements was larger, then the control word will be incremented.

By following the rules described above, the down converter output current is continually maximized, guaranteeing PV array operation at the maximum power point at all times. A listing of the maximum-power-point computer program is provided in Appendix 4-1.

At very low speeds the back-EMF of the flywheel motor-generator is small, and consequently the required dc-to-dc converter output voltage is also small. In this case, full array power would result in a very large dc-to-dc converter output current. To protect against this situation, the dc-to-dc converter is equipped with a current limit, set to approximately 6-amps dc. The maximum-power-point tracker is defeated, and the array is operated to the open-circuit voltage side of the array maximum power point, until the flywheel speed reaches approximately 3,600 RPM.

4.3.2.2 Motor Drive Inverter Bridge

The motor drive inverter bridge section is a 3-phase, 6-pulse, inductor-fed, phase-controlled rectifier set operated in the inverting region. The rectifier set is naturally (line) commutated by the motor-generator back-EMF when the machine runs at high ac voltage and is force-commutated when the ac voltage is not sufficient to guarantee natural commutation. The inverter bridge section contains the gate-driven control and inverter power-stage components.

The gate-drive control operates: 1) to generate gate-firing pulses and 2) to change the bridge commutation mode at low speeds. In normal operation, the position signals from Hall-effect sensors in the motor assembly are amplified and combined to form nearly sinusiodal reference signals which have zero crossings at 15° before the generator line-to-line voltage zero crossings. These signals are squared up and gated to form a group of six 120°-wide pulses corresponding to the desired on-times of the six silicon controlled rectifiers (SCRs) in the bridge. The gate pulses then are processed by protective gating logic which prevents undesirable modes of operation, including reverse rotation and out-of-sequence firing. The 120°-wide gate pulses are then buffered by small transistors for transmission to the SCR gate driver circuitry. In this way, the gate firing timing is determined, using the output signals from the three Hall-effect rotor position sensors.

The actual gate-firing angle is 165° corresponding to a margin of 15°. Theoretically no margin angle is required in this system; this is due to the negligible commutation overlap angle which results from the very low ac side inductance. However, the RCA 4003-type SCRs used in this circuit have a measured blocking recovery time of 20 μsec (9° at 1250 Hz) when operated at the 7-amp rating.

The gate-drive control also determines the commutation mode of the SCR bridge. In order to reduce SCR stress when operating within the flywheel operating speed range, the SCRs are allowed to commutate off naturally using the back-EMF of the synchronous motor-generator. At very low speeds (below about 3,000 RPM), this mode is not possible due to insufficient motor back-EMF. At these times, the SCRs are forcibly turned off under control of the gate driver.

The phase-controlled rectifier/inverter power stage uses six SCRs connected in a three-phase, six-pulse bridge configuration. The particular type of SCR which was used in this design is called a Gate-Turn-Off SCR (GTO-SCR). This device has a characteristic which is uncommon among SCRs, namely, that it can be turned off by gate control. The gate turn-off feature is used when the motor voltage is too small to guarantee reliable back-EMF commutation. A photograph of the motor-drive system hardware is shown in Fig. 4-34.

CP267-5617

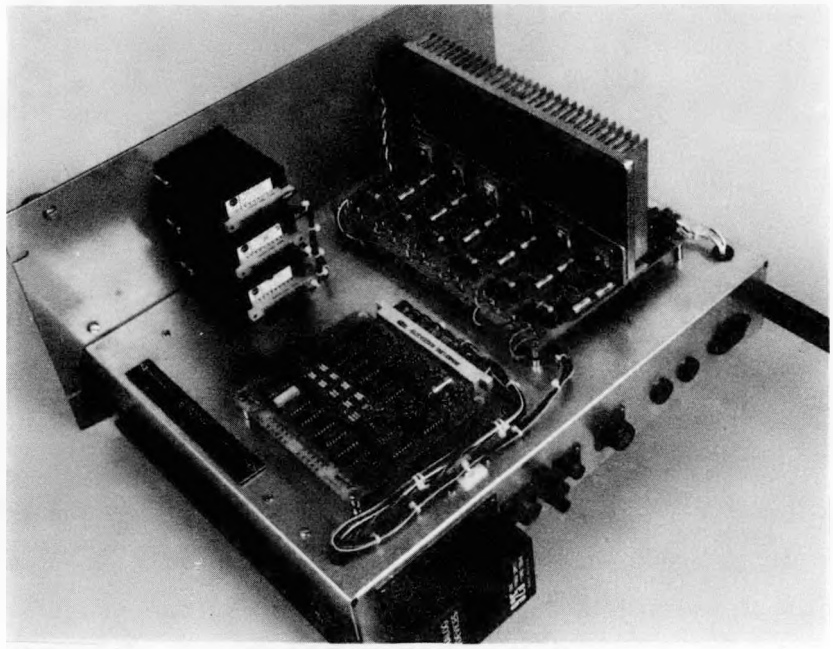

Figure 4-34. Motor-drive electronics.

4.3.3 Motor-Generator

A permanent-magnet ironless-armature, axial-gap motor-generator was selected as the most suitable configuration for the flywheel application. Its operational speed range is 7,500 to 15,000 RPM, but it must also be capable of self starting. The rated power is 0.625 kW for the prototype system. The three-phase armature (stator) is fixed and the two permanent-magnet field rotors are part of the magnetic bearing and shaft assembly. Mechanical stress limitations for containment of the permanent magnets in the

rotor requires at least 10 poles for the 8-kW (40-kWh storage) residential motor-generator, and the prototype subscale unit incorporates this same number. A steel ring completes the magnetic flux return path outside the working gap. Figure 4-12 earlier showed an exploded view of the motor-generator configuration. Figure 4-35 is a photograph of the completed armature stator.

CP267-5002

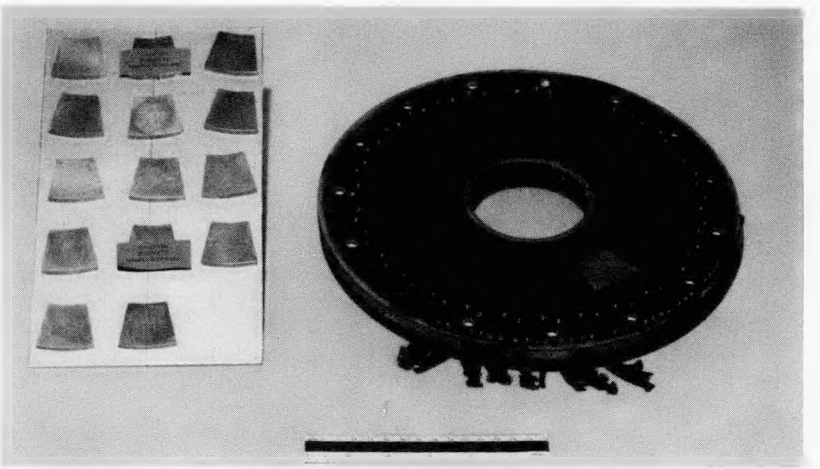

Figure 4-35. Photograph of the armature stator.

A peak EMF of 240 V per phase was specified at the maximum speed of 15,000 RPM for the residential 8-kW motor-generator (40-kWh unit). This requires a peak line-to-line output of 410 volts for a "Y" connected, three-phase armature. Because of the limited availability of power controlling semiconductors with this voltage rating, for the prototype unit, each phase was subdivided into two parallel windings to reduce the generated EMF to one half. This results in a peak line-to-line output of 205 V at maximum speed and a corresponding peak individual phase ac voltage of 120 V. The prototype 0.625-kW motor-generator is wired with each phase having two parallel series of 5 coils. The motor-generator electrical frequency varies from 625 to 1250 Hz over the speed range from 7,500 RPM to 15,000 RPM. In the design calculations of the generator, however, the complete 10-coil series phase connection is assumed.

At a constant system power rating, the current is maximum at minimum speed since the voltage is proportional to the speed. Resistive power

dissipation is greatest therefore at the lowest speed. At 7,500 RPM the required peak ac phase voltage V_o (line to neutral) is 120 V. The required back-EMF generator constant is:

$$K_B = \frac{V_o}{\omega} = 0.15 V/rad/sec$$

where: ω = rotation rate of the conductor in the magnetic field.

The voltage generated in an armature conductor is dependent on the length of conductor moving in a magnetic field, therefore the peak generated EMF is:

$$EMF = rL\omega B$$

where:

r = average radius of the armature conductor
L = length of conductor in gap field
ω = (already given)
B = magnetic field around conductor.

The armature coil dimensions are shown in Fig. 4-36, where the conductor length is assumed equal to the magnet radial dimension. The motor gap field is calculated from magnetic characteristics and the geometric relationship of the magnets and gap, noting that there are two magnets bounding the gap:

$$\frac{Bm}{Hm} k = 2 \frac{Lm}{Lg}$$

where: Lm = magnet length
Lg = gap length
K = flux leakage derating factor
$\frac{Bm}{Hm}$ = magnet load line.

From Bm/Hm = 1 at the SmCo maximum energy product, Fig. 4-37, Lg = 0.54 in. and k = 0.85, Lm = 0.23 in. The effective gap field, Bo, is 0.85 x 0.4 tesla (the optimum magnet field) or 0.34 tesla.

C74-1560

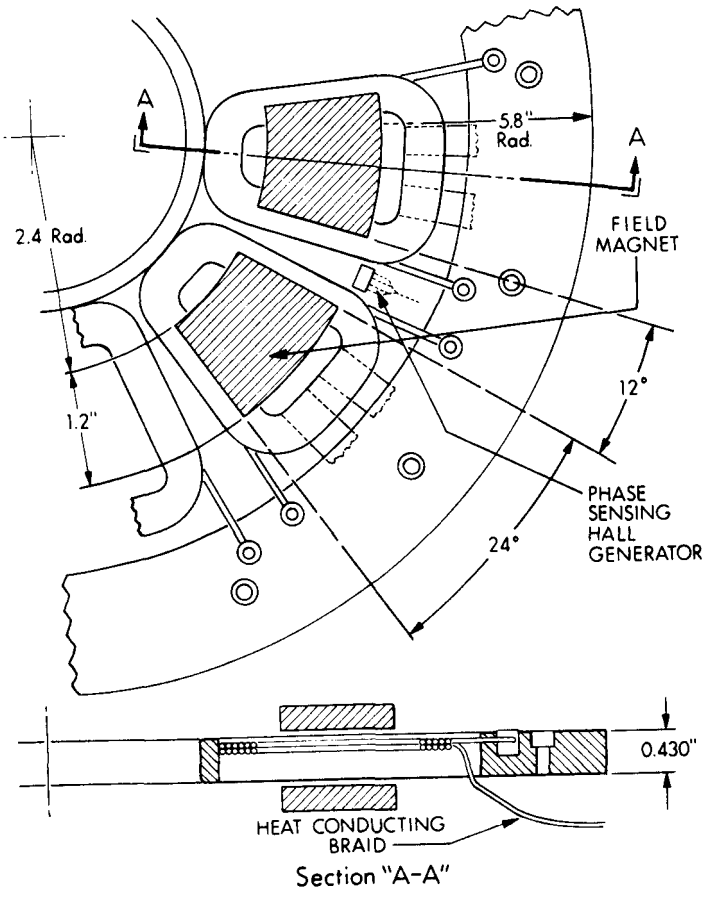

Figure 4-36. Armature layout for each phase.

C74-1544

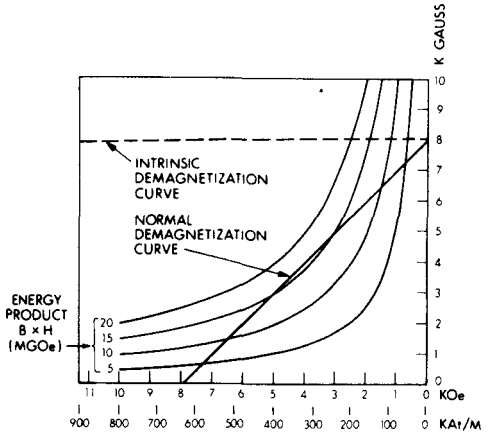

Figure 4-37. Samarium-cobalt permanent magnet characteristics.

The field uniformity in the gap can be calculated from:

$$1 - \frac{B}{Bo} = 0.27e^{-\pi \frac{x}{h}}$$

where h = 1/2 gap = 0.27 inch

x = distance from magnet edge

x_{max} = 0.6 inch (1/2 of magnet dimension).

The result of solving the equation above is:

location x =	.6	.2	.1	0
$\frac{B}{B_o}$ =	1.0	.97	.89	.73.

If the average field volume uniformity is conservatively estimated to be 90% and B_o = 0.34T, $B_{avg} \sim 0.28$T. For the 625-W motor-generator at the minimum speed of 7,500 RPM, EMF = 0.55 V/conductor.

The required number of coil turns to generate V_o may be calculated from the relationship:

$$V_o = \text{EMF } 2 \text{ PN}$$

where P = number of field poles

N = number of turns per pole.

This formula predicts that 11 turns are required for 10 poles to produce 120 V.

In the actual generator design, a coil with an even number of turns was chosen (N = 12). For this configuration, V_o = 127 V and K_B = 0.16 V/rad/sec, thus meeting the required output performance. The three-phase line-to-line output at 7,500 RPM with the armature connected to generate 50% of the full phase voltage is:

$$V_{L-L} = \frac{Vo\sqrt{3}}{2\sqrt{2}} \quad \text{RMS}$$

$$= 78 \text{ V}$$

and

$$V_{in} = 0.95\sqrt{2}\, V_{L-L} \quad \text{AV}$$

V_{in} = 105 V RMS for the complete armature.

The current per phase can be found in terms of the average input as follows:

$$P_{phase} = \frac{1}{3} P_{in}$$

$$I_{LN} \times V_{LN} = \frac{1}{3} P_{in}$$

Divide by V_{avg}:

$$I_{LN} = \left(\frac{V_{in}}{V_{LN}}\right) \frac{1}{3} P_{in} \qquad \frac{V_{in}}{V_{LN}} = .95\sqrt{2}\sqrt{3}$$

$$I_{LN} = \frac{.776\ P_{in}}{V_{in}}$$

for P_{in} = .625 kW at 7,500 RPM the current in each phase is:

$$I_{LN} = 4.6 \text{ amp.}$$

The V_{rms} per one-half phase is:

$$V = \frac{V_o}{2\sqrt{2}} = 45\ V_{rms}.$$

The rms current per phase is the same as the current line to line which is defined by the input current:

$$I_{\text{per phase}} = I_{L-L} = 0.95\sqrt{2}\ I_{IN}$$

where $0.95\sqrt{2} = \frac{V_{IN}}{V_{LL}}$.

Two phases in series will dissipate 2/3 of the input power:

$$I_{L-L} = \frac{2\sqrt{2}}{3} (.95) \frac{P_{IN}}{V_{IN}}$$

therefore when P_{IN} = 625 W at 7,500 RPM:

$$I_{L-L} = I_{phase} = 5.3\ A_{rms}.$$

Due to the high resistivity of the permanent magnets and the lack of iron in the rotor, the transient time constant of the machine is much shorter than a period of the ac output waveform and can therefore be considered equal to zero for all practical purposes. Consequently, the subtransient, transient and synchronous reactances of the machine are indistinguishable insofar as electrical loads are concerned. Because of this, the machine is said to have equal subtransient, transient and synchronous reactances.

The reactance of the motor-generator is a key parameter when interfacing to solid-state, phase-controlled rectifier-inverter combinations used to transfer power into or out of the flywheel. The presence of generator reactance gives rise to rectifier commutation overlap which may produce undesirable effects of reducing the loaded rectified output voltage and compromising the reliability of rectifier/inverter commutation. These effects were considered in the design and were evaluated using the classic formulas of Witzk et al.

4.3.3.1 Armature Coil Design

The armature coils are wound from Litz wire composed of 60 No. 36 insulated copper strands to minimize eddy currents in the armature wiring. This conductor is 0.06 inches in diameter and has a resistance of 6.4×10^{-3} ohms/foot at 23°C. Each coil is wound with two layers of six turns each and each phase consists of ten coils. The coils are placed 36-deg. apart with the radial legs at 24 deg. The coil array minimum diameter occurs when adjacent coils are just tangent to each other and the radial extent of the coil is sufficient for the return bends to clear the magnet field area. Figure 4-36 illustrates the armature layout geometry. The coils for each phase are located 12-deg. apart and the armature thickness is governed by the minimum dimensions for three coil layers plus the covering insulation. All coil ends are terminated externally to permit a variety of output configurations. Figure 4-38 is a photograph of the complete coil assembly before encapsulation. The completed coil assembly is encapsulated with thermally conductive epoxy which enhances thermal conduction from the interior to the mounting edge and also provides a mechanically rigid structure.

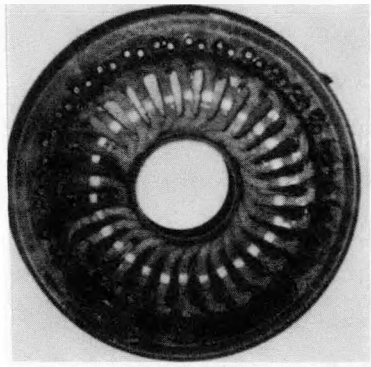

Figure 4-38. Photograph of the armature coil assembly.

The resistance of each 12-turn coil is 0.043 ohms at the terminals and the five coils in series will have a resistance of 0.215 ohms. At the maximum current of 4.6 A/phase, the resistive power dissipation is 2.3 W per phase or 7.5 W for the complete armature; about 1.1% of the rated power. This conservative rating was provided to give a safety margin in an experimental machine. The motor-generator can actually be operated at 1 kW with a resistive loss of approximately 25 W or 4% of the rated power.

To insure adequate heat removal from the armature when it operates in its vacuum environment, copper wire braid (to minimize eddy current loss) is installed between the coil turns and terminated on the mounting structure where the heat is conducted away.

The heat condition path consists of three segments: 1) a radial segment along the coil wire to the outer armature perimeter; 2) a short segment across the interface between coil and the copper braid which is dominated by the coil encapsulant thermal conductivity; and 3) the final segment along the braid to the structure.

For a given heat input, the resulting temperature difference to conduct this heat may be calculated from:

$$\Delta T = \frac{QL}{KA}$$

where:

Q = heat input

L = length of the thermal conduction path

K = thermal conductivity

A = area for heat transfer.

The total temperature gradient for all segments is calculated as 5°C at the dissipated power of 0.3 W/coil, with the greatest temperature difference across the coil-braid interface. This small temperature rise is also indicative that the 0.625-kW rating for the motor-generator is conservative. Continuous operation at 1 kW would increase the calculated temperature rise to 12°C. Three Hall sensors (F. W. Bell Model 700) are installed in the coil assembly to supply phase signals for commutation at starting and low speed. A thermistor is included to monitor the armature temperature.

The eddy current loss magnitude in the stranded armature conductors moving in the permanent magnet field can be calculated from the following equations:

$$Q_{AC} = \left(\frac{Bd}{\pi}\right)^2 \frac{f}{2\rho} \quad (\text{joules/m}^3)$$

$$P_{AC} = Q2fV \text{ (watts)}$$

where:

- B = maximum magnetic field around conductors
- d = strand diameter
- f = magnetic field frequency in Hz
- V = volume of conductor subjected to changing field
- ρ = conductor resistivity

assuming:

- d = .0058" (No. 36 wire)
- B = .28T
- ρ = $1.8 \times 10^{-8} \Omega$ - m
- f = $\frac{1500}{6} \times 5 = 1250$ Hz
- V = 56 cm^3.

For the dimensions of the armature coils and the gap field, $P_{AC} \sim 1$ W at the maximum speed of 15,000 RPM. The thermally conductive braid will be subjected to a similar field change and adds ~ 0.3 W to make a total loss of ~ 1.3 W.

4.3.3.2 Measured Motor-Generator Performance

When the machine was initially tested with each phase composed of two parallel windings, it was found that the voltages of the two parallel connected legs did not match exactly and an impedance limited circulating current existed. The circulating currents were of sufficient magnitude that solutions were explored to reduce or eliminate them. This undesirable loss was finally eliminated in this system by installing center-tapped inductors or so-called "inter-phase reactors" between the parallel connected windings. The center taps of the reactors then became the phase outputs of the motor-generator.

The motor-generator performed very closely to the design calculations. The RMS line-to-line voltage V_{L-L}, was found to be 81 volts, exceeding the design value of 78 volts. The armature dissipation for 625 watts input to the motor was found to be 10 watts ($\sim$1.3% of input) with a temperature rise of 6°C. These values are only slightly higher than calculated. The eddy current loss was estimated from the measured armature temperature rise without power input or output, and was approximately 3.5 watts at 14,000 RPM.

4.3.4 Power Conversion Systems

Variable-frequency, variable-voltage ac output power from the generator is provided directly to a cycloconverter power converter for stand-alone applications, Fig. 4-25, or to a utility-interactive inverter for utility applications.

The stand-alone cycloconverter-type power converter was the first power conversion unit type to be designed, fabricated and tested in conjunction with the flywheel storage unit. A breadboard unit of the cycloconverter was completed and tested in the summer of 1979. A prototype version of the cycloconverter was bench tested in the fall of 1979 and then tested as part of the flywheel storage unit, in early 1980. Shakedown testing of the flywheel system with stand-alone cycloconverter continued through the spring of 1980. The first round of flywheel efficiency tests with the cycloconverter was completed in April 1980. (Results are reported in Section 4.6 of this report.)

The utility-interactive inverter followed by some months the development of the cycloconverter. The breadboard inverter was tested in May of 1980 and the prototype unit was completed in the summer of 1980. Bench tests of the prototype were initiated in September 1980.

In the text that follows, the stand-alone cycloconverter design characteristics will be presented first in Section 4.3.4.1. Discussions of the utility-interactive inverter follow in Section 4.3.4.2.

4.3.4.1 Stand-Alone Cycloconverter

For stand-alone operation, the flywheel system has been tested with a power-frequency changer or cycloconverter to convert the flywheel output to 120-V, 60-Hz, single-phase ac. A system diagram for the cycloconverter is shown in Fig. 4-39. The cycloconverter consists of two 6-pulse, phase-controlled rectifier sets with outputs connected in inverse parallel, Fig. 4-40. The cycloconverter control circuitry automatically selects rectifier firing angles in order to construct a nearly sinusoidal output-voltage waveform from appropriate "pieces" of the motor-generator phase voltages, Fig. 4-41. A feedback loop regulates the output voltage at 120 VAC. An output filter is provided, Fig. 4-42, to improve the output waveform quality and produces the filtering effects illustrated in Fig. 4-43. The cycloconverter unfiltered output spectrum between 0 and 700 Hz is illustrated in Fig. 4-44. As shown in Fig. 4-45, the cycloconverter operates at power factors in the range from 0.35 to 0.83 (average power factor of 0.50) for resistive loads and lower power factors for inductive loads. The total harmonic distortion of the output waveform after filtering is less than 5%, Fig. 4-46. The cycloconverter control section and power section hardware are shown in Figs. 4-47 and 4-48, respectively.

C74-1465

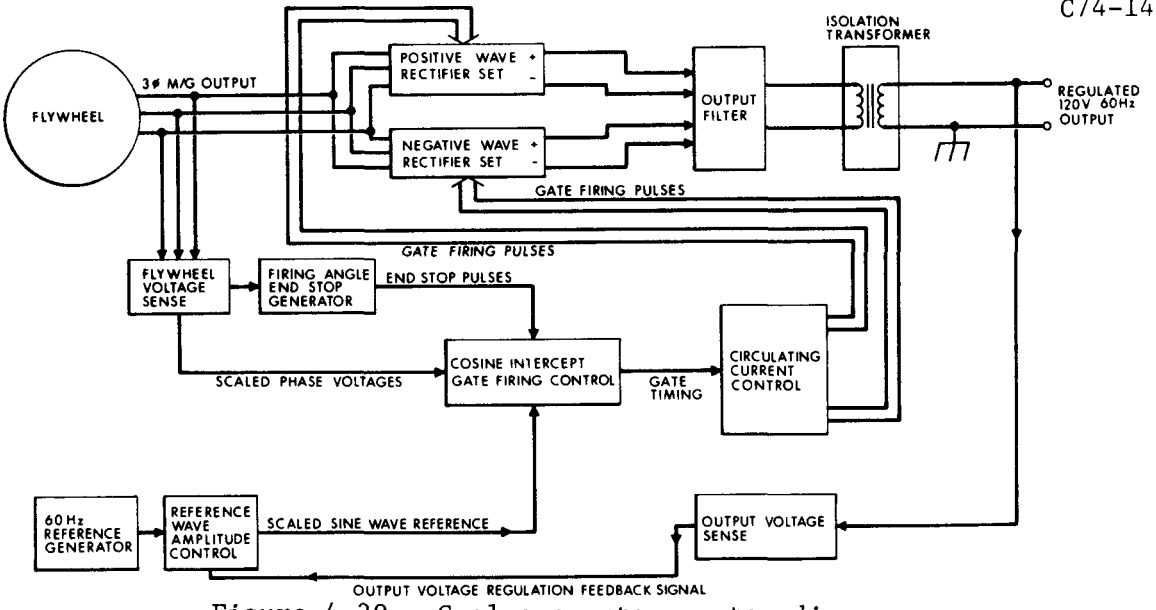

Figure 4-39. Cycloconverter system diagram.

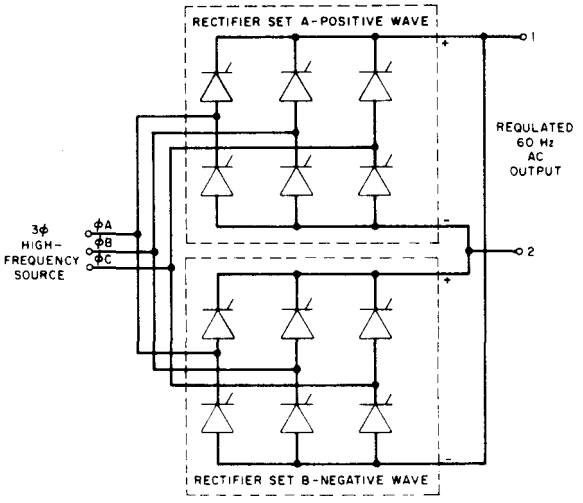

Figure 4-40. Basic cycloconverter power section.

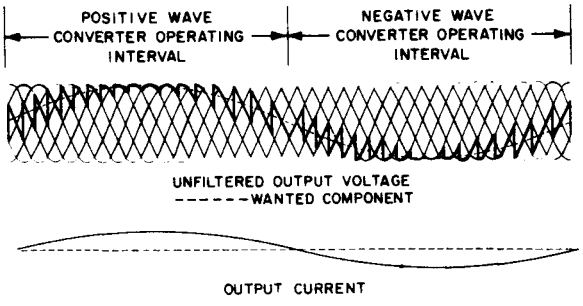

Figure 4-41. Theoretical cycloconverter output voltage and current waveform.

C74-1319

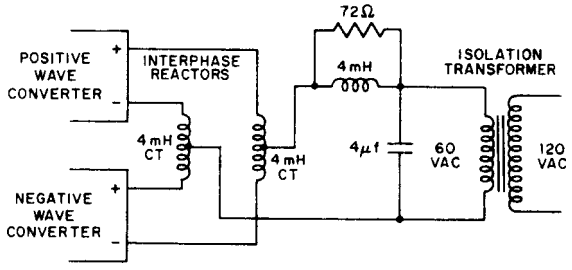

Figure 4-42. Cycloconverter output filter.

C74-1321

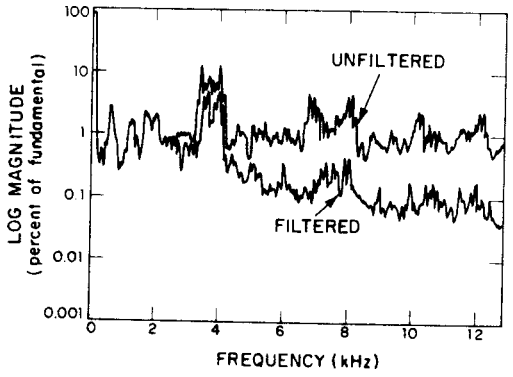

Figure 4-43. Cyclcoconverter filter output voltage spectrum.

C74-1320

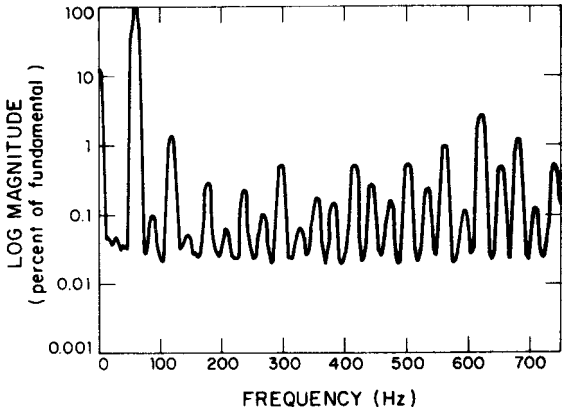

Figure 4-44. Cycloconverter unfiltered output spectrum - expanded.

C74-1373

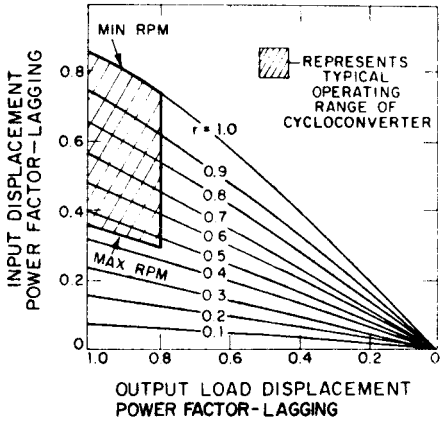

Figure 4-45. Relationship between input power factor, output power factor and output voltage ratio for the cyclo-converter system.

C74-967

115-VAC, 60-Hz,
420-W load

Figure 4-46. Cycloconverter output waveform (less than 5% total harmonic distortion).

CP267-4998

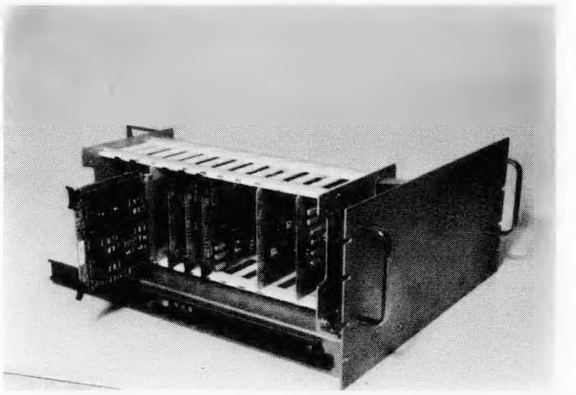

Figure 4-47. Cycloconverter control electronics.

CP267-5616

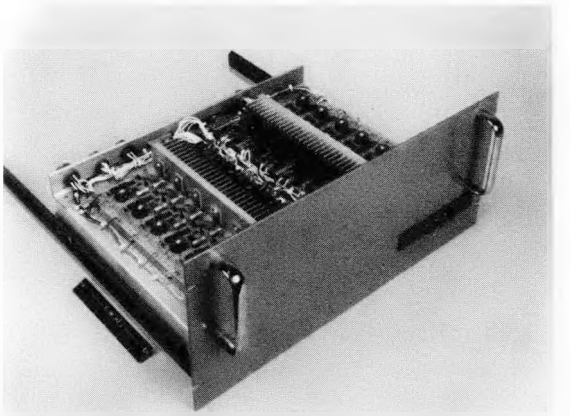

Figure 4-48. Cycloconverter power electronics.

4.3.4.2 Utility-Interactive Inverter

When the flywheel system is used in a utility-interactive application, the flywheel system output voltage at the utility tie point is set by the utility, and the utility current is set by the inverter. The inverter thus acts as a utility-synchronized, 60-Hz, ac-current source. Power flow from the flywheel to the utility is as follows: first the flywheel motor-generator output is rectified; next, the rectified dc is shaped into a 60-Hz, full-wave rectified current using a 20-kHz switching regulator; and finally, the full-wave rectified current is "unfolded" (inverted) into a distortionless 60-Hz sine wave which is fed to the utility, Fig. 4-49. The topology of the current waveshaper and current unfolder is also noted in Fig. 4-49.

C74-1430

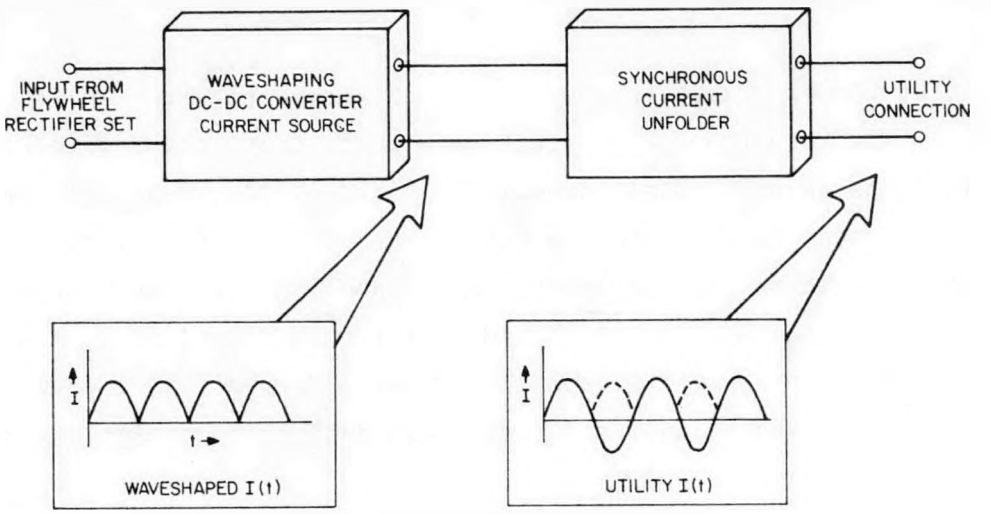

Figure 4-49. Utility-interactive inverter principle.

The current waveshaper uses a modulated dc-to-dc switching-type power converter to shape the dc-current source into the form of a rectified sine wave. The waveshaper includes the following features: continuous measurement and comparison of the output current to a rectified sine wave reference which is generated using phase information from the utility voltage; automatic adjustment of the magnitude of the rectified sine wave reference to control the dc-to-dc converter output to the desired magnitude; dual-speed output magnitude control counting to handle safely loss of array or loss of utility shutdown situations; and power transistor switching to cause the output current to track the reference signal. The current unfolder is a force-commutated output bridge in which on/off control signals for alternate pairs of inverter switches (SCRs) are derived from zero crossings of the reference utility voltage signal.

A 1-kW, utility-interactive inverter of this type has been built, Fig. 4-50. It has been found to exhibit excellent output power waveform quality, with less than 2% total harmonic distortion, Fig. 4-51. In preliminary bench tests, it exhibited an efficiency of about 92%, Fig. 4-52. With this utility-interactive inverter, the flywheel motor-generator always operates at a power factor greater than 0.95 for high efficiency. Also power supplied directly to the utility from the PV array does not go through any flywheel power conditioning and is consequently delivered at high efficiency.

CP267-6117

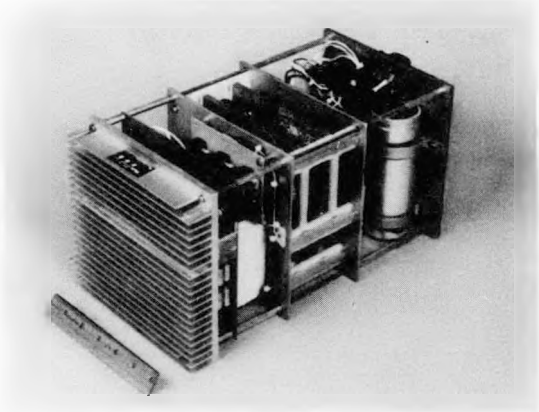

Figure 4-50. 1-kW utility-interactive inverter.

OUTPUT POWER .75 KW

C74-1009

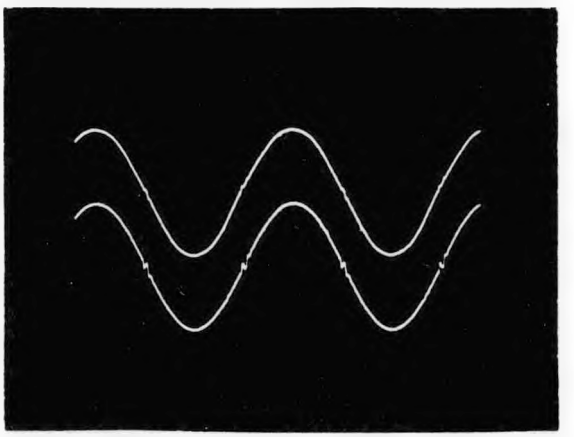

UPPER TRACE - UTILITY VOLTAGE
LOWER TRACE - UTILITY CURRENT

Figure 4-51. Utility-interactive inverter output power waveform (less than 2% total harmonic distortion).

C74-1291

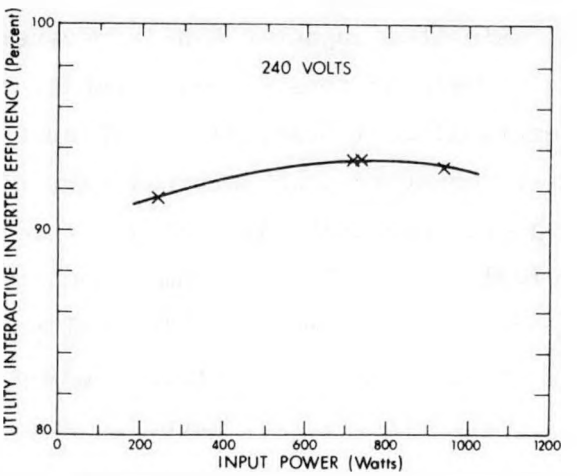

Figure 4-52. Utility-interactive inverter efficiency.

4.4 Magnetic Bearing Design

4.4.1 Design Concept

The magnetic bearing in the 1/10-scale prototype system represents a quantum improvement in the long-term reliability and lifetime expectancy of high-speed spinning assemblies. A combination of permanent magnet fields and electromagnet active control is used to levitate a rotor suspended below the magnetic bearing unit. The permanent magnet field provides all of the required lifting force when the flywheel system operates at its design magnetic gap. The electromagnet is powered only to counter displacements of the magnetic suspension from its nominal operating gap. Therefore the electrical power consumption of the magnetic bearing unit during levitation is quite small, and in the 1/10-scale prototype unit a power consumption of only 4 watts is needed to control the position of the 400-pound rotor assembly. As an example of magnetic bearing system reliability, the 1/10-scale prototype unit was operated continuously in one test series for over 2,200 hours before making a normal stop. In previous tests, magnetically suspended rotors for satellite applications have been run continuously at Lincoln Laboratory for over 20,000 hours without incident, another indicator of the high reliability of the approach.

The magnetic bearing provides a "soft" support because its restoring spring constant is relatively weak in comparison to other support systems such as mechanical bearings. Also the magnetic bearing system is characterized by clearance dimensions in mils or tens of mils, rather than the tens of micro-inches typical of conventional ball bearings. Such soft bearings effectively isolate the rotor from its mounting when internal vibrations or external disturbances occur. Magnetic bearings also allow a rotor with imbalance to spin about its principal axis with a minimum effect on system performance. This quality may be important when composite flywheel rotors are used in inertial energy storage systems. Should composite rotors develop rotor imbalance during service due to creep or other effects, the magnetic suspension will naturally compensate for the imbalance.

The 1/10-scale prototype unit uses a permanent magnet, axially active, radially passive, magnetic bearing design. The magnetic bearing system is divided vertically into two separate sections, each containing three magnet bearing units. The physical separation between the magnetic bearing section is chosen to assure positive pendulum static stability. The magnetic bearing design, shown in Fig. 4-7, is based on a design previously employed in a satellite momentum wheel experimental system[4-1] and utilizes the analyses of fields and forces of a tooth and slot magnetic gap reported by Mechanical Technology Inc.[4-3] The bearing has two magnetically attractive gaps with fringing rings which provide a positive radial centering force. A control coil driven from the axial position servo modulates the bearing magnetic flux to maintain a stable magnetic bearing axial position. The control coil is integral to the magnetic bearing stator. The permanent magnet is located in the stator and is radially magnetized. The flux path passes across the outer gap, through the rotor, across the inner gap and returns to the magnet. Copper wire is inserted in the stator slots between the fringing rings to increase damping. Six bearing elements were chosen on the basis of bearing separation and radial stiffness for gimballing rotation stability of the shaft. The bearing dimensions were determined from a number of considerations including the load to be supported, the design attractive force, and space requirements for control coil cross section. The ratio of fringing ring width to gap is 1:1 and the slot to ring width ratio is 3:1.

4.4.2 Static Stability Considerations

The static stability of a flywheel suspended from multiple magnetic bearings is defined in terms of the moments acting on the system to cause gimbal rotation of the shaft and rotor about an axis through the center of the bearing assembly, Fig. 4-53. The static stability may be evaluated using the dimensions of the magnetic bearing and the geometry of the bearing and rotor assembly. General equations are presented below in terms of unit magnetic bearing pressure, bearing inside and outside diameter ratio, and bearing separation to diameter ratio.

C74-1575

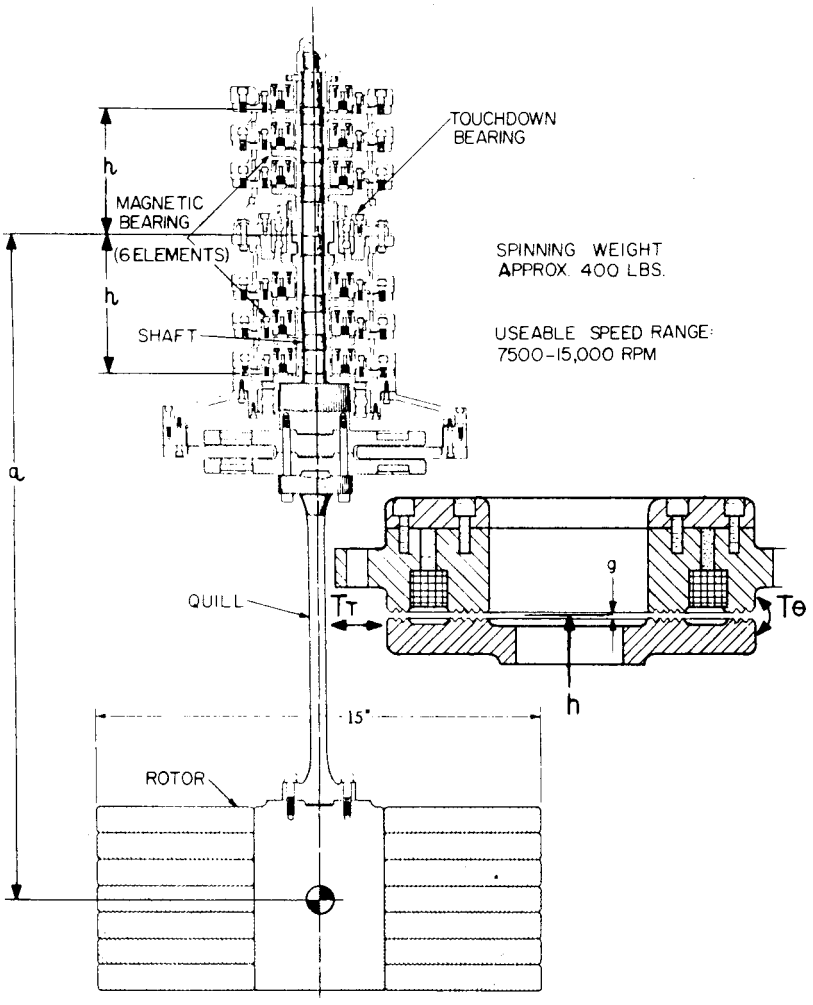

Figure 4-53. Nomenclature for 1/10-scale prototype flywheel.

When the magnetically suspended flywheel unit rocks as a pendulum about a center of rotation at the middle of the magnetic bearing, three torques are generated: a torque, T_θ, due to rotation of the bearing rotors with respect to the bearing stators; a torque, T_T, due to translation of the bearing rotors with respect to the bearing stators; and a torque, T_w, from the gravity restoring moment generated by flywheel rotor tilt from the vertical. Equations for each torque are developed below.

The rotational bearing torque, T_θ, is a destabilizing torque which arises as a consequence of the nonlinear force/gap ratio when the bearing rotor tips along a diameter. Tipping of the rotor along a diameter causes the gap to decrease on one side and increase on the other. The attractive force between the stator and rotor is increased on the side of the bearing with decreased gap and decreased on the side with the increased gap. A torque, T_θ, is generated by the unequal forces. This torque may be expressed in terms of a stiffness, dF_a/dg, defined at the operating gap, g. The torque due to rotation of a single bearing is:

$$T_\theta = -R_m \frac{dF_a}{dg} dg$$

where R_m = rms radius of the fringe rings

F_a = axial destabilizing force

g = width of gap.

T_T, the torque arising from radial translation of the bearing rotors with respect to the bearing stators, is a stabilizing torque. When the flywheel system rocks, bearing rotors above the center of rotation translate in one direction with respect to the bearing stators while the rotors below the center of rotation translate in the opposite direction. The restoring forces set up at each bearing are in a horizontal plane and in a direction toward the magnetic bearing center line. The system of forces above and below the center of rotation are in opposite directions and form the moment couple, T_T. The restoring moment, T_T, may be expressed in terms of a translational stiffness, dF_T/dx.

The torque of a single bearing due to translation, T_T:

$$T_T = h' \frac{dF_T}{dx} \quad dx$$

where F_T = translational force

dx = radial translation distance

h' = distance of bearing gap from the center of rotation.

The torque, T_w, due to the gravitational centering effect of the rotor mass w at a moment arm, may be expressed as:

gravitational restoring torque, T_w

$$T_w = w\ a \sin\theta.$$

For static stability the sum of the torques acting on the suspended flywheel unit must be greater than zero:

$$T_{T_{total}} + T_{\theta_{total}} + T_w > 0.$$

The torque equations may be put into a general form by defining the bearing stiffnesses in terms of unit magnetic pressure and bearing gap area:

Rotation $\quad P_A = F_A/A$

Translation $\quad P_T = F_T/A$

where $A = \frac{\pi}{4} (D^2 - d^2)$

and D = bearing outside diameter

d = bearing inside diameter.

The resulting moment stiffnesses for the complete six-bearing assembly are:

$$\frac{dT_{\theta_{total}}}{d\theta} = K_\theta = -n \left(\frac{dP_A}{dg}\right) \frac{\pi}{4} (D^2 - d^2) \left(\frac{D^2 + d^2}{8}\right)$$

$$\frac{dT_T}{d\theta} = K_T = (\bar{h})^2 \left(\frac{dP_T}{dx}\right) \frac{\pi}{4} (D^2 - d^2) \quad f(n)$$

$$\frac{dT_w}{d\theta} = K_w = n \; a \; P_A \; \frac{\pi}{4} (D^2 - d^2)$$

where n = number of bearings

$$f(n) = \left[\left(\frac{h_1}{\bar{h}}\right)^2 + \left(\frac{h_2}{\bar{h}}\right)^2 + \left(\frac{h_3}{\bar{h}}\right)^3\right]$$

$$\bar{h} = \sqrt{\frac{2}{n} (h_1^2 + h_2^2 + h_3^2)}$$

$$R_m^2 = \frac{(D^2 + d^2)}{8}$$

h_n = distance from the center of rotation to the nth bearing gap.

Substituting the moment stiffnesses in the bearing torque equation and solving for the required moment arm, a, Fig. 4-68, to just achieve static stability, we find:

$$a > \frac{D^2}{P_A} \left[\frac{1}{8} \left(\frac{dP_A}{dg}\right) \left(1 + \left(\frac{d}{D}\right)^2\right) - \frac{f(n)}{n} \left(\frac{\bar{h}}{D}\right)^2 \left(\frac{dP_T}{dx}\right)\right].$$

The design variables for the 1/10-scale prototype unit are as follows:

P_A = 20 psi @ g = 0.0105 in.

A = 3.31 $in.^2$ (effective)

$\frac{dF_A}{dg}$ = 5500 lb/in., $\frac{dP_A}{dg}$ = 1660 psi/in

$\frac{dF_T}{dx}$ = 640 lb/in., $\frac{dP_T}{dx}$ = 190 psi/in

$\bar{h}$ = 3.8 in.

$D = 3.12$ in.

$d = 1.39$ in.

$n = 6\ f(n) = 5.9$

$R_m = 1.2$ in.

$a = -15$ in.

For these variables, the translational stiffness, K_T, is found to be 54,000 in.-lb/rad and the destabilizing stiffness, K_θ, is -47,500 in.-lb/rad. The difference is 6500 in.-lb/rad of positive moment, thus the system is stable. The stabilizing moment is increased by the addition of the rotor moment, K_w, of 9090 in.-lb/rad. An additional consideration which affects the choice of the moment arm a, comes from satisfying the dynamic requirements of the rotating assembly described in Section 4.4.2.3.

Evaluating the inequality using the prototype design variables results in a negative a, which is obvious from the fact that the second term, K_T, must be equal to or greater than K_θ, for static stability. This inequality will be useful, however, in designing magnetic bearing suspensions as it contains the major system parameters in a convenient form. The relative values of K_T and K_θ can be adjusted to obtain any degrees of positive stability desired. A guide for determining an arbitrary minimum stability can be obtained by making $T_T/T_\theta \approx 2$ for a single bearing which results in $\bar{h}//R_m \approx 4$. This ratio in the prototype is 3.3, which is an acceptable value.

4.4.3 1/10-Scale Magnetic Bearing Design

The bearing magnetic circuit analysis was first performed by employing elementary manual computations. The dimensions of the fringing rings were based on the analytical and experimental work performed by Mechanical Technology Inc[4-3]. The following equations were used to calculate the required field and the resulting magnetic flux in the gaps:

$$B_g = \left(\frac{2\ F\mu_o}{A_p/C}\right)^{1/2} \qquad \phi_g = \frac{B_g\ A_P}{C}$$

where ϕ_g = magnetic flux in the gap - webers (wb)

F = force across each gap (50% of the total)

A_p = area of a pole (at the base of the fringe rings)

C = Carter coefficient to account for the presence of slots between the fringing rings[4-4], Fig. 4-69

B_g = field between fringing ring faces - tesla (T).

The inner and outer pole areas were taken equal in the design. The Carter coefficient, C, accounts for the change in gap flux distribution due to the presence of the fringing rings and slots compared to smooth pole faces.

C74-1577

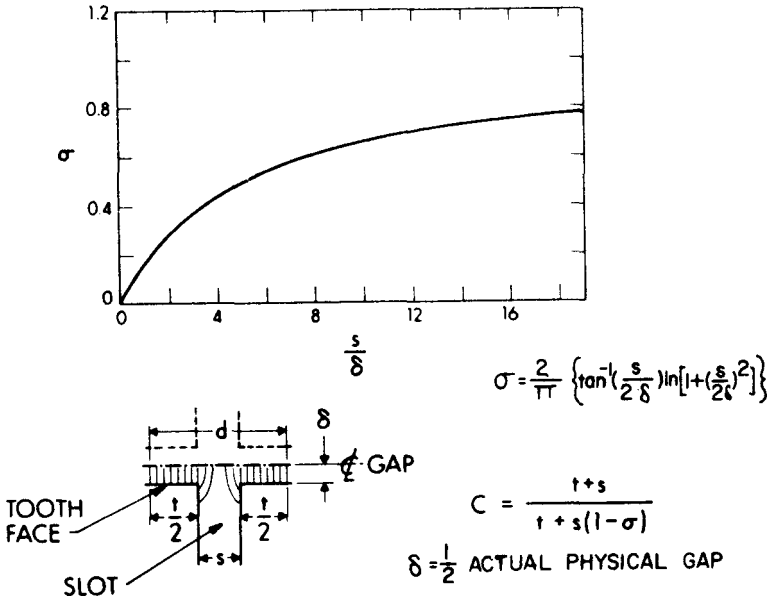

Figure 4-54. Definition of the Carter coefficient for toothed air gap.

The total required magnet flux, ϕ_m, is then estimated by adding 20% to the gap flux, an engineering assumption which is usually made to compensate for the leakage flux which is difficult to calculate. The magnet area, A_m, is found from the samariam-cobalt demagnetization curve, Fig. 4-37,

at an assumed flux density, B_m of 0.45 tesla (near the maximum energy product point):

$$\phi_m = B_m A_m = 1.2\ \phi_g \text{ (webers)}.$$

To find the magnetic thickness, t_m, it is necessary to sum the magnetomotive current around the magnetic circuit:

$$MMF_{total} = 2MMF_{gap} + MMF_{Iron} = 2\frac{\phi_g C \ell_g}{\mu_o A_g} + \frac{\phi_i \ell_i}{\mu_o\ rA_i}.$$

The six bearings were originally designed to support a total weight of 500 pounds (83 pounds per bearing) at an operating gap of 18 mils and a bearing magnetic pressure of 26 psi. A space to fringe land width ratio of 3:1 and a land width to gap ratio of 1:1 were selected for the bearing fringe rings. The sum of the circuit MMF is divided by the demagnetization field strength of the magnet, Hm, at an induction B_m = 0.45 tesla, to yield the magnet thickness in the magnetized direction. Two-percent silicon steel was selected for the rotor and stator because of its high resistivity (60 $\mu\ \Omega$ cm) and expected good permeability, μ_r; the high resistivity reducing unnecessary eddy currents.

The preceding equations were then solved under the assumptions:

F = 83 lb

A_g = 3.4 $in.^2$ at 24 psi

C = 1.7

g = 0.018 in.

μ_r = 1100 (est).

The following results were obtained:

B_g = 0.8 tesla (peak)

ϕ_m = 6.74×10^{-4} Wb

B_m = 0.45 tesla at A_m = 16 cm^2

MMF_{total} = 1160 amp

ℓ_m = 0.144 in.

The flux control coil peak ampere turns were designed to generate a flux equal to the permanent magnet flux at the design gap in order that the control coil could provide initial liftoff forces, when required. The coil was not designed to provide this flux continuously but as momentarily required for liftoff:

$$\text{MAX NI coil} = 2 \times \text{MMF gap} + \text{MMF magnet}$$
$$= 1500\text{-amp turns.}$$

A magnetic bearing system of this design was then fabricated and assembled. Experimental measurements of the permanent magnetic lifting force at the design gap were found to be approximately 50% of the value expected. The prototype magnetic bearing was found to provide a lifting force of 39 pounds rather than the expected value of 83 pounds at the design gap of 18 mils, Fig. 4-55. Upon inspection, the silicon steel used for the bearing stator and rotor was found to have an unexpectedly low permeability of under 200, rather than an assumed value of over 1,000. This increased the fringing field loss and also increased the required MMF in the iron circuit. The measured carbon content was found to be 0.5% and the presence of a small permanent magnetization indicated that silicon tool steel had actually been used rather than the desired electrical grade silicon steel (customarily available only in sheet form). It was apparent from these measurements that the leakage flux was substantially greater than the assumed rule of thumb. This conclusion was reinforced when the peak field in the gap was found to differ by 30% between the inner and outer bearing gaps, another indicator of large flux leakage.

A finite element computer program which had been developed concurrently with the magnetic bearing construction but had not reached a sufficient state of maturity to be used in the initial bearing design was then exercised for the 1/10-scale prototype bearing geometry. This computer program confirmed the higher than expected leakage flux and predicted bearing lift forces within 10% of the measured experimental data. A computer-generated picture of the magnetic flux distribution and flux leakage in the prototype magnetic bearing units is shown in Fig. 4-56. These results were generated by the methods described in Reference 4-5. The finite element results and the magnetic flux

distribution calculations showed that the flux leakage correction should have been chosen much larger than the 20% correction used in the initial calculations which formed the basis for the design of the prototype magnetic bearing.

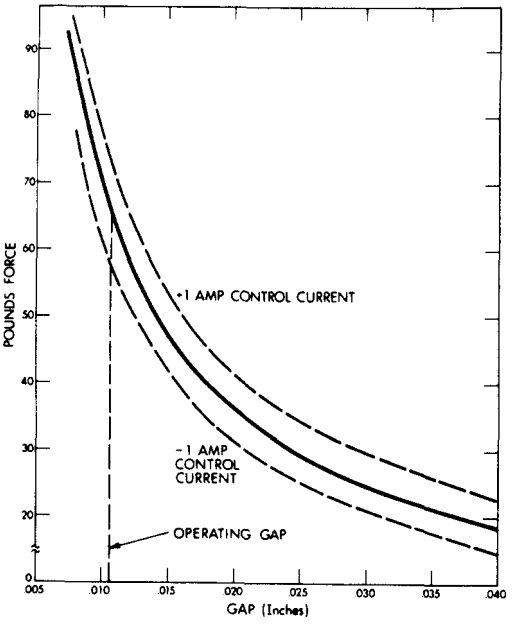

Figure 4-55. Magnetic bearing lifting force.

Rather than construct new magnetic bearing units, the prototype bearings units were utilized by reducing the operating gap from 18 mils to 10 mils to improve the lifting force per bearing and by reducing the total supported design weight from 500 pounds to 400 pounds. A reduction in operating gap width was made possible by the excellent component tolerance control maintained in construction of the prototype magnetic bearing unit; tolerance control not thought possible before construction of the unit. This improved tolerance quality actually made obsolete the initial design gap choice of 18 mils and allowed the reduction to 10 mils.

At the new design gap of 10 mils, the measured single bearing lifting force is 66 pounds, Fig. 4-55, and the measured axial stiffness is 4,500 pounds/inch, Fig. 4-57. The measured radial centering force and transverse stiffness at this gap are shown in Fig. 4-58 and 4-59, respectively. The ratio of axial to radial stiffness is 8:1 and is similar in ratio to that measured by other experimenters for similar geometries. The negative gimballing spring rate, defined as $\frac{dF}{dg} R_M^2$, where R_M is the mean fringe ring radius, is 6000 in-lb/rad to a maximum displacement of approximately 0.010 inch.

C74-1561

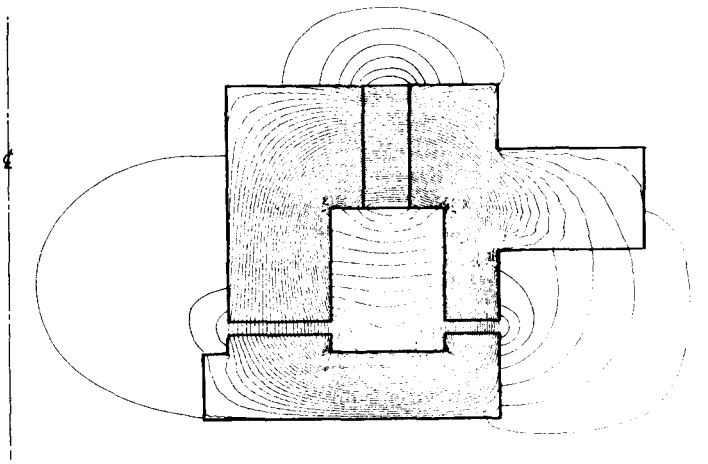

Figure 4-56. Magnetic bearing flux lines.

C74-1578

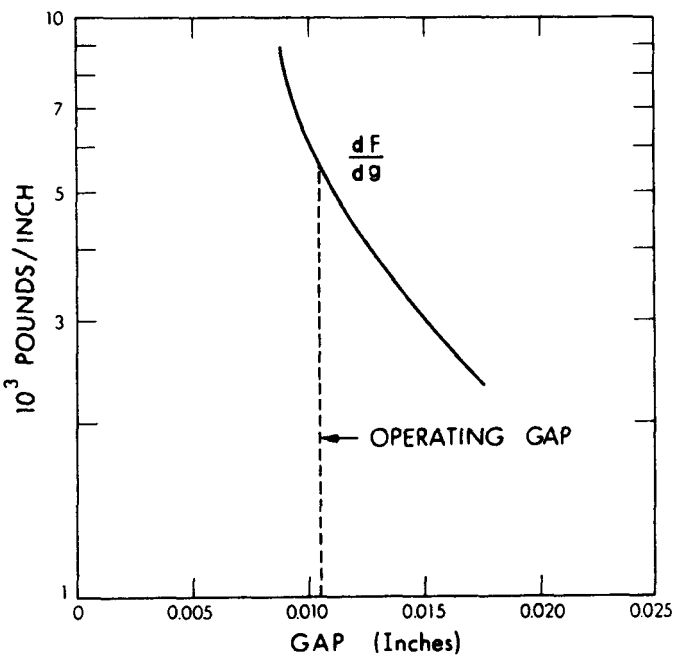

Figure 4-57. Magnetic bearing axial stiffness.

C74-1550

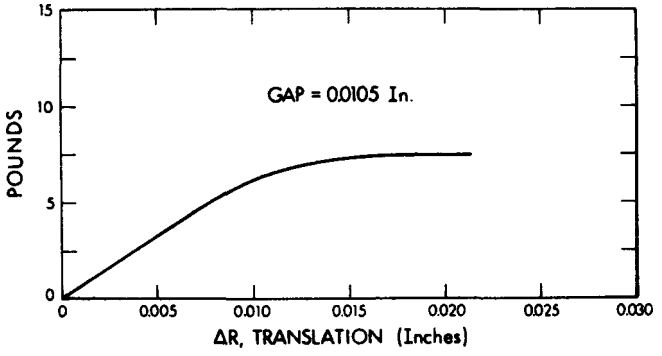

Figure 4-58. Magnetic bearing transverse centering force.

C74-1579

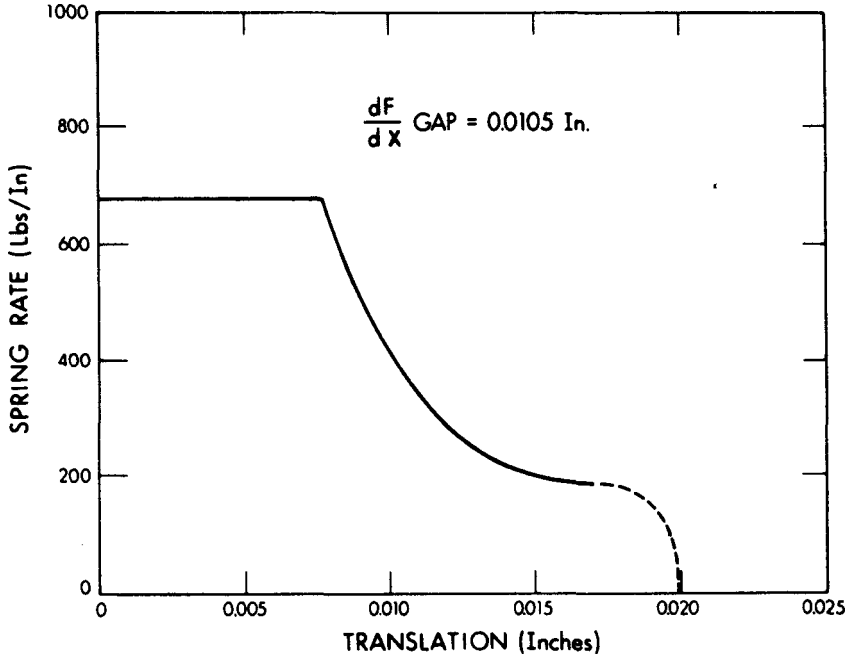

Figure 4-59. Magnetic bearing transverse stiffness.

The change to a smaller magnetic bearing gap in no way compromised the flywheel operation. In retrospect, it appears that the original design gap of 18 mils was just greater than needed to accommodate actual multiple assembly tolerances and the minimum touchdown clearance allowance of 4 mils.

4.4.4 Improved Magnetic Bearing Design Procedure

Based on the experience gained with the 1/10-scale magnetic bearing design as discussed in Section 4.4.3, an improved method for the design of the magnetic bearing circuit was formulated which uses the following equations:

$$B_g = \left(\frac{2F\mu_o}{A_p}\right)^{1/2} \tag{1}$$

$$B_M A_M = f_g A_p B_g \tag{2}$$

$$H_m L_M = f_R H_g C\ell_g + H_i L_i$$

$$= f_R \frac{B_g}{\mu_o} C\ell_g + \frac{B_i L_i}{\mu_o \mu_r} \tag{3}$$

where B_g = average field in gap

A_p = area of pole at base of fringing rings.

In equation (2) the correction factor f_g accounts for fringing flux around the gap and the ratio A_g/A_m is adjusted to have B_M fall near the maximum $Sm\text{-}Co_5$ magnet energy product, between 0.4 and 0.5T. The correction factor f_R in equation (3) defines the total magnetomotive force (MMF) and accounts for the reluctances present in the complete magnetic circuit as a percentage of gap reluctance:

$$R = \frac{H\ell}{\Phi} = \frac{\ell}{\mu_o A} \quad \text{(in air)} \tag{4}$$

$$R_g = \frac{C\ell}{\mu_o A} . \tag{5}$$

ℓ and A are the appropriate length and area through which the flux is conducted.

The leakage flux is significant at several locations in Fig. 4-56: a) adjacent to the gap, b) across the permanent magnet thickness, and c) between the stator poles. The dimensions of ℓ and A are estimated from geometrical proportions of the regions in question, noting that field intensity (and flux) decreases with the square of the distance from the source potential, the magnetic pole. The inner and outer gaps are separately calculated:

$$f_g = 1 + \frac{R_a}{R_g}$$

$$f_R = 1 + \frac{\sum R}{R_g} = 1 + \frac{(1/R_a + 1/R_b + 1/R_c^{-1})}{R_g} .$$

For a given lifting force, F, the required magnet field is calculated from equation (2). The magnetic circuit, MMF, equation (3), is used to find the required magnet thickness, where H_M is found from the second quadrant demagnetization curve of the permanent magnet (SmCo) at the design field, B_M, Fig. 4-37. Using these equations and inserting appropriate dimensions results in gap fields and forces much closer to the measured values than those obtained by the previous method.

4.4.5 Damping In Magnetic Bearing Systems

Damping in the magnetic bearing system is due to its intrinsic damping characteristics plus any external damping added to improve the overall system damping level. In this section, the intrinsic damping of the 1/10-scale magnetic bearing unit is estimated using analytical methods and the estimates compared with experimental measurements. Experimental measurements of the overall damping of the magnetic bearing unit with an external mechanical damper are also reported. Experimental measurements of the intrinsic magnetic bearing damping and the contribution to damping of an external mechanical damper were made in the course of eliminating a low-frequency (2-Hz) whirl mode that became excited when flywheel rotor speeds exceeded about 11,000 RPM. The excitation of the whirl mode by internal hysterisis in the rotating elements and its elimination by the addition of external damping are described in depth in Section 4.5 of this report.

The intrinsic damping in the magnetic bearing system is due to damping forces that are generated between the bearing rotor and stator as a result of induced eddy currents in these components in response to rotor displacements. No significant damping effects arise from the spinning rotor since there is a uniform azimuthal magnetic field intensity.

Displacement motions between the rotor and stator can be either parallel translation of the shaft or gimbal rotation around a horizontal axis through the rotor diameter. If the bearing gap is displaced along the shaft from the gimballing center, translation will also take place. Nonshorted copper wire rings were inserted in the stator slots for additional damping.

Eddy currents are generated by a change in the magnetic flux which penetrates a conductive medium. Defining the configuration of the eddy current paths requires making assumptions of the effective volume and direction of the eddy currents. The basic relationships are:

$$\text{Generated potential } E = \frac{\Delta\phi}{\Delta t} = BA\omega \text{ (volts)} \qquad (1)$$

$$\text{Effective resistance } R = \frac{\rho L}{a} \text{ (ohms)} \qquad (2)$$

$$\text{Damping Power } P = \frac{E^2}{2R} \text{ (watts)} \qquad (3)$$

where $\Delta\phi = \Delta B \times A$

B = magnetic field change

A = area of ΔB

ω = disturbing frequency

ρ = material resistivity

L = characteristic depth (length) of ΔB

a = area of eddy current normal to ΔB vector.

The magnitude of ΔB in the bearing material is dependent on the relative change in position of the fringing rings across the gap, referring to Fig. 4-60.

Gimbal Geometry

$$\Delta B = B_o \frac{x}{g}$$

$$\Delta B_{pole} = \Delta B \ (1/C)$$

C = Carter coefficient (Reference Section 4.3).

Translation Geometry

$$\Delta B = B_o \left(\frac{\sqrt{g^2 + c^2}}{g} - 1 \right)$$

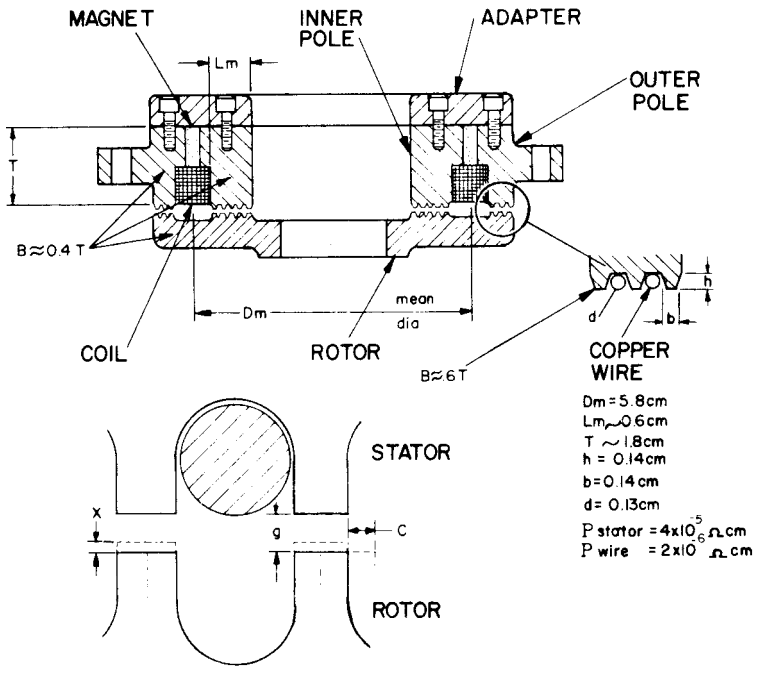

Figure 4-60. Bearing geometry for damping calculations.

Gimbal rotation of the rotor will cause the gap to become smaller on one end of a diameter and larger on the other, which results in a flux redistribution throughout the magnetized volume.

Referring to Fig. 4-60, for the stator:

$$E_\theta = \Delta B \omega (D_m L_m)$$

$$R_\theta = \frac{\rho D_m}{2 L_m T}$$

$$P_\theta = \frac{(\Delta B \omega)^2 L_m^3 D_m T}{\pi \rho} .$$

Rotor damping power is proportional to the rotor/stator thickness ratio.

Translation of the rotor will cause the flux in the fringe ring to increase in the corners, but will have no effect on the flux distribution in the stator volume; therefore, let us only consider the mean diameter of a fringe ring and multiply the calculated power by the total number of fringe rings in the complete bearing:

$$E_T = 2\,\Delta B\omega\,(D_m h)$$

$$R_T = \frac{\rho \pi D_m}{hb}$$

$$P_T = \frac{32(\Delta B\omega)^2 h^3 b D_m}{\pi\rho} \qquad \text{(16 fringe rings)}.$$

As a consequence of the translational flux change in the fringe ring adjacent to the copper wire, a current is induced along the wire. The eddy current effect is the same as in the fringe ring and is calculated with the substitution of wire diameter for the rectangular dimensions of the fringe ring:

$$E_{Cu} = \Delta B\omega \frac{d\pi}{2} D_m$$

$$R_{Cu} = \frac{D_m}{\pi d^2/4}$$

$$P_{Cu} = \frac{(\Delta B\omega)^2 \pi D_m d^4}{8\rho} \qquad \text{x (6 wires)}.$$

Gimbal rotation alone will not induce eddy currents in the copper wires because there is an equal flux change on either side of the wire.

As noted previously, these equations are only approximations since they are based on assumptions of magnetic flux changes and the resulting eddy currents. Therefore, the computed damping power based on the equations will be only an order of magnitude estimate.

Experimental measurements of the effective damping rate of the 1/10-scale magnetic bearing due to intrinsic damping were made by measuring the amplitude decay rate of the flywheel oscillation using the radial shaft position probes to measure the oscillation amplitude versus time. The radial pendulum

oscillation was initiated by releasing the nonspinning flywheel rotor from a displaced position; the pendulum oscillation simulating closely the predicted mode shape of the excited, low-frequency whirl mode (Section 4.5) of 1 Hz. The damping ratio was calculated from:

$$\rho = \frac{\ell n \frac{x_2}{x_1}}{\omega \Delta t}$$

where: x_2/x_1 = amplitude decay ratio

Δt = time interval

ω = oscillation frequencies.

The variation of the measured intrinsic damping ratio with time (or oscillation angular amplitude) is shown in Fig. 4-61. The damping ratio is 3/10% at the start of the measurement when the oscillation amplitude is maximum at 0.002 radians. The damping ratio falls quickly to 1/10% as the oscillation amplitude decreases to 0.001 radians. The damping ratio remains constant at 1/10% for oscillation amplitudes between 0.001 radian and 0.0004 radian, typical of observed whirl amplitude oscillations which remain stable.

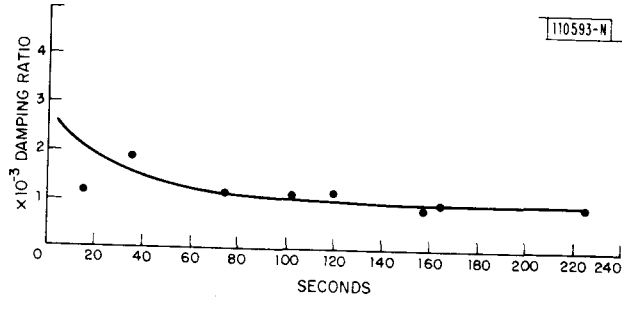

Figure 4-61. Measured damping ratio - magnetic bearing only.

The damping power can be obtained, using the experimental measurements, from the following equation:

$$P_D = \pi K_\theta \rho \theta^2$$

where K_θ = Gimbal spring constant

ρ = damping ratio

θ = oscillation amplitude.

Using K_θ = 78,750 lb/in. rad. obtained from a direct measurement of the torque required to displace the shaft through a known angle, a damping ratio equal to 0.001, and θ = 0.0004 rad; P_D is equal to 4.4×10^{-6}W. For comparison, an estimated damping constant of 4.34 in.-lb sec per bearing used in the initial dynamic whirl analysis (Section 4.5) results in an assumed damping power of 7.5×10^{-6}W for the same oscillation amplitude.

To ascertain whether the design eddy current damping assumptions are valid, the damping power was calculated for the three modes using the same displacement assumed above and the dimensions given in Fig. 4-60. The results for the 6 bearings are:

Gimbal P_θ	$\simeq 4.2 \times 10^{-6}$W
Translation P_T	$\simeq 1.4 \times 10^{-7}$W
Copper Wire P_{cu}	$\simeq 1 \times 10^{-6}$W.

The total calculated damping power of 5.3×10^{-6}W is of the same magnitude as that measured experimentally. The lower damping power for the translational mode can be explained on the basis that a very small volume of material is affected by flux changes from translation and that the magnitude of the flux change is quite small for small displacements. Gimbal rotation is estimated to provide the most effective source of damping. It is likely that the actual ΔB in gimballing is reduced by the action of the bearing lift servo since the effective lift is increased as the oscillation angle increases and the servo is designed to maintain a constant vertical shaft position. A factor of two reduction in ΔB is estimated from this effect which will reduce the damping

power to 2.7×10^{-6}W, smaller than the measured value. Contrary to the original assumption that high resistivity of the bearing magnetic iron is desirable to reduce losses due to eddy currents generated by action of the flux control coil, it is obvious that damping due to eddy currents can be enhanced by using low resistivity materials.

When the flywheel unit was run with only the intrinsic damping of the magnetic bearing present, a stability problem arose at shaft speeds over 11,000 RPM. Unstable growth of the 2.0-Hz whirl mode was experienced which prevented the flywheel from reaching the design speed of 15,000 RPM. After investigating the possible energy sources which might drive the resonance (see Section 4.5), a mechanical damper using polyurethane rubber was attached to the top of the bearing shaft. This increased the damping ratio from ζ=0.0005 at small amplitudes to 0.003 with a maximum of ζ=0.006, at larger amplitudes, Fig. 4-62, and completely eliminated further problems with the 2.0-Hz whirl mode. The installation of the mechanical damper also eliminated the large displacements at the 40- and 75-Hz resonances. The full design speed of 15,000 RPM could be reached without difficulty thereafter. A comparison of the measured damping time constant versus oscillation amplitude is shown in Fig. 4-63 before and after installing the external damper. At the assumed oscillation amplitude of 0.0004 radians, the damping time constant was reduced from 4.5×10^5 to 1.2×10^5 sec/rad. This change means that the damping time constant power has increased more than four times with the mechanical damper. The experimental data also shows that the damping time constant for the bearings exhibits an abrupt increase at less than 0.0007 rad. This abrupt change is probably due to a redistribution of the oscillating flux paricularly in the fringing rings and copper wires. Interestingly, the effect is still observable when the mechanical damper is added to the system results. All of the computation results and data presented should be considered as approximate. The low magnitude of the power loss being estimated, the difficulties in making accurate measurements, and the number of assumptions required to define the eddy current phenomena, all contribute to the approximate nature of the results. Furthermore, the effective damping ratio is not constant, but is proportional to the relative displacement between the moving and stationary elements.

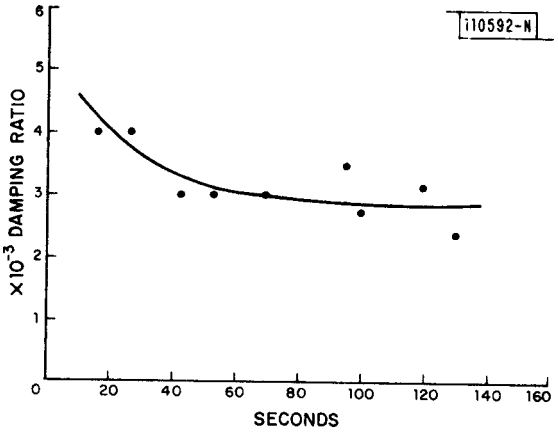

Figure 4-62. Measured damping ratio with mechanical damper.

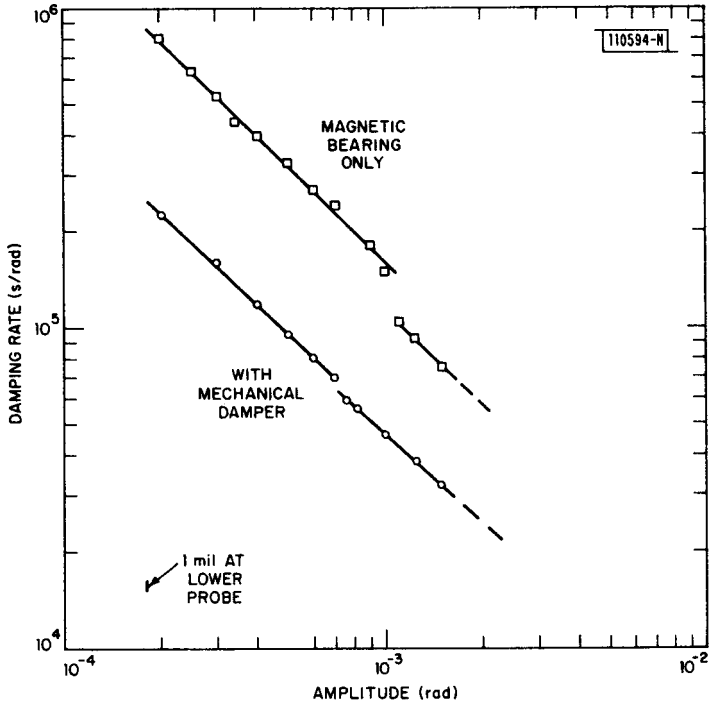

Figure 4-63. Measured damping rate--non rotating pendulum.

4.5 Dynamic Analysis of a Magnetically Suspended Flywheel

A number of dynamic analyses were carried out in support of the design of the 1/10-scale prototype flywheel system. The analyses investigated:

1. Whirl mode shapes and frequencies of the flywheel unit.
2. Dynamic response for given damping and flywheel imbalances.
3. Estimates of the amount of internal (hysteretic) damping that can cause self-excited instabilities.
4. The addition of an external damper to eliminate experimentally observed hysteretic instabilities.
5. The effect of earthquakes on a magnetically suspended flywheel unit.

Each of the above considerations is discussed in some detail in the following paragraphs.

4.5.1 Introduction

Two key considerations in the design of the magnetically supported flywheel system were that no critical frequencies should be in the 7,500 RPM to 15,000 RPM (125 Hz to 250 Hz) operating range of the flywheel and that the magnetic suspension system should be capable of operating with an advanced composite rotor which might develop an imbalance during the course of its life. Elimination of critical frequencies in the operating range of the flywheel was accomplished through careful analysis and design of the magnetic suspension and the support structure which attaches the flywheel system to the vacuum chamber. A flexible quill approach was selected to accommodate any imbalance or misalignment that may exist initially in the wheel or develop in use. The quill shaft was also sized so there are no critical frequencies in the operating range.

4.5.2 Equations of Motion

The equations of motion of the rotating shaft with respect to a rectangular Cartesian coordinate frame fixed in space are:

$$\begin{bmatrix} M & 0 \\ 0 & M \end{bmatrix} \begin{Bmatrix} \ddot{q}_y \\ \ddot{q}_z \end{Bmatrix} + \Omega \begin{bmatrix} 0 & G \\ -G & 0 \end{bmatrix} \begin{Bmatrix} \dot{q}_y \\ \dot{q}_z \end{Bmatrix} + \begin{bmatrix} C & 0 \\ 0 & C \end{bmatrix} \begin{Bmatrix} \dot{q}_y \\ \dot{q}_z \end{Bmatrix} \tag{1}$$

$$+ \begin{bmatrix} K & 0 \\ 0 & K \end{bmatrix} \begin{Bmatrix} q_y \\ q_z \end{Bmatrix} + \mu \begin{bmatrix} 0 & K_H \\ -K_H & 0 \end{bmatrix} \begin{Bmatrix} q_y \\ q_z \end{Bmatrix} = \begin{Bmatrix} Q_y \\ Q_z \end{Bmatrix} .$$

The shaft is assumed to be rotationally symmetric and inertias are lumped at the nodes. Elements of the skew symmetric gyroscopic matrix containing [G] are the rotary inertias of the disks taken about the spin axis of the shaft. In this analysis of the MIT Lincoln Laboratory flywheel, only the gyroscopic effects of the flywheel and of the motor-generator were considered significant. The effects of structural damping are included through the term $\mu[K_H]$ where $[K_H]$ is the stiffness matrix of those elements which introduce hysteretic damping. The matrix, [C], is the viscous damping matrix. Damping was assumed to be present only at the magnetic bearings. The nodal displacements (Fig. 4-64) are given by:

$$[q_y] = [v_1 \psi_{z_1}\ v_2 \psi_{z_2} \cdots v_n \psi_{z_n}]$$
$$[q_z] = [w_1 \psi_{y_1}\ w_2 \psi_{y_2} \cdots w_n \psi_{y_n}] . \qquad (2)$$

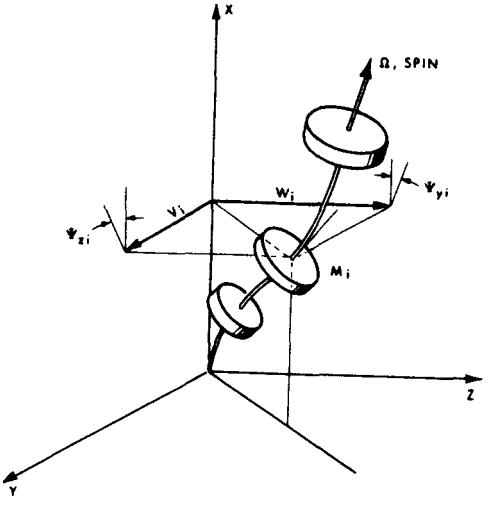

Figure 4-64. The nodal displacements.

The applied forces at the first node arising out of any imbalance in flywheel are given by:

$$Q_{y_1} = m\Omega^2 e \cos\Omega t$$
$$Q_{z_1} = m\Omega^2 e \sin\Omega t \qquad (3)$$

where m is the mass of the wheel and e is the static imbalance (c.g. offset with respect to the spin axis). Any dynamic imbalance (inclination of the principal axis with respect to the spin axis) can be taken into account in a similar manner.

4.5.3 Natural Frequencies and Mode Shapes - Nonspinning Shaft

In the analysis of possible whirl states and investigation of the stability of these states, the mode shapes of the nonrotating shaft will be used as generalized coordinates. These are solutions to the eigenvalue problem obtained from the equations of free vibration:

$$\begin{bmatrix} M & 0 \\ 0 & M \end{bmatrix} \begin{Bmatrix} \ddot{q}_y \\ \ddot{q}_z \end{Bmatrix} + \begin{bmatrix} K & 0 \\ 0 & K \end{bmatrix} \begin{Bmatrix} q_y \\ q_z \end{Bmatrix} = 0. \qquad (4)$$

Because a rotationally symmetric shaft is assumed, the eigenvalue problem in 2n degrees of freedom reduces to one in n degrees of freedom. In modal form, Equation (4) becomes:

$$[K]\{\psi\} - \omega_c^2 [M]\{\psi\} = 0. \qquad (5)$$

The system can now be modeled as a planar structure as shown schematically in Fig. 4-65. The magnetic bearings were modeled as linear elastic springs; the axial deformations were assumed to be decoupled from lateral deformations. These two assumptions are consistent with a linear analysis based on small deformation theory. It is of interest to note that the magnetic bearings possess negative stiffness in rotation and, accordingly, were modeled as such. The bearings, each having a positive stiffness in translation, were positioned along the shaft to ensure that the overall rigid body rotational stiffness was positive. The flywheel was modeled as a point mass with associated inertias.

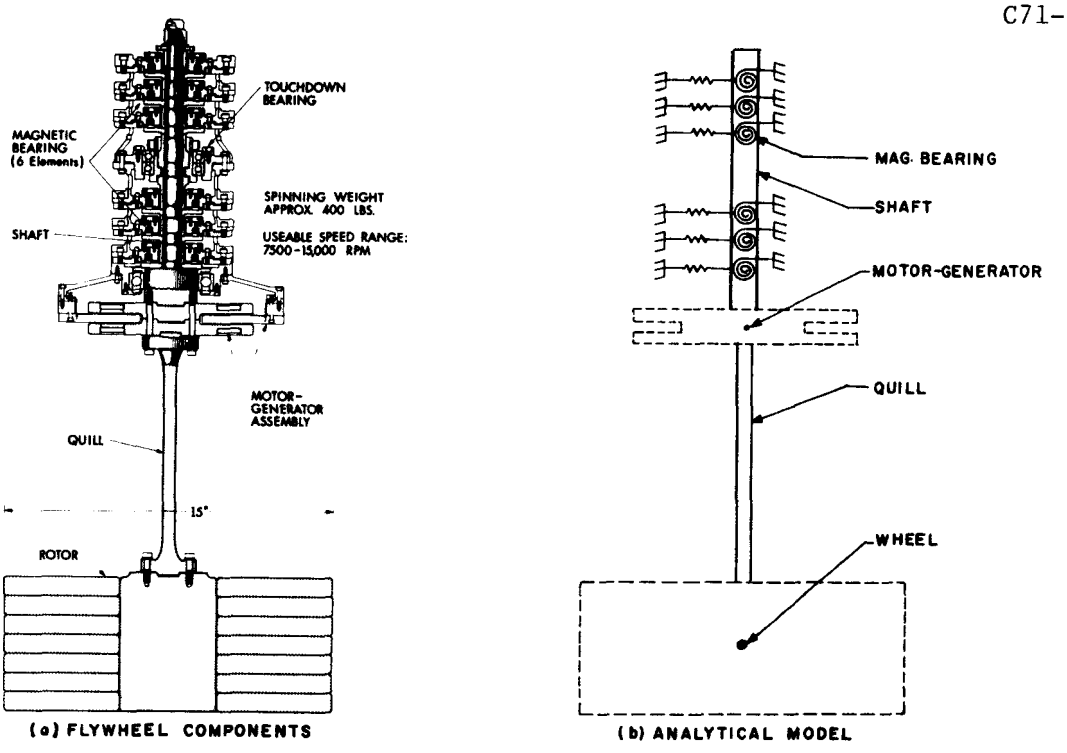

Figure 4-65. Modeling of the 1-kW experimental flywheel.

Letting ω_{cj} be the j^{th} natural frequency and $[\Psi_j]^{cj}$ the corresponding mode shape, and choosing to normalize the latter with respect to the mass matrix:

$$[\Psi_i][M]\{\Psi_j\} = \begin{cases} 0 & i \neq j \\ 1.0 & i = j \end{cases} \tag{6a}$$

hence

$$[\Psi_i][K]\{\Psi_j\} = \begin{cases} 0 & i \neq j \\ \omega_{c_i}^2 & i = j \end{cases} \tag{6b}$$

The eigenvalues and the normalized eigenvectors were obtained using STRUDL[4-6], a structural design language, available in a time-sharing mode at MIT Lincoln Laboratory. The model had eleven nodes and twenty-two degrees of freedom. The lowest five eigenvalues and normalized eigenvectors obtained

from this analysis were then read directly by another computer program that was developed to perform the dynamic analysis of the spinning system. The mode shapes obtained from the STRUDL analysis are shown in Fig. 4-66.

C71-1125

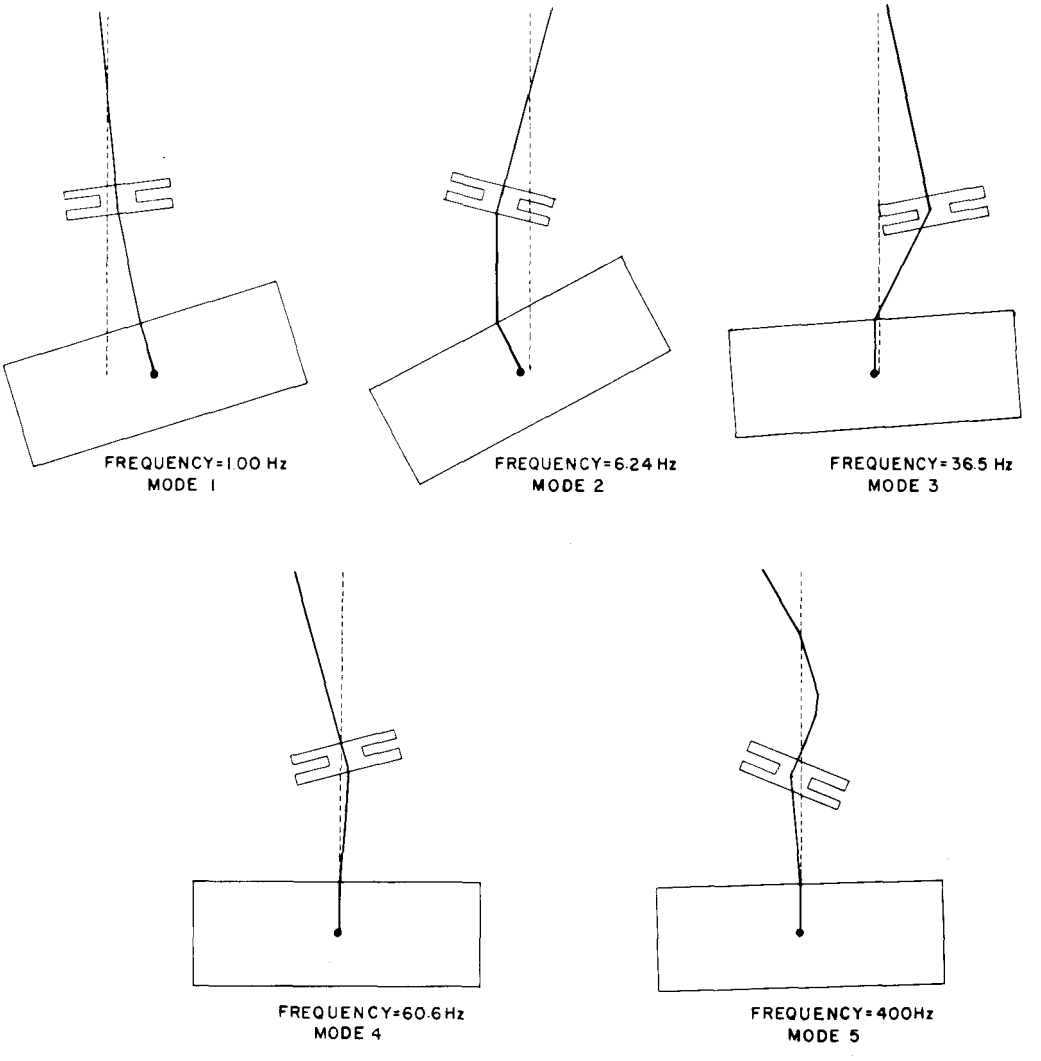

Figure 4-66. Mode shapes and frequencies for the nonspinning case.

The lowest frequency mode, Mode 1, is the one that is excited by internal hysterisis effects, if any are present, and it is interesting to note that this mode is of pendulum type with a center of rotation about midway up on the magnetic bearing shaft. In this mode, the uppermost end of the magnetic bearing shaft undergoes displacements from the vertical axis of system. As discussed later, this property is used to advantage when an external mechanical damper is added to the flywheel system at this point to eliminate a low frequency whirl mode.

It is now possible to rewrite the equation of motion in terms of the modal coordinates, if we set:

$$\{q_y\} = [\psi][\omega_c^{-1}]\{\eta\} \tag{7a}$$

$$\{q_z\} = [\psi][\omega_c^{-1}]\{\zeta\} . \tag{7b}$$

Eq. (1) may be written as:

$$\begin{bmatrix} \omega_c^{-2} & 0 \\ 0 & \omega_c^{-2} \end{bmatrix}\begin{Bmatrix} \ddot{\eta} \\ \ddot{\zeta} \end{Bmatrix} + \Omega\begin{bmatrix} 0 & A \\ -A & 0 \end{bmatrix}\begin{Bmatrix} \dot{\eta} \\ \dot{\zeta} \end{Bmatrix} + \begin{bmatrix} D & 0 \\ 0 & D \end{bmatrix}\begin{Bmatrix} \dot{\eta} \\ \dot{\zeta} \end{Bmatrix}$$
$$+ \begin{bmatrix} \lambda & 0 \\ 0 & \lambda \end{bmatrix}\begin{Bmatrix} \eta \\ \zeta \end{Bmatrix} + \mu\begin{bmatrix} 0 & B \\ -B & 0 \end{bmatrix}\begin{Bmatrix} \eta \\ \zeta \end{Bmatrix} = \begin{Bmatrix} F_\eta \\ F_\zeta \end{Bmatrix} \tag{8}$$

where

$$[A] = [\omega_c^{-1}][\psi]^T[G][\psi][\omega_c^{-1}] \tag{9a}$$

$$[D] = [\omega_c^{-1}][\psi]^T[C][\psi][\omega_c^{-1}] . \tag{9b}$$

$$[B] = [\omega_c^{-1}][\psi]^T[K_H][\psi][\omega_c^{-1}] \tag{9c}$$

are all real, symmetric, and positive semidefinite.

4.5.4 Whirl-Mode States

It is well known that the gyroscopic motion of the spinning disks will alter the system's natural frequencies and mode shapes[4-7, 4-8]. In the following analysis, we determine how these vary with spin speed, Ω. The eigenvalue problem for the whirl-mode shapes and frequencies is obtained from:

$$\begin{bmatrix} \omega_c^{-2} & 0 \\ 0 & \omega_c^{-2} \end{bmatrix} \begin{Bmatrix} \ddot{\eta} \\ \ddot{\zeta} \end{Bmatrix} + \Omega \begin{bmatrix} 0 & A \\ -A & 0 \end{bmatrix} \begin{Bmatrix} \dot{\eta} \\ \dot{\zeta} \end{Bmatrix} + \begin{bmatrix} I & 0 \\ 0 & I \end{bmatrix} \begin{Bmatrix} \eta \\ \zeta \end{Bmatrix} = 0 \tag{10}$$

by seeking solutions of the form:

$$\{\eta\} = \{r\} \cos \omega t \tag{11a}$$

$$\{\zeta\} = \{r\} \sin \omega t . \tag{11b}$$

This implies that the shaft undergoes planar bending, the plane of bending itself whirling around at frequency ω. If ω is positive, we have forward whirl, if negative, retrograde whirl.

Again, the problem reduces to one in five degrees of freedom:

$$-\omega^2 [\omega_c^{-2}] \{r\} + \omega \Omega [A] \{r\} + [I] \{r\} = 0. \tag{12}$$

Introducing an auxiliary vector,

$$\{q\} = \omega [\omega_c^{-1}] \{\eta\} \tag{13}$$

enables us to write the eigenvalue problem in the standard form:

$$\begin{bmatrix} -\Omega[A] & \omega_c^{-1} \\ \omega_c^{-1} & 0 \end{bmatrix} \begin{Bmatrix} \eta \\ q \end{Bmatrix} - \lambda \begin{bmatrix} I & 0 \\ 0 & I \end{bmatrix} \begin{Bmatrix} \eta \\ q \end{Bmatrix} = 0 \tag{14}$$

where $\lambda = 1/\omega$.

Since the matrix on the left is real and symmetric, we are assured that all eigenvalues, ω_j, will be real.

Figure 4-67 shows the loci of the eigenvalues (the whirl frequencies, ω_j) as a function of spin rate, Ω. The solid curves are forward whirl states, the dotted retrograde (ω should be read as $-\omega$ when viewing the latter). The gyroscopic effect is most pronounced on the second mode. In this case, the forward-whirl frequency always remains greater than the spin speed of rotation because the ratio of the moment of inertia about the spin axis to that about a transverse axis passing through the c.g. of the flywheel is greater than 1.0. The points on these curves, where the spin speed Ω equals the whirl frequency ω, are designated "critical frequencies." The calculated whirl modes shown in Fig. 4-67 are for the 1/10-scale prototype flywheel unit which has a quill of 8-inches length and 7/16-inch diameter. These quill dimensions were chosen after a parametric study showed that such a quill would yield critical frequencies lying outside the operating range and ensure lateral shaft displacements in the operating region that were not excessive.

C71-1127

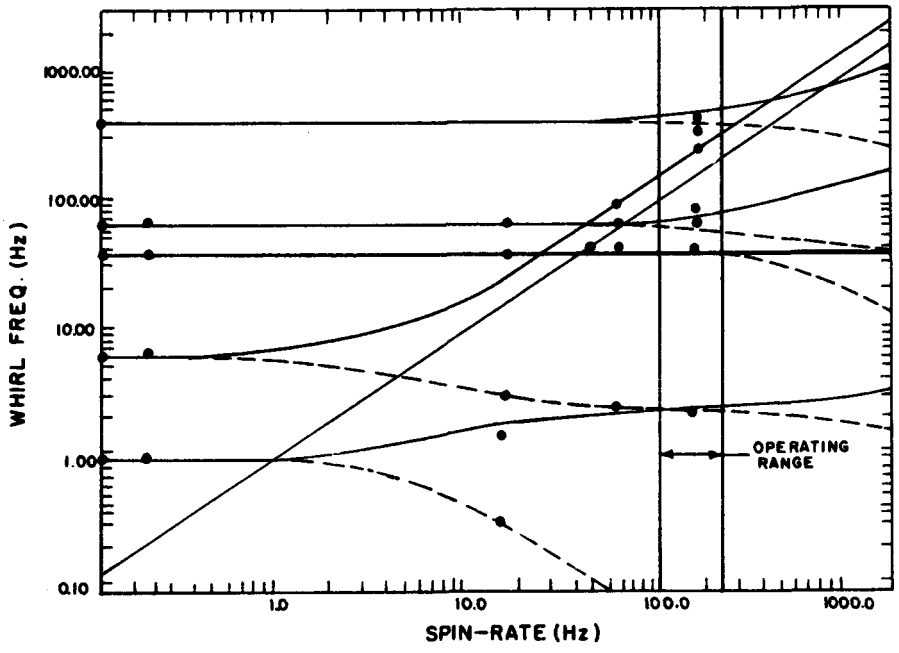

Figure 4-67. Whirl-spin states.

Figure 4-67 illustrates another aspect that must be considered in the design of a flywheel system. It shows that as the flywheel is accelerated up to operating speed (125 Hz to 250 Hz) from a stopped position, it passes through three critical frequencies where the spin rate and whirl frequencies are equal. If the flywheel were to remain for any length of time at one of these critical frequencies, the amplitude of that mode would grow until touchdown occurs, an undesirable situation. Touchdown may be avoided by providing sufficient motor acceleration to propel the flywheel through the critical frequency with a rapidity that does not allow the oscillation amplitude to build up or by providing sufficient external damping, again to limit the amplitude buildup.

4.5.5 Initial Test Results

The variation of whirl-mode frequencies with rotor spin speed was determined by performing a spectral analysis of magnetic bearing shaft position as measured by one of the Kaman Sciences inductive position probes. The equipment used to perform the spectral analysis is shown in Fig. 4-68. The experimental measurements of whirl frequency are compared with analytical predictions in Fig. 4-67, the experimental data being represented by the dots. The experimental results are in close agreement with predictions thus validating the prediction techniques.

P267-1087

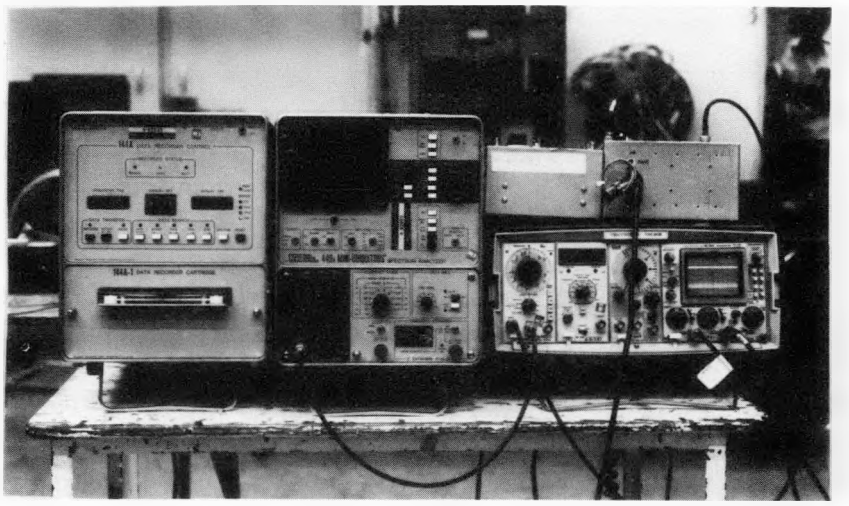

Figure 4-68. Spectral analysis equipment.

During initial shakedown runs of the flywheel system, buildup of a 2-Hz subsynchronous whirl was observed at a rotor spin speed of approximately 10,500 RPM. The presence of internal hysterisis and the lack of adequate damping were quickly identified as the probable causes of the subsynchronous whirl. The viscous damping of the flywheel assembly was then measured experimentally to help in the evaluation of the hysteretic whirl phenomenon. Analyses for the stability of whirl states in the presence of internal damping and the determination of forced response of the flywheel unit were developed and used for comparisons with experimental data as described below.

4.5.6 Stability of Whirl States

Structural damping, represented by the term in Eq. (1) containing the factor μ, can lead to self-excited oscillations, i.e., to instability. Internal damping provides a mechanism for transferring energy of spin about the shaft axis to kinetic and strain energy of whirling. In what follows, the possibility of instability in the vicinity of the whirl states at any given spin rate is investigated.

Premultiplying equation (8) by [0], integrating by parts, and noting that

$$[\dot{\eta}\ \dot{\zeta}]\begin{bmatrix} 0 & A \\ -A & 0 \end{bmatrix}\begin{Bmatrix} \dot{\eta} \\ \dot{\zeta} \end{Bmatrix} = 0 \tag{15}$$

due to the symmetry of [A], we obtain:

$$\begin{aligned} &\frac{d}{dt}\left\{\frac{1}{2}[\dot{\eta}\ \dot{\zeta}]\begin{bmatrix} \omega_c^{-2} & 0 \\ 0 & \omega_c^{-2} \end{bmatrix}\begin{Bmatrix} \dot{\eta} \\ \dot{\zeta} \end{Bmatrix} + \frac{1}{2}[\eta\ \zeta]\begin{bmatrix} k & 0 \\ 0 & k \end{bmatrix}\begin{Bmatrix} \eta \\ \zeta \end{Bmatrix}\right\} \\ &= -[\dot{\eta}\ \dot{\zeta}]\begin{bmatrix} D & 0 \\ 0 & D \end{bmatrix}\begin{Bmatrix} \dot{\eta} \\ \dot{\zeta} \end{Bmatrix} + \mu\left[[\dot{\zeta}][B]\{\eta\} - [\dot{\eta}][B]\{\zeta\}\right]. \end{aligned} \tag{16}$$

In the vicinity of the j^{th} whirl mode, $[\phi_j]$ at whirl frequency ω_j, we have

$$\{\eta\} = \{\phi_j\}\cos\omega_j t$$
$$\{\zeta\} = \{\phi_j\}\sin\omega_j t. \tag{17}$$

The above equation then reduces to

$$\frac{d}{dt}\{E_j\} = -\omega_j^2[\phi_j][D]\{\phi_j\} + \mu\omega_j[\phi_j][B]\{\phi_j\} \tag{18}$$

where E_j is the total energy of the j^{th} whirl mode; kinetic plus strain energy. It is seen that the total energy will increase without limit if the external damping, [D], is not sufficiently large relative to the hysteretic damping, μ[B]. That is, for stability, the latter must be confined as follows:

$$\mu < \frac{\omega_j[\phi_j][D]\{\phi_j\}}{[\phi_j][B]\{\phi_j\}}. \tag{19}$$

Now the sign of the hysteresis factor μ is fixed by

$$\mu = \frac{(\Omega-\omega)}{|\Omega-\omega|}. \tag{20}$$

Assuming, without loss of generality, that Ω is positive and, for the moment, considering forward-whirl-mode behavior, $\omega > 0$, Eq. (18) shows that for instability we must have $\mu > 0$

and hence $$\Omega > \omega. \tag{21}$$

Thus we note that hysteresis induced self-excited oscillations are always at a frequency lower than the spin speed. A similar observation was made by Bolotin[4-9].

This analysis also leads to the conclusion that for this particular damping mechanism, retrograde whirl modes can never be unstable, for if ω_j is negative, then the right-hand side of Eq. (18) is always negative. Hence, in this case, $\frac{dE_j}{dt}$ is always less than zero.

4.5.7 Forced Response

Any eccentricity in the location of the flywheel center of mass relative to the spin axis (or any inclination of the principal axis) will generate a forcing function with a frequency equal to the spin rate and an amplitude proportional to the square of the spin rate. To obtain estimates of the excursion of the shaft as the flywheel is brought up to speed, Eq. (1) was solved with a forcing function:

$$Q_{y_1} = me\Omega^2 \cos\omega t \qquad Q_{\psi_{z_1}} = (I_d - I_p)\epsilon_\theta \cos\omega t \tag{22a}$$

$$Q_{z_1} = me\Omega^2 \sin\omega t \qquad Q_{\psi_{y_1}} = (I_d - I_p)\epsilon_\theta \sin\omega t \tag{22b}$$

and damping matrix based, as before, on the best estimates of the damping characteristic of the magnetic bearings. The effect of hysteretic damping was neglected in this part of the analysis.

For this particular forcing function, the maximum response occurs in forward whirl at frequencies equal to the spin rate (at the intersection of the $\Omega = \omega$ line on Fig. 4-67 with the forward-whirl-mode contours).

4.5.8 Allowable Hysteresis in the Prototype Unit

The analysis described in Section 4.5.6 was used to predict the maximum allowable hysteresis that could be present in the prototype unit before whirl instability onset. Figure 4-69 shows the value of μ required for instability of the forward whirl modes as a function of spin rate Ω. In evaluating Eq. (19), the matrix $[K_h]$ was taken as the stiffness matrix of the whole structure, [K]. This implies that all structural elements contribute equally to structural damping. Viscous damping was assumed to be derived solely from the magnetic bearing and in particular from the copper in the magnetic bearings incorporated for that very reason. The damping associated with each of the six bearings was taken as 4.34 in-lb-sec in rotation and zero in translation.

C71-1128

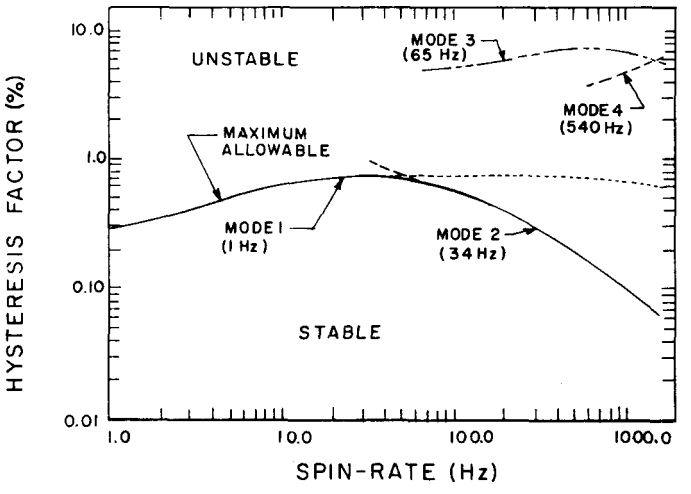

Figure 4-69. Maximum allowable hysteresis for stability.

The stability analysis of the whirl states suggests that hysteretic damping of the order of 0.1 to 1% might lead to unbounded growth of the lower whirl modes for the prototype magnetic bearing design without any additional external damping. To ascertain the actual level of internal hysteresis in the prototype bearing, load-deflection tests were performed on a duplicate flywheel assembly. The duplicate flywheel assembly included all components except the rotor. The assembly was set up in the MTS Universal Testing Machine in such a configuration that when load was applied at the motor-generator location, normal to the shaft axis, the deflected shape would be similar to the predicted 2-Hz whirl-mode shape. The test was conducted for amplitudes of deflection of 2.5, 5 and 7.5 mils (half amplitude) at 1-Hz and 2-Hz load applications. The resulting load deflection curve was plotted on an x-y plotter and the area enclosed by the hysteresis loop was determined. The average value of the measured hysteresis was found to be 1.2%.

The agreement between the predictions for the maximum allowable hysteresis and the actual measurements for hysteresis confirmed internal hysteresis as the mechanism responsible for the observed whirl mode instability and simultaneously suggested a cure for the instability through the addition of external damping.

4.5.9 External Damper Unit

Several options of implementing an external damper were considered. These included electromagnetic dampers and mechanical dampers ranging in location from the bottom of the flywheel to the top of the rigid magnetic bearing shaft. A simple parametric analysis indicated that the damper would be most effective when installed directly on the rigid shaft, either at the top or at the bottom. It was decided from implemention considerations that the top of the rigid shaft was the most accessible position in the prototype hardware and that the damper should be located there. In the interests of a timely demonstration of the proof of concept that external damping would eliminate the whirl, a mechanical external damper design rather than an electromagnetic design was selected for implementation.

A detailed description of the damper is given in Section 4.2.7, and only a brief review will be given here. The molded polyurethane damper was fabricated by casting polyurethane around a low friction bearing which is attached to the axial position nut at the top of the shaft (Fig. 4-20). A simplified dynamic analysis was performed which showed that the radial force on the bearing is very small, especially because the spring rate of the molded polyurethane section is smaller than the magnetic bearing stiffness in the lateral direction. In fact, the required spring constant for the damper was set at less than 1000 lbs/in. in order that there would be no significant shifting of the critical speeds.

A prototype of the molded polyurethane damper was then fabricated and a cyclic test was performed on the damper to determine its equivalent viscoelastic damping constant. This was done by loading the damper cyclically (in its plane), at 1 Hz and 2 Hz, and plotting the resulting hysteresis loop. The area inside the loop is the amount of energy dissipated by the damper in one cycle and it can be related directly to an equivalent viscous damping constant. The test was done at 5- 10-and 15-mil half amplitudes, and the results are summarized in Table 4-5 and in Fig. 4-70. The tests were conducted for two orientations of the damper with respect to the cyclic deflection in order to obtain average properties for the damper. The dynamic spring stiffness at

Table 4-5

Mechanical Damper Characteristics

110587-N

												AVERAGE			
FREQUENCY f (Hz)	AMPLITUDE × (PEAK) ($\times 10^{-3}$ in.)	WORK/CYCLE A (10^{-3} ft lb/cycle)	DYNAMIC STIFFNESS, k_D (lbs/in.)	LOSS FACTOR, η_S ($A/\pi k_D x^2$)	DAMPING CONSTANT, C (lb-s/in.)	DISSIPATED POWER, P ($\times 10^{-3}$ W)	A	k_D	η_S	C	P	k_S	η_S	C	P
1	5	6.00	156	0.49*	12.16*	0.68*	3.25	141	0.29	5.59	0.37	151	0.29	6.59	0.37
	10	15.20	162	0.30	7.70	1.72	12.20	147	0.26	6.18	1.38		0.28	6.94	1.55
	15	25.30	156	0.23	5.70	2.85	26.20	150	0.25	5.90	2.96		0.24	5.80	2.91
	20	38.80	156	0.20	4.91	4.38	42.60	150	0.23	5.40	4.81		0.22	5.16	4.60
	30	76.80	144	0.19	4.32	8.68	86.90	150	0.20	4.89	9.82		0.20	4.61	9.25
2	5	5.40	179	0.38	5.47	1.22	3.25	150	0.28	3.29	0.74	162	0.33	4.38	0.98
	10	13.97	171	0.26	3.54	3.16	18.40	150	0.39	4.66	4.16		0.32	4.10	3.66
	15	28.60	167	0.24	3.22	6.47	26.80	155	0.24	3.02	6.06		0.24	3.12	6.27
	20	41.40	162	0.20	2.62	9.36	48.00	159	0.24	3.04	10.80		0.22	2.83	10.08
	30	126.60	172	0.26	3.56	28.60	122.50	156	0.28	3.45	27.70		0.27	3.51	28.20
QUASI-STATIC STIFFNESS, k_S		129 lbs/in.					124 lbs/in.					126.5 lbs/in.			

* DISCARDED FROM AVERAGES.

2 Hz is 162 lbs/in. (about 30% higher than the quasi-static stiffness). The overall loss factor, defined as the ratio of energy dissipated to energy stored is 0.25 at 1 Hz and 0.28 at 2 Hz.

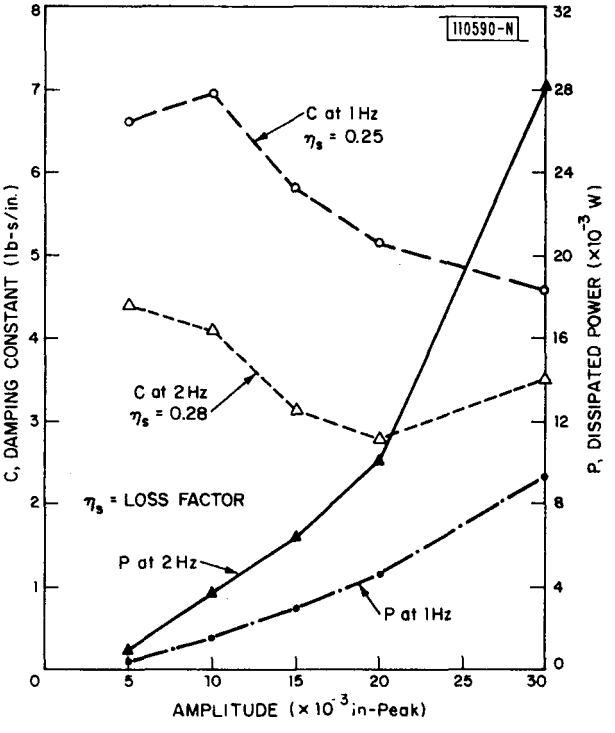

Figure 4-70. Damping characteristics of the molded polyurethane damper.

A dynamic analysis of the system with the mechanical damper in place was performed. The damper was assumed to have the experimental characteristics of the polyurethane damper. The maximum allowable hysteresis for whirl stability was increased as shown in Fig. 4-71 by the addition of the damper. The results predicted that with the new mechanical damper the flywheel system should be stable to whirl for all rotor speeds to its maximum operating speed of 15,000 RPM (250 Hz). The results of the dynamic analysis with damper showed that the effect of the damper on natural frequencies was minimal. The third critical frequency was found to shift up from 70 Hz to 75 Hz and the other critical frequencies were not significantly affected.

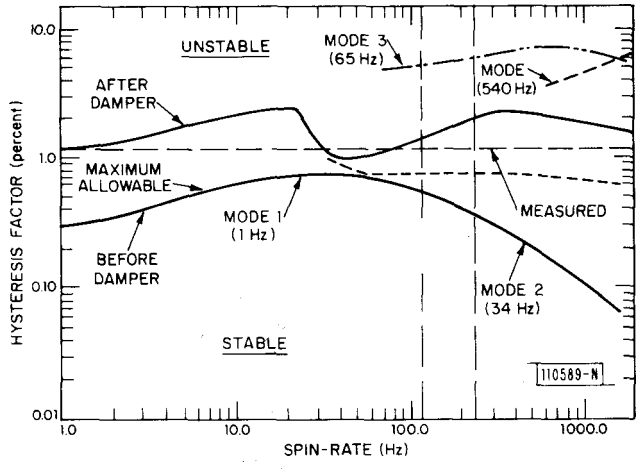

Figure 4-71. Maximum hysteresis for stability with external mechanical damper.

The damper was installed in the flywheel system and the wheel spun up. Two effects were observed: 1) the addition of the damper made transversing of the critical speeds easier and 2) the subsynchronous whirl was eliminated. The maximum flywheel operating speed of 15,000 RPM was reached without difficulty. To date, the flywheel has been operated continuously at 15,000 RPM for thousands of hours without observation of any whirl buildup. Thus, the addition of external damping in the form of the mechanical damper eliminated all low-frequency whirl oscillations.

4.5.10 Earthquake/Alignment Analyses

Preliminary analyses have been carried out to determine the effects of seismic forces and ground settlement on magnetically suspended flywheels.

An attempt has been made to answer the following questions:

1. Can a magnetically suspended flywheel survive the earthquakes that are known to occur frequently in California and in the southwest region of the U.S.?
2. What are the effects of ground settlement (either due to soil compaction over a long period or as a post-earthquake phenomenon) on flywheel performance? An implied question here is, how accurately does a residential flywheel unit need to be leveled during installation?

The investigations described below are directed toward obtaining "first-order" answers to these questions since more detailed studies were precluded by project constraints of time and funding. It was necessary to make a number of simplifying assumptions to obtain these "first-order" solutions and the assumptions that were made are of a type that should overpredict the response of the flywheel to seismic and ground settlement effects. Therefore, the "first-order" results should be considered as conservative and it is suggested that a more encompassing study of these phenomena be carried out as part of any future program to design and fabricate a full-scale residential flywheel storage system.

4.5.10.1 Seismic Effects

A general evaluation of the effect of earthquakes on a flywheel energy storage system located at a specific site would require that the combined spatial and temporal probability of an earthquake be known at that locale. The spatial probability requires a knowledge of where the epicenter of the expected quake is in relation to the location of the flywheel unit since ground acceleration intensity is bell shaped--largest at the epicenter and decreasing away from the epicenter. When the probability function (in time) is combined with the spatial probability function described above, it is possible to predict the probability of exceeding a given level of ground acceleration at a given area in certain number of years. This combined probability is of pertinent interest in assessing the capability of the flywheel unit installed at a specific location.

Since the commitments of time and money required to develop the generalized analysis outlined above were in excess of those available in the present program, it was necessary to take a less involved look at the seismic question. In order to proceed with a "first-order" analysis, the simplifying assumption was made that only the temporal probability of the earthquake would be considered, thus assuming that the flywheel was always at the epicenter of the earthquake. It was also assumed that "small" earthquakes only would be considered. Finally, it was assumed that an adequate containment system could be designed and therefore the question of safety need not be considered.

In order to answer the seismic question, first one needs to know the largest level of earthquake that has a high probability (greater than 95%) of occurrence at least once during the lifetime of a flywheel unit (20 years). The results of preliminary investigations suggest that a 0.03 to 0.05 g peak ground acceleration (approximately 4 on the Richter scale) can be expected to occur at least once during a period of 20 years. This conclusion is also substantiated by Fig. 4-72 from Reference 4-10 if extrapolation to smaller g's is made.

C74-1552

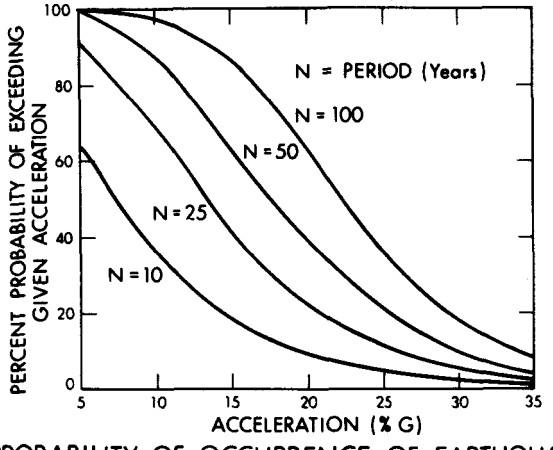

PROBABILITY OF OCCURRENCE OF EARTHQUAKES

REF: G.W. HOUSNER, "STRONG GROUND MOTION," CHAPTER 4 EARTHQUAKE ENGINEERING, R.L. WIEGER, COORDINATING EDITOR, PRENTICE-HALL, 1970

Figure 4-72. Probability of occurrence of earthquakes.

In answering the seismic question one must also define what is meant by a magnetically suspended flywheel "surviving" an earthquake. One possible definition of survival is that the damage sustained by the flywheel due to the earthquake is repairable. Another definition of survival might be a scenario in which the magnetic suspension of the flywheel is lost and the flywheel touches down on its mechanical touchdown during the earthquake but can be levitated and spun-up again subsequent to the earthquake. A third definition of survival might require that the flywheel remain magnetically levitated during any number of earthquakes of a given magnitude and be instantaneously ready to provide power as required after each earthquake. The third and last definition above for "survival" was selected here. In the following discussions, the flywheel system is defined to survive if it remains magnetically levitated during any and all earthquakes of 0.03-g to 0.05-g peak ground acceleration.

With the peak acceleration values and a definition of survival available, the response of the spinning flywheel was computed based on the combined earthquake response spectrum (Fig. 4-73, page 106). This spectrum predicts the

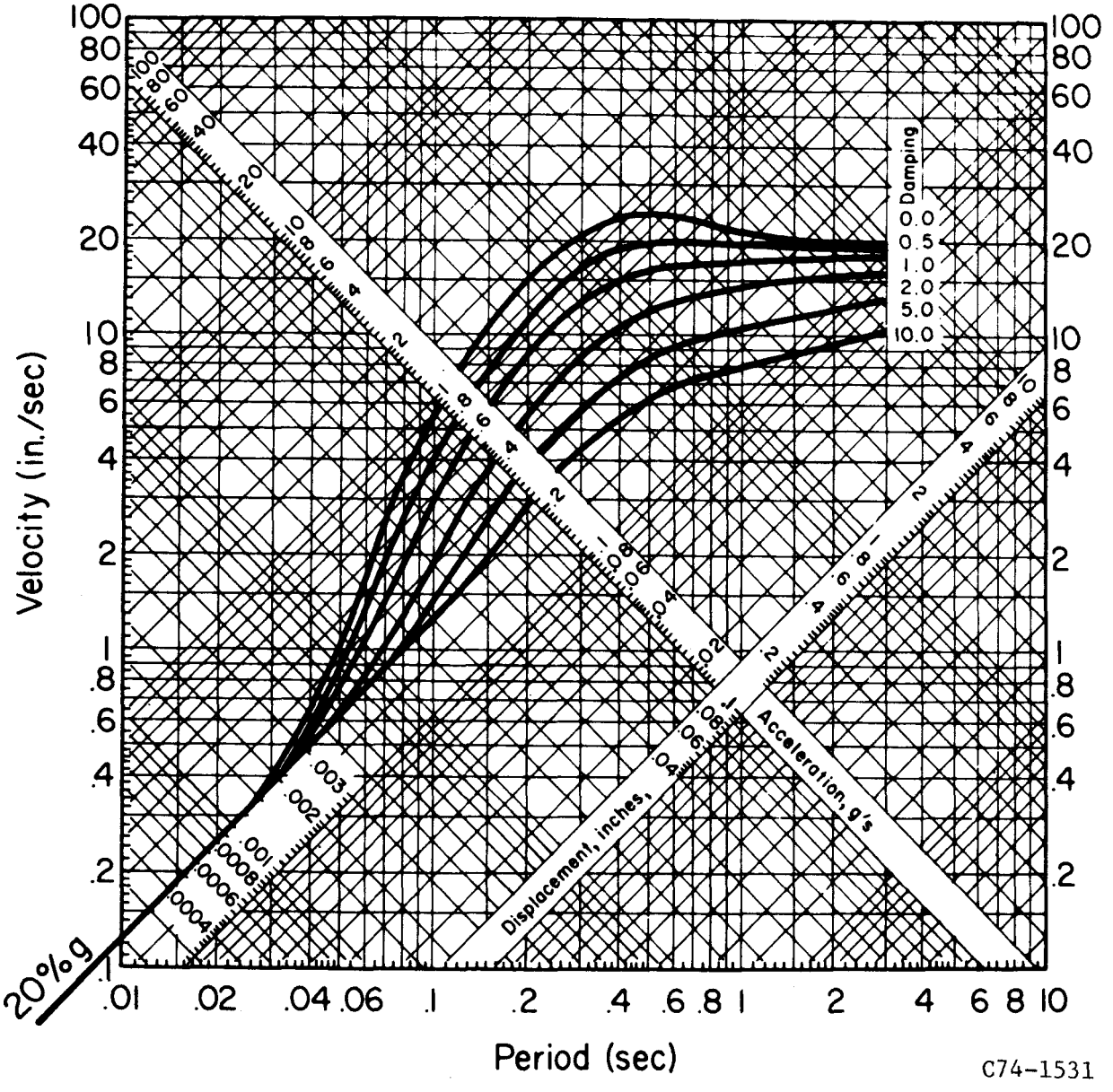

Figure 4-73. Combined earthquake response spectrum.

Ref: Earthquake Engineering, Ed. Robert L. Wiegel Prentice-Hall, Inc. Englewood Cliffs,NJ 1970

response of a single degree of freedom oscillator to a base motion of 20% g peak acceleration, whose spectrum is an average of typical ground motions that have been measured over the years. In the following analysis it has been assumed in computing the response that only the lowest mode, a rigid-body rocking motion on the magnetic bearings, has any significant participation. This is a reasonable assumption considering that (a) the spectral content of ground motion is predominated by low-frequency oscillations and that (b) the higher frequencies of the flywheel system are at least one or two orders of magnitude higher than the lowest mode.

The response of the 1-kWh, 1/10-scale prototype test unit was obtained by applying a static force at the wheel c.g., and constraining the deformations such that the deflected shape (Fig. 4-74) corresponds to the first mode shape (Fig. 4-75). The static response was then multiplied by dynamic amplification factors (of 1.5 for damping = 5% or 2 for damping = 2.5%) obtained from Fig. 4-73. The calculations show that in the prototype test unit, the rigid shaft will not hit the touchdown bearings for 0.03-g peak acceleration and 5% damping.

C74-1553

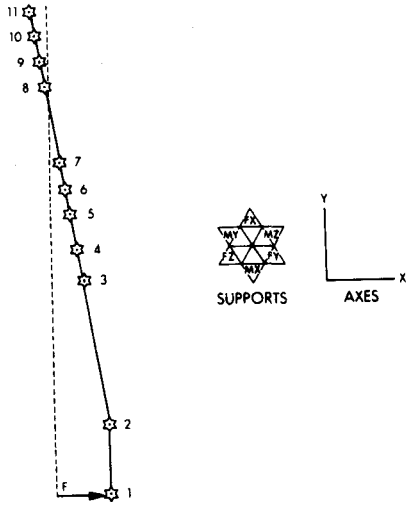

Figure 4-74. Deflected shape of test unit--force applied at wheel c.g.

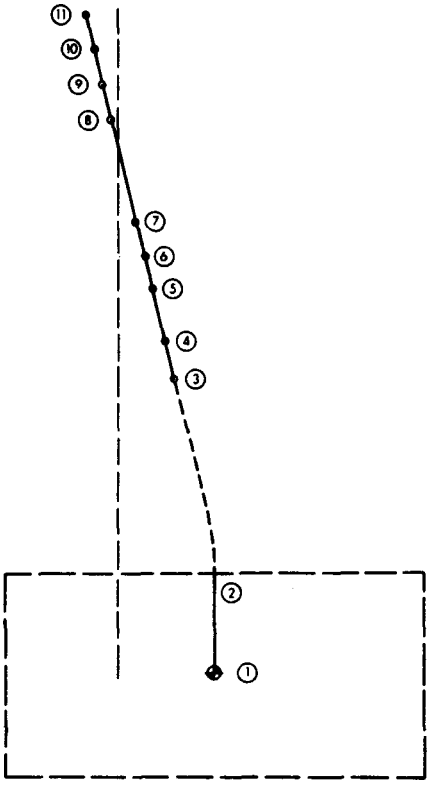

Figure 4-75. The lowest mode shape of 1-kWh test unit operating speed.

Having established by configuration specific calculations that the 1/10-scale prototype unit would survive any and all Richter 4 earthquakes, the development of a more generalized rationale for the preliminary sizing of magnetically suspended flywheels subjected to seismic shocks was undertaken. The question to be answered was: "What geometric characteristics should the flywheel system have which will prevent touchdown from occurring during an earthquake?" Analyses are developed below for both vertical and horizontal flywheel directions.

4.5.10.1.1 Vertical Touchdown Model

The flywheel geometry considered in the vertical model is shown in Fig.4-76. We assume that the rotor is suspended from a set of six magnetic

bearings, that the magnetic bearings are spaced equidistant along the magnetic bearing shaft and are of equal stiffness, that mechanical touchdown bearings are provided at the top and bottom of the bearing shaft, and that effects of the magnetic bearing, axial position servo control system on the results may be neglected.

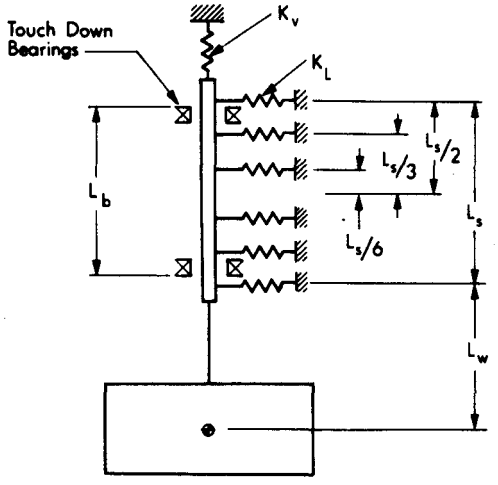

C74-1545

Figure 4-76. Analytical model.

Summing forces in the vertical direction, we find:

$$K_V, \text{ spring constant} = \frac{W}{6\ S_g}$$

where

W = weight of wheel

S_g = mag bearing gap.

Assuming the force in the vertical direction is 2/3 of the lateral force due to seismic effects, i.e:

$$F, \text{ force} = \frac{2}{3} \times \text{lateral acceleration} \times \text{weight (in g's)}$$

$$= \frac{2}{3}\ \alpha\ W.$$

The vertical deformation S_V is:

$$\text{deformation } S_V = \frac{F}{K_V} = \frac{2}{3}\ \alpha\ W\left(\frac{6S_g}{W}\right)Q = 4\ \alpha\ QS_g$$

where:

Q = effective dynamic amplification factor

For no touchdown,

$$S_v \leq S_g$$

or

$$4\alpha Q < 1.$$

For α = 0.03 to 0.05

and typical Q = 1.5 to 2 (ζ = 5% to 2.5%)

$$4\alpha Q = 4 \times 1.5 \times 0.03 = 0.18 < 1$$

$$4 \times 2 \times 0.05 = 0.4 < 1.$$

Therefore, it can be concluded that there is no touchdown in the vertical direction if the axial touchdown gap is greater than 40% of the magnetic gap.

4.5.10.1.2 Lateral Touchdown Model

The geometry to be considered in the lateral direction is shown in Fig. 4-77. In general, two mechanisms for touchdown are possible. First, touchdown may occur if the magnetic bearing shaft rotates through an angle θ_1 and contacts the mechanical touchdown bearings. Touchdown may also occur if a rotation angle θ_2 occurs between a magnetic bearing stator/rotor pair. In this case, the fringe rings of the magnetic bearing will come in contact. The design approach which is followed below is to select a geometry so that touchdown on the mechanical bearings is the only possible scenario. From Fig. 4-77, we see that

$$\tan \theta_1 \approx \theta_1 = \frac{S_r}{L_b}$$

$$\sin \theta_2 \approx \theta_2 = \frac{2S_g}{d}$$

C74-1546

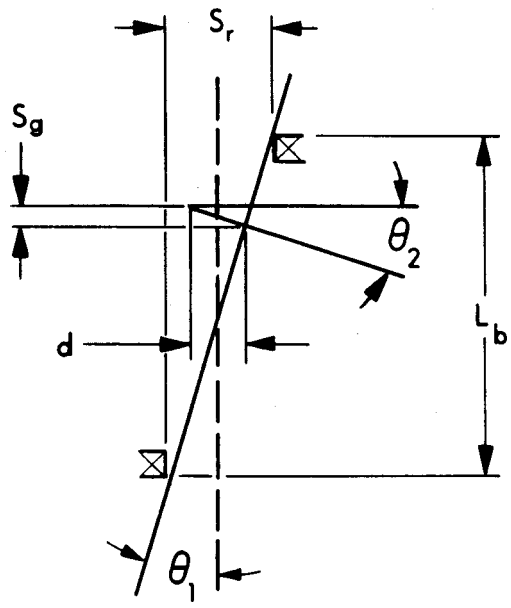

Figure 4-77. Touchdown in the lateral direction.

C74-1547

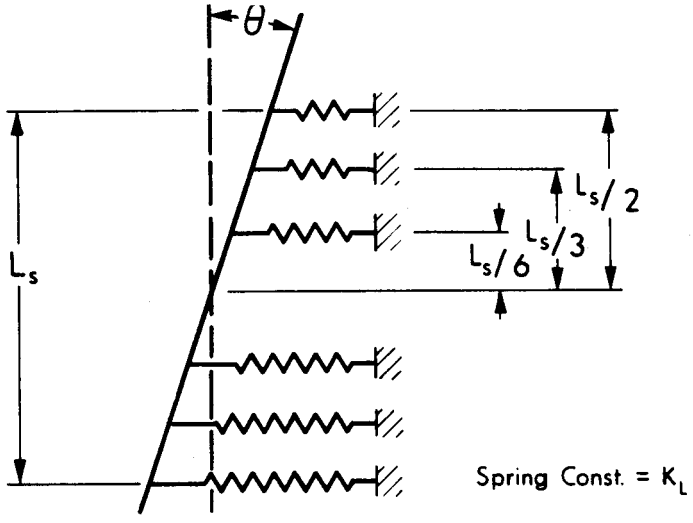

Figure 4-78. Equivalent torsional spring constant.

radial TD bearings to be effective:

$$\theta_1 \leq \theta_2$$

$$\frac{S_r}{L_b} \leq \frac{2S_g}{d}$$

$$\text{Max. } S_r = 2S_g \frac{L_b}{d} .$$

(Note: $S_r = S_{rtb} + S_{rbb}$

Where S_{rtb} = radial gap at top TD bearing

S_{tbb} = radial gap at bottom TD bearing)

Computing the torsional spring constant of the bearing set according to the geometry of Fig. 4-78 and assuming the negative rotational spring stiffness at each bearing is small, we find that:

$$M = 2\theta \; K_L \; L_s^2 \quad \left(\frac{1}{4} + \frac{1}{9} + \frac{1}{36}\right)$$

$$K_t = \frac{M}{\theta} = \frac{7}{9} \; K_L L_s^2$$

$$K_L = 0.1 \; K_v = \frac{W}{60 S_g}$$

$$K_t = \frac{7}{540} \quad \frac{WL_s^2}{S_g} .$$

Computing deformations for a lateral force, F, applied at the wheel, an equivalent force and moment can be applied at the shaft center (see Fig. 4-76 and Fig. 4-79):

$$M = F \left(L_w + \frac{L_s}{2}\right)$$

$$\theta = \frac{M}{K_t}$$

$$\Delta h = \frac{F}{6K_L} + \frac{M}{K_t} \quad \frac{L_b}{2}.$$

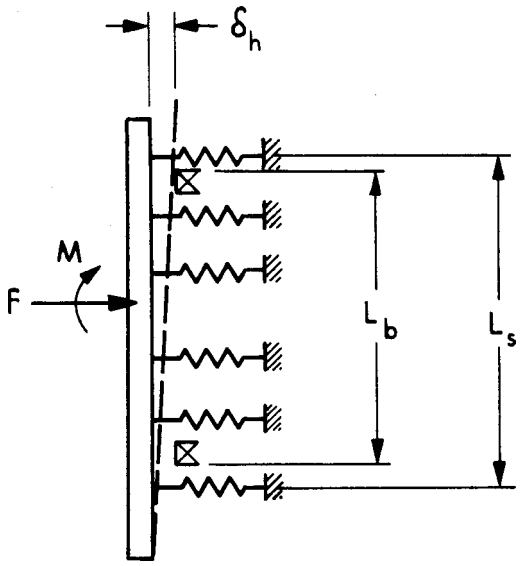

C74-1548

Figure 4-79. Lateral deformation of rigid shaft.

Therefore:

$$\Delta h = F \frac{1}{6K_l} + \left(L_w + \frac{L_s}{2}\right) \frac{L_b}{2K_t} .$$

Assuming that the top and bottom radial gaps are equal to $\frac{S_r}{2}$, for no touchdown:

$$\Delta h = \frac{S_r}{2} \quad \text{where Max. } S_r = 2S_g \frac{L_b}{d} .$$

Substituting for M, F, K_t and K_L, and after algebraic manipulation, it can be shown that for no touchdown:

$$\frac{L_s}{d} \geq 3.86 \frac{L_w}{L_s} + 2.93$$

$$\frac{L_b}{L_s} \geq \frac{1}{L_g - 1.93 - 3.86 \frac{L_w}{L_s}} .$$

These two equations together provide a preliminary guide for sizing the flywheel unit.

The second of the two equations above is solved and the results are shown in Fig. 4-80 for two combinations of seismic force and percent critical damping. Curve (a) represents a realistic condition (5%-g seismic force and 2.5% critical damping) while curve (b) represents a more optimistic case. It should be noted that Fig. 4-80 should be used only as a preliminary guide, keeping in mind the simplifying assumptions that have been made in arriving at this result.

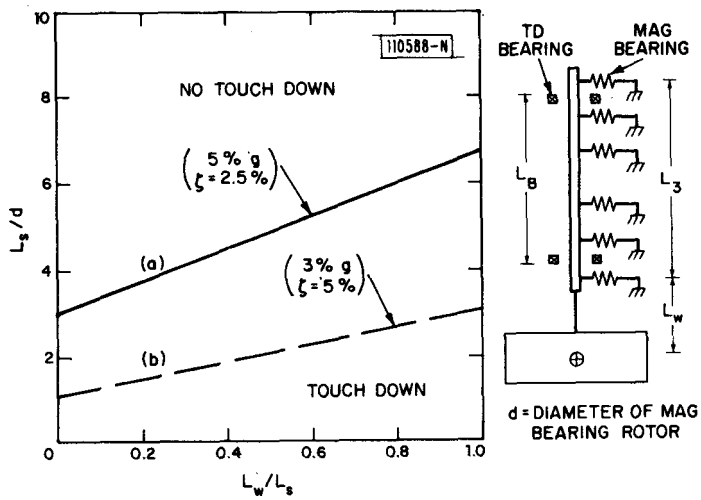

$$\frac{L_B}{L_s} \geq \frac{1}{\frac{L_s}{d} - 1.93 - 3.86\frac{L_w}{L_s}}$$

Figure 4-80. Guide for preliminary sizing.

As an application of this method, let us consider a specific case. Let us assume that $L_w/L_s = 0.5$, $L_s/d = 5$

$$\text{then } L_b/L_s = 0.88.$$

For a magnetic bearing rotor diameter of 6 inches, the distance between the touchdown bearings should be about 27 inches and the wheel c.g. cannot be more than 15 inches below the bottom most magnetic bearing rotor. This example illustrates that it is feasible to size the flywheel unit so that the rigid shaft does not touch down.

4.5.10.1.3 Comparison of Building Code Earthquake Design Requirements with Flywheel Structural Design Limits

Seismic Risk Zones for Flywheel Systems

Some additional work was done to clarify the seismic capabilities of a flywheel energy storage system by comparing earthquake building code lateral acceleration requirements to the structural design acceleration limits of the existing 1/10-scale prototype flywheel unit and of a similar 1/10-scale unit employing a telescoped quill for increased earthquake resistance. Applicable seismic risk zones for a flywheel storage system were determined through superposition of the regions of the United States where photovoltaic systems have high economic potential onto a seismic probability map, as shown in Fig. 4-81. Studies discussed in Reference 4-11 have shown the economic viability of photovoltaic systems will be realized first in regions of the the Southwest and California, Texas and mid-Atlanic states.

The superposition, Fig. 4-81, shows that the highest seismic risk for flywheel systems is found to occur in regions of California, Nevada and upstate New York designated Risk Zone 3 where a maximum epicentral lateral acceleration of 0.33 g's is possible. For reference, Zone 3 comprises 12% of the total area where photovoltaic systems may have high economic potential. The maximum ground accelerations experienced in Zones 2, 1 and 0 are 0.16 g's, 0.08 g's and 0.04 g's, respectively, and these regions represent 24%, 35% and 25%, respectively, of the total area of high economic potential for photovoltaic systems. Even though these figures do not consider population densities, it is evident that regions of high seismicity form a relatively small part of the area where photovoltaics is expected to have high economic potential. It is seen that if a magnetically suspended flywheel system is designed to survive the earthquake environment of California, it will be adequate for all other regions of the United States. Conversely, a requirement placed on a flywheel storage system that it must survive California-type earthquakes, may have an unfavorable impact on costs, especially if the perceived market for such a flywheel system is in another region of much reduced seismic activity.

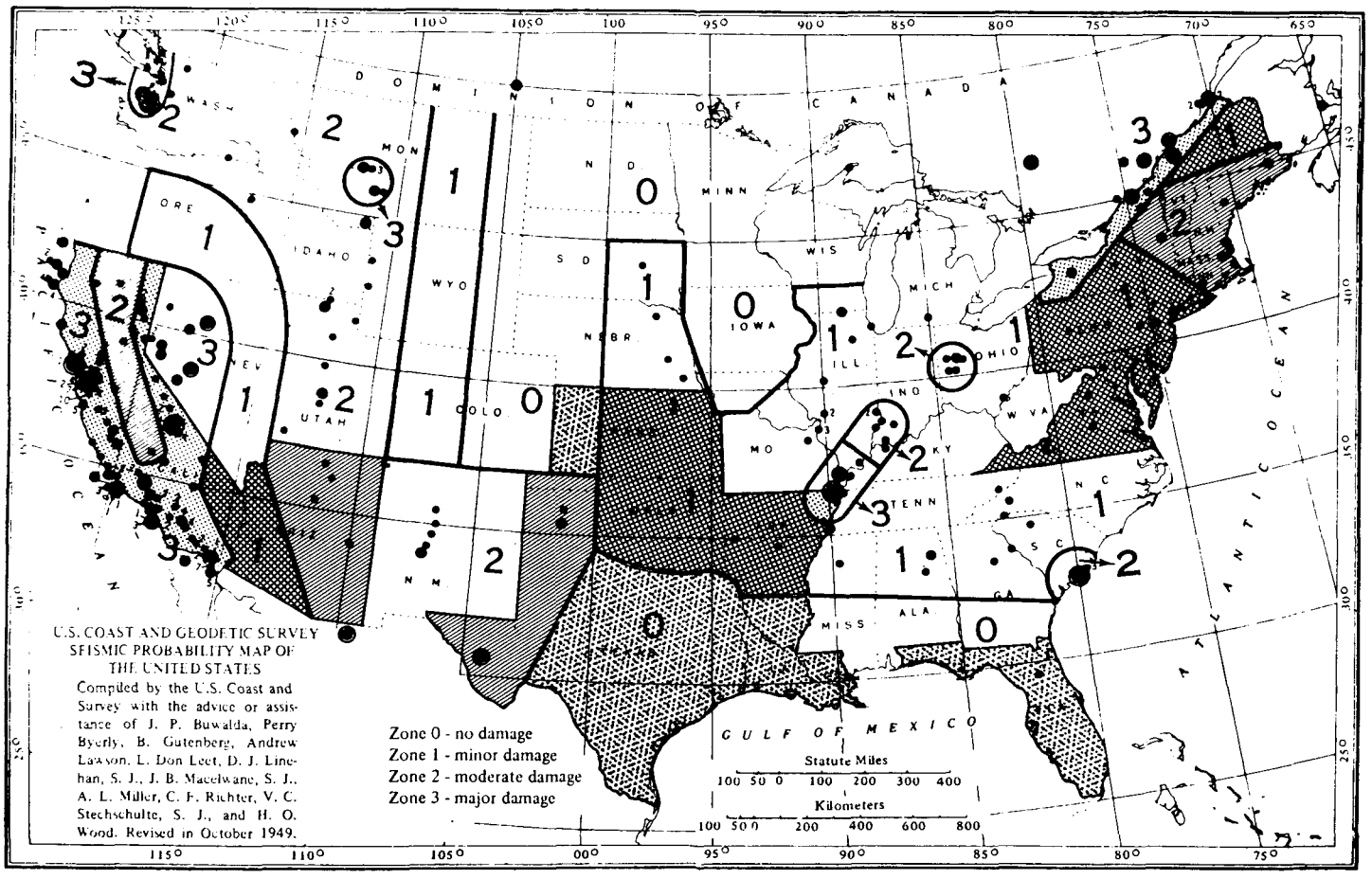

Fig. 2 Seismic probability map of the United States. This map is commonly used to establish seismic design criteria; the following maximum ground accelerations are associated with the zones: Zone 3, 33 % g; Zone 2, 16 % g; Zone 1, 8 % g; Zone 0, 4 % g. In Zone 3 close to a major active fault the maximum ground acceleration is estimated to be approximately 50 % g.

Figure 4-81. Seismic activities in areas of the United States having high potential for solar photovoltaic systems.

The relationship between maximum zonal acceleration in g's, Zone designation and Richter scale was obtained from Reference 4-10 and is graphed in Fig. 4-82. A Zone 3, 0.33-g earthquake is equivalent to magnitude seven, M = 7, on the Richter scale.

C74-1715

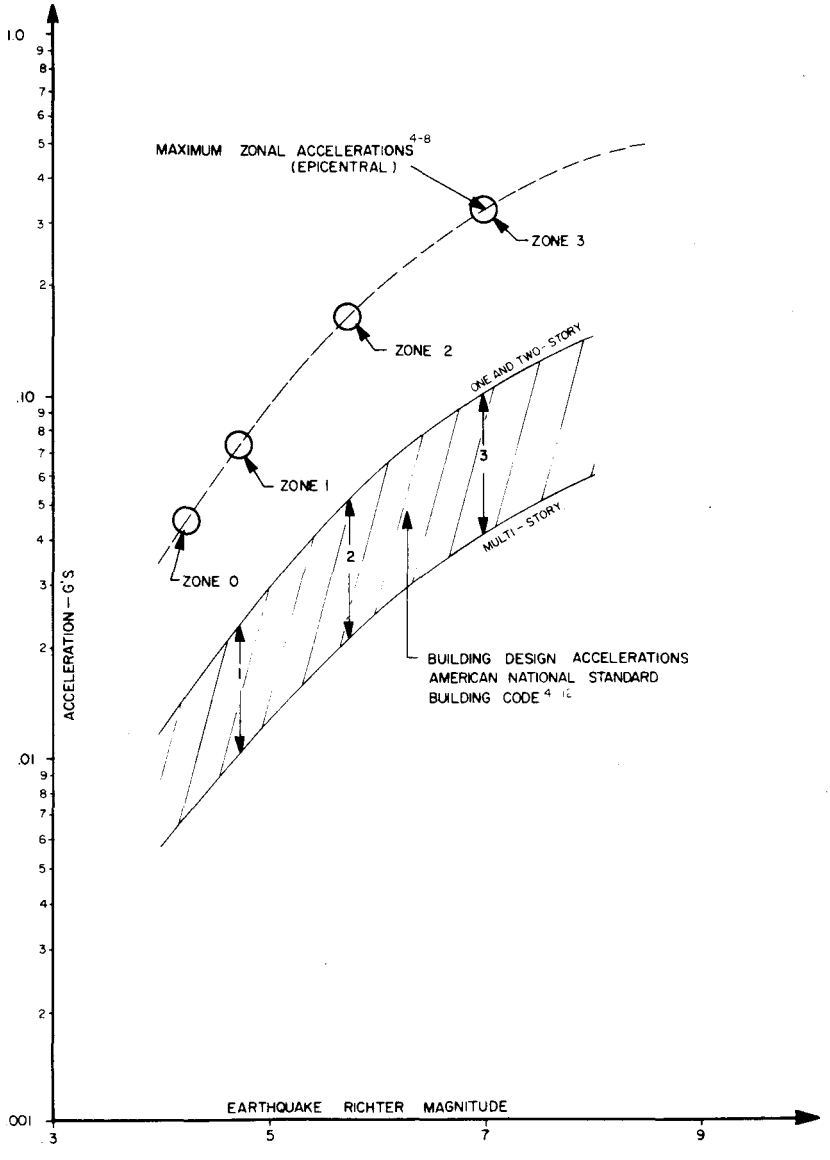

Figure 4-82. Comparison of earthquake building code requirements with maximum zonal accelerations.

Building Code Earthquake Design Requirements

Building design acceleration for the various risk zones were calculated using the methods described in the American National Standard Building Code[4-12] and these design accelerations are compared with maximum epicentral accelerations in Fig. 4-82. The comparison shows that buildings designed to the earthquake code are required to meet derated acceleration loads which are 1/3 to 1/8 of the maximum epicentral earthquake acceleration expected for that region. The selection of code design acceleration levels lower than the epicentral accelerations corresponds to the acceptance of a certain amount of risk in a given building design.

C74-1716

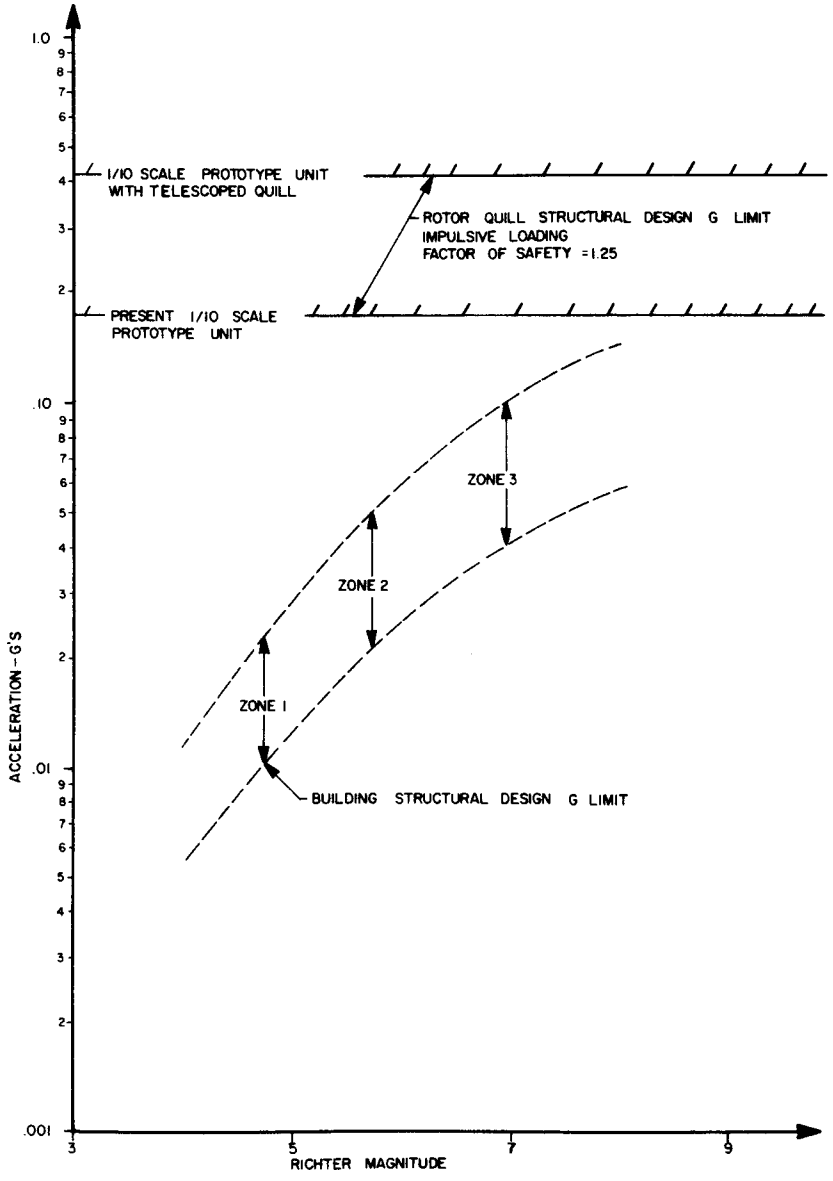

Figure 4-83. Comparison of flywheel structural limits with building code requirements.

Flywheel Structural Design Limits

The thin quill which supports the flywheel rotor is the element which sets the maximum structural acceleration limit for the flywheel system. In a severe earthquake, the lateral "g" load displaces the flywheel rotor suspension against the ball bearing touchdown system and the quill resists the load as a simple cantilivered beam. First-order calculations were made for the existing 1/10-scale experimental flywheel system which showed that the maximum operating stress limit of the Vascomax 250 quill would be induced by a 0.175 g, impulsively applied load. The corresponding quill shaft deflection at the rotor end was 2.1 inches. An allowable stress of 250,000 psi, a modulus of 26×10^6 psi, a diameter of 0.437 inches, a factor of safety of 1.25 and a moment arm (length of cantilivered beam) of 13.5 inches were assumed. Calculations were also performed for a proposed prototype unit in which the quill is telescoped up inside a hollow cylindrical region within the magnetic bearing. This is the same approach originally used in the full-scale residential unit concept to decrease its overall height. Telescoping of the quill into the magnetic bearing was found to increase the structural acceleration limit of the unit to 0.425 g's. This design change resulted in a shortened moment arm (unsupported quill length) of 5.5 inches, which in turn resulted in lower stress for a given acceleration level.

The rotor quill structural design acceleration limits for the prototype flywheel of 0.175 g's and for the prototype flywheel with telescoped quill of 0.425 g's are compared with building code acceleration requirements in Fig. 4-83. This comparison shows that the structural acceleration limit of the flywheel is a factor of 2 to 4 (depending on which quill geometry is chosen) higher than the building code requirement in Zone 3. In all other seismic regions, the flywheel's relative capability is even larger.

Flywheel Operational Design Limits

As described earlier, the prototype flywheel system will remain magnetically suspended on its magnetic bearing and operational to acceleration levels in the 0.03-g to 0.05-g range. The prototype unit with telescoped quill will operate to higher accelerations in the range from 0.05 g to 0.097 g.

A comparison of these operational g limits for the flywheel and the building code requirements is made in Fig. 4-84. We see that the present prototype system will operate satisfactorily in Zone 2 and lower seismic risk zones while the unit with telescoped quill will operate satisfactorily in Zone 3 acceleration values and in all lower seismic risk zones.

C74-1714

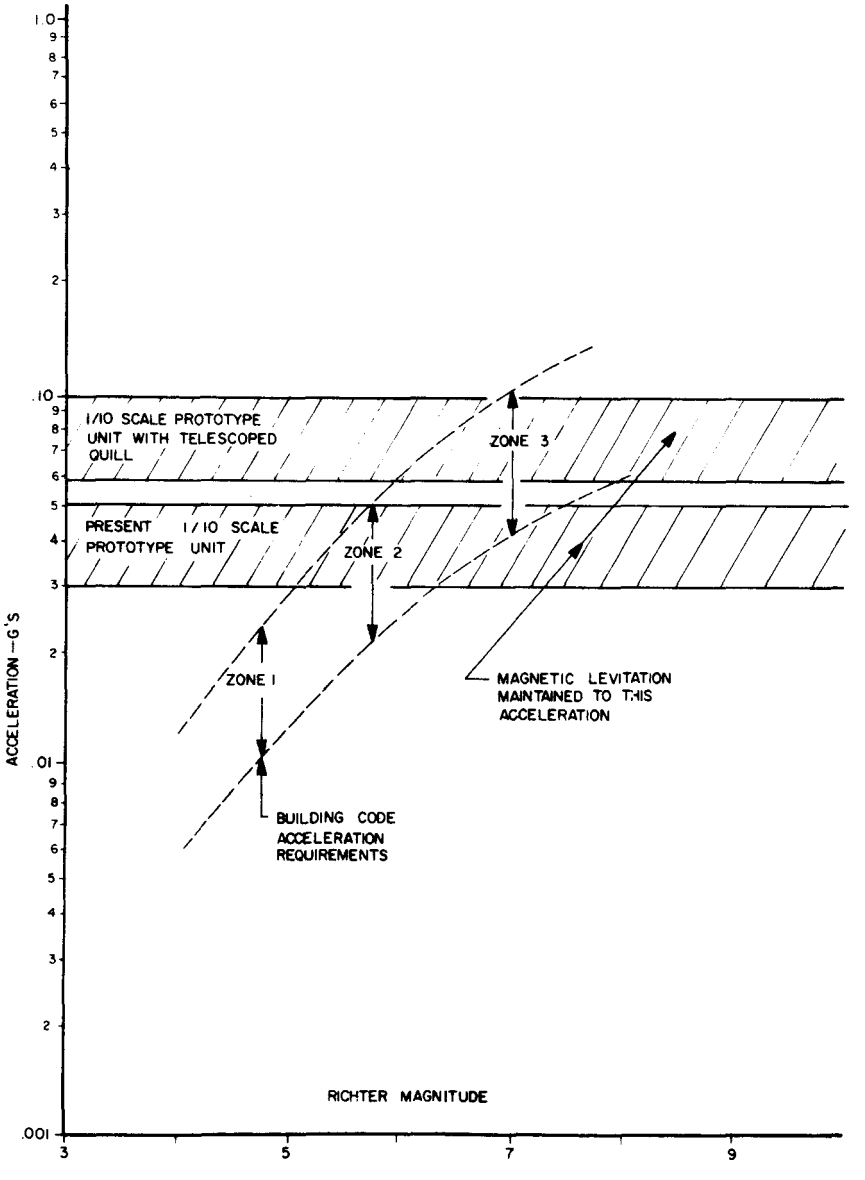

Figure 4-84. Flywheel earthquake resistance compared to building code requirements.

Future Work

Though the flywheel has been shown to be both structurally safe and continuously operational in all earthquake zones to the same requirements as buildings in those zones, based on first-order calculations, more work is warranted in this area. Detailed finite element analyses of the flywheel dynamics under earthquake excitation should be carried out to explore the nuances of designing a flywheel system for this environment. Such calculations would provide a deeper insight into this problem than can be realized from the first-order type of analyses that have been carried out to date. A particularly interesting problem that can only be carried out with the help of computer calculations is the determination of the trajectory of the flywheel rotor and quill shaft during an earthquake. This calculation requires that methods be incorporated in the computer program to handle the changing boundary conditions as the quill shaft strikes the touchdown bearing support system and then rebounds away from it. Work should also be continued to assess other building codes with regard to their earthquake design requirements. If the effect of large (but not catastropic) earthquakes on the life of magnetically suspended wheels is to be evaluated, a risk analysis should be performed. This study should consider the probability of occurrence of large earthquakes, the associated failures and repair costs. It would then be possible to assess more fully the economics involved in designing earthquake-resistant, magnetically suspended energy storage wheels.

4.5.10.1.4 Differential Settlement

Let us now consider the second question concerning the effects of ground settlement on flywheel performance. A very good discussion of ground subsidence after an earthquake can be found in Reference 4-10. To summarize, differential ground settlement across fault lines can be catastrophic. If a flywheel unit is installed on top of a fault line, there is obviously very little that can be done to save the flywheel unit (again safety is not a problem). However, it is not very likely that a flywheel will be installed right across a fault line, unless by mistake. There is also evidence to

suggest that there is ground settlement (or creep) in regions that contain faults. This creep, measured up to 1/2 in/yr. in places near Hollister, California, is not necessarily accompanied by earthquakes.

In spite of such relatively large ground surface settlement near faults, the type of motion we are concerned with is the relative (or differential) settlement across the foundation (assumed rigid) of the flywheel installation--a relatively small area (assumed to be approximately 5 ft. in diameter) in nonfault regions. Furthermore, this relative motion (or tilt) is more critical for spin-up through critical speeds rather than operation at speed. In order to understand the effect of tilt on the spin-up characteristics of the flywheel, we need to perform a dynamic analysis which considers cross-coupling between axial and lateral deformations. This is a nonlinear analysis requiring extensive computational effort and will not be pursued here. For the moment, we will impose that the relative tilt between the magnetic bearing stator and the rotor is such that the variation in gap shall be less than or equal to 10% of the original gap. This is approximately equivalent to having an initial imbalance in principal axis misalignment of the wheel of 0.03°. No difficulty in coping with this imbalance is expected and therefore an equivalent tilt of the outside structure should not pose any problem. It is of interest to note here that the equivalent imbalance (static or dynamic) due to tilting affects only the lowest critical frequency; it can be shown that gravity does not have any significant effect on the higher critical frequencies.

The effect of tilt was simulated analytically on the 1-kWh flywheel unit by applying a static horizontal force at the c.g. of the wheel. By setting the horizontal force equal to the component of gravitational force normal to the axis of the wheel, the relative rotation between the wheel principal axis and the spin axis was computed; any initial tilt of the supports has the same effect. Figure 4-85 shows the deflected shape when a horizontal force is applied at the wheel c.g. Parenthetically, the initial principal axis misalignment in the test unit was specified at 0.01° and the current tilt of the support arms is estimated to be 0.02°.

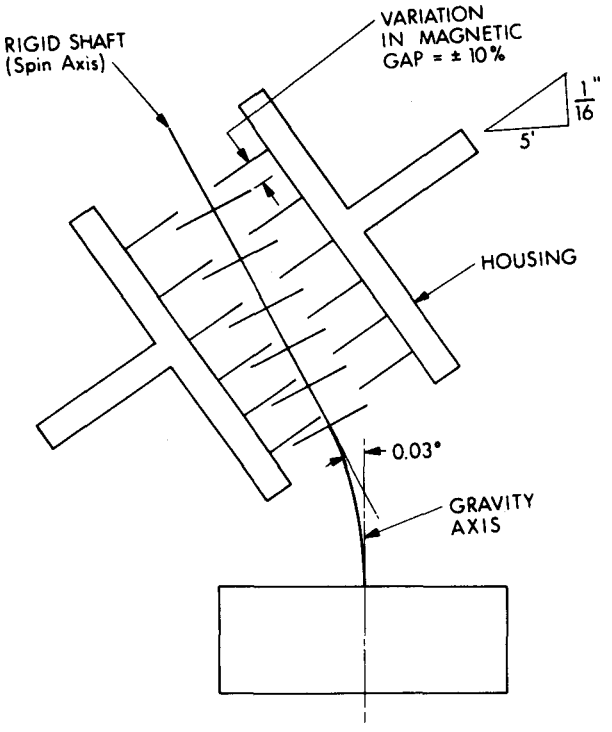

Figure 4-85. Effect of tilt.

The principal axis misalignment corresponds to a differential settlement of 1/16 inch over a 5-ft.-diameter tank and, based on past experience, it appears to be reasonable from our experience to expect the actual tilt to be smaller than this. It should be noted here that a more detailed analysis is required to determine if larger tilts can be tolerated.

4.5.10.1.5 Conclusions

The "first order" analyses conducted for seismic effects and ground settlement effects have shown that:

- Flywheel systems possess resistance to earthquakes comparable to that of the buildings which they would service. This is true even in the worst earthquake regions of the United States.

- o Differential settlement of the flywheel system foundation of 1/16 inch over a five-foot span (1 milliradian angular change) can be tolerated. This allowable settlement is greater than that expected to occur during the life of the system.

4.6 Experimental Tests

Efforts in this area have included preliminary measurements of flywheel energy storage system power transfer efficiencies, tests with a whirl mode damper, the development of a Flywheel System Test Plan for an improved measurement program, and the completion of this improved measurement program. Each of these items is discussed below in more detail.

4.6.1 Preliminary Test Results with Stand-Alone Cycloconverter

4.6.1.1 Introduction

System shake-down testing began in January 1980 when the 1/10-scale, 1-kWh energy storage unit was installed in the vacuum tank. During initial testing, attention was primarily directed toward debugging the power-handling electronic systems at progressively higher power levels and measuring and analyzing the dynamic vibrational characteristics of the rotating magnetic bearing shaft, quill and rotor. Efficiency data were only taken only on a secondary basis and only at shaft speeds to 10,000 RPM due to the effects of an unstable and undamped whirl mode at higher shaft speeds. Subsequently, the whirl mode was eliminated by installation of a damper (after completion of the tests described here) and full-speed operation to 15,000 RPM was possible thereafter. For the tests to be discussed below, the flywheel was operated with a stand-alone cycloconverter power converter. A higher efficiency utility-interactive power converter was built late in FY-80 and was tested in conjunction with the flywheel in early FY-81.

Preliminary test measurements were made during the period from mid-January to mid-April, 1980. During that time, the unit ran continuously, accumulating 2,200 hours of operation between 6,000 and 10,000 RPM. Throughout the shakedown period, power measurements were taken: 1) at various combinations of input and/or output power (to approximately 700 W) and at

different rotor speeds; 2) of power transferred to or from the rotor as measured by an increase or decrease in rotor speed, and 3) of the zero power rotor spin-down loss at various vacuum pressures and different shaft speeds.

4.6.1.2 System and Instrumentation Description

The test setup block diagram is shown in Fig. 4-86, including the magnetic bearing portion of the system. The complete power system includes:

- o DC-DC down converter (maximum power point tracker).
- o DC-3 Ø motor drive commutated from Hall signals at start and from back-EMF at operating speeds. Rating 650 W (maximum 700 W).
- o Motor-generator; permanent-magnet rotating field, 3 Ø "Y"-connected ironless armature. Each phase has 10 coils in two parallel series of 5 each. Operating frequency 625 to 1250 Hz, 105 to 210 V rms line-line, armature rated at 625 W (maximum 1200 W for 20 sec), operating speed is 7500-15,000 RPM.
- o Flywheel rotor which stores energy in rotational inertia.

  $E = 2.914 \frac{\omega^2}{2}$ joules. $\omega = 2\pi f$ f = rotor speed, rps
  E = 1 kWh, max
- o Cycloconverter output; changes variable frequency and voltage to constant 60 Hz, 117 V (adjustable). Operating input 600 to 1250 Hz, 110 to 240 V rms. Output rating 625 W.

The complete system was tested first from PV input to cycloconverter output to determine that all components operated together by connecting it to an existing PV array at Lincoln Laboratory. Subsequently all input power tests were made with a controllable dc power supply to maintain specific input power levels. The cycloconverter output power is load regulated and it has been tested with several household appliances. For the tests reported herein, incandescent light bulbs were used as an easily controllable load. All dc measurements were made with standard laboratory 1% meters and output ac power was measured with a Valhalla Scientific digital power meter. Rotor speed was measured with a digital frequency counter connected to the motor-generator terminals. In the reported tests, only the input and/or output power levels and rotor speed were measured. These measurements were used to obtain the power conversion efficiency of the total input and/or output system. No suitable

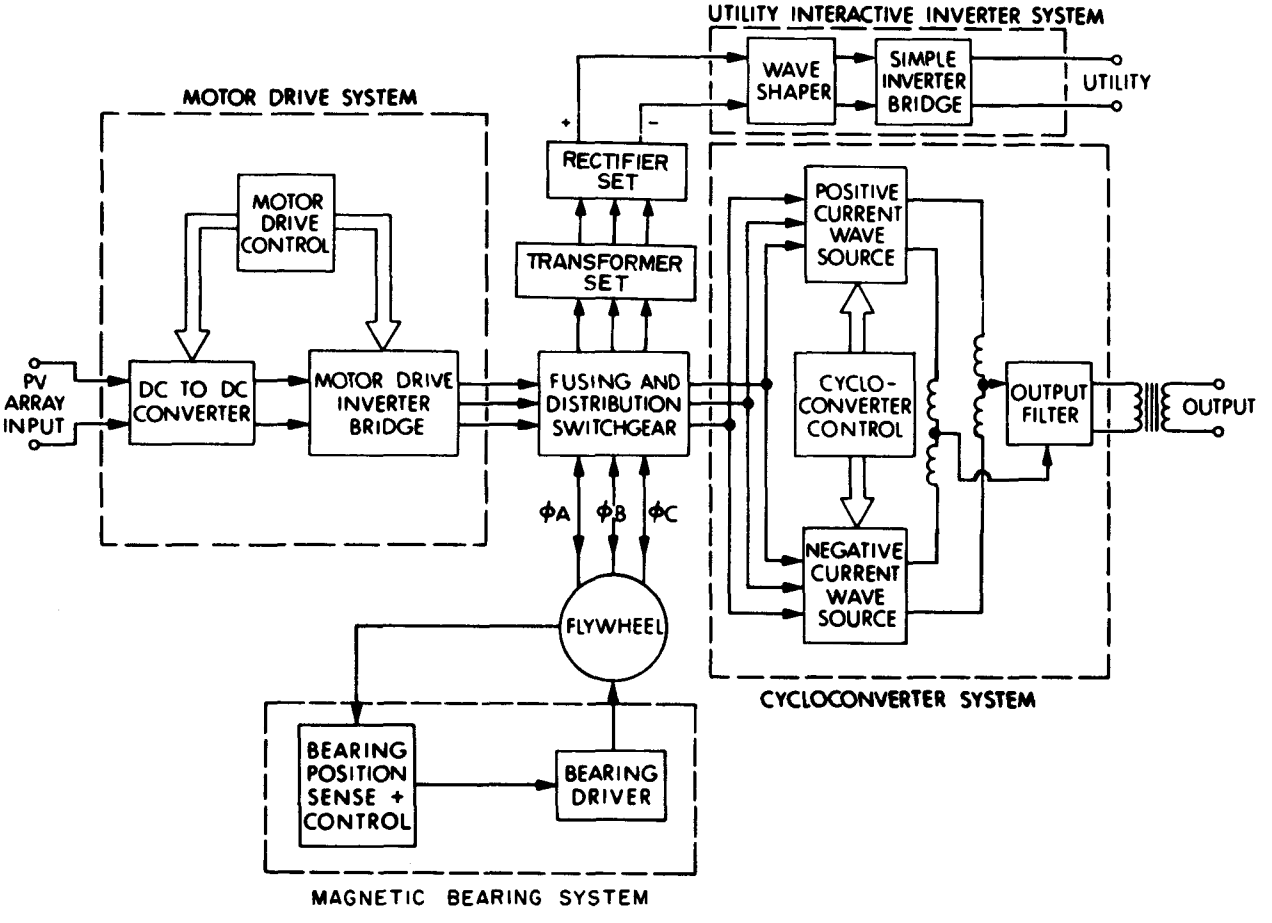

Figure 4-86. Flywheel electronic system diagram.

meters were available at the time of these preliminary measurements to measure the power loss in the motor-generator separately from either the motor bridge or the cycloconverter. Thermistors located in the motor-generator and on its support structure were used to measure temperatures and relative thermal dissipation and heat conduction associated with the motor-generator resistive losses.

4.6.1.3 Test Methods and Loss Calculations

The stored energy in the rotor is determined from the rotor rotational inertia and rotor speed. The internal power transferred into or out of the rotor is calculated from the stored energy difference divided by the time duration from the initial to the final stored energy state, $P_T = E/\Delta t$. This method was used to measure the parasitic (not power related) losses in the bearings, motor-generator and from air drag (if present). A description of these losses follows:

Rotor Air Drag

During the preliminary tests, the vacuum pumping system had a mechanical roughing pump which could reach a base pressure of 10^{-3} torr and an additional high-vacuum oil diffusion pump with a liquid nitrogen cold trap capable of maintaining a pressure of 10^{-6} torr. Because a large part of the testing effort over many weeks was concerned with debugging, measuring and reworking the several electronic sytems, only the roughing vacuum was maintained. Air-drag effects on the rotating elements may be significant in the roughing pressure range and the stored energy in the rotor must be corrected for this effect. The magnitude of the air drag was calculated, according to classical aerodynamic relationships,[4-13] for the operating range of pressures and rotor surface speeds and the results are plotted in Fig. 4-87. Only the rotor was considered in the calculations; the drag of the motor-generator rotors and magnetic-bearing rotors is insignificant in comparison. An experimental measurement of rotational spin-down

C74-1556

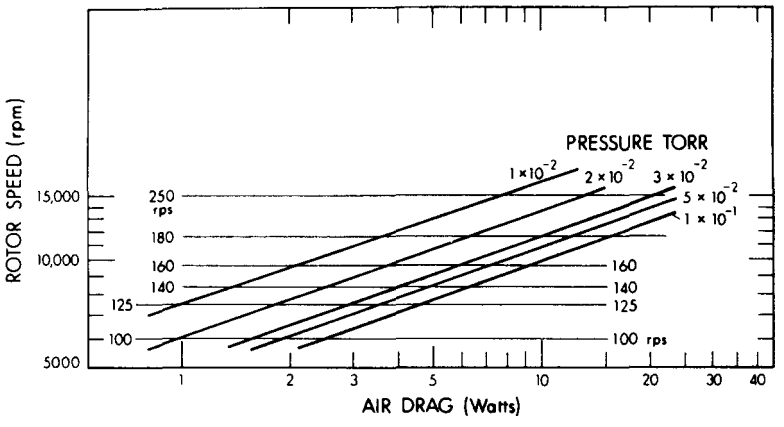

Figure 4-87. Calculated air drag.

C74-1557

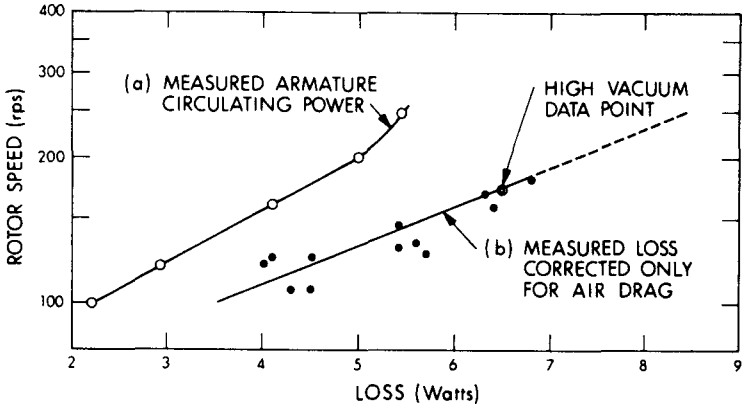

Figure 4-88. Spin-down loss corrections.

loss was made at high vacuum to provide a checkpoint for rotor air-drag corrections to the power-transfer measurements. Figure 4-88 shows the spin-down loss corrected for air drag versus the rotor speed. The data tolerance is approximatetly 0.5 W.

Motor-generator Non-power Related Losses

The three-phase "Y"-connected armature is wired with each 10-coil phase consisting of two parallel circuits of five coils in series. This was done to limit the maximum generated EMF to 240 V rms. Because of rotor-permanent-magnet non-uniformity ($\approx 5\%$) the generated EMFs in the two five-coil series are not necessarily equal and this resulting voltage differential may drive a circulating current around the 10-coil loop, in addition to any externally delivered current. Initially, no means was incorporated in the wiring to eliminate armature circulating currents generated by the mechanism described above and experimental measurements showed that circulating currents did indeed exist. The circulating current was measured for each phase at several shaft speeds and the power loss calculated using the armature resistance and this current. This loss is graphed as a function of shaft speed in Fig. 4-89. The necessary interphase transformers to eliminate armature circulating currents were installed after completion of this preliminary test series. Eddy-current losses in the armature coils and copper wire heat conductors resulting from the generator high frequency (≤ 1250 Hz) are minimized by using multistrand conductors (Litz wire). The presence of an eddy-current loss is qualitatively indicated by an increase in the stator temperature. The eddy-current loss was predicted in the original design calculations to be approximately 1-2 W, maximum.

Magnetic Bearing Losses

The bearing losses which directly affect rotor spin are from magnetic hysteresis which is due to nonuniform magnetic flux distribution around the bearing and damping flux motion from transverse shaft displacements. These losses are calculated to be on the order of 1/2 W.

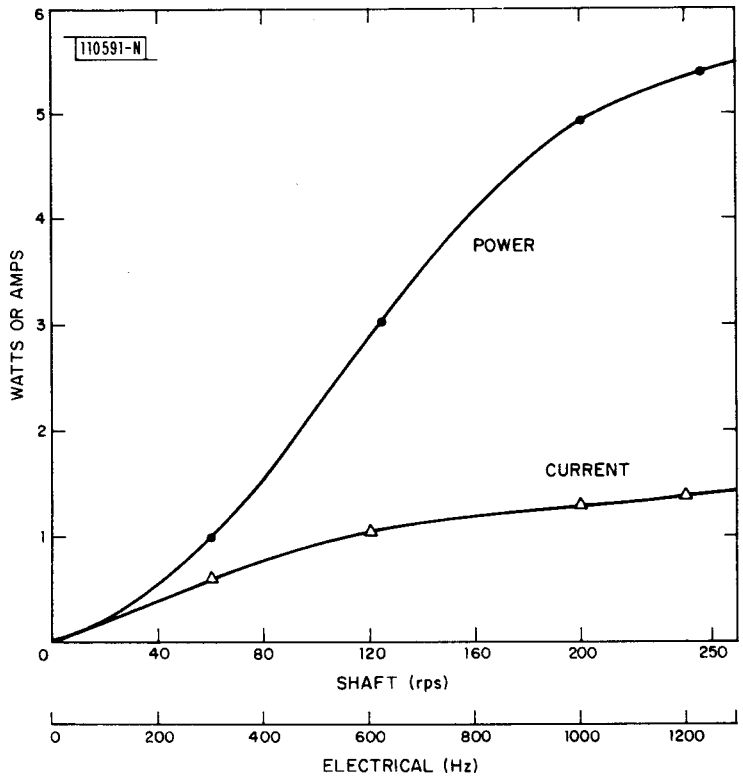

Figure 4-89. Magnitude of circulating current and power.

The intrinsic or tare loss was found by subtracting the armature circulating power from the corrected spin-down loss. This result is shown in Fig. 4-90 which gives the overall net loss including both motor-generator eddy-current and bearing hysteresis losses. A maximum total loss of 3 W was found for these two losses at 15,000 RPM and 3 W represents a decay rate of stored energy of 0.30% per hour. When finding power-transfer efficiencies, the power transferred, P_T, was corrected by compensating for both the air drag and armature circulating power losses which were characteristic of the operating conditions under which P_T was measured. For total system efficiencies these corrections were made on P_I.

The power efficiencies of the input and output systems are calculated as ratios:

$$\text{Input System,} \quad \eta_I = \frac{\text{Internal transferred power}}{\text{Input DC power}} = \frac{P_T}{P_I}$$

$$\text{Output System,} \quad \eta_O = \frac{\text{Output AC Power}}{\text{Internal transferred power}} = \frac{P_o}{P_T}$$

$$\text{Total System,} \quad \eta_{I-O} = \frac{\text{Output AC power}}{\text{Input DC power}} = \frac{P_o}{P_I}*$$

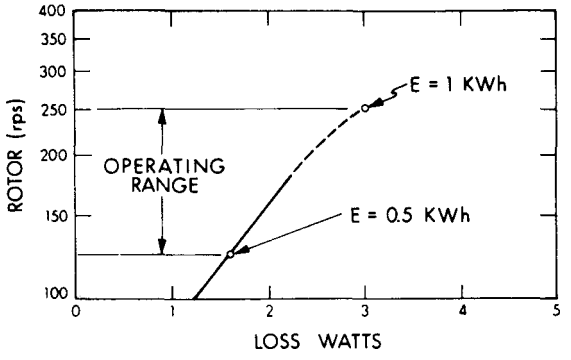

C74-1558

Figure 4-90. Intrinsic rotation loss (tare).

These efficiencies included all power-related losses from the electronics, reactive power between electronics and motor-generator, motor-generator resistive loss, and intrinsic losses, but do not include allowance for bearing lifting power.

4.6.1.4 Preliminary System and Component Efficiencies

The graphs in Figs. 4-91, 4-92 and 4-93 show power-transfer efficiencies to 650 W for all tests conducted during the last four weeks of the preliminary test series, corrected for losses. These tests were performed at spin speeds of 10,000 RPM or less. There is a large scatter in the data due to the precision of measurements ($\sim$5%), and in these graphs the efficiency variation shows a spread of $\sim\pm$ 4%. The input system efficiency of converting dc input power to stored energy, P_T/P_I, Fig. 4-91, reaches 92% over the input power range from 300-600 W. Efficiency decreases at low power because of the fixed loss in the motor-drive electronics. Measurements of the output system

*Input power was corrected for any P_T (power transferred by increasing or decreasing the rotor) which occurred during the test.

efficiency, i.e., output system power relative to the power transferred from the rotor, P_0/P_T, Fig. 4-92, suggest a maximum efficiency of 80%. The measured efficiency of the complete system from motor-drive input to cycloconverter output (including any power transferred to or from the rotor) P_0/P_I, shown in Fig. 4-93, reaches 75% for input power levels above 200 W. The flywheel system had undergone shakedown and was operating in a near perfect manner when the data, Figs. 4-91 through 4-93, were taken.

C74-1580

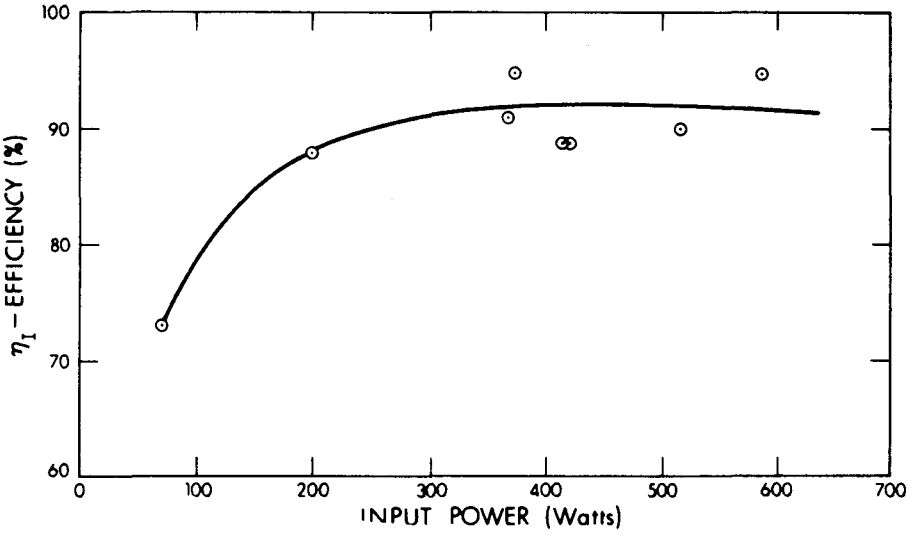

Figure 4-91. Input system efficiency P_T/P_I versus input power, data from March-April 1980 period.

C74-1566

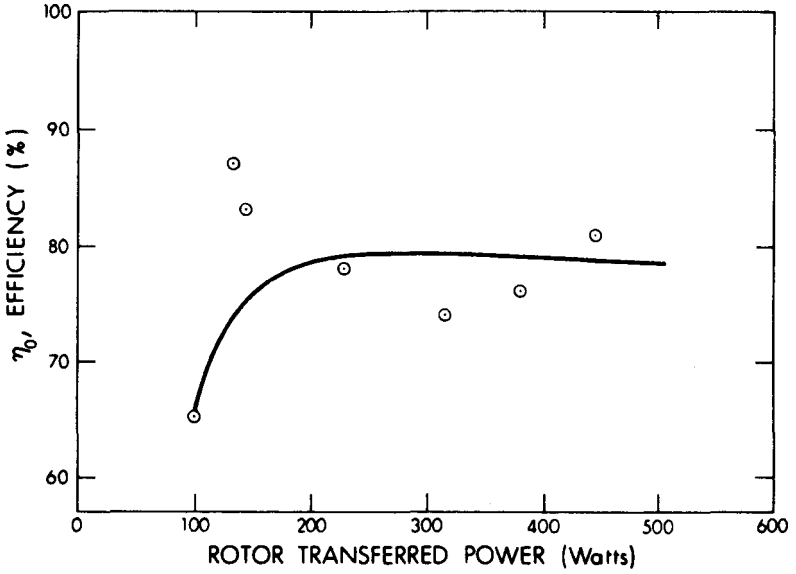

Figure 4-92. Output system efficiency P_0/P_T versus transferred power, data from March-April 1980 period.

C74-1568

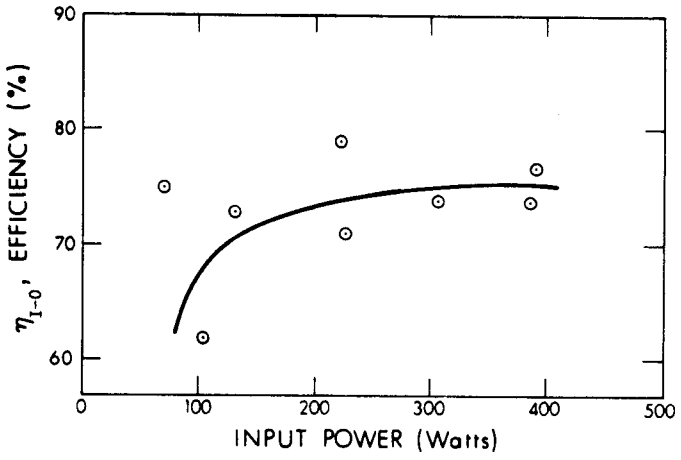

Figure 4-93. Total throughput efficiency P_O/P_I versus input power, data from March-April 1980 period.

4.6.1.5 Conclusions from Preliminary Test Data

The experimentally measured efficiencies are compared with estimated values in Table 4-6.

TABLE 4-6

POWER-TRANSFER EFFICIENCY COMPARISON

Flywheel System with Stand-Alone Cycloconverter

Preliminary Data

	Estimated		Preliminary Experimental Results (Resolution ± 4%)
Motor Electronics	96%		
		94%	92% (Input eff.)
Motor	98%		
Generator			
		87%	80% (Output eff.)
Generator Electronics			
Combined Efficiency		82%	75% (Overall eff.)

The measured input efficiency of 92% was close to the expected value. However, the output transfer efficiency of 80% was lower than the design expectation of 87% and produced an overall throughput efficiency that was slightly less than expected. A major part of the power loss in the generating mode was found to occur in the armature as indicated by a temperature rise of approximately twice that measured in the motoring mode for equal power. Additional measurements of the circulating currents in the parallel windings of the generator established this loss as the major cause for the lower efficiency. Subsequent to the preliminary measurement program, a method to eliminate the circulating currents by the addition of interphase transformers was developed and installed in the flywheel system for future testing. Tests of the improved system are reported in Section 4.6.4.

4.6.2 Tests with Whirl Mode Damper

An external mechanical damper was installed in the flywheel system following the preliminary test series. The damper was added to eliminate the 2-Hz whirl mode buildup experienced in this test series when rotor speeds above 11,000 RPM were attempted. A physical description of the damper unit is given in Section 4.2.7 and its damping characteristics are described in Section 4.5.9. Measurements of the system damping decay rate with damper are described in Section 4.4.6.

With the mechanical damper in place, the flywheel system was accelerated up to its operating range. The addition of the damper was found to eliminate the 2-Hz whirl mode for all rotor speeds up to the maximum design speed of 15,000 RPM. The addition of the damper also reduced the amplitudes of oscillations experienced as the rotor speed passed through structural resonant frequencies lying below the flywheel operating speed range.

4.6.3 Flywheel System Test Plan

The flywheel storage unit reached a mature state with the addition of a whirl mode damper and subsequent operation of the flywheel to speeds of 15,000 RPM. Though the preliminary test measurements were sufficient to characterize the overall in-out efficiency of the flywheel in the cycloconverter mode at about 75%, examination of these data showed substantial data scatter and a need for more thorough measurements. Uncertainties in the

preliminary data centered around corrections for flywheel aerodynamic drag losses, armature circulating current losses, the measurement accuracy of the instrumentation, and the lack of instrumentation to measure the cycloconverter component efficiency directly.

The flywheel system test plan was formulated to improve the flywheel experimental measurement data base. The test plan incorporated a series of measurements which determined individual component efficiencies as well as overall system in-out storage efficiencies. It included tests to measure the power-transfer efficiencies of the maximum-power-point tracker, the motor-drive system, the generator, and two types of output power conditioners, the stand-alone cycloconverter and the utility-interactive inverter. The test plan's main improvements were the use of a hard vacuum of approximately 10^{-6} torr in the vacuum test chamber to eliminate data corrections for aerodynamic drag losses, the installation of new, calibrated power measurement equipment to increase the accuracy of the power readings, the addition of interphase transformers to eliminate the generator circulating currents, and the addition of the external damper to allow tests to be conducted to the maximum design speed of 15,000 RPM.

4.6.4 Improved Experimental Measurements Program

An experimental measurement program, which followed the new flywheel system test plan, was initiated late in FY-80. By mid-FY-81, improved efficiency measurements had been taken on all components and spin-down tare losses had been remeasured. A description of results in the new test series follows. An electrical efficiency measurement accuracy of $\pm$.5% was achieved with the improved instrumentation and test procedures.

4.6.4.1 Test Description

The overall in-out electrical storage efficiency of the flywheel system was measured as were the power-transfer efficiencies of individual components and the spin-down tare losses due to effects of the magnetic bearing, mechanical damper and armature (see Fig. 4-94). Power-transfer efficiencies of the dc-to-dc down converter, motor electronics and utility-interactive

inverter were determined from measurements of the input power to and output power from the component, while motor-generator/rectifier and cycloconverter efficiencies were determined by measuring the change in the stored energy (rotor-spin speed) for measured input or output power levels. Spin-down tare speed versus time were measured with the system electrically isolated from all inputs or outputs. Measurements typically were made at input and output power levels in the range from 100 to 600 W and at flywheel spin speeds covering the range from 7,500 to 15,000 RPM.

C74-1267

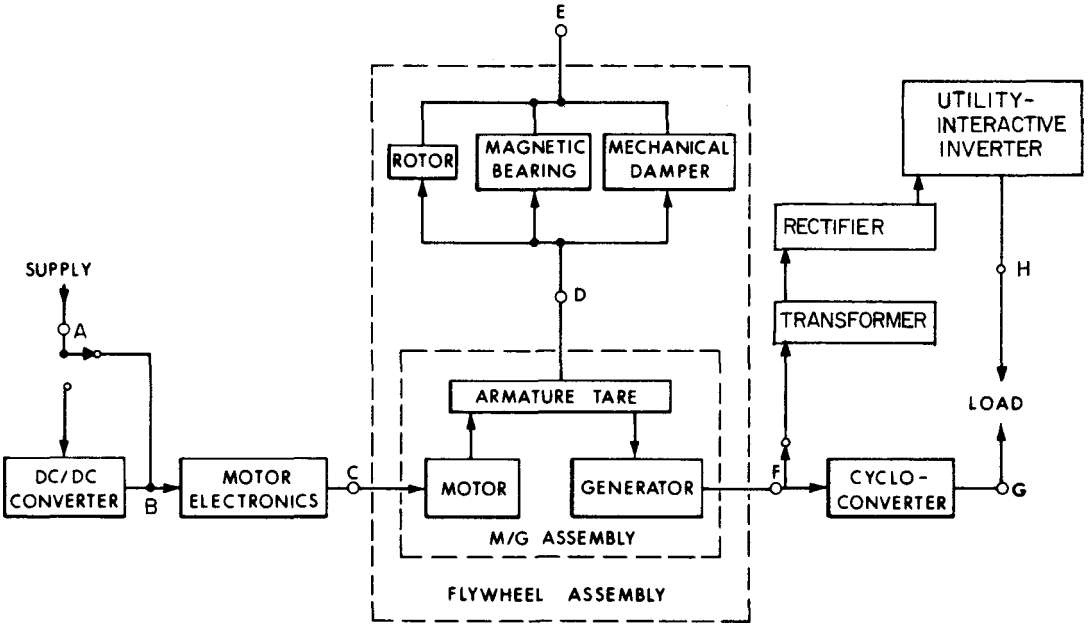

Figure 4-94. Power losses diagram.

Power measurements were made at points A, B, C, G and H in Fig. 4-94. The change in rotor speed with time was measured at power E with a Data Precision Corporation Model 5740 multifunction counter. Spin-down tare losses were measured with the flywheel assembly electrically isolated at points C and F from the rest of the system. Measurements were not possible at point D because it is integral physically to the flywheel assembly. Power measurements were not made at point F because of a lack of suitable instrumentation at hand.

4.6.4.2 Experimental Data

Experimental measurements of the efficiencies for the dc-to-dc converter, motor electronics, motor, combined motor electronics and motor, and motor spin-down tare losses are shown in Figs. 4-95 through 4-99, respectively. The linear variation of spin-down tare loss with rotor RPM was unexpected.

C74-1287

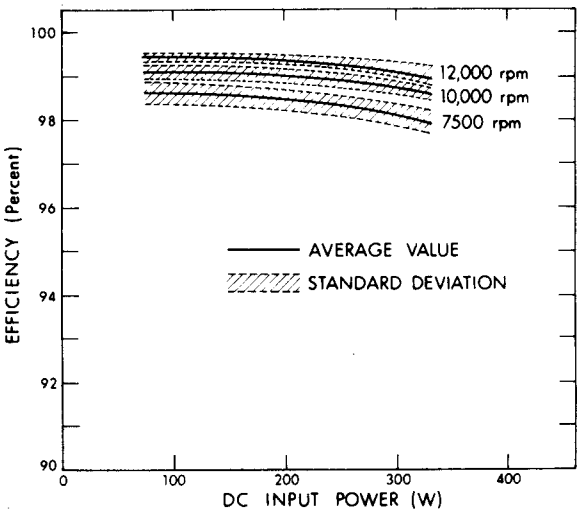

Figure 4-95. DC-to-DC down converter efficiency.

C74-1212

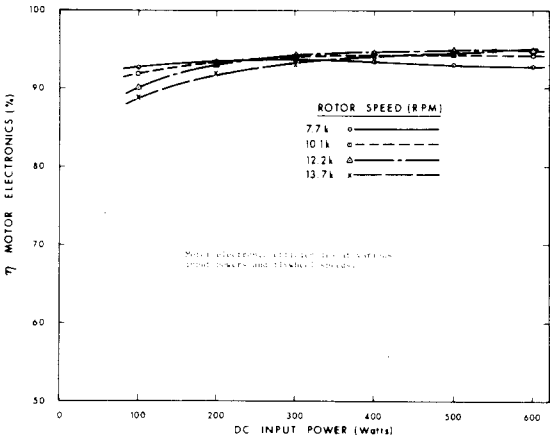

Figure 4-96. Motor electronic efficiencies at various input powers and flywheel speeds.

C74-1286

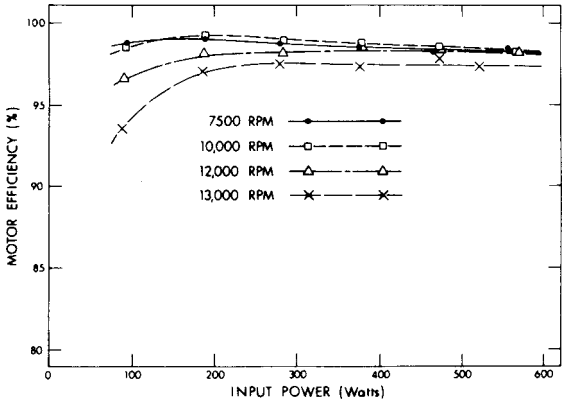

Figure 4-97. Motor efficiency.

C74-1213

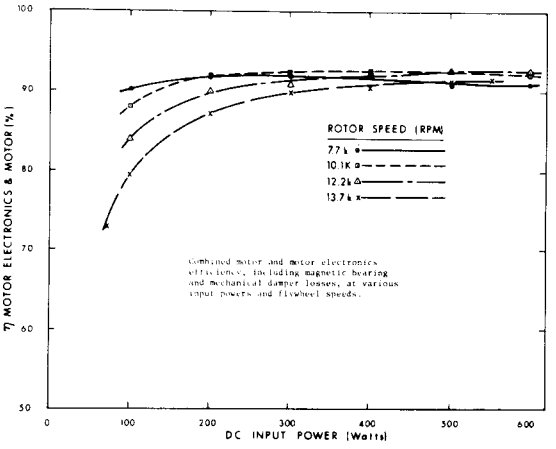

Figure 4-98. Combined motor and motor electronic efficiency, including magnetic bearing and mechanical damper losses.

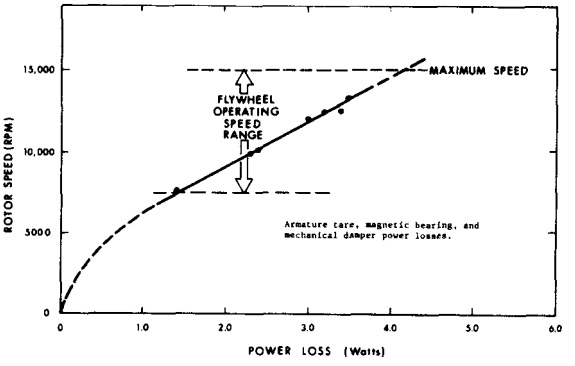

Figure 4-99. Spin-down tare loss.

4.6.4.3 Operating Efficiencies in Utility-Interactive Mode

When the flywheel system is operating in the utility-interactive mode, the electrical output from the flywheel generator is rectified and then converted to 120-V, 60-Hz power in the utility-interactive inverter, (Path F to H, Fig. 4-94).

Measured efficiency characteristics for the generator/rectifier and for the utility-interactive inverter components are shown in Figs. 4-100 and 4-101, respectively. The component efficiencies and overall in-out efficiencies for the overall flywheel system in the utility-interactive mode are listed in Table 4-7. Table 4-7 tabulates the component efficiencies and overall efficiencies versus flywheel spin speed under the assumption that the prototype flywheel system is operating at 300-W input and 500-W output. The overall in-out efficiency of the flywheel system operating in the utility-interactive mode is 80 to 82%, for electricity stored for one hour and then removed, and 77 to 80%, for electricity stored for 10 hours before removal. These round-trip storage efficiencies are 10 to 15 points higher than those presently achieved by battery storage/inverter power systems for the same application. It should be noted that the reported efficiencies are based on measurements made on existing equipment with specific electrical circuit

topologies. In the course of performing and analyzing the test results, certain modifications were identified which, if incorporated into the flywheel unit, could increase the round-trip storage efficiency by 2 to 5 additional points.

C74-1285

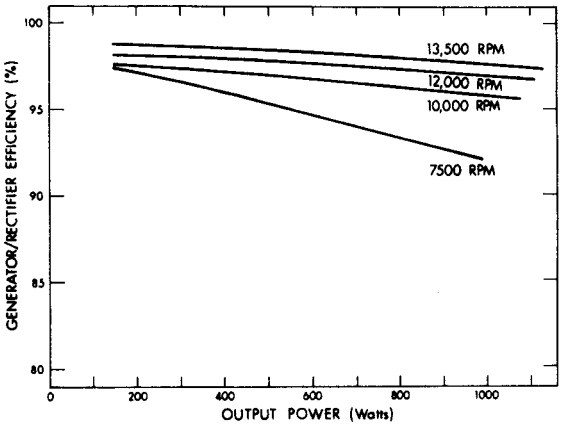

Figure 4-100. Generator/ rectifier efficiency characteristics.

C74-1431

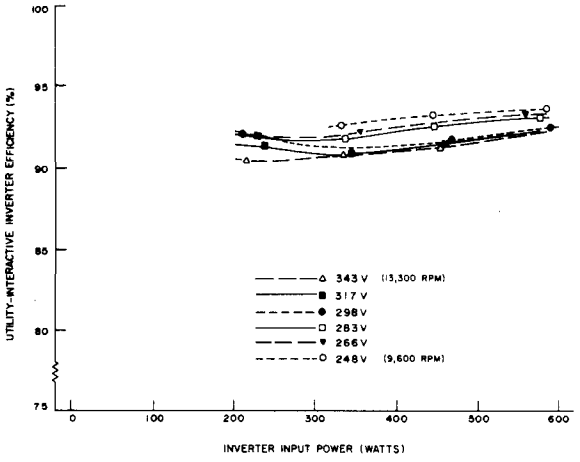

Figure 4-101. Utility-interactive inverter operating efficiency.

TABLE 4-7

MEASURED EFFICIENCY - UTILITY-INTERACTIVE MODE

300 Watts In
500 Watts Out

Component	Flywheel Speed 10,000 RPM (percent)	12,000 RPM (percent)	13,500 RPM (percent)
DC-to-DC-converter	98.7	99.1	99.5
Motor electronics	94.2	94.3	93.0
Motor	98.9	98.2	97.5
Generator/rectifier	95.0	96.9	96.7
Utility-interactive inverter	93.4	92.5	92.1
Tare loss (per hour)	99.8	99.7	99.6
Overall In-Out Efficiency			
(1-hour storage time)	81.4	82.0	80.0
(10-hour storage time)	79.9	79.8	76.9

4.6.4.4 Operating Efficiencies in the Stand-Alone Mode

When the flywheel system operates in the stand-alone mode, electrical power flows from the generator through a cycloconverter to the load (Path F to G, Fig. 4-94). Measured efficiencies for the cycloconverter component are presented in Fig. 4-102. Component efficiencies and overall conversion efficiencies in the stand-alone mode are listed in Table 4-8 for four spin speeds. For one-hour storage of electricity before removal, the stand-alone system storage efficiency is in the range from 61% to 70%, while for a 10-hour storage time, the system efficiency is in the range from 59% to 69%, best efficiency being measured at the lowest speed. Additional measurements made on the cycloconverter unit showed that the operating (tare) loss associated with the present design is high: 20 watts at 8,000 RPM and almost 30 watts at 10,000 RPM. However, this can be reduced substantially through

the addition of more sophisticated filters. The designer of the present cycloconverter unit believes that an increase in component efficiency of from 5 to 10 points is possible for a redesigned cycloconverter with improved filtering.

C74-1713

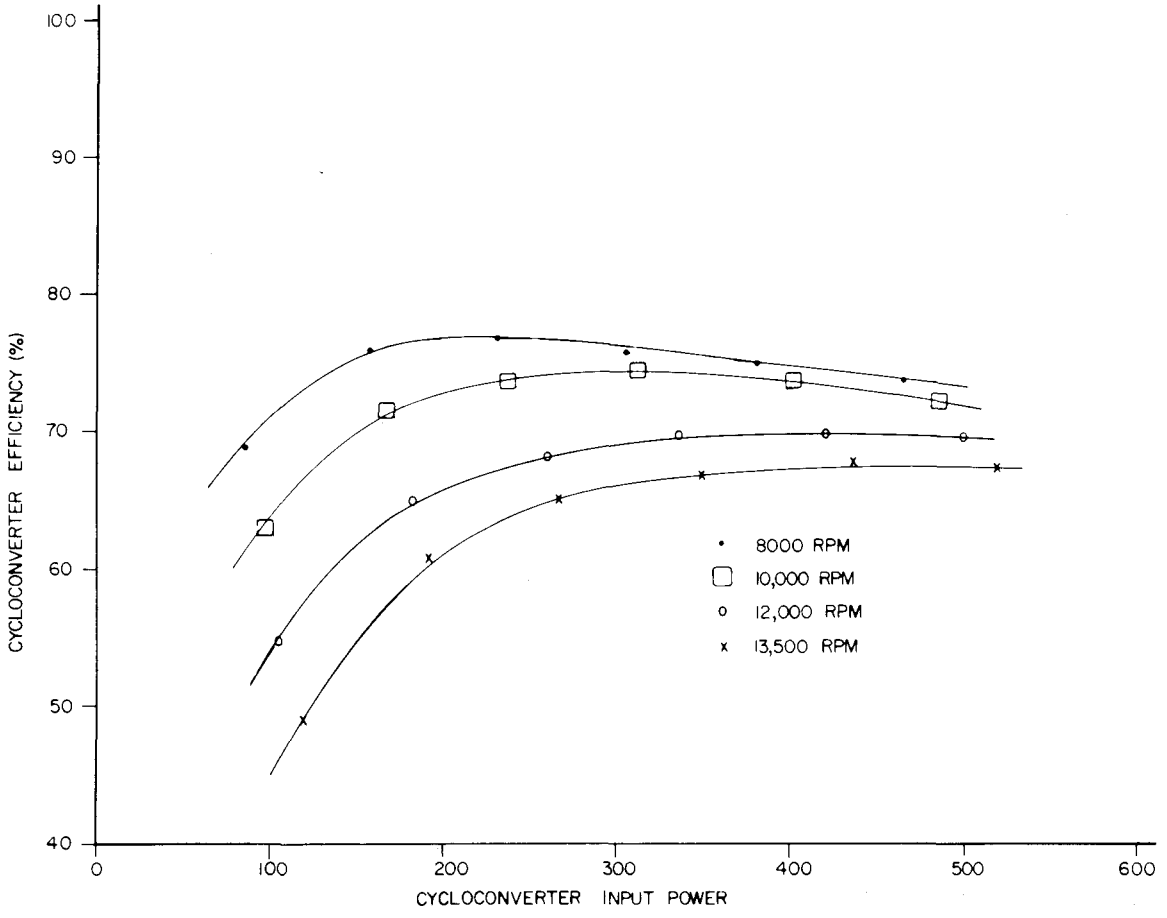

Figure 4-102. Stand-alone cycloconverter efficiency.

The stand-alone cycloconverter efficiencies measured in this more careful series of measurements are 4 to 7 points less than the preliminary efficiency measurements described in Section 4.6.1 for the rotor speed range of 6,000 RPM to 10,000 RPM. The difference can be attributed only to more accurate measurement methods.

TABLE 4-8

MEASURED EFFICIENCY - STAND-ALONE MODE

300 Watts In
500 Watts Out

Component	Flywheel Speed 7500 RPM	10,000 RPM	12,000 RPM	13,500 RPM
DC-to-DC converter	98.1	98.7	99.1	99.5
Motor electronics	94.0	94.2	94.3	93.0
Motor	98.6	98.9	98.2	97.5
Generator/cyclo-converter	76.6	72.5	70.0	68.0
Tare Loss (per hour)	99.9	99.8	99.7	99.6
Overall In-Out Efficiency				
(1-hour storage time)	69.5	66.5	64.0	61.1
(10-hour storage time)	68.9	65.3	62.3	58.9

5.0 MANUFACTURING COST STUDIES

5.1 40-kWh Residential Flywheel

5.1.1 First-Generation, FY-80 Technology Design

In FY-80, cost estimates for the manufacture of a full-size, 40-kWh, 8-kW residential flywheel system were prepared for MIT Lincoln Laboratory by three industrial concerns: Theodore Barry Associates, Garrett AiResearch and Kelsey-Hayes. These firms were selected from responses received to a competitive solicitation released to industry. The firms were provided with the MIT Lincoln Laboratory design layout, Fig. 4-1, for a 40-kWh flywheel storage unit and requested to provide cost estimates for manufactured quantities of 1,000, 10,000 and 100,000 units per year. The baseline 40-kWh flywheel design provided by Lincoln Laboratory represented FY-80 technology since it was the model for the 1/10-scale prototype flywheel system which was undergoing fabrication at that time.

At the start of their contracts, each firm was requested to review the baseline design and to incorporate any obvious changes in the design that would make the unit easier and less costly to manufacture. Each of the firms then carried out detailed cost estimations on their improved design. The firms were also asked to report at the end of the contract on additional conceptual design improvements that they might have identified in the course of carrying out their contract work that would improve manufacturability.

The cost estimates prepared by the three industrial firms for production of the 40-kWh system in units of 10,000 per year are summarized in Table 5.1. These total cost figures are the sum of component costs plus an allowance for markup and distribution. The flywheel rotor cost of $4,000 ($100/kWh) which is included in Table 5-1 was supplied to the contractors by Lincoln Laboratory and is in 1979 dollars. All other cost figures were estimated by the industrial firms and are also in 1979 dollars. A production quantity of 10,000 units per year was selected as being most representative of the near-term market for flywheel storage systems based on assumed penetration of PV systems in the market place.

Table 5-1

MANUFACTURING COST ESTIMATES[1]
40 kWh, 8 kW
FLYWHEEL ENERGY STORAGE UNIT
• 10,000 UNITS PER YEAR FY 1980 TECHNOLOGY, 1979 DOLLAR COSTS

ORGANIZATION	THEODORE BARRY	GARRETT AIRESEARCH	KELSEY-HAYES RESEARCH	MIT LINCOLN LABORATORY[3]
FLYWHEEL ROTOR	4,000[2]	4,000[2]	4,000[2]	5,000
MOTOR-GENERATOR	2,200	2,100	2,300	1,200
MAGNETIC BEARING ASSEMBLY	2,600	4,100	5,100	2,500
VACUUM SYSTEM AND ENCLOSURE	2,400	1,100	1,500	1,200
ELECTRONICS	1,200	3,500	2,600	1,800
SYSTEM CHECKOUT	200	500	1,200	–
INSTALLATION	1,000	1,500	900	800
SUB TOTAL	13,600	16,800	17,600	12,500
MANUFACTURING MARKUP AND DISTRIBUTION	3,400	5,000	2,700	–
TOTAL	17,000	21,800	20,300	–

(1) PRELIMINARY

(2) FLYWHEEL COST SPECIFIED BY MIT LINCOLN LABORATORY

(3) A.R. MILLNER, A FLYWHEEL ENERGY STORAGE AND CONVERSION SYSTEM MIT LL REPORT COO-4094-48

Examination of Table 5-1 shows substantial differences between contractors in the estimation of individual component costs. However, total costs show much less of a variation between contractors. The total cost estimates for a 40-kWh, 8-kW flywheel storage unit of FY-80 technology fall in the range from $17,000 to $21,800 ($425/kWh to $545/kWh). The variations of flywheel system cost with production rate, as predicted for the 8-kW, 40-kWh residential unit by the three industrial firms, are shown in Figure 5-1.

C74-1559

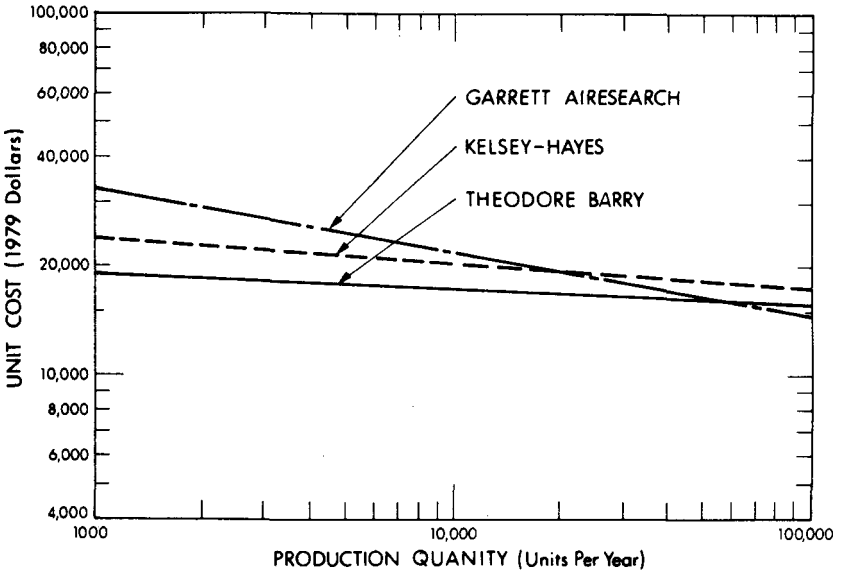

Figure 5-1. Variation of flywheel system cost with production rate, 8-kW, 40-kWh residential unit ($1979).

Garrett AiResearch made detailed cost estimates for only one production rate. Cost estimates for other rates were made using learning curve effects. The learning curves used in Garrett's study were based upon historical industry data. Garrett AiResearch selected an 85% learning curve because it is representative of savings realized by AiResearch in high production turbocharger manufacture. An 85% learning curve means that as production doubles, a unit sell price becomes 85% of its former value. As described in the following section, additional design changes suggested by the industrial firms and further design simplifications identified by MIT Lincoln Laboratory are expected to lower the costs of a 40-kWh unit to the $8,500-$11,000 range ($210/kWh-$275/kWh) by 1985.

The power rating (8 kW) and storage capacity (40 kWh) of the full-size residential flywheel storage unit were selected based on the best information available at that time for estimates of the load, daily energy use, and required PV array for a PV residence. These specifications were representative of a fully air-conditioned residence for the Southwest or an all-electrically heated residence in the Northeast. Substantially more work has been completed on the design of PV residences since these earlier specifications were selected. Certain trends for PV residences can be perceived in this new work. The new PV residential designs tend to be more energy conservative. Presently the preferred PV array size falls in the 5- to 6-kW range and the daily energy use is estimated at 20 kWh. The trend to more energy-efficient designs with lower PV array power requirements and smaller storage requirements is expected to continue. A 20-kWh, 5-kW flywheel storage unit of FY-80 technology is projected to cost in the range of $8,500 to $10,000 based on a linear extrapolation of the manufacturing cost studies of a 40-kWh unit, and this 20-kWh unit is projected to cost in the range from $4,200 to $5,500 by 1985 in production quantities of 10,000 per year. A 20-kWh flywheel unit is now the preferred size for residential applications.

Design changes incorporated by the industrial firms prior to estimation of unit manufacturing costs are summarized below.

THEODORE BARRY ASSOCIATES REDESIGN

Theodore Barry Associates redesigned the baseline layout as follows:

Motor-Generator

- Both upper and lower rotors are designed identically, even though certain aspects of the geometry are nonfunctional (upper rotor only).
- Molded polyester/fiberglass enclosure discs are molded in identical halves with depressed and raised faces to facilitate coil placement.
- Coils are attached together by copper connectors rather than each coil terminating at an individual terminal.
- Coils are laid in three layers rather than in an overlapping array.
- A heat sink ring is utilized to facilitate transmission of heat generated within the coils during operation.

Magnetic Bearings

- Rotors are secured to the bearing shaft with the use of a split taper sleeve, hydraulically rammed into place with a measured preload. Advantages of this approach include: 1) minimized tolerance control (face run-out) for machine parts; 2) reduction of rotor weight; 3) recycling of disassembled rotors without appreciable damage.
- Tension rods are used to hold the assembly together between the upper and lower castings. Advantages include: 1) accessibility for alignment and adjustment; 2) three-point support.
- Simplified stator assembly.

Vacuum System

- Steel cylinder with elliptical heads.
- Three-point support built into a continuous ring. The ring acts in two ways: 1) stiffener support for the tank allowing minimum wall thickness; 2) barrier from the possiblity of water pen etrating the vault enclosure.
- Direct transfer of assembly and flywheel weight to external supports; eliminating vessel stresses other than those caused by the vacuum itself.
- Quick release vacuum seal with flanged disconnect.

KELSEY-HAYES REDESIGN

The Kelsey-Hayes residential redesign included the following changes:

Motor-Generator

- Major change in support structure reduces the thermal path and therefore stator temperatures.
- Use of a preform to locate each coil and a thin layer of glass mat between coils to avoid circulating currents.

Magnetic Bearings

- Replace samarium-cobalt magnetic bearings (6) with integrated electromagnetic control coils by two (2) large permanent-magnet (ALNICO 8) bearings and one double-electromagnet servo lifter containing the height sensor. The servo coils are removed from the permanent-magnet bearings to avoid demagnetization of the ALNICO when initial bearing separation from the rest is performed.
- Minimize the tolerance stackup.

Vacuum System

- Fabricate the bottle from 3 pieces of cold rolled steel welded together. Attach a convex bottom so that the unit will stand on its own base and accommodate a rotor cage unit which protects the system during shipment.
- Use smaller vacuum ways to reduce unit height within trucking limits.

Support System

- Provide flywheel support with cheaper and more easily handled plate and beam structure. Use plate for mounting for vacuum pump, electronics and wiring.

Electronics

- Use transistors rather than SCRs because 1) the parts count is lower, 2) the di/dt is reduced making noise output (RFI) less and 3) the switching energy is much greater making accidental operation less likely.

GARRETT AIRESEARCH REDESIGN

Garrett AiResearch included the following redesign features:

Motor-Generator

- Extend quill shaft through the top of the motor-generator. Cut threads in quill shaft above upper rotor so a single nut assembles the quill shaft, bushing, upper and lower rotors. Use keys between the upper and lower rotors and between the lower rotor and bushing.

Magnetic Bearing

- Relax tolerances to reduce required machining time.
- Modify shaft to facilitate assembly. Step shaft to provide precise locating stops for bearing rotors. Key the bearing rotors into the bearing shaft. Construct the bearing rotors in two pieces, an outer rotor ring of high-strength magnetic steel and an inner clamp ring of low carbon steel. Assemble with an interference fit. Lock bearing rotor in place with a conical nut.

Electronics

- Add fusing to protect against external fault or internal component failure and to assure human safety when servicing unit.

5.1.2 Design Improvements for "Manufacturability"

At the completion of their manufacturing cost studies of the 40-kWh, 8-kW flywheel storage system, the industrial firms recommended that additional changes be incorporated in the system to reduce costs further. The recommendations of each firm are considered below.

Theodore Barry Associates recommended the following changes:

- o Reduction of the number of magnet bearings.
- o Deletion of permanent magnet material from both the motor-generator and magnetic bearing assemblies.
- o Substitution for Litz wire.
- o Reduction in cost of vacuum pump and chamber cost by possible incorporation with support housing.

Theodore Barry and Associates concluded from their study that "the flywheel energy storage and conversion system concept utilizing magnetic bearings and vacuum chamber appears to our staff as a sound and viable product which, with further refinements, can become economically competitive with battery storage systems." "At maximum production levels for the residential unit, the unit cost of a Flywheel Storage System based on our redesigned concept* is: ($16,054); but, we feel strongly that with further development, the following results can be attained at maximum production levels:

- o 30 to 40% reduction in cost of magnetic bearing assembly
- o 25 to 30% reduction in cost of vacuum chamber
- o 20 to 30% reduction in assembly plant tooling costs."

Kelsy-Hayes recommended additional changes in the design in the following area:

- o Substantially lower costs may be realized by selective relaxation of specifications and development of special-purpose manufacturing equipment/parts.

This firm also provided the following general guidelines to follow to reduce costs:

1. Solicit vendors to develop components that meet specification. They will design them for manufacture by procedures that they are comfortable with and therefore are low in cost.

*Including markup and distribution as well as integration.

2. Find ways to use everyday materials that are cheap and easy to machine and require no heat treatment, etc.
3. Redesign so tight tolerances are not necessary and specify tolerances only in the way that is essential, i.e., substitute concentricity for absolute on pole teeth.
4. Reduce number of parts.
5. Reduce tolerance build-up stringency.
6. Develop simple, functional go-no-go tests for parts rather than 100% dimensional accuracy.
7. Make parts interchangeability easy to establish.
8. Avoid clean room assembly.

Garrett AiResearch recommended the following additional changes:

1. Eliminate samarium-cobalt permanent magnets from the design. Give careful and serious consideration to alternative materials and design. Misch-metal cobalt magnets could reduce costs slightly while keeping a high energy product. Ceramic magnets would cost far less than $SmCo_5$ and are readily available, but considerable redesign would be necessary to compensate for the lower energy product.
2. Utilize a composite rotor for the lowest cost energy storage. An E-glass/epoxy composite rim with an aluminum hub would provide the least-cost flywheel. The 120$/kWh cost is roughly equal to the cost quoted in the statement of work. The major advantage that can be realized by using the composite rim is a 25% reduction in weight. Reduced flywheel weight leads to less cost in magnetic bearings, and thus, is worth looking into further.
3. Eliminate the chopper unit in the motor-drive system by substituting controlled firing angle thyristors. Vary the voltage by controlling the firing angle of the thyristors. Add a small low power chopper to commutate the motor during startup. This scheme requires the control logic to increase in complexity by 10 to 15%, but the advantage of reducing the number of expensive high-power components may compensate for these disadvantages.
4. Replace the cycloconverter circuit with a rectifier circuit and a line-commutated inverter. The present cycloconverter does not properly utilize the power semiconductors and it leads to an extremely poor power factor for the motor-generator. Control logic would be reduced by 50% with the rectifier/inverter scheme, and the power factor is increased significantly. The residential system with a cycloconverter requires 12 thyristors compared with four thyristors and six rectifiers with the rectifier/inverter. Such an approach would offer a great cost advantage in larger storage applications.

5. Consider different types of motors, especially the homopolar motor. "It is the opinion of AiResearch personnel that the homopolar inductor machine offers very low system cost with minimum losses and that it is a desirable design for both residential and larger applications."

5.2 Comparison of Flywheel and Battery Storage System Costs

Following the completion of the Manufacturing Cost Studies of the flywheel storage system, a cost comparison between flywheel and battery storage systems for the same PV application was developed. A stand-alone, 40-kWh storage capacity was selected for cost estimation because that was the size considered for flywheels in the Manufacturing Cost Studies and because flywheel operating efficiencies in the stand-alone mode had been experimentally measured at this time. The object was to develop battery storage system costs since a battery system is composed of a number of required elements in addition to the batteries themselves. Battery storage systems built and fielded by Lincoln Laboratory in a variety of photovoltaic applications have always included batteries, battery charger, microprocessor control, environmental space conditioning, dedicated space in a building and an inverter. Microprocessor control is required for battery state of charge and battery equilization charge management. Space conditioning includes air conditioning or heating of the battery room to maintain battery temperatures near 70°F. Much lower temperatures than this will reduce the usable battery storage capacity; much higher will reduce actual battery lifetime. Environmental conditioning also includes the requirement to vent any hydrogen gas produced by the battery storage system to provide safety explosion protection. Finally, the inverter is required to convert dc power from the battery to the required ac. Those items normally included, such as control electronics, safety system and power conditioning/inverter systems, must be added to the battery costs in a battery storage system to arrive at total battery storage system costs. Only then is a direct comparison of costs between flywheel and battery storage systems proper.

To arrive at battery system costs, two photovoltaic field test and application projects constructed by Lincoln Laboratory for DOE which contained battery storage systems were examined for actual costs. Actual battery

system component costs on per kWh or per kW basis are listed in Table 5-2 for the two applications. The costs shown include purchase and installation of the equipment but do not include any engineering development costs. The costs are in 1979 dollars. The battery storage system is of the lead-acid type. These battery system component costs based on recent PV applications were then used to arrive at the total cost of a present-day, lead-acid battery storage system of 40-kWh capacity, Table 5-3. A lifetime of 8 years was assumed for the present-day, lead-acid battery system whereas a flywheel system was assumed to have a lifetime of 20 years. A total present value of $23,110 was arrived at and it included replacement of the battery system at 8-year intervals. Costs of borrowing the capital over the lifetime of the system are not included in these figures.

TABLE 5-2

BATTERY SYSTEM COMPONENT COSTS BASED ON RECENT PV APPLICATIONS (1979$)

	Application #1	Application #2	Average
Lead-acid batteries ($/kWh)	170	200	185
Inverter ($/kW)	490	600	545
Battery charger ($/kW)	380	375	378
Microprocessor ($/kWh)	13	25	19
Battery room ($/kWh)	34	25	30

The total present value of an advanced battery system with 14-year battery was also estimated in Table 5-3. Battery and inverter costs for the advanced battery system were based on attainment of the 1986 DOE goal of $67/kWh for batteries and of the 1986 DOE goal of $380/kW installed for inverters. Battery charger costs were lowered by 35% to reflect the same percentage cost reduction as predicated by DOE for advanced inverter systems. Microprocessor and battery room costs were arbitrarily kept at the same level in present day and advanced battery system examples. A total advanced battery storage system cost of $10,490 is estimated in 1980 dollars.

TABLE 5-3

TOTAL PRESENT VALUE OF BATTERY STORAGE SYSTEM
FOR 40-kWh, 8-kW PV RESIDENTIAL APPLICATION
20-YEAR SYSTEM LIFE, 1980$

	PRESENT DAY LEAD-ACID (8 YR. LIFE)	ADVANCED BATTERIES (14 YR. LIFE)
BATTERIES	$13,210	$3,380*
INVERTER	$ 4,620	$3,040+
BATTERY CHARGER	$ 3,210	$2,000
MICRO-PROCESSOR	$ 800	$ 800
BATTERY ROOM	$ 1,270	$1,270
	$23,110	$10,490

*1986 DOE GOAL OF $67/kWh

+1986 DOE GOAL OF $380/kW INSTALLED

The total battery system costs shown in Table 5-3 should not be compared directly to flywheel system costs at this point because the battery and flywheel systems operate at different overall in-out electrical storage efficiencies. In closely monitored tests, stand-alone lead-acid battery storage systems have been found by Lincoln Laboratory to operate at 67% round-trip efficiency. At the time the cost comparison was made, the round-trip efficiency of the flywheel system in stand-alone mode was expected to be 74% based on the preliminary measurements. The battery system with the lower operating efficiency requires a larger photovoltaic array in order to supply equivalent delivered energy. The incremental cost of the larger PV array required by the battery storage system must be charged against the battery storage system to arrive at a cost that may be compared directly to a flywheel storage system. The total storage system costs for battery and flywheel systems for equivalent delivered energy are summarized in Table 5-4. The cost figures for the flywheel storage unit are larger than those quoted at the end of Section 5.1.1 because the costs in Table 5-4 are in 1980 dollars rather than 1979 dollars. The lead-acid battery storage system was penalized for extra PV array at the 1980 price of $9.70/peak watt installed while the advanced battery system was penalized for extra array at the 1986 DOE goals of $1.10/peak watt installed. A comparison of the battery storage system and flywheel storage system costs of Table 5-4 show that the flywheel is projected to cost about three times less than a present day lead-acid battery storage system and to cost about the same as an advanced battery system. Thus flywheel systems are seen to be a reasonable alternative to battery storage systems.

The cost comparisons shown in Table 5-4 were made prior to the improved experimental measurements program discussed in Section 4.6.4. The more precise measurements program showed a round-trip storage efficiency in the utility-interactive mode of 80 to 82% while in the stand-alone mode actual efficiencies in the range from 64 to 65% were measured. Thus the battery storage system should be penalized more for the additional PV array required in the utility-interactive mode than was done in Table 5-4 and penalized less

than done in Table 5-4 in the stand-alone mode. Also a 20-kWh residential storage capacity is now preferred rather than the 40-kWh system capacity which was the basis of Tables 5-3 and 5-4.

TABLE 5-4

TOTAL STORAGE COSTS FOR EQUIVALENT DELIVERED ENERGY
STAND-ALONE PV RESIDENTIAL APPLICATION (40 kWh, 8 kW)
(1980$)

COMPONENTS	BATTERY SYSTEM η = 0.67		FLYWHEEL SYSTEM‡ η = 0.74	
	PRESENT LEAD-ACID	ADVANCED†	HIGH ESTIMATE	LOW ESTIMATE
STORAGE SYSTEM*	23,110	10,490	11,700	9,000
PV ARRAY ADDITIONS	8,100	920	–	–
TOTALS	$31,210	$11,410	$11,700	$9,000

* INCLUDES BATTERY, INVERTER, BATTERY CHARGER, MICROPROCESSOR AND BATTERY ROOM COSTS

† 1986 DOE PRICE GOALS MET FOR BATTERY, INVERTER, AND ARRAY

‡ COMPLETE 1985 DESIGN PRODUCED AT 10,000 UNITS/YEAR

6.0 USER WORTH ANALYSIS

In FY-80, a flywheel storage system worth analysis was conducted by the MIT Energy Laboratory for Lincoln Laboraory which considered the economic feasibility of flywheel energy storage for photovoltaic systems of the residential and multifamily apartment type. There were two objectives to this study. First, the appropriate sizing of a flywheel unit had to be determined for two application types: a single-family residence utilizing a PV array of 8-kWp capacity, and a multifamily load center utilizing an array size of 100 kWp. The second objective was to simulate a range of technical and economic environments to determine sensitive market parameters. The study considered stand-alone and utility-connected residences in Boston and Phoenix, flat versus time-of-day utility rates in both locales and utility system electrical power buy-back rates from 0 to 100%. The multifamily apartment application was studied for a Phoenix locale only. The reliability of stand-alone systems with and without backup diesel generators in addition to the flywheel storage system was also considered. The complete results of the User Worth Study are documented in Appendix 6-1 of this report so only a brief summary will be given below. The User Worth Study was initiated prior to the Manufacturing Cost Studies and Flywheel Efficiency Measurement Program and therefore is based on the best available technical and cost information at that time. The User Worth Study was completed in February of 1980.

To perform the economic analyses, it was necessary to make a number of technical assumptions with regard to the flywheel system, photovoltaic array and diesel backup [economic assumptions for residential and multifamily load centers, utility rate structure assumptions and flywheel cost assumptions (see pages 13 through 18 of Appendix 6-1)]. The residential flywheel system cost assumptions are shown in Table 6-1. High-, medium- and low-cost categories have been assumed which represent 1980 technology and 1985 technology with probable and optimistic costs, respectively.

The results of the MIT Energy Laboratory study are presented as a value which is the difference between the benefits and the cost to the homeowner

TABLE 6-1

RESIDENTIAL FLYWHEEL SYSTEM COST ESTIMATES
1980 DOLLARS

	"HIGH" 1980 TECHNOLOGY ($)	"MEDIUM" 1985 HIGH ESTIMATE ($)	"LOW" 1985 LOW ESTIMATE ($)
STORAGE CAPACITY $/kWh	375	200	120
INPUT $/kWDC	130	90	40
OUTPUT $/kWAC	220	185	60
20 kWh TOTAL AT 8 kW	10,300	6,200	3,200
40 kWh TOTAL AT 8 kW	17,800	10,200	5,600

of a PV installation. This Break-Even Capital Cost (BECC) is defined as:

$$BECC = \sum_{i=1}^{life} \frac{Benefits-Costs}{(1 + r)^i}$$

where

Benefits = Total dollar equivalent of utility electricity displaced by the PV flywheel system, plus, for stand-alone applications, distribution-line costs otherwise incurred.

Costs = All costs of the system not to be included in the BECC figure (see below).

Life, i = Assumed lifetime of the system: 20 years.

r = Discount rate (the true cost of borrowing money).

The System BECC accounts for all costs associated with (1) the flywheel storage unit, (2) the photovoltaic modules, and (3) all balance-of-system (BOS) costs including mounting, electrical wiring of the photovoltaic modules, and all maintenance over the life of the system.

The Flywheel BECC includes the costs associated with power conditioning and is the system BECC less the cost of nonflywheel components such as PV modules.

6.1 Utility-Interactive Residential Flywheel Storage Systems

The MIT Energy Laboratory report shows that for a utility-interactive residence in Phoenix with a flat-rate price structure and 0% buy-back from the utility, system BECC is \$5,000 with an 80-m^2 array and no flywheel (Fig. 6-1a). The system BECC increases to \$11,500 and \$13,000 when flywheels of 20- and 40-kWh usable capacity, respectively, are added. Flywheel BECC under the same conditions is a function of assumed BOS costs and photovoltaic module costs. Figure 6-1b is for an 80-m^2 PV array. For a 20-kWh-capacity flywheel and photovoltaic modules at the 1985 cost goals of \$0.70 Wp (1980\$), including BOS costs, the flywheel BECC is \$300/kWh (Fig. 6-1b). Note that the worth is above the "medium" cost estimate of Table 6-1 showing that flywheels are an economical addition to a PV system when utility buy-back rates are low.

C74-1030

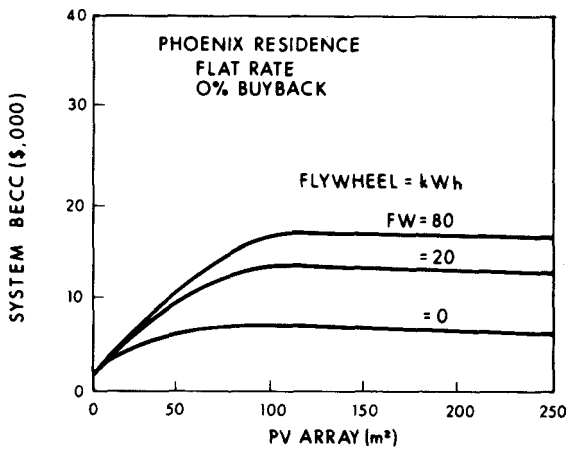

Figure 6-1a. System BECC vs. PV array - utility-interactive residence.

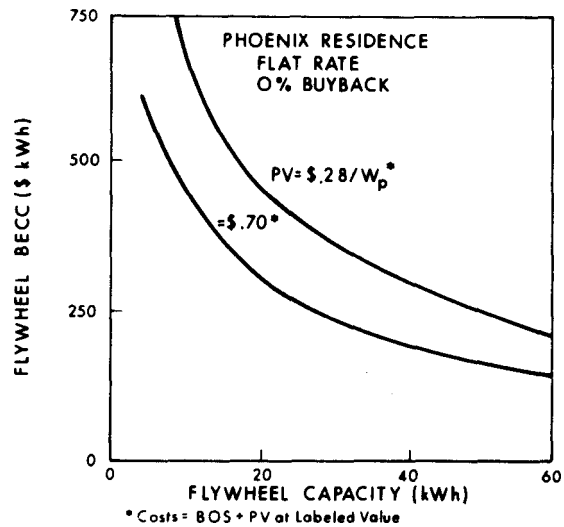

Figure 6-1b. Flywheel BECC vs. capacity - utility-interactive residence.

In general, the addition of storage serves to increase the optimum capacity of installed photovoltaics when hardware costs are assumed low enough to yield a positive return on investment. When storage is dedicated to the photovoltaic array alone, it is shown to have the greatest value when buy-back rates by the utility for excess photovoltaic-generated electricity are low. This is true since marginal benefits to a fixed-storage capacity decline as buy-back rates are increased. Depending on flywheel and BOS cost assumptions, at some utility buyback rate below 50%, the addition of storage capacity effects an increase in investment net benefits.

Using the most reasonable set of cost and financing projections for 1985, a photovoltaic-flywheel system will begin to look economically attractive when the cost of electricity, in 1980 dollars, exceeds $0.09/kWh (starting cost, assuming 3%/year real escalation thereafter, Fig. 6-2). Variations in time-of-day rate setting by the utilities are only significant in affecting storage economics if electricity is bought and sold directly from the storage device, thus acting in a dispersed-system storage mode. It was also found that the discount rate, r, is an important parameter in influencing system worth.

C74-1029

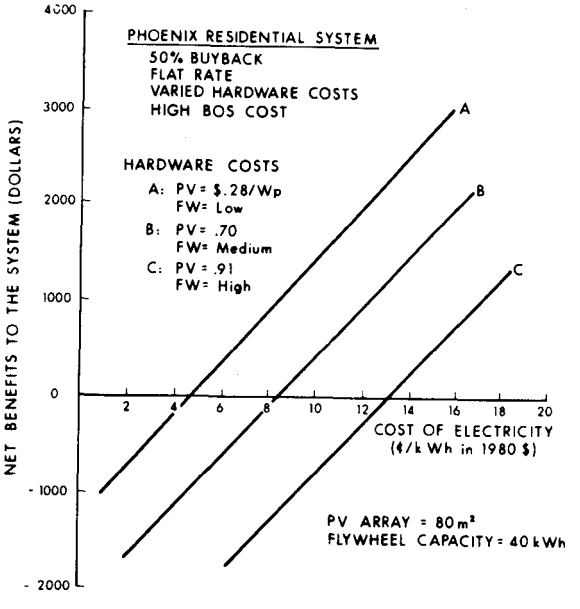

Figure 6-2. Utility interface PV and flywheel system net benefits vs. cost of electricity.

6.2 Remote Stand-Alone Residential Flywheel Storage Systems

For stand-alone (non-grid-connected) applications, the optimum configuration and sizing for the photovoltaic and flywheel without diesel backup was found to be quite sensitive to the desired service reliability, Fig. 6-3, where reliability index is defined as the number of customer hours served divided by the number of customer hours demanded.

C74-1031

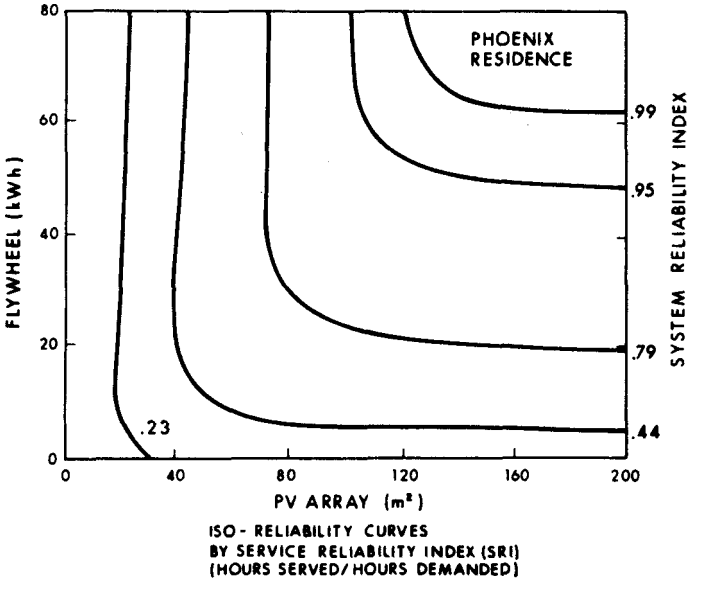

Figure 6-3. Remote stand-alone residential system: PV and flywheel only. No diesel backup.

When a diesel generator is added as backup to the photovoltaic and flywheel system, the issue of supply reliability is eliminated, under the assumption of a ready means for obtaining diesel fuel. For such a system, it was found that at just over one mile from a utility grid, positive net benefits begin to accrue to such isolated, total energy configurations.

6.3 Multifamily Load Center

The multifamily load center was also studied in the MIT Energy Laboratory investigation. It was found that breakeven cost figures are lower for the load center application due to higher discount rates and delay of benefits due to longer construction lags. A more detailed explanation of this result may be found in Appendix 6-1.

7.0 ADVANCED PROTOTYPE FLYWHEEL STORAGE UNIT

7.1 Full-Scale, 20-kWh Residential Flywheel System Design

A program was undertaken to develop a new design for an advanced prototype flywheel storage unit which would make use of the experience gained in the the design and testing of the 1/10-scale prototype flywheel storage unit, incorporate an advanced composite rotor in combination with magnetic suspension, and be responsive to manufacturing cost, user worth and residential flywheel simulation studies which had established that a second-generation flywheel storage unit should have a reduced storage capacity of 20 kWh (from the 40-kWh capacity initially assumed, Section 4.1) and be of a simplified design with a lower parts count and reduced cost.

The discussion which follows reports on improvements made to the load-carrying ability of magnetic bearings, the sizing of a synthetic design for a 20-kWh composite rotor to update the full-scale residential flywheel design layout, and the design of a two-bearing element, magnetic-bearing suspension for the 20-kWh composite rotor. A flywheel storage unit configuration incorporating these changes is described.

7.1.1 Advanced Magnetic Bearings

New designs for the magnetic bearings were explored with the goal of improved lifting capability with a fixed amount of magnetic material. Magnetic-bearing configurations were built and tested in which the location of the magnets in the stator was varied and where the fringe ring geometry was changed.

The baseline magnetic-bearing configuration used in the 1/10-scale prototype flywheel system has a 3:1 ratio of slot to fringe ring width and an annular permanent $SmCo_5$ magnet, radially polarized, located in the stator body, Fig. 7-1A. As reported earlier, this bearing had an unexpectedly high percentage of leakage flux and had less lift than expected with a force chracteristic "A" in Fig. 7-2. At the 10-mil operating gap in the 1/10-scale prototype, this bearing design would support 67 pounds per bearing.

The first attempt at an improved magnetic-bearing configuration had the permanent-magnet material divided into two portions and located in the inner

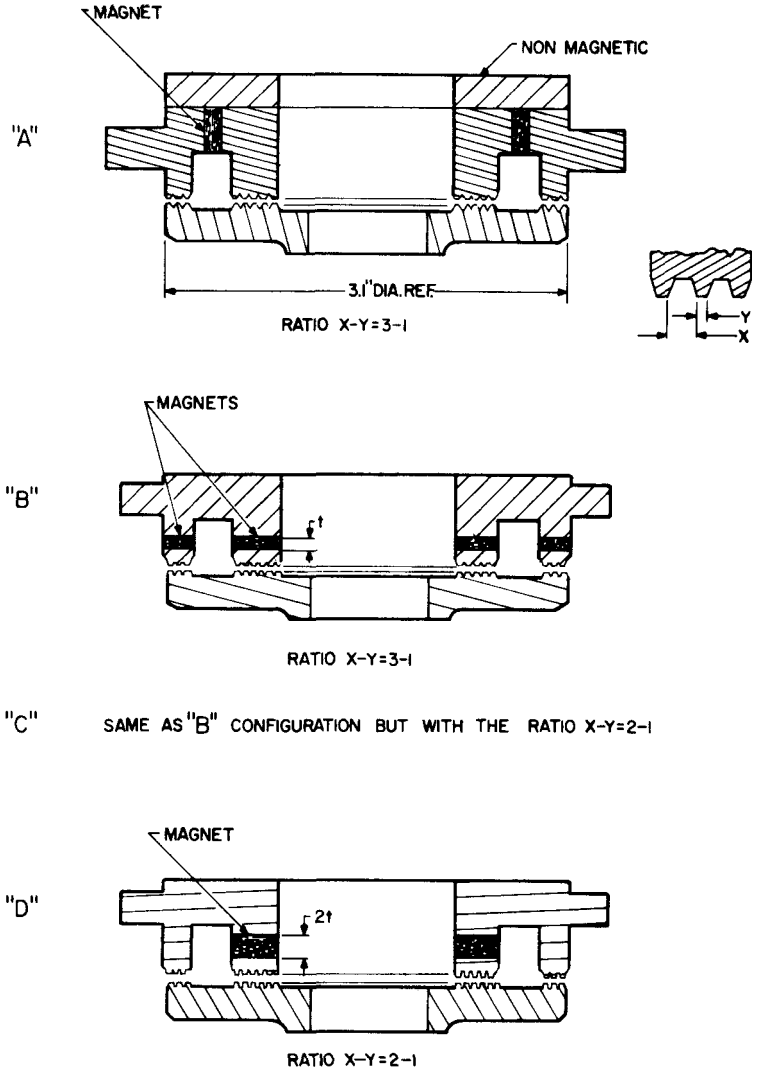

Figure 7-1. Magnetic-bearing configurations.

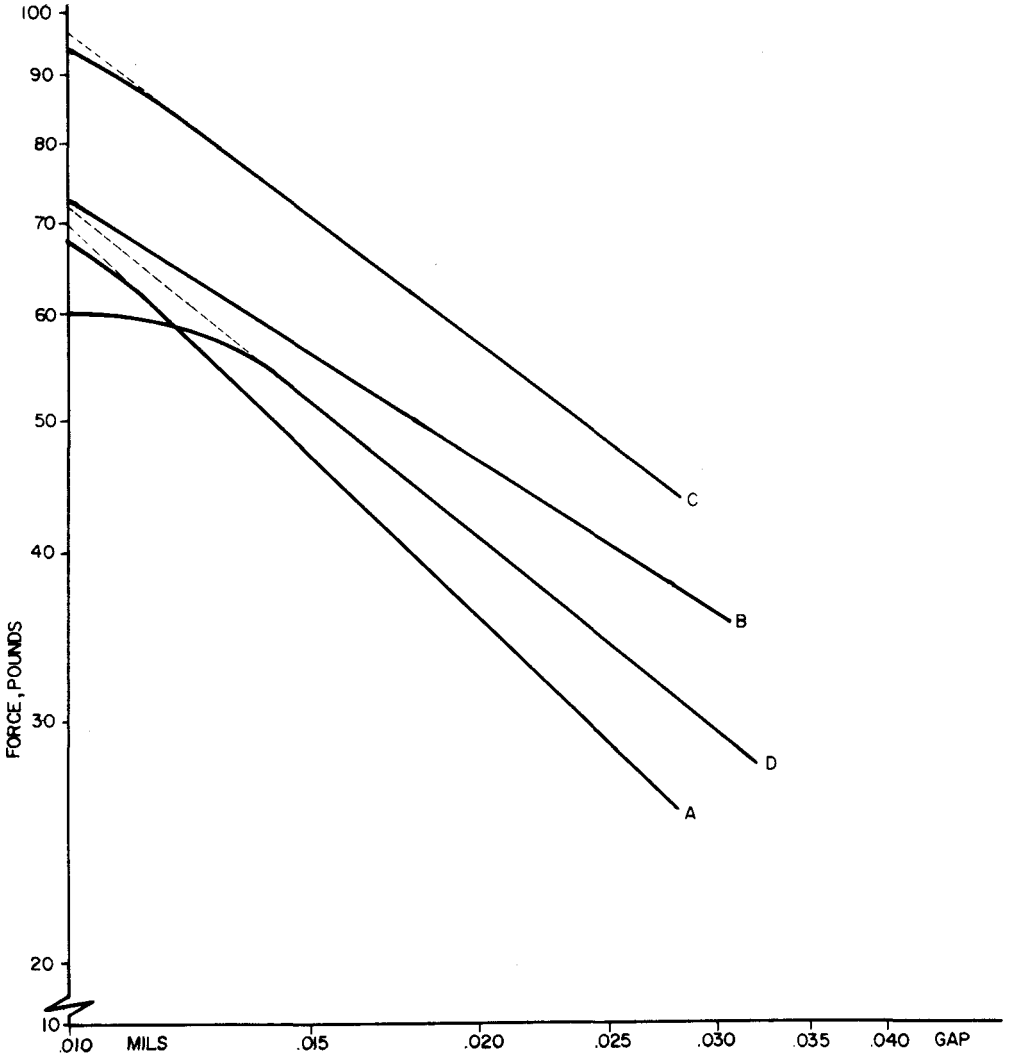

Figure 7-2. Magnetic-bearing force-gap characteristics.

and outer stator legs, respectively, Fig. 7-1B. The magnets were magnetized in the thickness direction and the 3:1 ratio of slot to fringe ring width was maintained. This change improved the lift by 33% at large gaps, but by much less at small gaps, Fig. 7-2B. The decreased slope of the force characteristic was felt to be due to magnetic saturation of the fringe rings which is also evident at the 0.01-inch gap in configuration "A". The actual

magnet volume for configuration "B" is 93% of configuration "A". For comparison, this configuration would support 73 pounds at an operating gap of 10 mils, a 10% improvement in lifting capability.

Further analysis of the fringe ring-to-slot ratio indicated that although the maximum field in the gap increases at higher ring-to-slot ratios, the gap reluctance also increases. An increase in gap reluctance requires a greater magnet length (volume) to maintain a given total flux. By making the slot-to-fringe-ring ratio 2:1, the gap reluctance decreases by 20% (for constant gap) and the saturation effects are greatly reduced.

The second magnetic-bearing configuration tested had the magnets located in the inner and outer stator legs and a 2:1 slot/ring ratio, Fig. 7-1C. This configuration improved the lift by 66% at large gaps and 50% at small gaps in comparison to the baseline magnetic bearing, Fig. 7-2C. The actual magnet volume for configuration "C" is 93% of configuration "A". At a 10-mil gap, this bearing supports 94 pounds, a 40% improvement. Some small saturation effects are still observed at gaps near 0.010 inch. The transverse spring constant was measured for configurations "B" and "C" and was found to be the same for 3:1 and 2:1 slot-to-fringe-ring ratios.

An experiment was also conducted where all the magnet material was placed in the inner stator leg with a 2:1 ratio of slot-to-fringe ring width, Fig. 7-1D. This configuration had a lifting capability at large gaps which was only slightly greater than the baseline configuration "A" and a lifting capability at small gaps below the baseline units, Fig. 7-2D. This bearing supports 60 pounds at ten mils; a 10% reduction. The decrease in lift of configuration "D" is probably due to a larger leakage flux circulating in the stator. The leakage flux appears to increase as the gap decreases causing a shunting effect which limits the bearing force to 60 pounds.

From these measurements it is evident that locating the $SmCo_5$ magnets adjacent to the gap in each leg of the stator results in the most efficient use of the magnet volume and the greatest bearing lift force. In addition, reducing the slot-to-fringe-ring-width ratio from 3:1 to 2:1 decreases the gap reluctance and increases the lift by 40% with the same magnet volume and bearing gap. Based on these tests, configuration "C" was selected as the design approach for the advanced magnetic bearing element.

7.1.2 Sizing of a 20-kWh Composite Flywheel Rotor

A synthetic design for a 20-kWh advanced composite rotor was sized in order that the full-scale residential flywheel system design layout could be updated. The objective of the work was to determine the total suspended weight for the 20-kWh storage unit and to use this information as an input into a subsequent study as to whether the number of bearing elements in the magnetic bearing system might be reduced from the six-element design originally evaluated for manufacturing costs by three industrial manufacturers. Attention was directed at the design of a two-element magnetic bearing, since a reduction in the number of magnetic elements would translate into a lower parts count and a reduced cost for the bearing unit.

The philosophy adopted in the sizing study was to evaluate the level of available technology as of February 1981 as demonstrated by spin tests of actual rotors and to base the synthetic flywheel system on these results. It should be realized that this represents a snapshot in time of the technology and that any significant changes that may have occurred since that date should be incorporated in any future design.

The test performance of filamentary composite rotors has shown a trend of increasing performance with time as measured by the stored energy density in watt hours per kilogram (the energy density in Wh/lb, divided by 2.2). In initial development tests, the rotors failed as stress levels substantially below the design stress. As experience was gained in successive fabrication and test cycles, the stored energy density rose and, as of February 1981, stored energy densities at failure of 75 watt hours per kilogram (Wh/kg) had been obtained, with the largest rotors tested to date storing less than 2 kWh of energy. Assuming a safety factor of two in operating stress below the failure stress, the energy density will also be decreased by a factor of two. Thus 34 Wh/kg or 17 Wh/lb was used for rotor sizing purposes as of February 1981.

The Department of Energy is sponsoring the development of a variety of composite flywheel rotor designs. Two of the designs that had achieved 75 Wh/kg at failure were selected for more detailed examination to determine

what physical size and weight these rotors might have when their designs were extrapolated to 20-kWh capacity. One rotor design that was considered was a filament-wound, epoxy-impregnated rim rotor with inside-to-outside-radius ratio of $R_i/R_o = 0.8$. William Brobeck Associates[7-1] has constructed such rotors using a Kevlar outer ring over a fiberglass inner ring with constant tension spokes connecting the rim to a hub. The second rotor design selected was that of AVCO[7-2] which utilizes a thick cylinder of epoxy-impregnated fiberglass where the radial and circumferential fiber density is adjusted to achieve the optimum radial stress distribution and tensile modulus. AVCO states that their design offers the potential for low-cost fabrication and the most efficient use of the swept volume in terms of kWh/ft^3.

Information listed in Table 7-1 was available for Brobeck and AVCO rotor designs for smaller units with storage capacities of 6.3 kWh and 5.3 kWh, respectively, at a spin speed of 15,000 rpm. Because the AVCO rotor required the least design extrapolation and because it had an operating energy density equal to the projected state-of-the-art value as of February 1981, it was selected for scaling to 20-kWh size. This was accomplished simply by increasing the height from 5 to 19 inches while maintaining other design parameters constant. The characteristics for the synthetic rotor based on the AVCO design are listed in Table 7-1. The moment of inertia ratio, $I_{polar}/I_{diameter}$, for the synthetic rotor is 1.2 which satisfies the requirement for pendulum rotor suspension stability. The synthetic rotor of 20-kWh capacity has a projected diameter of 36 inches, a height of 19 inches and weighs 1180 pounds.

TABLE 7-1

COMPOSITE ROTOR CHARACTERISTICS

	Brobeck (6.3 kWh)	AVCO (5.3 kWh)	Synthetic (20 kWh)	Units
$2R_o$	32.6	35.5	35.5	inches
$2R_i$	26.7	12.0	12.0	inches
R_m	14.9	13.6	13.6	inches
h	12.0	5.0	19.0	inches
h/R_m	1.2	0.4	1.4	--
I_p/I_d	1.4	1.9	1.2	--
wR_o	2130	2320	2320	ft/sec
N	15	15	15	krpm
e	26	17	17	wH/lb
E	6.3	5.3	20	kWh
W*	244	315	1180	lbs

*The rotor weight without hub.

Symbol definitions:

R_o = rotor outside radius

V_1 = rotor inside radius

R_m = mean rotor radius

h = vertical height of rotor

I_p = polar mement of inertia

I_d = diametral moment of inertia

wR_o = rotor surface speed

N = rotor speed, thousands of revolutions per minute

e = rotor unit energy density

E = maximum stored energy

W = rotor weight

Mounting the rotor in an energy storage unit requires the addition of a mounting hub and the shaft assembly of motor-generator and magnetic bearing rotors. The hub and shaft assembly weights must be added to the rotor weight in Table 7-1 to arrive at the total weight to be supported by the magnetic bearings. The total suspended weight for the synthetic flywheel system is tabulated in Table 7-2 and is 1480 pounds. The total weight is calculated on the basis that the hub weight is 4% of the rotor weight and that the shaft assembly weight is 20% of the complete rotor weight. The assumption for hub weight is based on AVCO's rotor design while the assumption for shaft assembly weight is based on Lincoln Laboratory's experience with the 1/10-scale prototype flywheel system. Had the Brobeck wheel been selected for extrapolation to 20-kWh size, a hub weight of 25% of the rotor weight would have been used. Any improvements in stored energy density at failure above the assumed 75 Wh/kg would proportionally decrease the suspended weight of the 20-kWh rotor system.

TABLE 7-2

SUSPENDED WEIGHT TOTAL FOR 20-kWh STORAGE

Synthetic rotor weight	1180 lb
Hub weight addition ratio	1.04
Complete rotor	1230 lb
Suspension addition ratio	1.2
Complete energy storage rotating weight	1480 lb
Rotor swept volume	11 ft^3
Assembly energy density	13.5 Wh/lb
Rotor volumetric energy density	1.8 Wh/lb^3

7.1.3 Design for a 10-inch-diameter, 750-pound Lift, Magnetic-bearing Element

The design of a two-element magnetic bearing for the 20-kWh inertial energy storage system was undertaken using the improved magnetic bearing design procedure discussed in Section 4.4.4. The weight of the suspended shaft assembly and rotor was taken as 1500 pounds (862 kg), Section 7.1.2,

which can be supported with two magnetic bearings of 750 pounds (341 kg) lift each. The operating bearing gap was chosen to minimize the volume of permanent magnet required and to be large enough so that at an extreme gimbal rotation of the bearing shaft (around a cross axis approximately midway between the bearings) of 10^{-3} radians, the change in gap at the outer diameter of the magnetic bearing is less than 20%. For a bearing radius of 5 inches, this requires the operating gap to be g = 0.025 inch.

The magnetic bearing geometry shown in Fig. 7-3 will support a load of 750 pounds and was designed with A_m/A_g = 1.3, B_m = 0.49 tesla, F/A_g = 20 psi, C = 161, B_g inner gap = 0.6 tesla, B_g outer gap = 0.62 tesla. A_g inner = 18.9 $in.^2$, and A_g outer = 17.8 in^2. Using the gap areas given above and the average gap fields in equation 1, Section 4.4.4, F was actually calculated to be 393 lb for the inner and outer gaps, respectively, making a total lift of 782 pounds. This design provides a margin of 32 pounds over the design load of 750 pounds. Continuing the computations with the first term in equation 3, the required magnetic magnetomotive force, $H_m L_m$, is found to be 546 amperes and 605 amperes for the inner and outer gaps, respectively. The second term of equation 3 is evaluated with the dimensions of the iron circuit shown in Fig. 7-3 for f_r = 2000 and B_i = 0.4 tesla and is equal to 30 amperes. This is divided equally between the two gaps, making the maximum mmf = 620 amp (the minimum is 561 amp). H_m for $SmCo_5$ at 0.49 tesla is 2.7×10^5 amp/m which results in a required magnet thickness of 0.23 cm or 0.092 inch. To be conservative, an actual thickness of 0.100 inch is specified for each inner and outer magnet location. In equation 2, A_m is the actual magnet area required; however, the magnet pole area is made 10% larger to allow for the magnet area filling factor.

The axial force spring constant is estimated from the difference in lift force per unit of gap increase (or decrease). For a small gap difference the change in the gap force is approximately proportional to the square root of the initial and final gap ratio. At 0.025-inch gap the axial spring constant for this bearing is estimated to be 16,000 lb/inch.

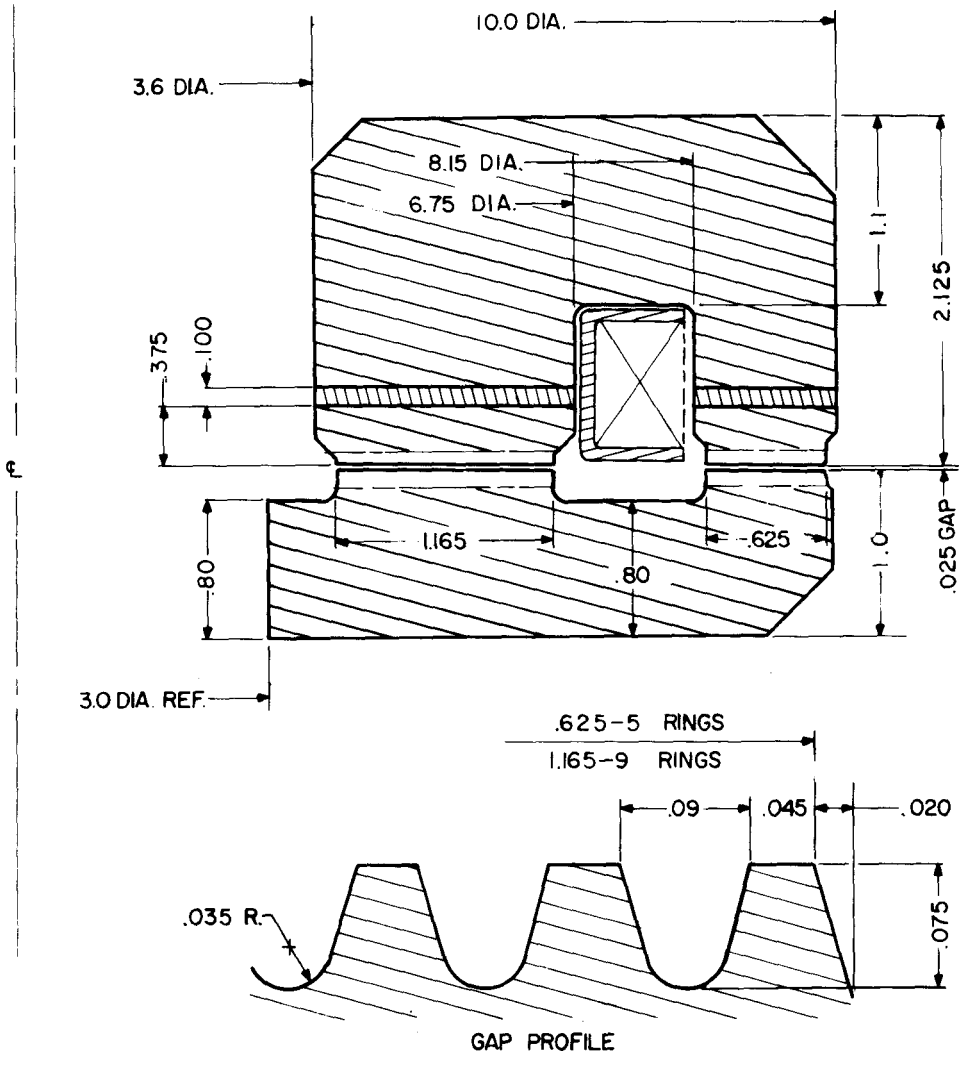

Figure 7-3. 10-inch-diameter, 750-pound lift, magnetic bearing.

The transverse restoring force which arises when the stator and rotor are displaced is more difficult to estimate from simple analytical relationships, because it results from the difference in magnetic pressure across a fringe ring due to the displacement. A figure for the transverse restoring force can be derived from past experience with a similar gap geometry where the axial to transverse forces was found to be 8 to 1. The transverse force per unit displacement is constant for a given geometry and fixed gap up to about 40% fringe-ring-width displacement and is estimated to be 2000 lb/in.

7.1.4 20-kWh, 6-kW Residential Design With a Two-Element Magnetic Bearing

The features of the full-scale, 20-kWh residential flywheel storage system employing a magnetic bearing with two magnetic-bearing elements which supports a rotor system weight of 1500 pounds are shown in Fig. 7-4. The overall height of the flywheel unit including the vacuum tank and support arms is four feet, 8 inches and the overall width is 3 feet, 10 inches. The motor-generator has been placed at the top of the system for easy access and a telescoped quill has been employed to reduce the overall height. Both features were originally used in the 40-kWh design, Fig. 4-1. New elements in Fig. 7-4 include the use of a cylindrical casting to support the two magnetic-bearing elements and a welded vacuum enclosure constructed from low-cost, standard metal tank ends and cylindrical sections.

7.2 Residential Flywheel Storage System Simulation

7.2.1 Introduction

A digital simulation of the operation of a dedicated, on-site flywheel storage system in conjunction with a residential solar photovoltaic (PV) power system was conducted to determine the appropriate storage capacity of the flywheel system. The overall system was of the utility-interactive type and includes the following features: a) the flywheel storage system supplies the residential electrical loads whenever possible, b) electrical power is purchased from the utility whenever the flywheel cannot supply the load, c) excess power from the residential PV array is sold to the utility, d) the flywheel operates anywhere in the region between a minimum storage capacity of 25% and full-storage capacity (110%).

Realism was achieved in the simulation by using actual electrical load data from a monitored, lived-in residence, actual electrical output data taken on a full-size residential PV array (recorded simultaneously with the residential electrical load data) and flywheel system and component efficiencies as measured in the 1/10-scale prototype system tests. The residential load and PV array electrical output data were generated at Lincoln Laboratory as

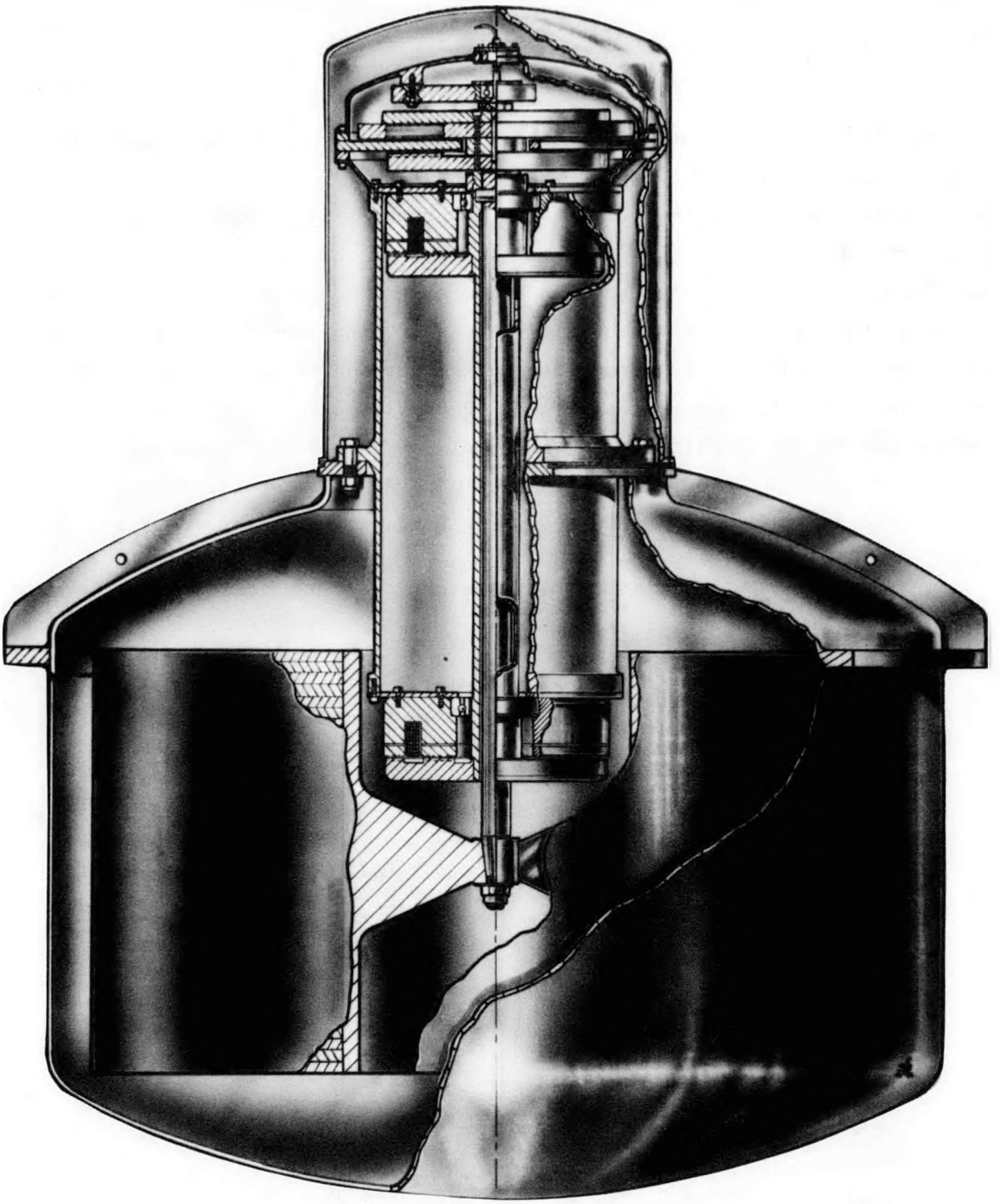

Figure 7-4. 20-kWh flywheel energy storage unit.

part of DOE-sponsored work on residential PV systems, particularly the Northeast Residential Experiment Station (NE RES),[7-3] where five complete full-scale prototype residential PV systems were constructed and are being tested.

7.2.2 Description of the Simulation

The simulation used actual electrical load and PV array data taken on a six-minute basis during a 38-day period in May-June 1981. Energy-flow possibilities in the system are illustrated graphically in Fig. 7-5. Energy from the PV array may flow directly through the inverter to the house load (Path 1), or to the flywheel and hence to the house load (Path 2, plus 6), or through the inverter to the utility (Path 3). The same inverter would be used to process the dc array power for subsequent supply to the house load (Path 1) or for sell-back to the utility (Path 3). Electricity purchased from the utility is supplied to the flywheel along Path 5 or to the total load (house load plus magnetic-bearing suspension power requirements) along Path 7. The energy losses accompanying the transfer of energy in each of the possible Paths are noted on Fig. 7-5 also. The assumptions underlying the simulation are expanded in Table 7-3.

C74-1746

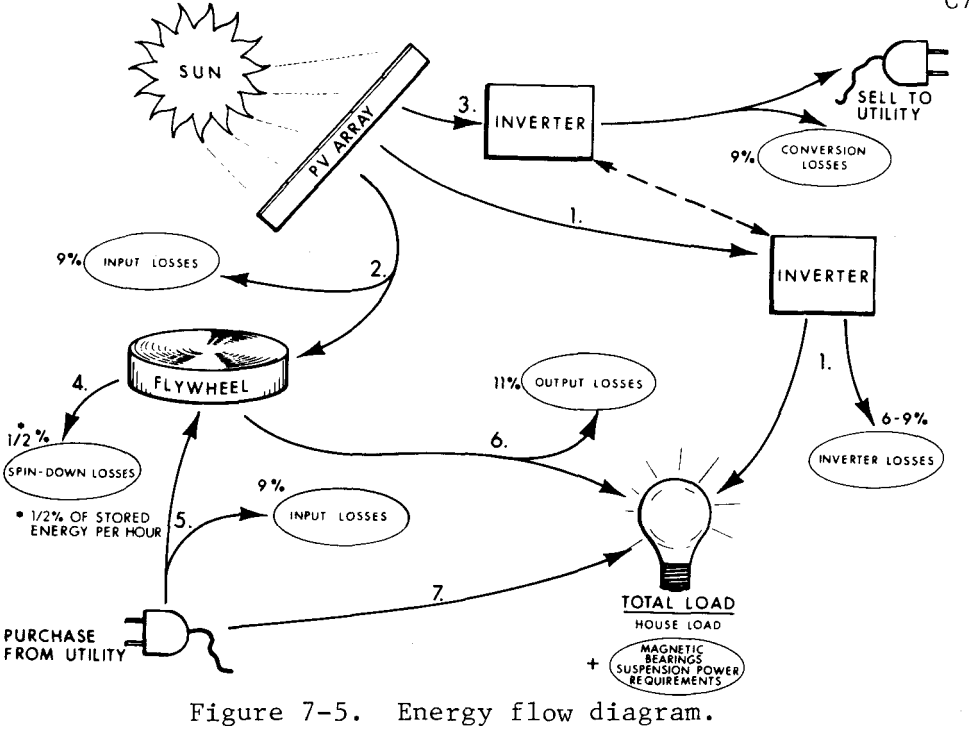

Figure 7-5. Energy flow diagram.

TABLE 7-3

PV/FLYWHEEL RESIDENTIAL SYSTEM SIMULATION ASSUMPTIONS

(Numbers refer to the energy flow diagram.)

1. The preferred energy path is from the array, through the inverter, to the load. The inverter efficiency varies linearly from 90.8% at 0-kW input, to 94.1% at 6-kW input.
2. If there is a surplus of array energy, beyond what must be sent to the inverter to meet the load, it can be stored in the flywheel or sold. The preferred choice is to store it. The efficiency of the converter from dc power to rotational energy is 91%.
3. If there is a surplus, and the flywheel is at maximum capacity, the surplus is sold. The conversion from dc to ac is assumed to be 91%.
4. The flywheel is constantly losing energy, due to friction. 0.5% of the stored energy is lost each hour. For the purposes of the simulation, this comes to .05% every six minutes.
5. The flywheel is not permitted to spin down below one-fourth of its maximum capacity. If friction losses would cause it to do so, and if the array is not providing a surplus to prevent this, power is bought from the utility to make up for the friction losses.
6. If the house load cannot be met entirely by the array power coming directly through the inverter, the difference can be made up by the flywheel or the utility. The preferred choice is to take energy from the flywheel. The efficiency of the conversion from rotational energy to ac power is 89%.
7. If there is a demand for energy caused by the load being greater than the output of the inverter, and the flywheel is bottomed out at its minimum energy, the difference is made up by a purchase from the utility.
8. The total load consists of measured house-load data plus a constant four watts for the magnetic bearings.

7.2.3 Simulation Results

A continuous, 38-day period in May-June 1981 was modeled for the utility-interactive flywheel system. Electrical load data from monitored house #6 was used in the simulation. The monitored house was a single-family

detached residence located in Concord, Massachusetts, with a family of four living in the house. One adult works during the daytime hours. The house is heated by oil with domestic hot water also provided by oil. Cooking and clothes drying is by electricity. The house is also equipped with an electric window air conditioner. PV array electrical output data from the TriSolarCorp prototype located at the NE RES were also used in the simulation. The Tri-SolarCorp prototype became operational in December 1980 and is designed to supply 4.8 kWp at operating conditions. The system has a PV array of 48' x 10.7', mounted at 45-degree tilt angle. Applied Solar Energy Corporation modules are used in the array.

7.2.3.1 20-kWh Flywheel System

A sample of flywheel system operation during the first two days of the 38-day simulation sequence is reproduced in Figs. 7-6 and 7-7, respectively, for a 20-kWh flywheel system. From midnight to 6 a.m. on Day 1, the flywheel energy storage level is drawn down to meet the electrical load demand. Between 6 a.m. and 12:30 p.m., the flywheel is at its minimum energy storage level and cannot supply the electrical demand. During this period, it is necessary to purchase power from the utility. From 12:30 p.m. to 5 p.m., the output of the PV array is sufficiently high to supply the electrical loads of the residence and to provide a surplus of energy for storage in the flywheel. The flywheel and the array jointly supply the electrical loads between 5 p.m. and 6:30 p.m. The flywheel system alone provides the total electrical power from sunset at 6:30 p.m. to midnight of Day 1. No power is purchased from the utility between 12:30 p.m. and midnight of Day 1.

On the second day, power is purchased from the utility from midnight to 7 a.m. After 7 a.m., the PV array powers the residence and accelerates the flywheel to its maximum energy storage level by 2 p.m. The flywheel, along with the array, services the house load from 5 p.m. to 7 p.m. From 7 p.m. to midnight, the load is supplied entirely by the flywheel.

C74-1733

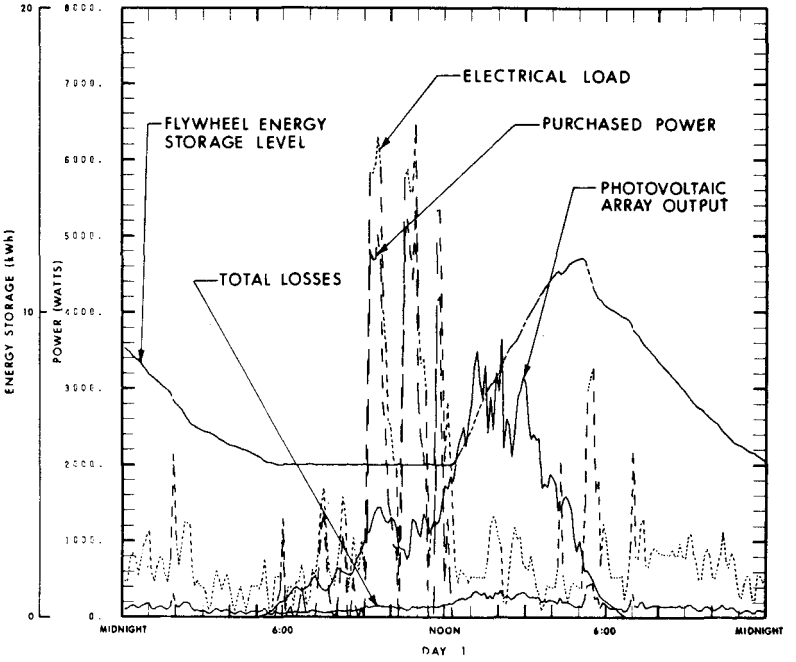

Figure 7-6. Flywheel storage system operation - Day 1.

C74-1767

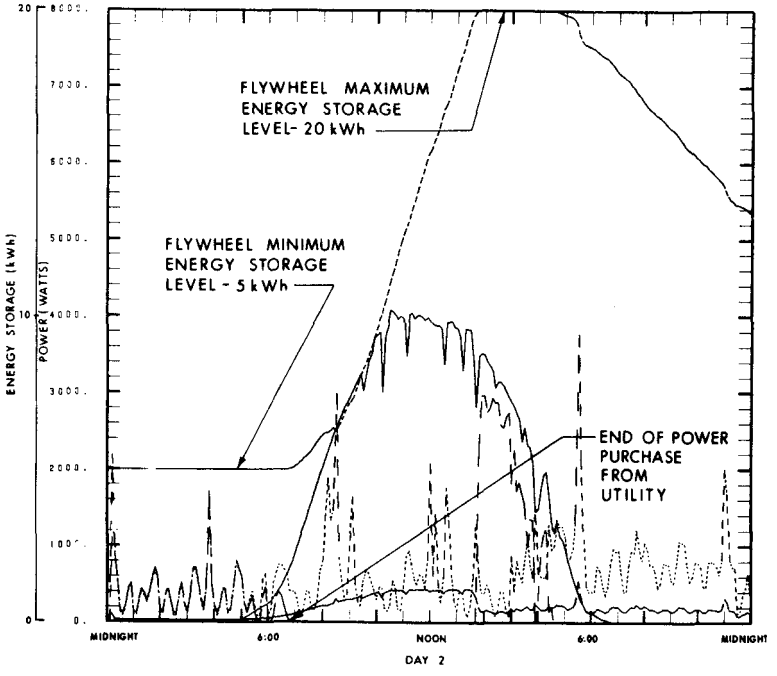

Figure 7-7. Flywheel storage system operation - Day 2.

The total energy flows over the 38-day period for the 20-kWh utility-interactive flywheel system are shown in Fig. 7-8 and a summary printout is presented in Fig. 7-9. The daily average time history (over the 38-day simulation period) for the electrical load, array power flywheel storage capacity, purchased power and sold power are provided in Figs. 7-10 through Fig 7-14. Figure 7-15 illustrates the residential load demand that must be supplied by the utility for three cases: a) the present demand of monitored house #6, b) the demand after installation of an on-site PV system (4.8 kW max), c) the demand after installation of both a PV array and a 20-kWh flywheel energy storage unit.

C74-1732

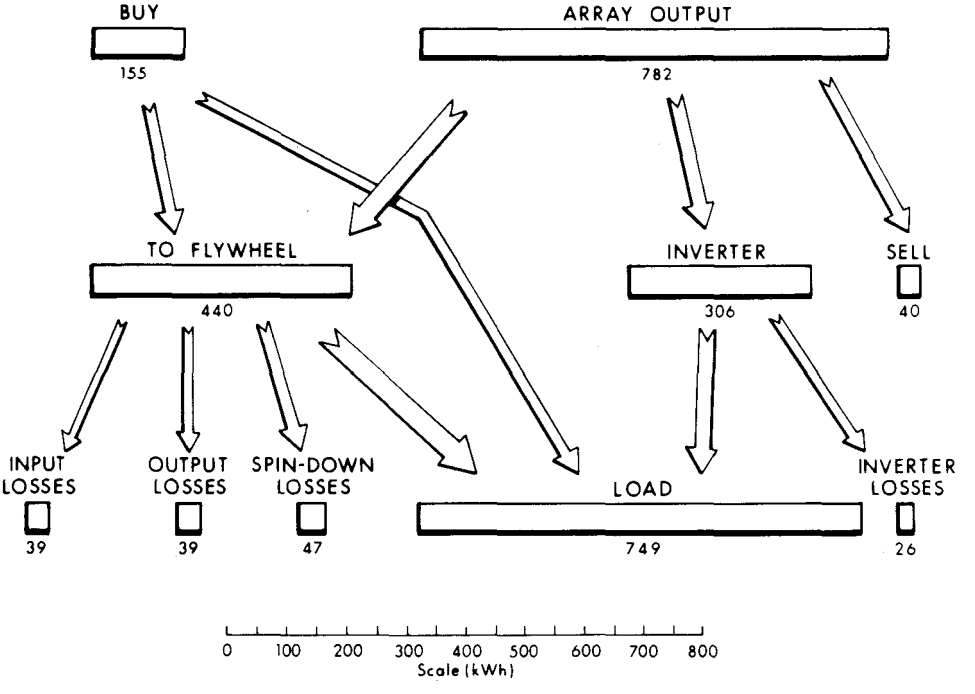

Figure 7-8. Total energy flows over 38-day period, 20-kWh flywheel system.

C74-1722

MAXIMUM STORED ENERGY: 20000. WATT HOURS

DAY	ARRAY	LOAD	BUY	SELL	E-AVG	E-FINAL	DIRECT	FLYWHEEL	FRICTION	INV-LOSS	OUT-LOSS	% ACTIVE
1	17195.	26804.	9357.	0.	7012.	5130.	9192.	8116.	845.	797.	1133.	79.
2	30572.	15167.	2449.	5161.	12207.	13401.	8045.	17529.	1464.	697.	684.	63.
3	9160.	15949.	1492.	0.	10011.	5000.	6394.	2826.	1208.	566.	1074.	91.
4	10712.	30325.	21588.	0.	5501.	5000.	7179.	3980.	662.	629.	326.	32.
5	21855.	14977.	4364.	0.	10647.	12375.	6404.	15657.	1277.	565.	616.	67.
6	28822.	14729.	0.	8435.	14858.	13413.	7142.	13245.	1787.	624.	1015.	82.
7	28497.	23231.	415.	0.	13071.	13518.	11490.	17013.	1572.	954.	1518.	99.
8	9220.	14506.	0.	0.	10092.	5040.	5723.	3497.	1218.	509.	1148.	100.
9	18410.	23385.	8268.	0.	6685.	5000.	9111.	9627.	804.	783.	880.	49.
10	7369.	15234.	9473.	0.	5338.	5000.	4459.	3362.	642.	397.	266.	29.
11	30537.	14346.	3012.	5832.	12470.	14046.	7238.	17627.	1495.	637.	605.	60.
12	27418.	18378.	0.	4945.	14930.	13176.	9474.	13000.	1796.	799.	1199.	88.
13	16072.	21682.	1545.	0.	10158.	5000.	8910.	7222.	1226.	747.	1487.	91.
14	22336.	16206.	5687.	33.	11470.	12681.	5419.	17088.	1376.	474.	714.	68.
15	22633.	20697.	0.	0.	12486.	9570.	8733.	13900.	1503.	724.	1568.	100.
16	26540.	15920.	0.	3185.	12574.	12228.	7038.	16316.	1511.	621.	1175.	91.
17	26351.	22889.	0.	0.	11855.	10670.	13106.	13244.	1427.	1060.	1340.	100.
18	26502.	28996.	1854.	0.	8809.	5000.	14485.	12080.	1062.	1163.	1716.	90.
19	27952.	18617.	2715.	0.	11453.	12368.	10031.	18084.	1374.	831.	848.	74.
20	24009.	17657.	0.	3613.	14110.	10258.	7534.	12862.	1698.	660.	1333.	90.
21	21875.	21708.	0.	0.	9355.	5807.	9785.	12090.	1127.	825.	1576.	100.
22	23458.	19371.	2844.	0.	10482.	8126.	7297.	16315.	1260.	643.	1239.	75.
23	23441.	20410.	333.	0.	9509.	6856.	9352.	14109.	1144.	793.	1426.	95.
24	10195.	21793.	11857.	0.	5618.	5000.	6711.	3771.	677.	591.	507.	53.
25	21352.	31668.	14203.	0.	7452.	5000.	9707.	11941.	896.	819.	1097.	53.
26	12326.	22648.	12844.	0.	6525.	5000.	5703.	6954.	785.	501.	610.	49.
27	25675.	18705.	2293.	126.	10609.	9429.	8015.	17692.	1274.	698.	1144.	73.
28	10533.	12944.	775.	0.	8207.	5000.	5784.	4785.	989.	515.	857.	95.
29	12799.	13585.	3436.	0.	6969.	5000.	5620.	7388.	838.	498.	647.	66.
30	23664.	22932.	4083.	0.	9729.	5000.	7479.	16383.	1170.	658.	1511.	68.
31	13393.	33083.	22016.	0.	5453.	5000.	8409.	5403.	656.	715.	469.	34.
32	26376.	15383.	3601.	2047.	11681.	13278.	7056.	17453.	1401.	614.	682.	66.
33	12840.	15430.	0.	0.	9866.	7057.	5457.	7382.	1190.	484.	1292.	100.
34	26182.	14707.	766.	2086.	11940.	12645.	6708.	17426.	1433.	592.	972.	87.
35	23169.	12654.	0.	4519.	15057.	14248.	5802.	12848.	1810.	514.	911.	86.
36	22473.	18791.	0.	151.	14423.	12724.	8626.	13696.	1736.	738.	1348.	98.
37	26569.	25806.	0.	0.	11660.	8243.	14157.	12411.	1405.	1140.	1581.	100.
38	13584.	17822.	3957.	0.	6907.	5000.	7300.	6438.	832.	638.	910.	76.
TOTALS:												
	782066.	749133.	155227.	40132.	10189.	5000.	306074.	440759.	46571.	26213.	39421.	77.

Figure 7-9. Summary printout - 20-kWh system.

C74-1726

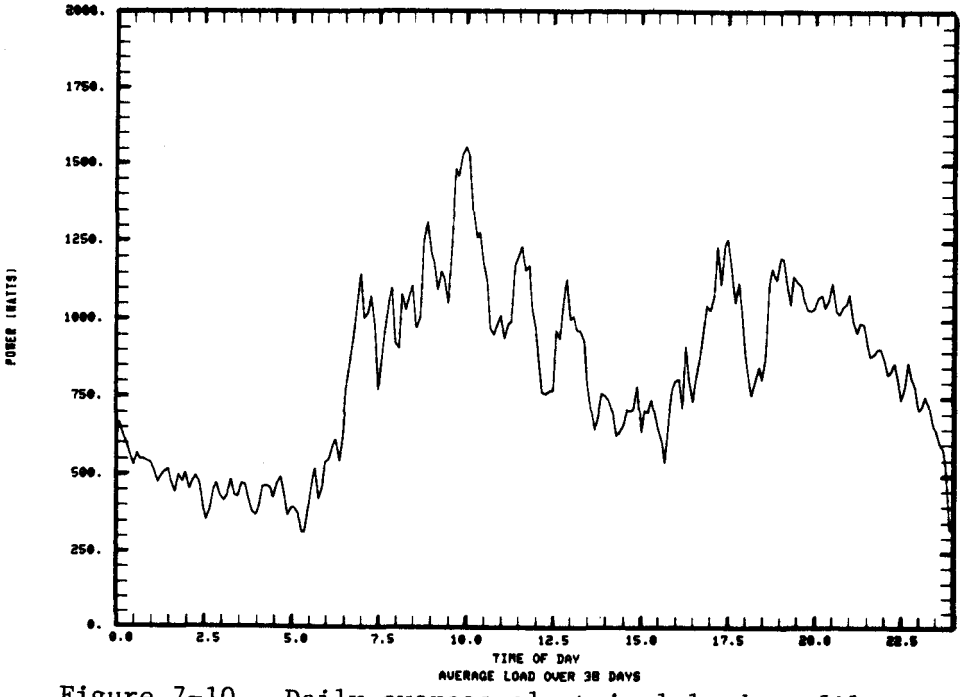

Figure 7-10. Daily average electrical load profile.

C74-1723

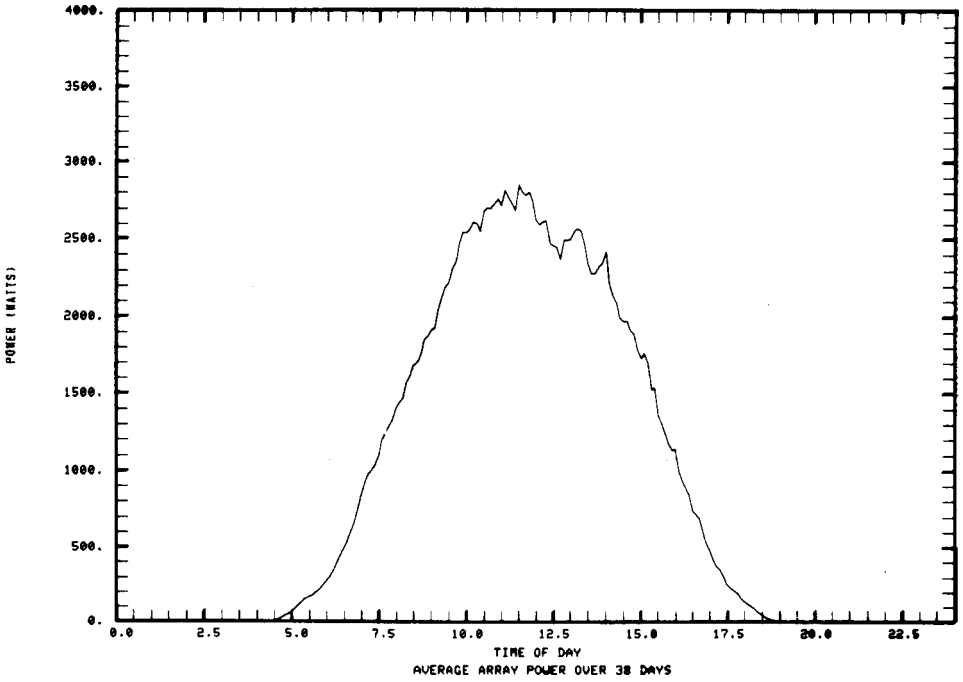

Figure 7-11. PV array power profile.

C74-1738

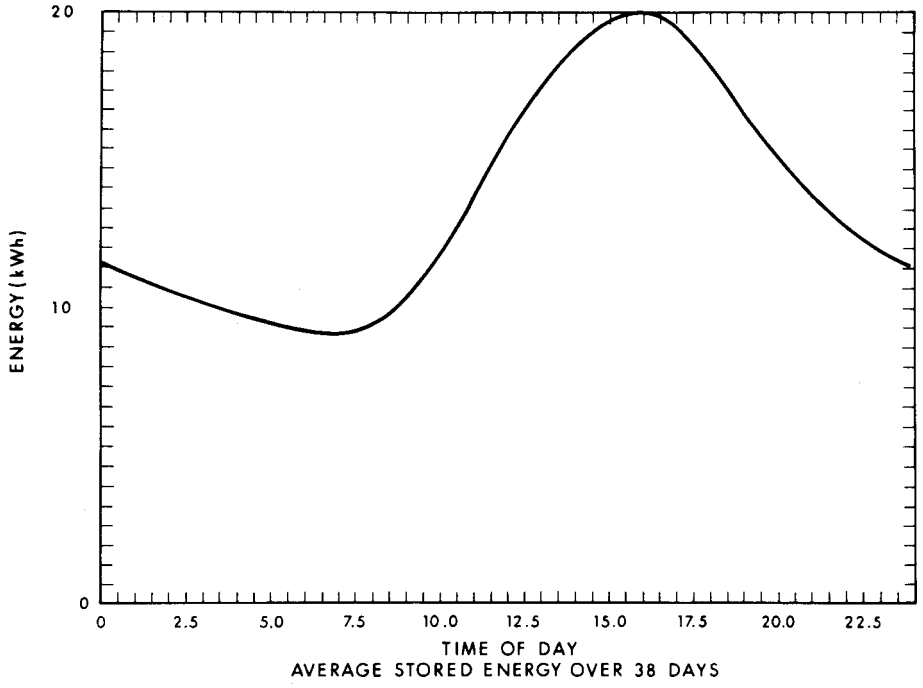

Figure 7-12. Stored energy profile - 20-kWh flywheel.

C74-1724

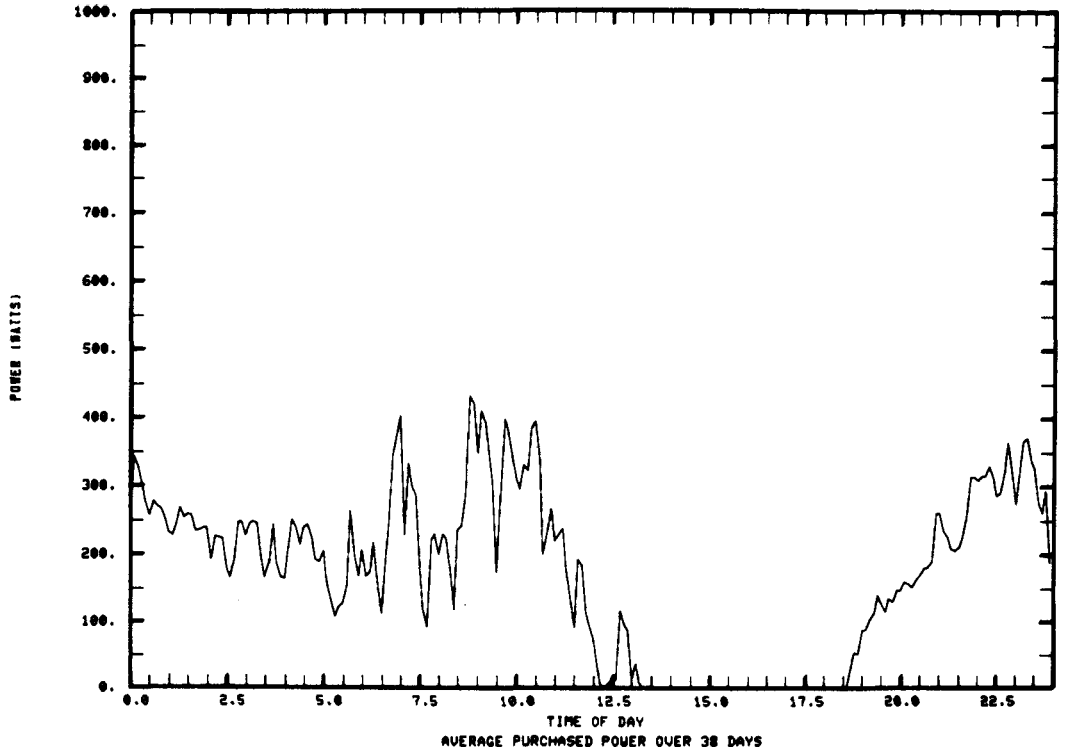

Figure 7-13. Purchased power profile - 20-kWh flywheel.

C74-1725

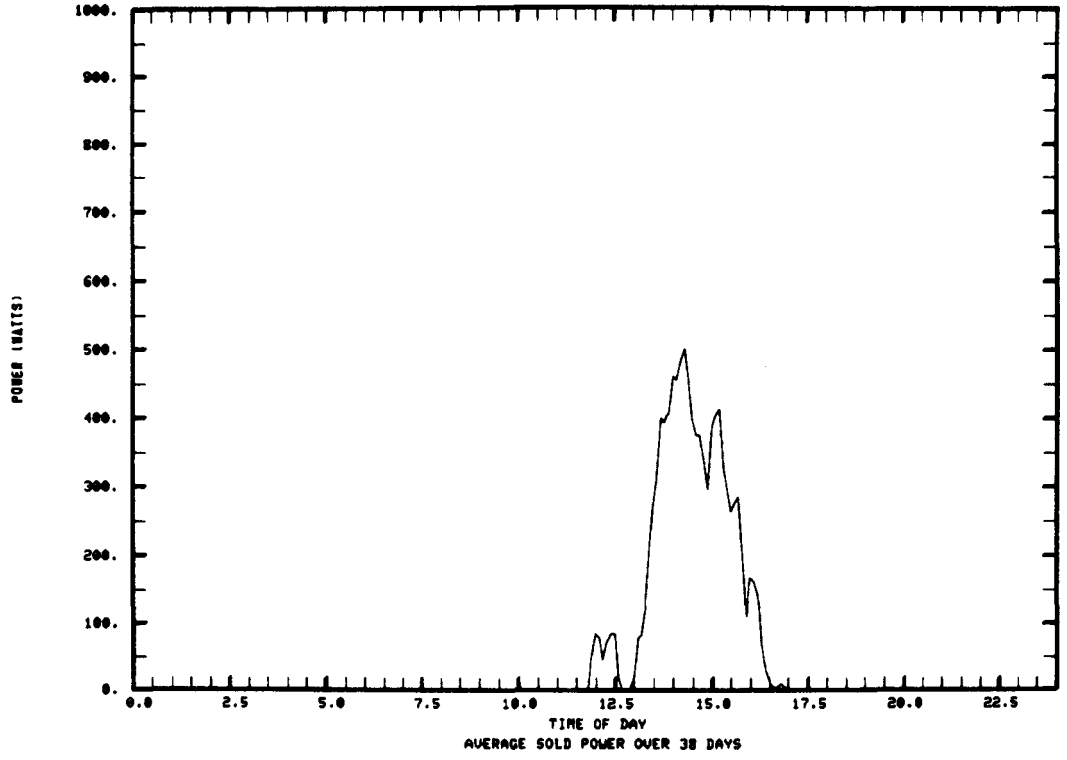

Figure 7-14. Sold power profile - 20-kWh flywheel.

C74-1739

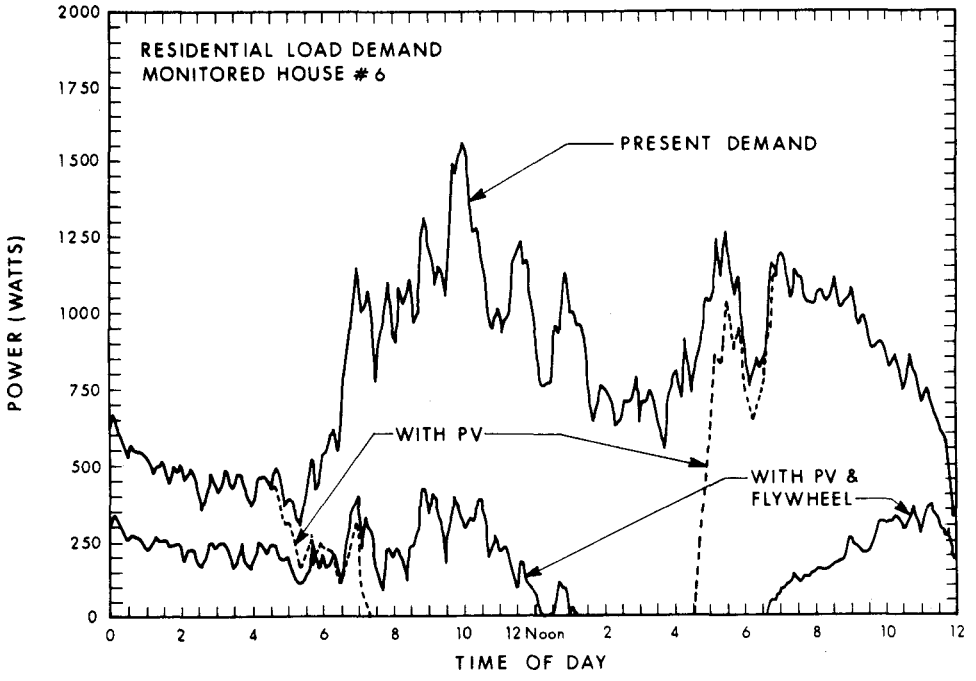

Figure 7-15. Residential load demand from utility - with and without 20-kWh flywheel energy storage system.

Some pertinent simulation results are tabulated in Table 7-4. Flywheel utilization, defined as the percentage of time the flywheel system is usefully operating (not at a minimum or maximum energy storage state), is 77% for the present case. Overall system efficiency is 80%, where overall efficiency is defined as the ratio of the kWh provided to the load to the sum of the PV array output and the purchased power, expressed as a percent. On the average, the flywheel operates at its mid-energy storage capacity, actually 51%. System losses, purchased power and power sold to the utility are 20%, 21% and 5.4%, respectively, of the residential load.

TABLE 7-4.

SIMULATION RESULTS - 20-kWh FLYWHEEL

Flywheel utilization (% of time)	77%
Overall system efficiency	80%
Average flywheel energy capacity	51%
Losses*	20%
Purchased power*	21%
Power sold to utility*	5.4%

*As percentage of load.

Some very dramatic changes in the load demand seen by the utility, Fig. 7-15, are possible when the house is equipped with a PV array and a flywheel energy storage system. The maximum demand of the residence at 8:30 p.m. (20.5 hrs), the time of utility system peak demand (see Section 7.2.3.2.), is reduced by a factor of five on the average. Also the average power demand over the day is lowered by about the same factor of five. The ability of the flywheel storage unit to reduce the peak demand of the utility is a significant result worthy of more encompassing investigations.

7.2.3.2 Flywheel Sizing Study

The flywheel simulation program was exercised for the same 38-day period considered above but with maximum flywheel energy capacities ranging from zero to 40 kWh and the results are shown in Fig. 7-16. Both the fraction of time the flywheel is utilized and the overall system efficiency increase as flywheel storage capacity is added to the PV residence. A maximum efficiency of 81% and a maximum utilization time of 82.5% occur at a flywheel capacity of 30 kWh.

The net energy purchased by the solar PV house as a function of flywheel storage capacity and buy-back ratio is shown in Fig. 7-17. At zero buy-back ratio, the addition of 20 kWh of flywheel storage decreases the power purchased by a factor of three. At buy-back ratios of 0.6 to 0.7, net energy

C74-1737

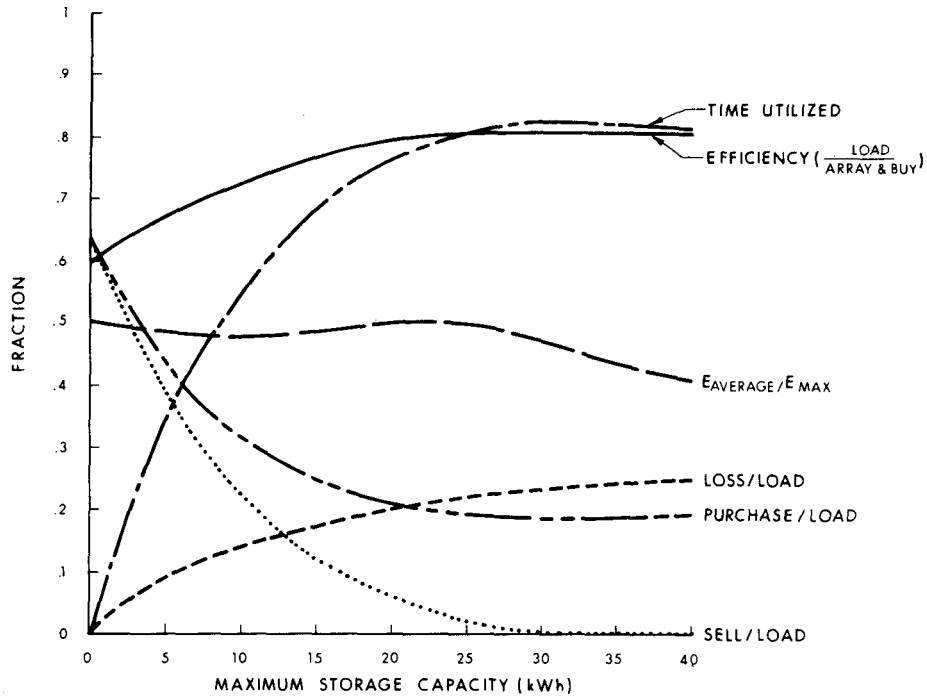

Figure 7-16. Flywheel sizing study.

C74-1736

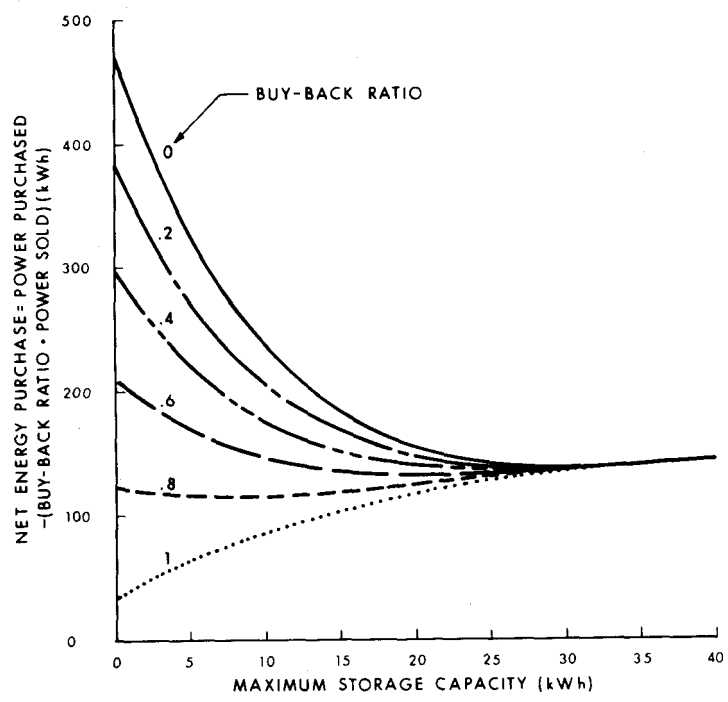

Figure 7-17. Energy purchase vs. storage capacity and buy-back rate.

purchase is not affected by storage capacity. From an approximate point of view, the results shown in Fig. 7-17 indicate that for the present simulation case, flywheel capacities greater than 15 kWh have very little effect on the net energy purchased no matter what buy-back ratio is selected.

7.2.3.3 Peak Demand Reduction

Data from five monitored houses was averaged over a month-long period to determine the daily average load profile for a cluster of houses as seen by the utility. It was assumed that the average load for a cluster of houses would be indicative of the load profile of the utility and that the time of peak demand for the utility could be discerned from such a profile. The average daily load profile for five monitored houses is presented in Fig. 7-18 and peak demand is seen to occur for this data sample at 8:30 p.m. (20.30 hours).

C74-1735

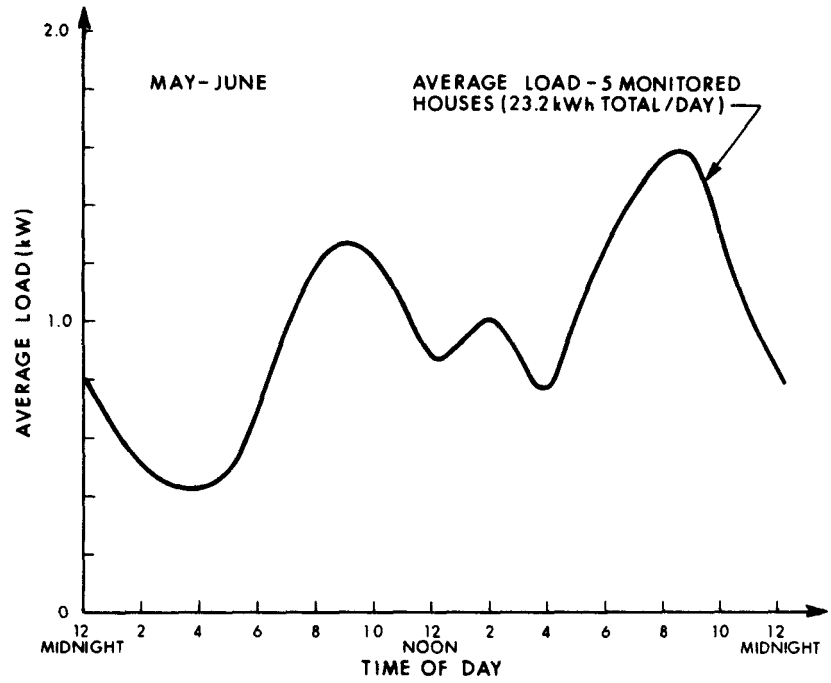

Figure 7-18. Average daily load profile for five monitored houses.

The flywheel simulation program was then exercised for the May-June 38-day period to determine how the reduction in peak demand with a flywheel energy storage system is affected by flywheel capacity. The residential load

demand profiles for flywheel storage capacities of 5, 10, 15, 20, 25 and 30 kWh are shown in Figs. 7-19 through 7-24. The residential peak power demand at 8:30 p.m. (20.30 hours) as a function of storage capacity is shown in Fig. 7-25. For example, the addition of 10 kWh of storage reduces the peak demand (38-day average) to 32% of the no flywheel storage case.

C74-1740

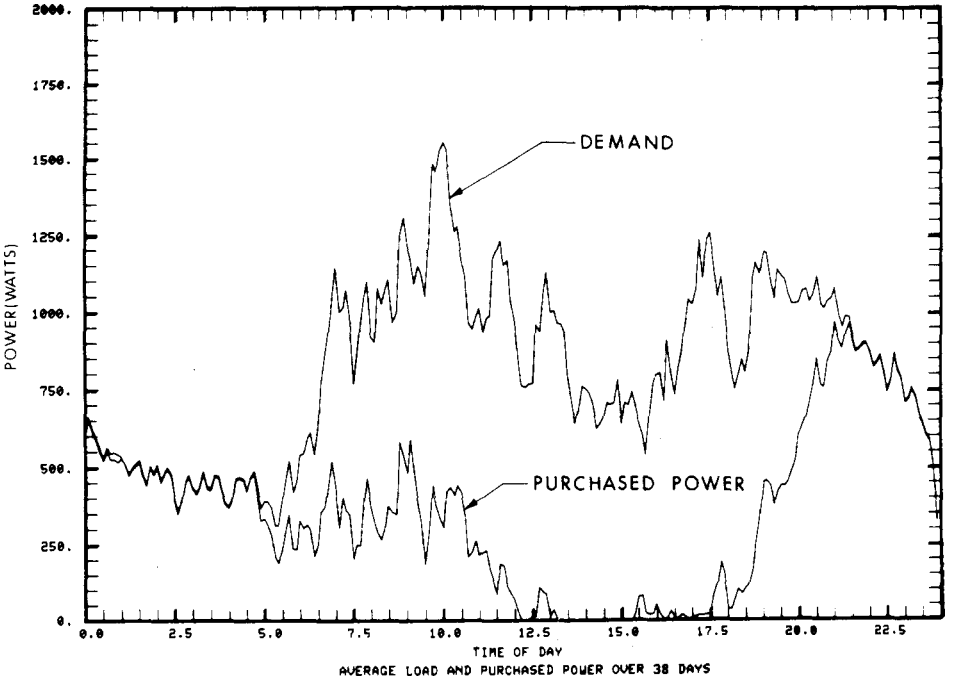

Figure 7-19. Purchased power with 5-kWh flywheel.

C74-1741

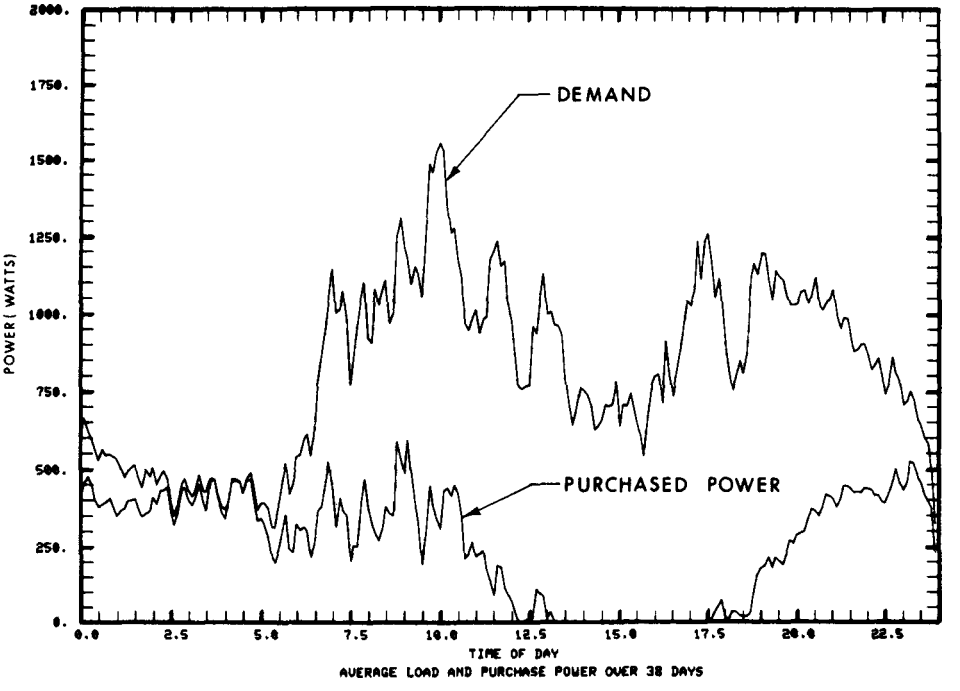

Figure 7-20. Purchased power with 10-kWh flywheel.

C74-1742

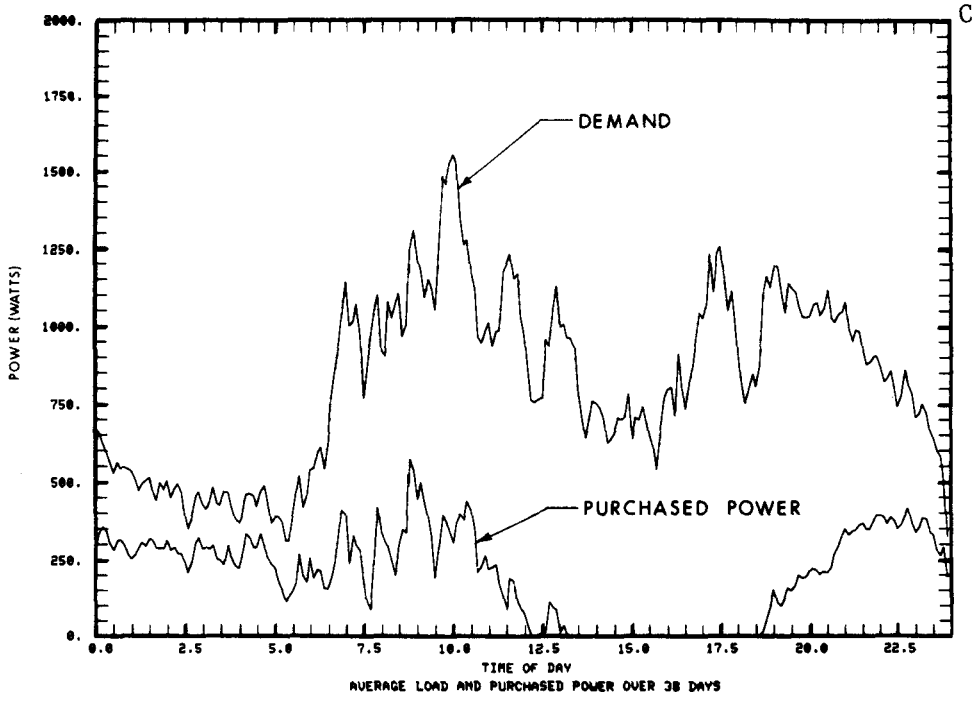

Figure 7-21. Purchased power with 15-kWh flywheel.

C74-1744

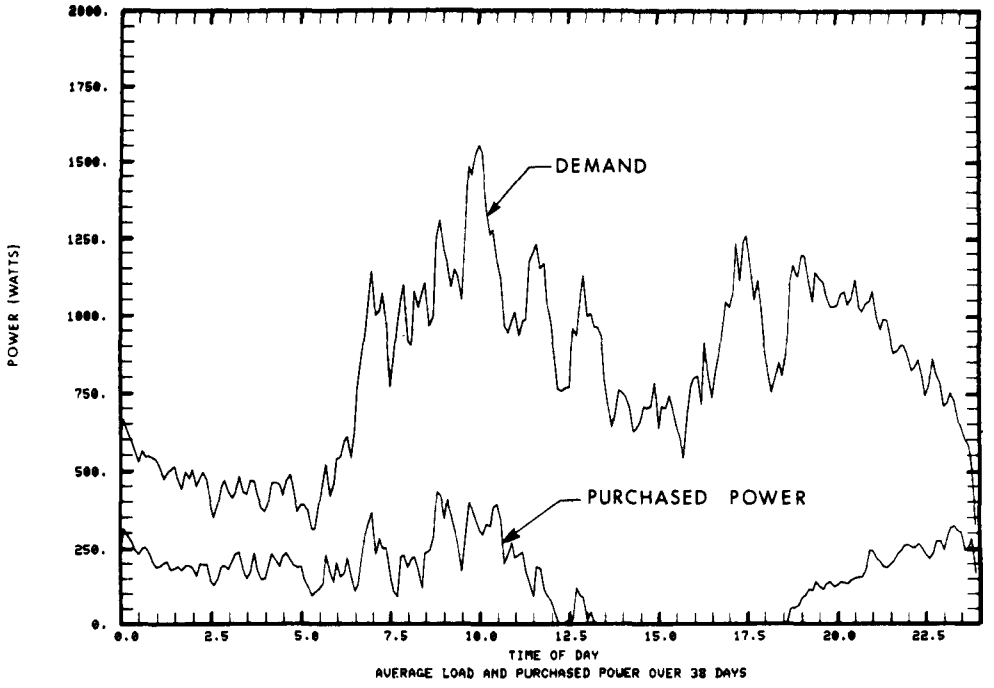

Figure 7-22. Purchased power with 20-kWh flywheel.

C74-1743

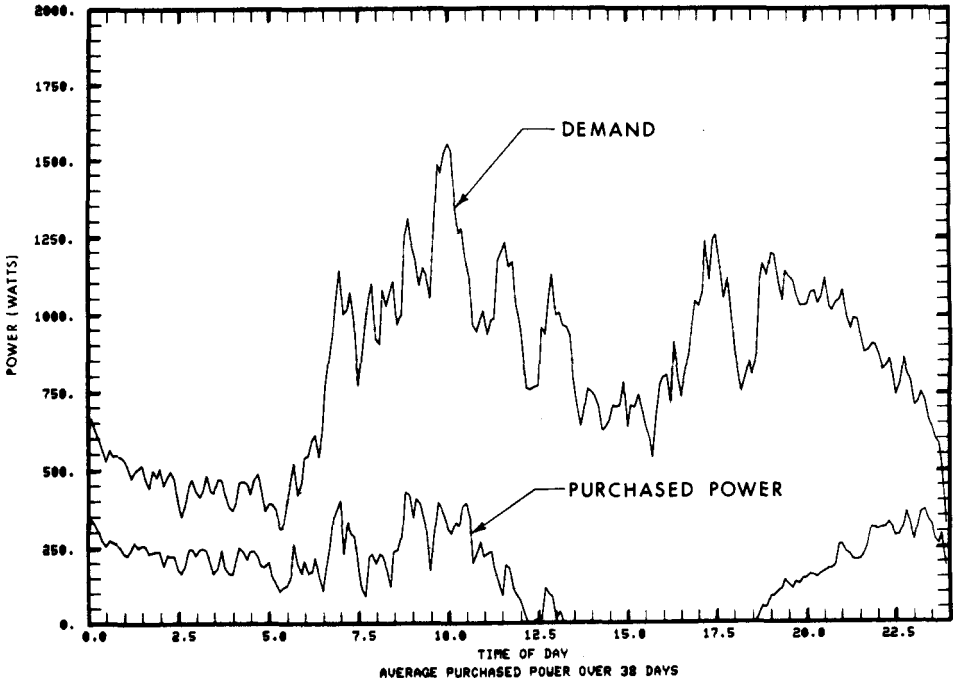

Figure 7-23. Purchased power with 25-kWh flywheel.

C74-1745

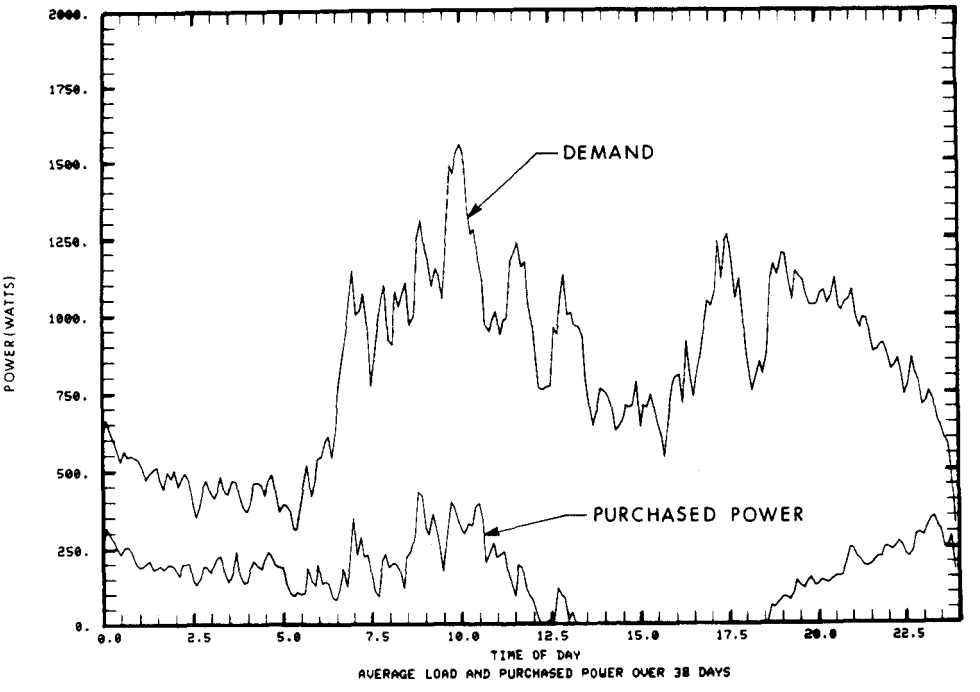

Figure 7-24. Purchased power with 30-kWh flywheel.

C74-1734

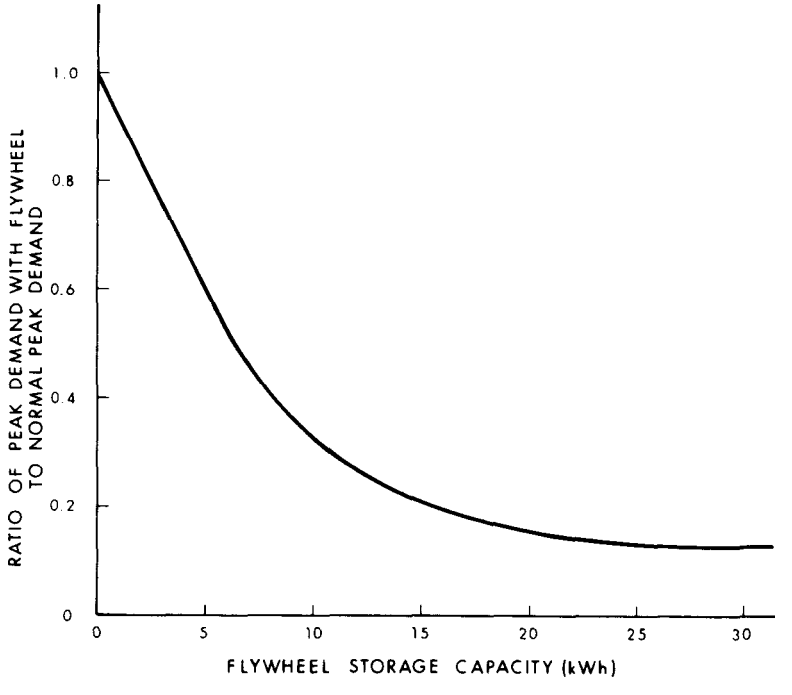

Figure 7-25. Residential peak power demand reduction with flywheel - 8:30 p.m. peak.

7.2.3.4 Comments

The residential flywheel simulation that has been carried out is to our knowledge the very first to use real load data and real PV array data taken on a six-minute basis and experimentally measured flywheel efficiencies. It has provided some interesting results showing that for the combination of monitored house load and PV array size chosen, a flywheel storage capacity of 15 kWh or less is a desirable choice from a technical basis. It also showed that substantial reductions in the peak demand seen by the utility may be realized with flywheel storage. It should be realized that the simulation is quite specific and limited to a small data sample. Also the economics of the flywheel storage system for the case simulated were not considered due to time and monetary constraints. However, it is a particularly promising method that should be exploited further. Simulations should be carried out at different times of the year and the economics of particular applications should be calculated.

7.3 Test of GFE Advanced Composite Rotor on Magnetic Suspension

7.3.1 Introduction

In FY-81, a program to test a GFE advanced composite rotor on magnetic suspension was carried out as part of Lincoln Laboratory's flywheel energy storage program. These tests of an available advanced composite rotor on magnetic suspension were the first such tests known to be done in the United States. The test program was undertaken for two reasons: (1) to determine the effects of the flexibility and structural vibration modes of an advanced composite rotor on the operation of the magnetic bearing axial servo loop and (2) to assess the external damping requirements of an advanced composite rotor (due to internal hysteresis effects) in comparison with those for a steel rotor. The development of low-frequency whirl modes due to internal hysteresis effects in the test of the 1/10-scale prototype steel flywheel system, and their elimination by the addition of external damping, was previously shown to be an important consideration in the design of flywheel systems, Section 4.4.6.

7.3.2 GFE Advanced Composite Rotor

An available advanced composite rotor was provided to Lincoln Laboratory by DOE through Lawrence Livermore Laboratory for the magnetic suspension tests. The rotor was originally designed for a vehicular application, an application differing from its present use as a long-term energy storage device. Its maximum speed and maximum stored energy capacity for the vehicular application are listed as 32,725 RPM and 4.95 kWh, respectively. Two identical rotors of this size were constructed in FY-79 for DOE under Sandia Contract No. 13-0291. The advanced rotor was made available for the present test because it exceeded the proof test capabilities of all rotor test facilities in the United States and could not be utilized previously.

The GFE rotor was of biannualate rim type with tension balanced spokes and was constructed for Sandia Laboratories by William Brobeck and Associates, Fig. 7-26. The rotor is 23.5 inches OD and 7.85 inches high, weighs 123 pounds (96-pound rim), and stores 1 kWh of energy at 15,000 RPM, the maximum spin speed of the present experiment. The catenary spokes that connect the hub to the outer rim produce a structural flexibility in the vertical (axial) direction. Magnetic levitation of such a configuration with structural flexibility in the direction of the magnetic-bearing servo loop control system presents a challenge to the designer and this particular rotor design may have represented the severest challenge possible due to its extreme flexibility.

CP267-6338

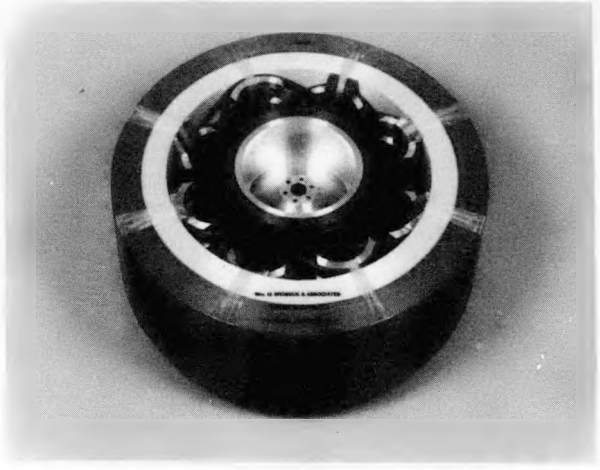

Figure 7-26. GFE advanced composite rotor.

A number of other features of the rotor are evident in Fig. 7-26 through Fig. 7-29. The outer portion of the rim is made with Kevlar 49/epoxy while the inner portion is made from S-2 fiberglass/epoxy. The aluminum hub has a Kevlar 49 overwrap and the tension-balanced spokes are Kevlar 29. Aluminum loading weights are attached to the spokes at the junctions with the rim. The centrifugal forces acting on these weights cause the spokes to expand radially. The weights are sized to produce spoke expansion to match that of the rim, thereby virtually eliminating radial loading on the rim. A substantial amount of balsa wood ($\sim$200 $in.^3$) is used as spacers between the vertical catenary spoke levels. A tape overwrap is provided at the junction of the spokes to the rim to provide a structural connection. In addition, the spokes are epoxyed to the rim and to the hub overwrap.

CP267-6342

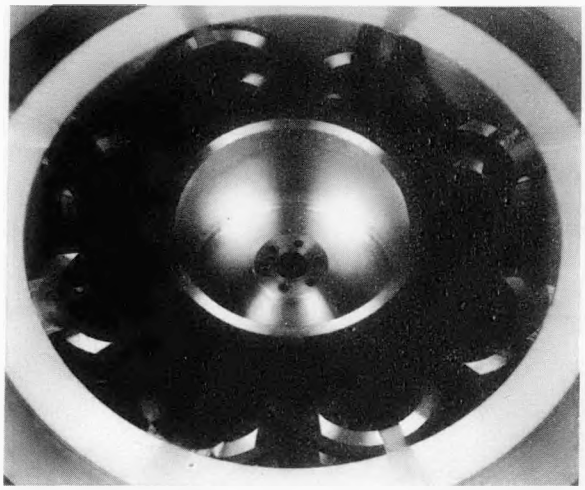

Figure 7-27. View of catenaries.

CP267-6343

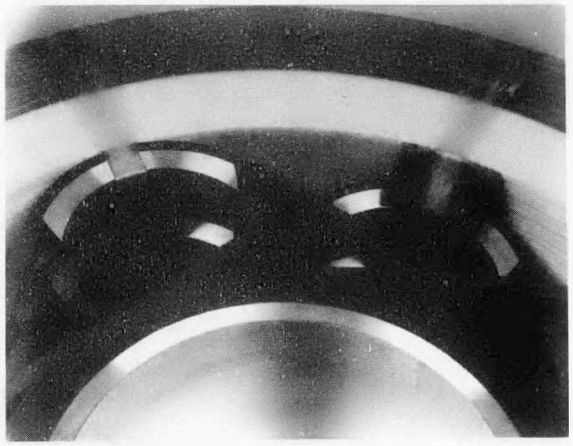

Figure 7-28. Closeup of outer hub attachment.

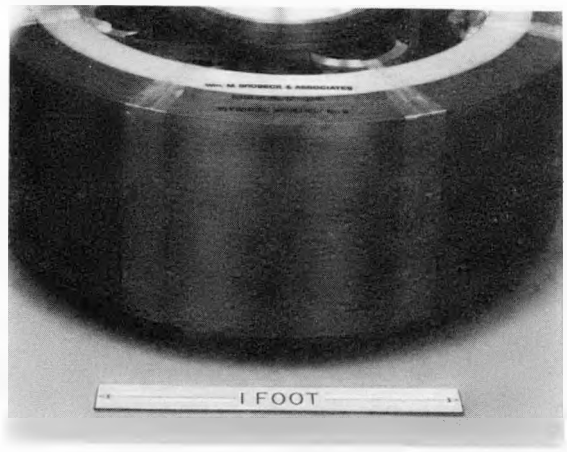

Figure 7-29. Outer rim face.

Little data were available on the GFE rotor from DOE or from the manufacturer other than its overall dimensions, weight and calculated moments of inertia. In fact, no data were available on how well it had been balanced before delivery to DOE nor on its structural vibration frequencies when non-spinning or spinning. Structural analyses had not been developed which could be used to calculate the variation of the catenary radial spring constant and catenary axial spring constant with rotational speed. Information was not available as to the rotor's internal hysteresis, outgassing behavior, and concentricity of hub and rim. The moments of inertia of the rotor had not been measured. Much of this missing data was required before operation of the GFE rotor on magnetic suspension could be predicted analytically.

Upon receipt of the GFE rotor, efforts were undertaken to develop a data base on the rotor. The rotor was inspected and measurements taken of all physical dimensions and concentricity of parts. The axial spring constant of the catenaries was measured. Outgassing tests were performed and the rotor was sent to Lindskog Balancing Corporation for a check of its imbalance and, if necessary, rebalancing. Finally a proof spin test to a 10% overspeed condition (16,500 RPM) was conducted on an air-bearing suspension system at Barbour Stockwell Company to qualify the rotor for safety before installation in the magnetic-suspension, spin-test vacuum tank facility at Lincoln Laboratory.

After the proof spin test, the rotor was returned to Lindskog Balancing Corporation for a check of its imbalance and a rebalancing, if required.

As a result of these investigations, a number of significant facts were learned which are summarized below. The as-received rotor was found to have excessively high imbalance, which caused its spin axis to be aligned more than 1/8 of a degree away from the vertical. This unsatisfactory balance was corrected by attaching balance weights to the inside surface of the outer rim. Using this method, the spin-axis was aligned to within 1/100 of a degree from vertical, an exceptable level for the tests but still several orders of magnitude higher imbalance than achieved when balancing the 1/10-scale prototype steel rotor. An axial spring constant of 20,000 pounds per inch was measured on the nonspinning rotor.

Exploratory outgassing tests, conducted under vacuum conditions over a continuous two-week period, showed excessive rotor outgassing even up to the end of the test period. With the vacuum pumps operating, a vacuum level of about 1×10^{-5} torr could be achieved with the advanced composite rotor in a vacuum test tank. If the pumps were shut off, the pressure would increase to 1×10^{-4} torr (one order of magnitude) in about one minute and to 1×10^{-3} torr (two orders of magnitude) in five minutes. This amount of outgassing did not present a problem in the present experiment because sufficient pumping capacity was available in the spin test vacuum tank to handle it. However, such high outgassing levels would be unacceptable for an installed residential flywheel system because of the pumping power requirements and safety considerations should vacuum pumping be lost (such a rotor will burn itself up if operated at pressure levels of 1×10^{-2} torr or higher for more than a few minutes). It should be a design goal for advanced composite rotors that their outgassing can be handled by on-site maintenance pump-downs at intervals of several months.

The source of outgassing was not identified in the course of the experiments due to limitations of time and funds. However, tests were conducted on balsa wood samples which showed that up to 7% weight percentage of moisture was released as the samples were subjected to vacuum and that reabsorption of this

amount of moisture would occur overnight if the samples were exposed to air. Approximately 200 $in.^2$ of balsa is used in the Brobeck rotor. Another source of outgassing may be the epoxy itself. It is recommended that more attention be given to the selection of materials with less outgassing in future advance composite rotor designs and that rotor designs be selected with outgassing performance criteria in mind. Also, the need to balance advanced composite rotors with attached weights seems to run counter to the concept of an "advanced" rotor. Finally, the air-bearing suspension overspeed tests to 16,500 RPM were accomplished without incident.

7.3.3 Magnetic Suspension Test Options

The 123-pound weight of the GFE advanced composite rotor was substantially less than that of the 400-pound steel rotor that was magnetically suspended during the prototype experiments on the six-element, permanent-magnet, magnetic-bearing assembly. The composite rotor could not be installed directly on the six-element, permanent-magnet bearing because the mechanical gaps in the bearing assembly were set to supply 400 pounds of lift in the magnetically levitated position and the electromagnetic control coils in the axial servo loop control system were designed originally to provide on a continuous basis a constant bias force of only $\pm$10% of the permanent-magnet, lift-force setting. Thus sufficient bias force could not be generated in the prototype bearing to compensate for the large difference in rotor weights.

Three possible solutions for testing the 123-pound rotor on magnetic suspension were identified. In the first option, the prototype-bearing lifting force would be reduced by increasing the magnetic-bearing element gaps. This option would require that the prototype bearing be disassembled, each of the magnetic-bearing stators be reshimmed, and the bearing reassembled. A significant amount of time might have been required in this option for disassembly since all screws used in the prototype bearing had been fastened in position with Loc-Tite to prevent their unloosening due to vibration. In the scheme to be used, the four inner bearing gaps would be shimmed the most and the two outer end bearing gaps the least. In this way, a final configuration would be achieved in which the two outermost bearings would provide most of the lifting force.

All six gaps in the original prototype bearing were set at 10 mils. The new bearing geometry for the Brobeck rotor tests would require that the four central gaps be opened up to 50 mil and the two outermost bearing gaps be set at 13 mils.

In the second option, the prototype bearing would be left unchanged but an auxiliary steel rotor would be added to the composite wheel to bring the total suspended weight up to 400 pounds. The combination would then be mounted on the prototype bearing. Modification to and the disguising of the structural vibration modes of the composite rotor due to attachment of the auxiliary steel rotor were considered to be significant concerns of this approach.

The third option provided for the construction of a new two-element bearing of the advanced prototype system type that was appropriate to the new advanced composite wheel.

This latter option, the construction of a new two-element bearing, was selected as the most viable approach since it required the least expenditure of time and contract funds and, in addition, would demonstrate the two-bearing design approach selected for the 20-kWh advanced prototype flywheel system.

7.3.4 Advanced Prototype Flywheel System

7.3.4.1 Flywheel System Hardware

The advanced prototype flywheel system hardware is shown being tested in the Laboratory clean room, Fig. 7-30, and being lowered into the spin test vacuum tank after addition of the motor-generation, containment system and the top of the flywheel containment unit, Fig. 7-31. The advanced prototype hardware was assembled using the I-beam support system, motor-generator and quill of the original 1/10-scale prototype unit plus the new two-element magnetic bearing, Fig. 7-32, and the new GFE composite rotor, Fig. 7-26. A new, larger, 33-inch ID, 3-inch thick, containment unit was fabricated to accommodate the increased size of the GFE rotor, Fig. 7-33. Photographs of the vacuum tank interior after containment/flywheel installation are presented in Figs. 7-34 and 7-35.

CP267-6950

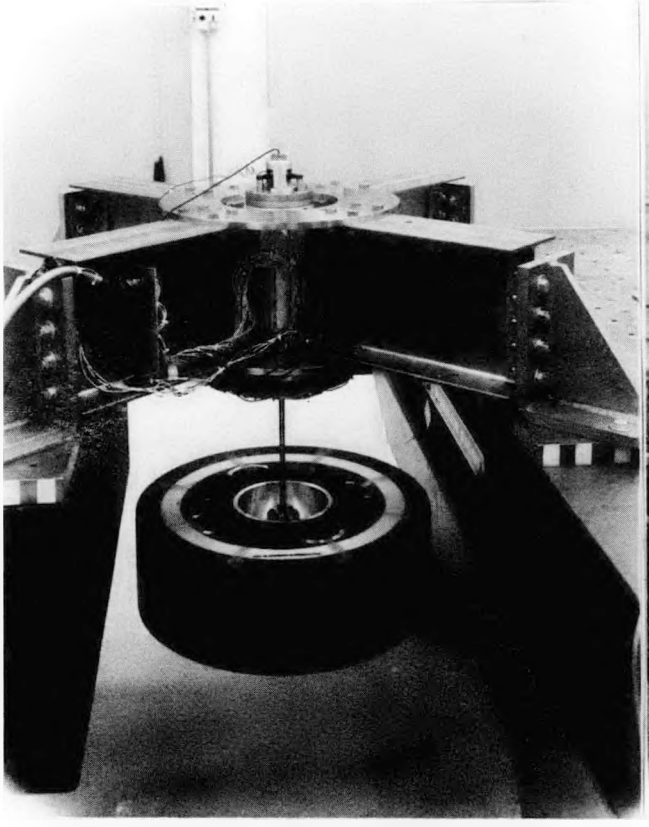

Figure 7-30. Advanced prototype flywheel system.

CP267-6975

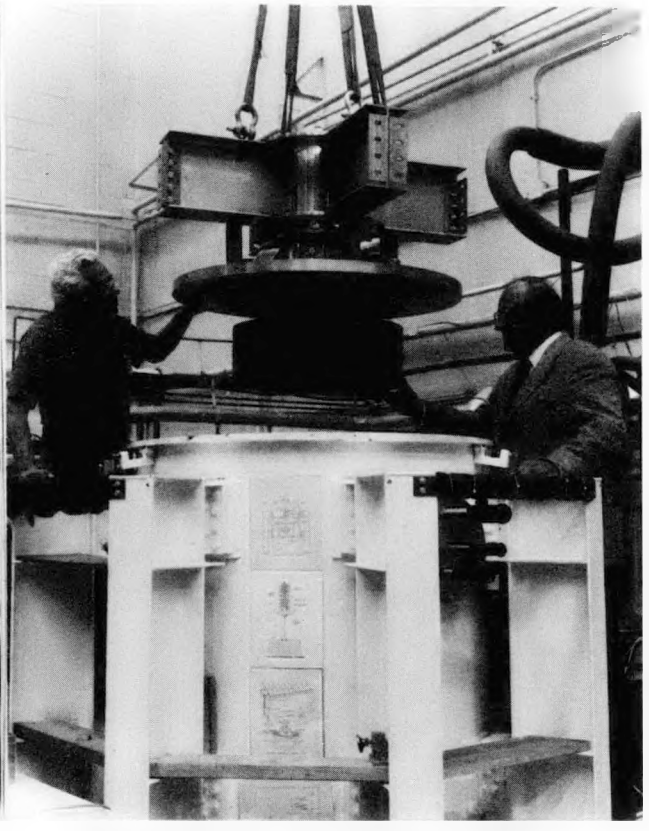

Figure 7-31. Installing the advanced flywheel system.

CP267-6942

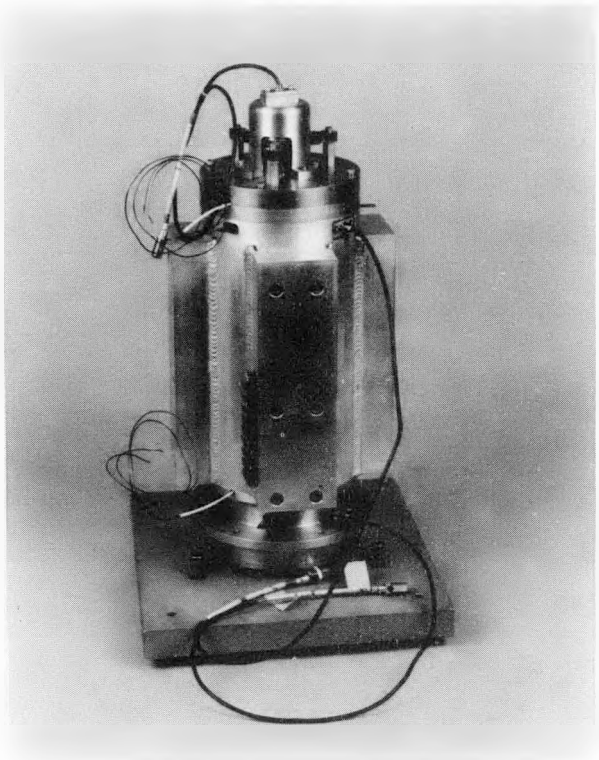

Figure 7-32. Two-element magnetic bearing.

CP267-6934

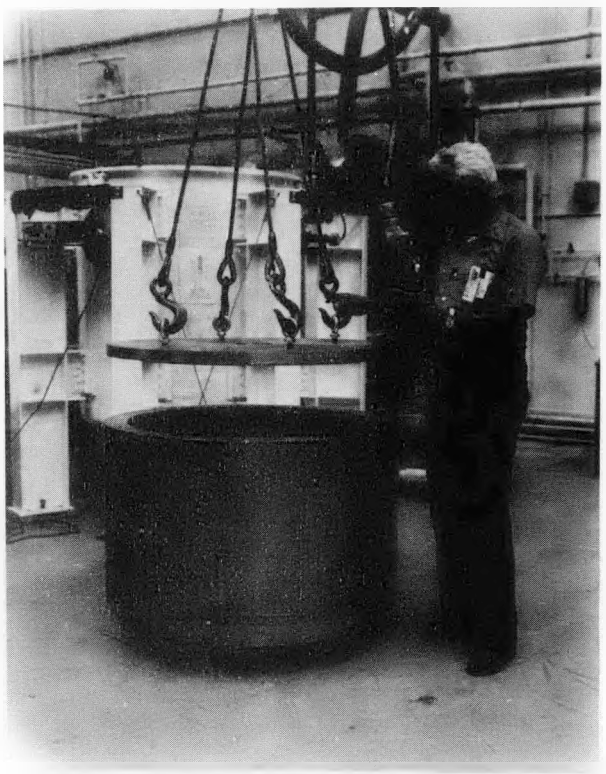

Figure 7-33. 33-inch ID containment unit.

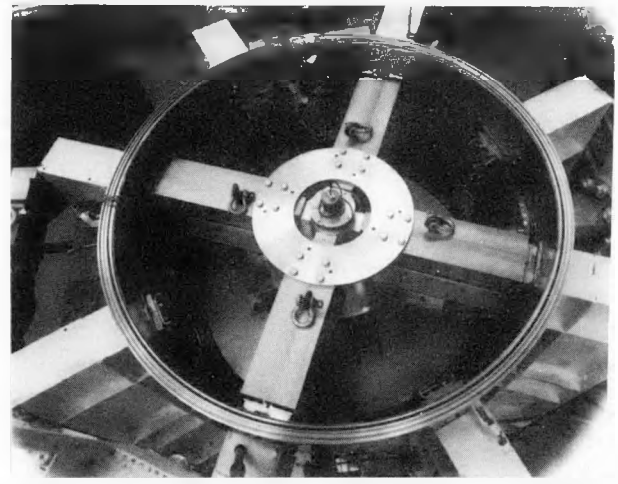

CP267-7058

Figure 7-34. Vacuum tank interior after containment flywheel installation.

CP267-7055

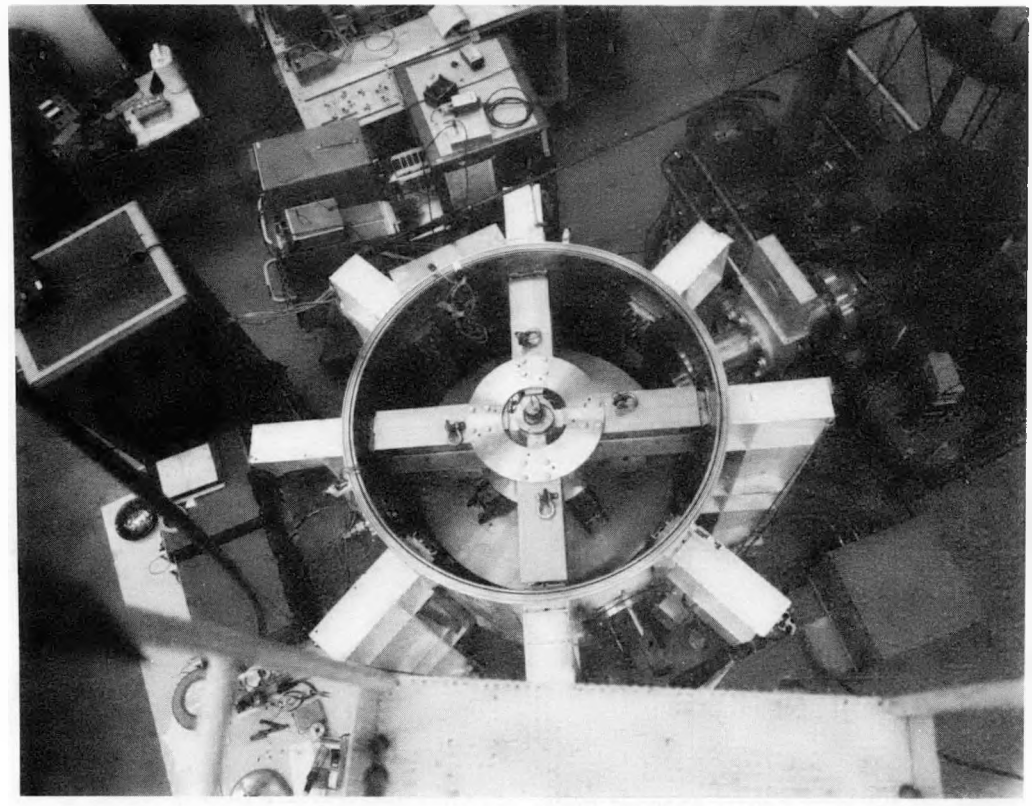

Figure 7-35. Vacuum tank/flywheel test setup.

A comparison of the new two-element magnetic bearing and the six-element original prototype bearing is made in Fig. 7-36. The two-bearing unit has a much reduced parts count over its predecessor. Most of the parts contained in the two-element bearing are shown in Figs. 7-37 and 7-38.

C74-1480

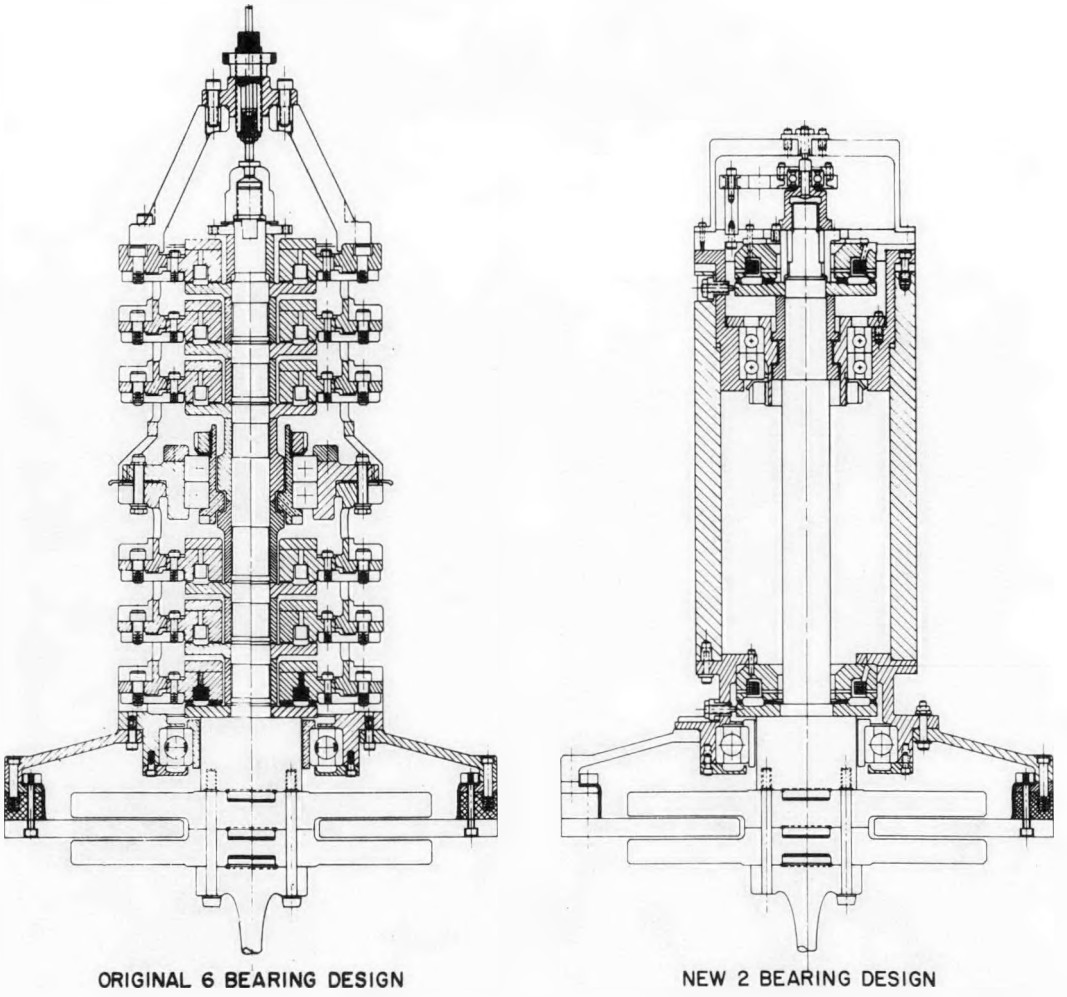

Figure 7-36. Comparison of the new two-element magnetic bearing with the original six-element prototype.

CP267-6900

Figure 7-37. Magnetic bearing parts.

CP267-6937

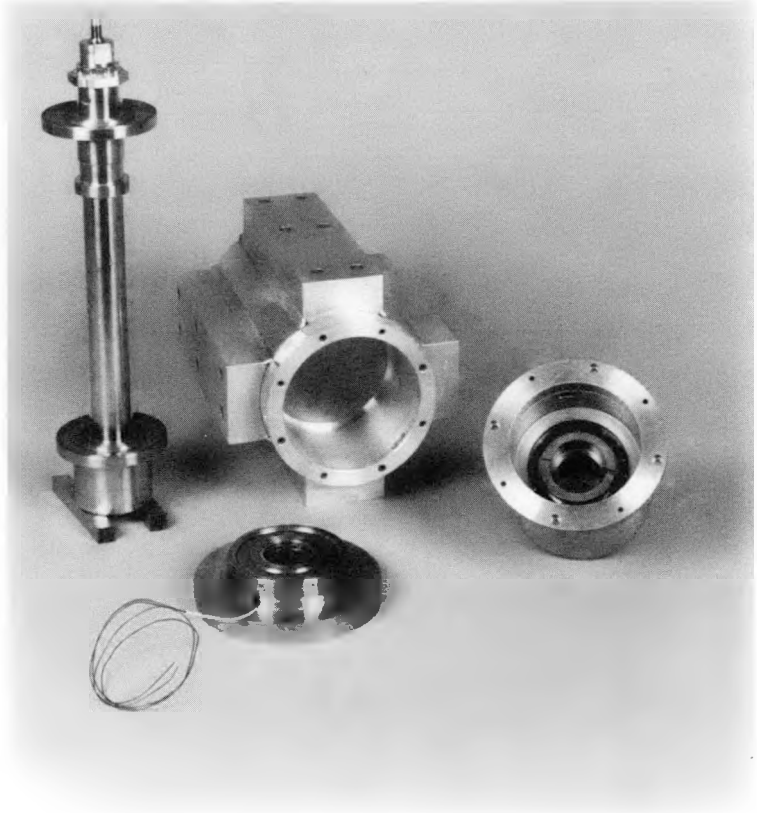

Figure 7-38. Magnetic bearing subassemblies.

Table 7-5 and Table 7-6 summarize the weight breakdown and intertia breakdown for the magnetically levitated portion of the new prototype system; rotor, quill, motor generator, magnetic-bearing shaft and rotors. The total magnetically levitated weight is 148.66 pounds and the moment of intertia is 10941 lb-in^2. The rotor weight breakdown is presented in Table 7.7. The total weight of rotating components above the catenaries is 43.86 pounds.

TABLE 7-5

MAGNETICALLY LEVITATED WEIGHT BREAKDOWN

Item	Weight (lbs)
Bearing shaft	5.52
Upper rotor	0.63
Lower rotor	0.58
Upper touchdown spacer	0.26
Lower touchdown spacer	0.23
Collar	0.29
Nut assembly	0.17
Motor-generator assembly	12.55
Bolts (m/g)	0.34
Quill shaft	2.85
Bolts (flywheel)	0.20
Flywheel	123.55
Flywheel adaptor	1.13
Adaptor washer	0.19
Adaptor bolts	0.17
TOTAL	148.66

TABLE 7-6

INTERTIA BREAKDOWN

Item	Weight (lbs)	Inertia (lb-in.^{2})
Shaft	4.20	0.781
Shaft hub	2.27	1.567
Upper and lower rotor	1.21	1.460
Motor-generator	12.55	76.282
Bolts (m/g)	0.34	0.299
Quill shaft	2.85	1.842
Bolts (flywheel)	0.20	0.176
Flywheel	123.55	10858.226
Flywheel adaptor	1.13	--
Adaptor washer	0.19	--
Adaptor bolts	0.17	--
TOTALS	148.66 lb	10940.633

TABLE 7-7

ROTOR WEIGHT BREAKDOWN (ESTIMATED)

Item	Material	Weight (lbs)
Hub	Aluminum/Kevlar 49 overwrap	18.75
Catenaries	Kevlar 29	5.02
Weights	Aluminum	1.47
Rim	Kevlar 49 outer rim S-2 glass inner rim	98.31
TOTAL		123.55

7.3.4.2 10% Overspeed Rotor Test

The advanced composite flywheel was overspeed tested to 16,500 RPM, which is 10% higher than its maximum use speed of 15,000 RPM, to satisfy safety requirements before installation in the magnetic suspension test chamber. The overspeed tests were conducted on an air-bearing suspension system at Barbour-Stockwell Company, Cambridge, Massachusetts. A photograph of the control console and spin pit is presented in Fig. 7-39 and a closeup of the composite rotor mounting system is shown in Fig. 7-40. The rotor hangs below the air-bearing on a slender cylindrical quill shaft which extends through and below the rotor. A position probe is mounted at the top of the cylindrical shaft and is used to measure shaft oscillation amplitude during the test. The rotor was spin balanced on the same cylindrical shaft fixture at Lindskog Balancing Corporation prior to the Barbour-Stockwell test.

CP267-6912

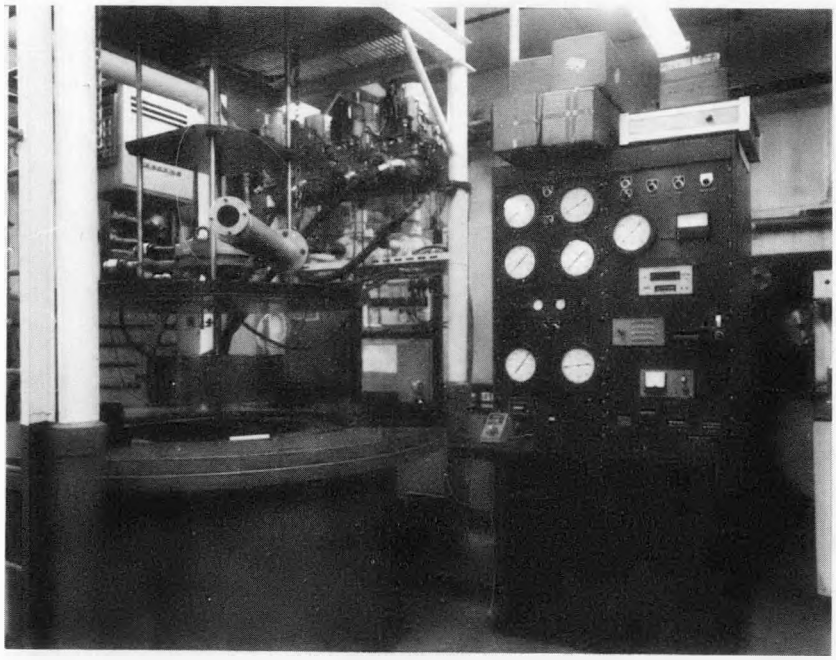

Figure 7-39. Barbour-Stockwell air bearing spin tests.

CP267-6917

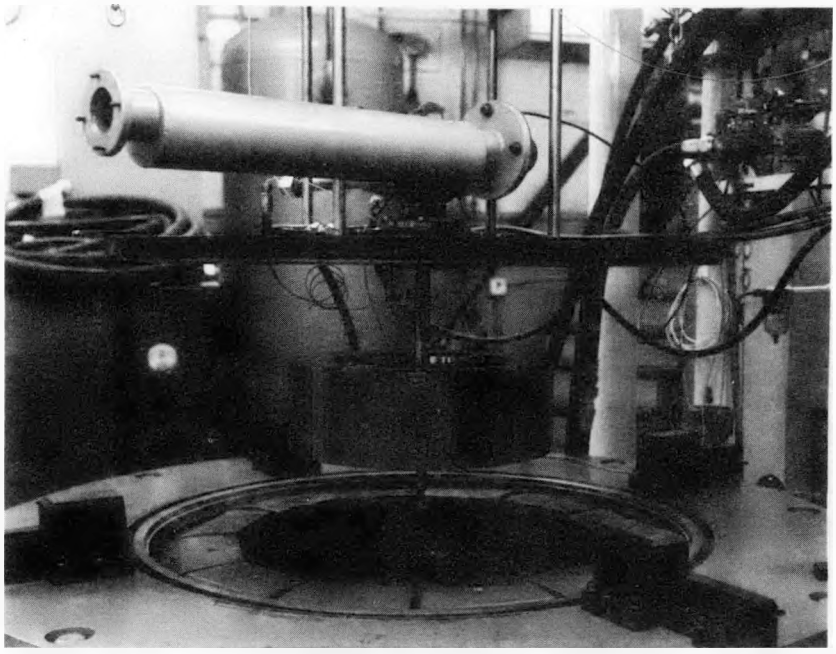

Figure 7-40. Composite wheel test mounting.

The rotor was accelerated to 16,5000 RPM following the spin speed time history shown in Fig. 7-41. The rotor was allowed to coast down freely for about 25 minutes after the maximum speed of 16,500 RPMs was achieved. Quill whirl radius during coast-down was measured, Fig. 7-42, and found to be about 2.5 mils average. Changes in whirl radius with speed are said to be an indication[7-4] of rotor geometry changes which produce differing imbalances and whirl amplitudes.

C74-1543

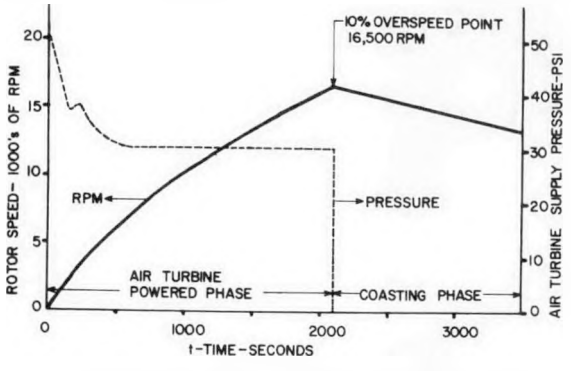

Figure 7-41. Spin speed time history.

C74-1542

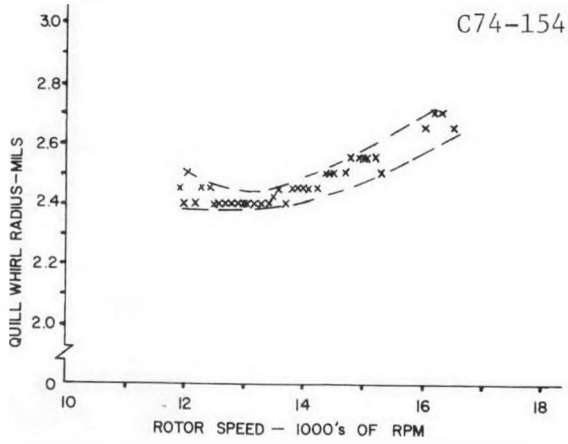

Figure 7-42. Quill whirl radius during coast-down.

The overspeed test to 16,500 RPM was accomplished without incident. Inspection of the rotor after the test showed some delamination of the catenary overwraps, Fig. 7-43 and Fig. 7-44; delamination having occurred in the white areas seen under the overwraps. Overwrap delamination was the only physical change observed as a result of the overspeed test.

The rotor was then returned to Lindskog for a check of its balance. Only slight changes from the original balance were found and they were corrected by rebalancing the wheel.

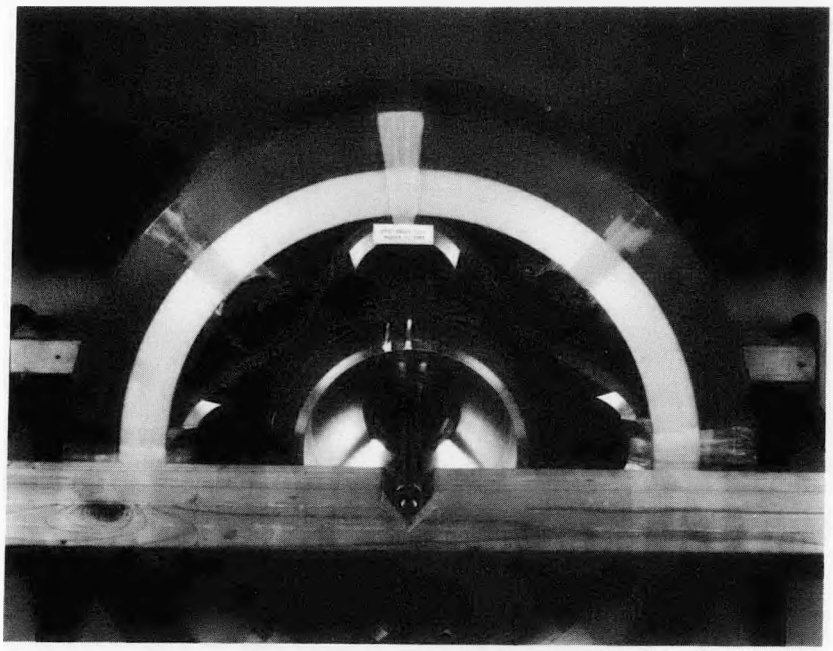

Figure 7-43. Catenary overwraps after proof test.

CP267-6952

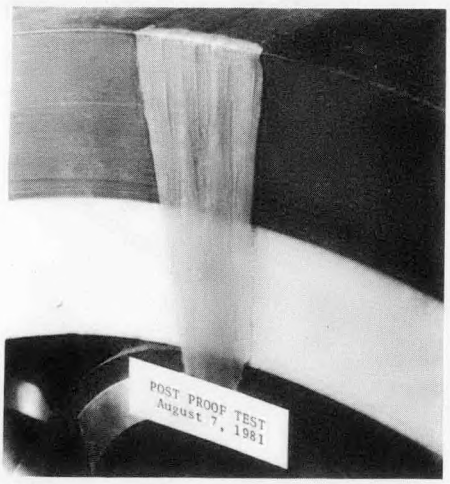

Figure 7-44. Catenary overwrap delamination.

7.3.4.3 Magnetic Levitation Tests

The new GFE composite rotor underwent magnetic levitation tests in the laboratory using the prototype magnetic-bearing axial-servo-loop electronics before it was installed in the vacuum tank. Stable lift-off and levitation could not be achieved with the original prototype servo loop in combination with the composite wheel due to rotor flexibility effects. A redesign of the axial-loop control system was undertaken so that magnetic levitation could be achieved. The methods by which this redesign was achieved are discussed below.

Initially, the Brobeck composite wheel was tested under static loadings to obtain estimates of the stiffness of the Kevlar spokes which connect the flywheel rim to the hub. Vertical (axial) static loading of the hub showed a catenary spring constant of 19,300 lbs/inch, Fig. 7-45, corresponding to a predicted oscillation frequency of the hub with respect to the rim of 100 Hz (or 44 Hz for rim with respect to a fixed hub). Radial static loading tests did not produce significant deformations for the loading limits possible (i.e., gravity loading of 123 lbs) so only an approximate spring constant in that direction could be determined statically. Dynamic oscillation tests were then conducted to confirm the statically measured axial spring constant and to determine the radial and rocking spring constants of the catenary structure. This was accomplished by measuring, with attached accelerometers, the acceleration response of the hub when the rotor was excited by vertical and lateral impulsive loadings. Examples of axial and lateral rocking dynamic responses obtained on the non rotating rotor as recorded on a frequency analyzer are shown in Figs. 7-46 and 7-47. From data of this type it was found that:

Vertical (axial)	$f_1 = 105$ Hz	$K_V = 21{,}150$ lb/in
Radial	$f_2 = 515$ Hz	$K_1 = 510{,}000$ lb/in
Rocking	$f_3 = 1455$ Hz	$K_\theta = 26\ (10)^6$ lb-in/rad

The stiffness results noted above were calculated from the recorded frequencies. The vertical stiffness measured dynamically was in good agreement with the statically measured value. The measured stiffness values were then utilized to make preliminary estimates of the structural vibration frequencies and also used as inputs to a computer program for the evaluation of the whirl-spin states of the new magnetic bearing/flexible rotor combination.

C74-1786

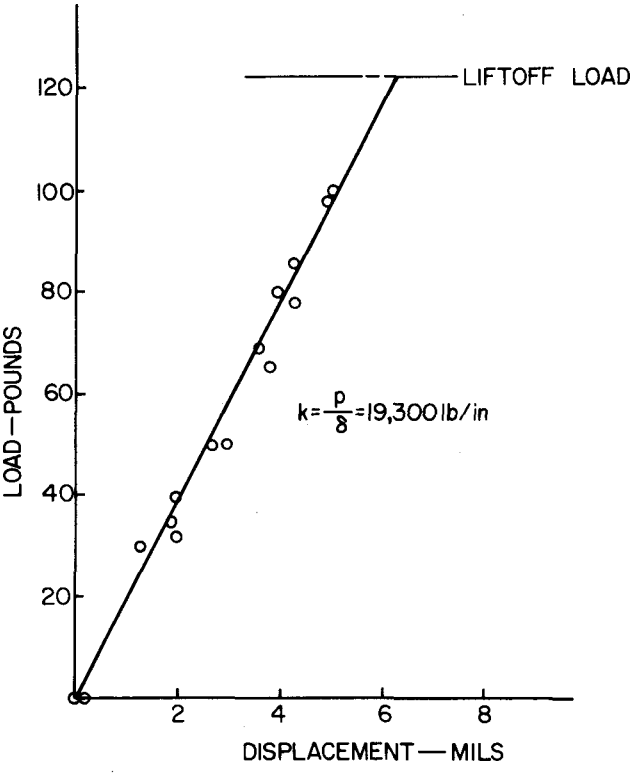

Figure 7-45. Static measurement of catenary axial stiffness.

C74-1787

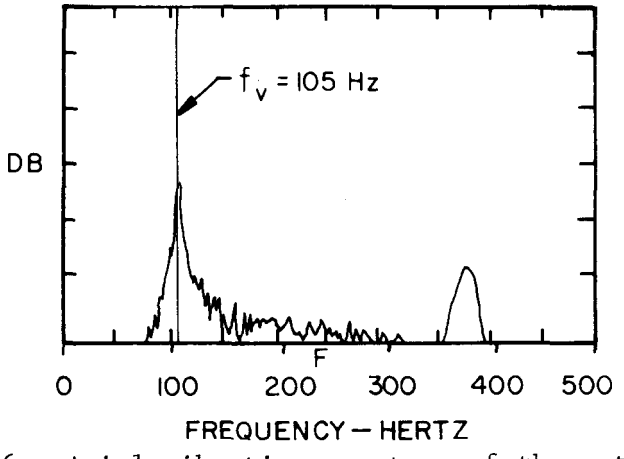

Figure 7-46. Axial vibration spectrum of the catenaries.

C74-1787

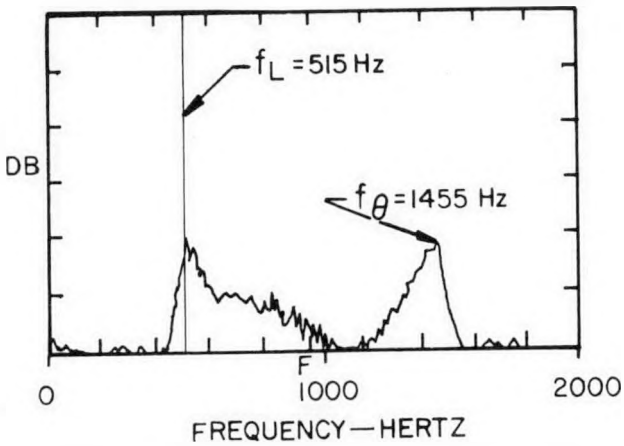

Figure 7-47. Lateral/rocking vibration spectrum of the catenaries.

To redesign the axial servo control system, it was necessary to locate the structural vibration frequencies interfering with control system operation when in a magnetically levitated position. However, it was not possible to levitate the composite rotor to make measurements of the interfering frequencies because of the rotor flexibility. A solution to this dilemma is shown in Fig. 7-48. First, the composite rotor was stiffened with bars which allowed it to be magnetically levitated. Then the stiffness of the rotor unit with bars was decreased gradually by lowering the clamping tension in the axial bolts and the frequencies of the structural resonances were determined by measuring the open-loop transfer function of the magnetic bearing with a Hewlett-Packard Model 5420 A digital signal analyzer.

CP267-6973

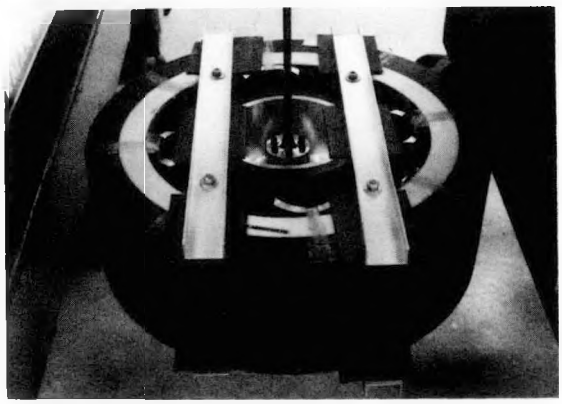

Figure 7-48. Composite rotor with stiffening bars.

Examples of bearing transfer functions measured at an axial bolt torque of 900 inch-ounces and then at a torque of 2-inch ounces are shown in Figs. 7-49 and 7-50, respectively. The structural vibration frequencies moved lower as the rotor stiffness was decreased. The frequency of the maximum amplitude point changed from 119 Hz to 87 Hz as the bolts were loosened while the frequency of the minimum amplitude point changed from 62 Hz to 48 Hz. These data were taken with a notch filter of 10-Hz width and -50db depth centered about 75 Hz. The variations of the frequencies at the minimum and maximum amplitude points with bolt torque are shown in Fig. 7-51. A case is also shown in Fig. 7-51 for a configuration in which the four bars were lying loose on top of the composite rotor. For this configuration, the frequencies of minimum and maximum amplitude occurred at 41 Hz and 69 Hz, respectively. Magnetic levitation could not be achieved if any of the loose bars were removed from the top of the rotor.

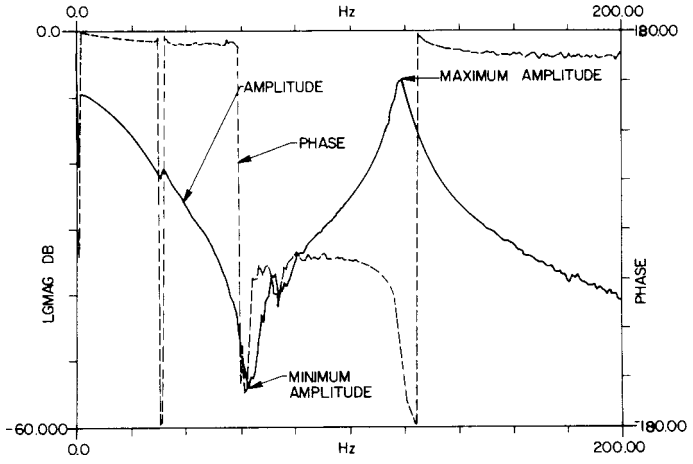

C74-1790

Figure 7-49. Transfer function at 900-inch-ounce bolt torques.

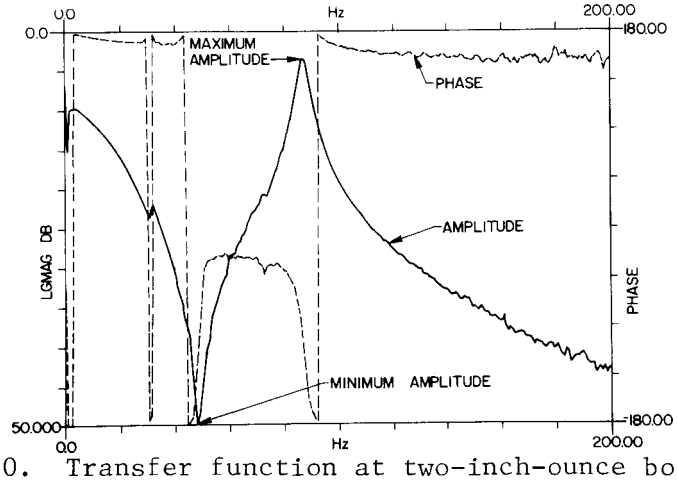

C74-1789

Figure 7-50. Transfer function at two-inch-ounce bolt torques.

C74-1788

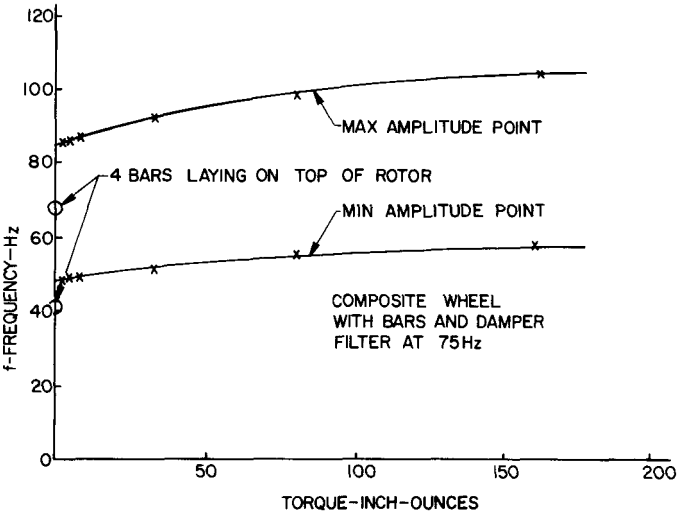

Figure 7-51. Bearing open-loop frequency variations with rotor stiffness.

The empirical results shown in Fig. 7-51 were used as a basis for the redesign of the servo system. It was assumed that the frequency of the maximum amplitude point, which interfered with control system operation, would follow a trajectory similar to that displayed in Fig. 7-51. When the composite rotor was nonspinning or slowly spinning and the catenary stiffness a minimum, it was assumed that the interfering frequency would be near 69 Hz. As the rotor spin speed increased and the catenaries became stiffer, it was assumed that the interfering frequency would move to 75 Hz or higher. A dual-notch filter was then designed and incorporated into the control system. A 10-Hz-wide, -50-db-deep filter centered at 65 Hz was combined with the one centered at 75 Hz. This provided a deep notch from 65 Hz to 90 Hz. A new method was also devised to control axial excursions during the transient period as the rotor is lifted off the mechanical bearings and is guided to its magnetically levitated position. As a result of these changes, magnetic levitation of the composite rotor was achieved.

7.3.4.4 Damper Tests

The advance prototype system was then exercised to determine its operating speed envelope with a variety of mechanical dampers of the type previously described in Section 4.2.7. The external dimensions of the original damper

were maintained but the wall thickness of the flexures on each of the three legs was varied by changing the diameter of the circular opening. Experiments were run for a single damper with wall thicknesses of 1/16, 1/8 (used in prototype tests), 11/64 and 14/64 inches and for a two-damper configuration where both dampers had wall thicknesses of 1/8 inch. The magnetic bearing shaft oscillation amplitude at the bottom magnetic bearing element was measured as a function of rotor speed from the Lissajou pattern generated from two Kaman Sciences KD 2300 series probes located 90° apart.

The effect of damper configuration on maximum attainable speed is displayed in Fig. 7-52. The highest operating speed of 12,020 RPMs was achieved with a damper configuration utilizing two 1/8-inch wall dampers. The next highest speed of 11,520 RPM was reached with a single, 1/8-inch wall damper. Maximum attained speeds with the other dampers were 11,040 RPM for the single, 11/64-inch wall damper; 10,080 RPM for the single, 14/64-inch wall damper, and 6,360 RPM for the single, 1/16-inch wall damper. The maximum operating speed is defined as that speed where touchdown on mechanical bearings occurs for the first time.

C74-1791

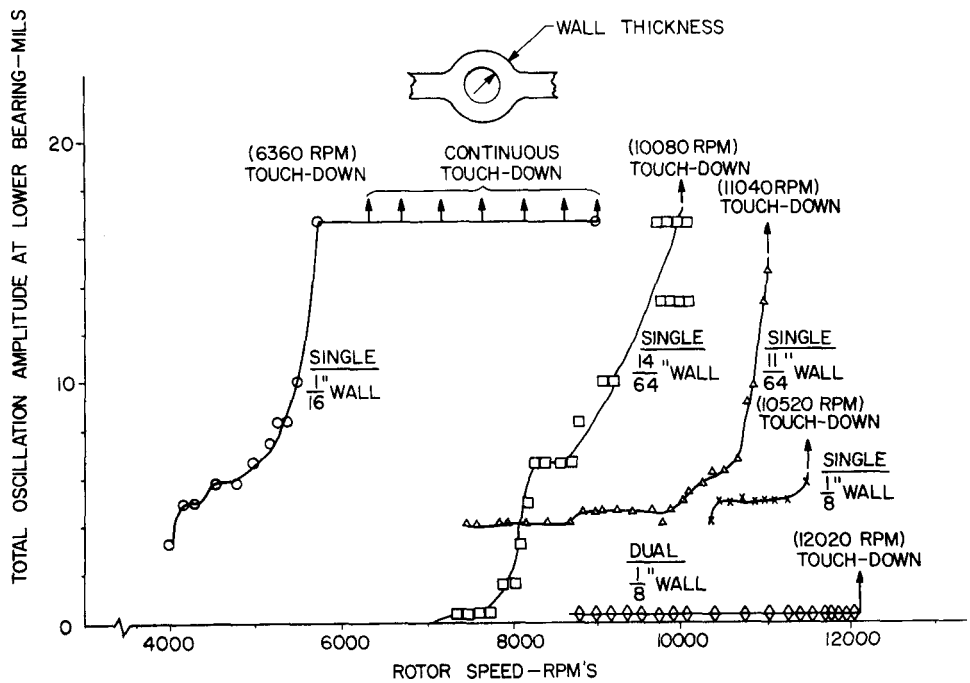

Figure 7-52. Effect of dampers on maximum attainable speed.

The 12,020 RPM two-damper test run was nearly ideal in that the magnetic bearing shaft radial oscillation amplitude remained constant at below 1/2 mil in total amplitude for a continuous RPM span of over 10,000 RPM. With two dampers, the flywheel unit also passed through the three low-speed critical resonant frequencies without touching down; the best test performance of any configuration. The transition from magnetic suspension to touchdown on mechanical bearings for this configuration occurred over a speed increase of less than 500 Hz, near the maximum operating speed of 12,020 RPM. Impending touchdown to mechanical bearings was signaled by the start of a low-frequency, vertical (axial) oscillation which could be seen on the output of the axial position probe of the magnetic suspension servo control loop. Initially, the vertical oscillation had no effect on the rock-solid, radial performance of the system. However, as the rotor speed increased further, momentary excursions in radial oscillation amplitude were noted in the Lissajou figure. Finally, a constant amplitude circular Lissajou pattern was observed which increased slowly in amplitude until touchdown occurred. Transitions to touchdown in the other tests also occurred in conjunction with the development of a vertical oscillation.

The effect of increasing the amount of damping was as expected. The maximum operating speed was found to increase as the amount of damping increased. This progression can be observed in Fig. 7-52 by examining the data for a single damper of 1/16-inch wall thickness, then that for a single damper of 1/8-inch wall thickness and finally the data for a two-element, 1/8-inch wall thickness damper. In this sequence of test cases, the damping is increasing and changes in stiffness are relatively small in comparison to the nominal 1/8-inch thick wall damper. However, the dampers with wall thicknesses of 11/64 inch and 14/64 inch add substantially more stiffness than the nominal damper. This added stiffness importantly affects the flywheel system vibration mode frequencies and the achievable damping effects and eliminates these two configurations from consideration.

A final test with three dampers was to have followed the two-damper test. To prepare for the final test, the rotor was to have been slowed to a stopped condition and then a change in the physical damper configuration was to have

been made. Deceleration at speeds above 60 RPM was normally accomplished by extracting electric power from the motor-generator and by dissipating that energy in resistance loads. Removal of magnetic suspension and touchdown on mechanical bearings at 60 RPM was the normal test procedure used to obtain a stopped condition in a reasonable time period following the motor-generator induced slowdown. The motor-generator slowdown technique was not useful at speeds below 60 RPM because of the low voltages generated and the small amount of power that could be extracted.

Following the 12,000 RPM two-damper test, the rotor was decelerated using the technique described in the previous paragraph. However, the magnetic suspension system was switched off at 120 RPM rather than at 60 RPM. Transition to the mechanical bearing suspension was accompanied by some noise from the flywheel system in the vacuum tank. Subsequent attempts to relevitate the nonspinning rotor on magnetic suspension were unsuccessful and measurements of magnetic bearing gaps at both the touchdown-down and touchdown-up positions showed dissimilar gaps on the upper and lower magnetic bearings.

The magnetic bearing, quill, and rotor unit were then removed from the vacuum tank and the magnetic bearing was disassembled. The lower rotor, originally shrunk-fit on the magnetic bearing shaft, was found to be loose with movement possible in the axial direction. The lower magnetic bearing outer stator fringe ring, originally bonded with epoxy on top of the permanent magnets, Fig. 7-38 foreground, was also found to be dislodged. Visual inspection of the quill and rotor elements showed no visible effects. It is conjectured that the damage to the magnetic bearing resulted from motions induced while on mechanical bearings at speeds of 120 RPM or less rather than as a result of high-speed operation.

The magnetic bearing unit was then repaired as described below. The lower rotor was electron-beam-welded to the magnetic bearing shaft along a circular interface between the shaft and the upper surface of the rotor, Fig. 7-38, upper left. A fillet at the circular interface on the underside of the rotor prevented electron-beam-welding at that interface. As is usual in the case of electron-beam-welding, some distortion of the welded rotor

piece was experienced. The flatness of the rotor and rotor fringe rings was disturbed over a 60° sector with a maximum uplift of 4 mils at the outer edge of the sector. Flatness of the fringe rings was restored by facing-off the rings in a lathe. The integrity of the outer fringe ring on the stator of the lower magnetic bearing was reestablished by placing a metal collar over its outer circumference and pinning the two pieces together, Figs. 7-53 and 7-54. A metal collar was placed over the inner fringe ring and epoxyed in place to improve its integrity though there was no evidence that any debonding of the inner fringe ring had occurred. The static force-gap characteristics of the modified bearing were measured and no changes from the original data were found due to the modifications incorporated. The magnetic bearing was reassembled, the quill and composite rotor reattached and the advanced flywheel unit remounted in the vacuum chamber for tests. Tolerances measured during reassembly of the magnetic bearing showed it to be restored to original condition.

CP267-7049

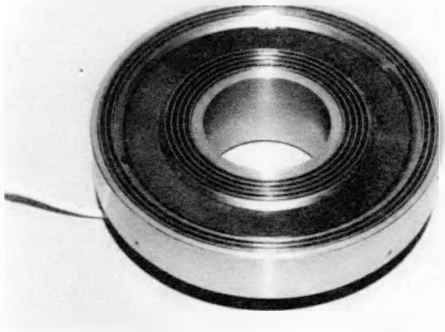

Figure 7-53. Top view of modified magnetic bearing stator.

CP267-7050

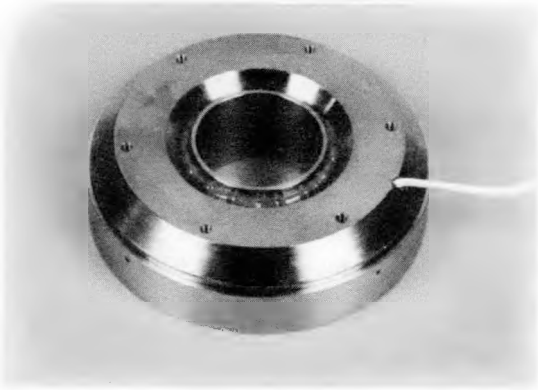

Figure 7-54. Bottom view of modified magnetic bearing stator.

The first experiment undertaken after restoration of the magnetic bearing assembly was a repeat of the dual-damper test. Unexpectedly, it was found that the operating limits of the flywheel system with two dampers had been reduced. Touchdown on mechanical bearings now occurred at 9600 RPM and buildup of the magnetic shaft oscillation amplitude was found to start at about 8000 RPM. These characteristics were different from those observed in earlier tests. However, system operation while passing through critical frequencies at low speeds appeared unchanged. No verifiable reason for the differences could be established from the available test data or from diagnostic tests that were performed. However, the observed characteristics of a less damped system with an earlier onset of magnetic bearing shaft motion suggested a situation of increased imbalance from the earlier tests. Because of these unexpected results, a decision was made to repeat other earlier damper tests to determine if those results would also differ from the previous tests. It was also decided that, rather than wait for the completion of the damper tests before making spin-down tare loss tests, spin-down tare loss test data would be taken concurrently with damper retests.

The flywheel system spin-down tare losses were then measured on the two-damper configuration following the method described previously in Section 4.6.4.1. Measurements were first made in the RPM regime below 8000 RPM, where magnetic shaft oscillation amplitudes were small. The spin-down tare losses in that region were found to vary linearly with RPM as had been observed earlier in the prototype tests and, though still small in absolute terms, they were 100% greater than had been measured on the prototype system, Fig. 7-55. Measurements were also made of the spin-down tare losses at speeds above 8000 RPM, where the magnetic shaft oscillation amplitude was finite and increasing with RPM. The tare losses were again found to vary linearly with RPM but at a rate substantially higher than the lower RPM results.

A retest of the single-damper configuration was run on the system and a maximum speed of 10,000 was attained before touchdown. The onset of magnetic shaft oscillation in this case occurred at about 6000 RPM. Again, these results differed from previous measurements. Operation of the system when passing through low RPM critical frequencies appeared unchanged. Spin-down

tare losses measured at speeds below 6000 RPM where shaft oscillation magnitudes were essentially small demonstrated a linear variation of loss with speed; the level of the loss being 50% greater than measured on the prototype system. A discontinuity in the variation of tare loss with RPM was observed at 6000 RPM, the point of Lissajou oscillation onset. The loss varied linearly with RPM but at a much higher rate above 6000 RPM.

A test without dampers was then undertaken so that the differential effects of the single and dual dampers on spin-down losses might be separated out from the measured system loss data. The flywheel system was being accelerated on magnetic suspension and had reached 2850 RPM when the system made an unexpected transition from a magnetically suspended condition to the mechanical touchdown support system. The motor-generator slow-down method was activated to reduce the rotational speed of the rotor. Subsequently, three unsuccessful attempts were made to relevitate the system on magnetic suspension by switching the magnetic control system off and then reenergizing it. At the end of the third relevitation attempt, the rotor speed had decreased to 1900 RPM under the effects of motor-generator power extraction. Shortly thereafter a loud noise was heard inside the vacuum tank suggesting that failure of the rotor had occurred.

The vacuum tank was opened and the rotor was examined. This examination showed that the outer rim of the rotor had separated from the rotor central hub, the quill shaft supporting the central hub had broken about two inches below the motor-generator and the hub/quill remnant was lying on top of the rotor rim, Fig. 7-56. The possibility that a magnetic suspension servo loop electrical failure had occurred during the test was eliminated from consideration by subsequently retesting the system with a new quill and a new simulated rotor of the same weight. With this new hardware, magnetic levitation was achieved without incident when the control system was energized.

An explanation of the probable sequence of events which occurred is offered below. The particular conclusions reached are based on a detailed examination of the rotor elements shown in Fig. 7-56, the relative location of these elements after motion ceased, and an examination of the scars and tracks on the inside of the containment cylinder and on the inner face of the containment

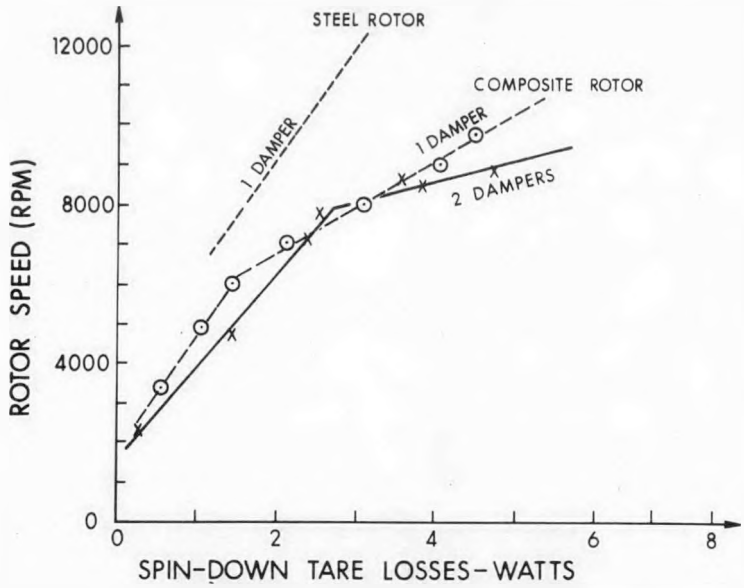

C74-1959

Figure 7-55. Spin-down tare losses with composite rotor.

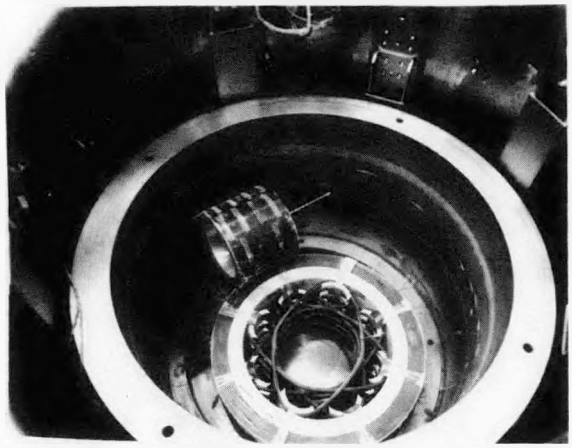

CP267-7084

Figure 7-56. Advanced composite flywheel after failure at 1900 RPM.

lid. Figures 7-57 through 7-59 are, respectively, photographs of the tank contents after opening of the vacuum tank (black witness marks have been placed on the pieces to document the scene and to help in future photointerpretations), after removal of the central hub with quill and after removal of the rotor rim. Figures 7-60 through 7-62 show top, side and bottom views of the rotor rim after removal from the vacuum tank. Side, top and bottom views of the central hub are offered in Figs. 7-62 through 7-65, respectively. A closeup of the catenary/central hub interface (looking upward) is presented in Fig. 7-66.

CP267-7075

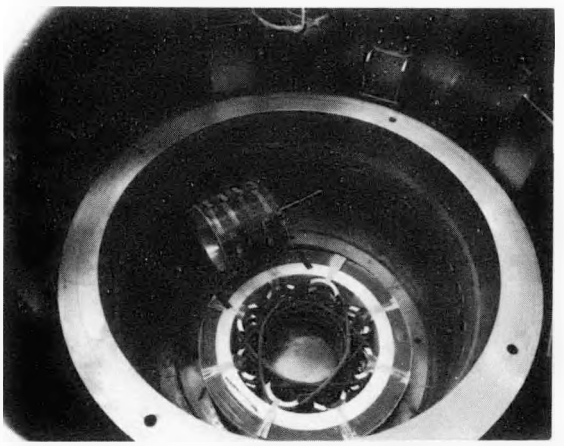

Figure 7-57. Witness mark locations.

CP267-7082

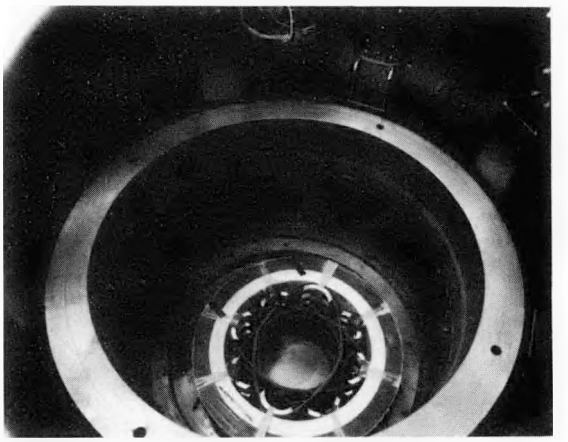

Figure 7-58. View with hub removed.

CP267-7079

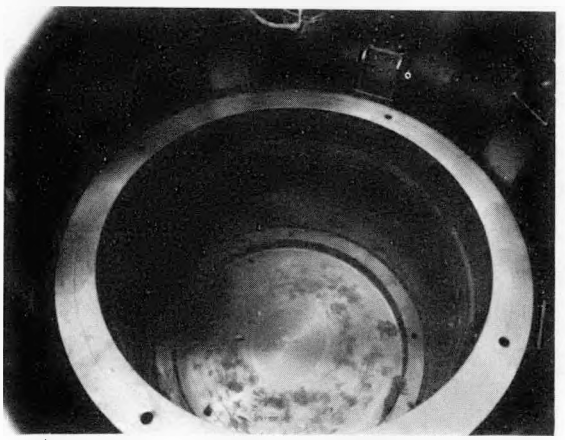

Figure 7-59. View with rotor rim removed.

CP267-7077

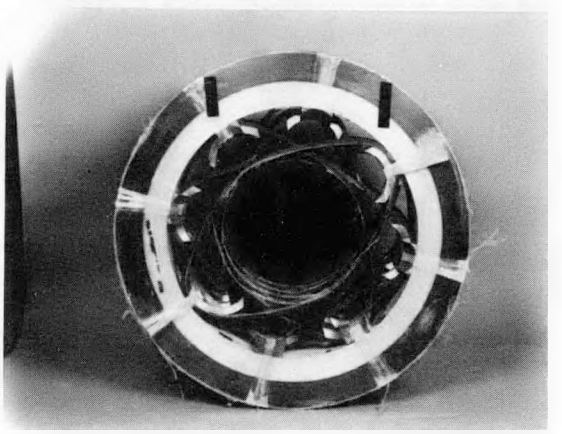

Figure 7-60. Top view of rim.

CP267-7073

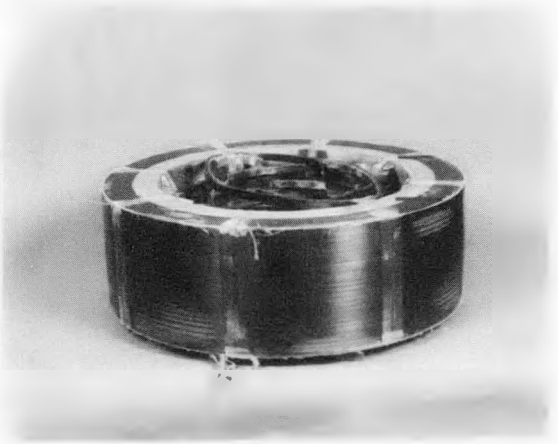

Figure 7-61. Side view of rim.

CP267-7083

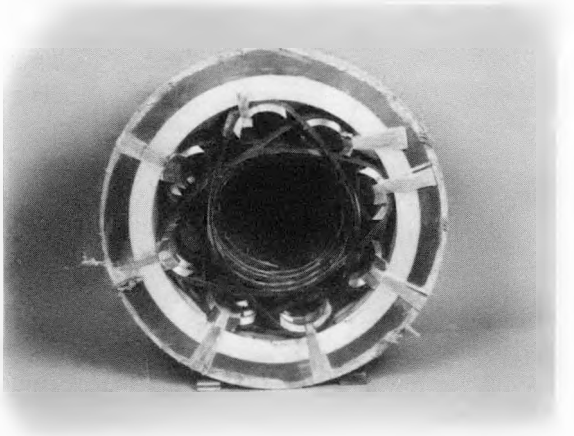

Figure 7-62. Bottom view of rim.

CP267-7085

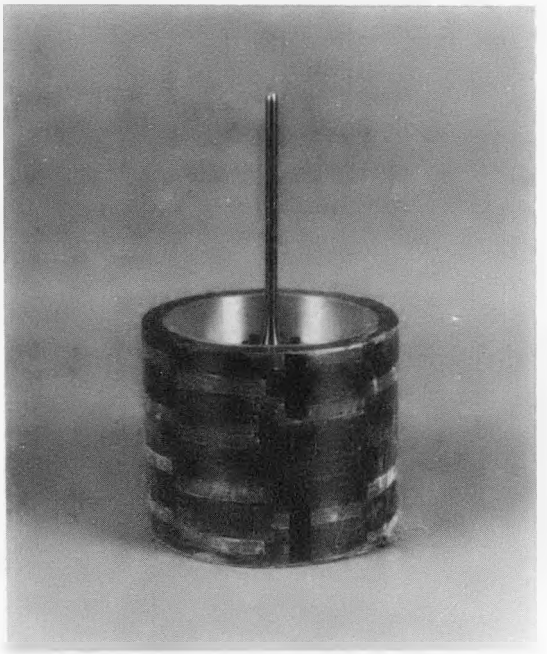

Figure 63. Central hub.

CP267-7067

Figure 7-64. Upper edge of hub.

CP267-7069

Figure 7-65. Bottom face of hub.

CP267-7098

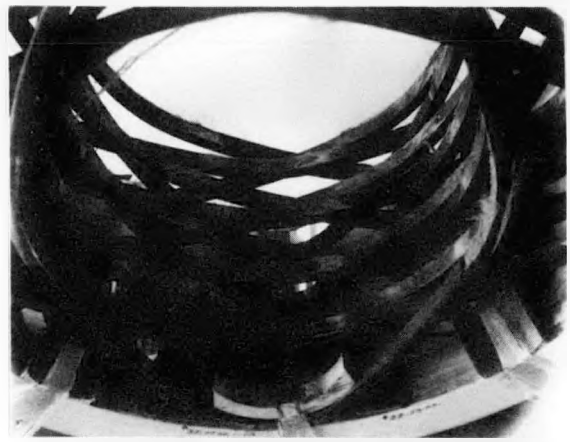

Figure 7-66. View of catenaries from below.

Close-ups of the central hub surface at 90° intervals are shown in Figs. 7-67 through 7-70 with the bottom of the hub facing upward. The end of the quill segment remaining attached to the central hub is photographed in Figs. 7-71 and 7-72. Some damage to the edges of the break has resulted from the end of the quill striking other objects before coming to rest. The end of the quill segment that remained attached to the motor-generator is shown in Fig. 7-73. Figure 7-74 is a view of the underside of the containment cover. The two diametrically opposed marks at 11 o'clock and 5 o'clock and at a distance of about one-third the cover radius are due to the edge of the central hub striking the cover before the quill had broken completely apart.

CP267-7101

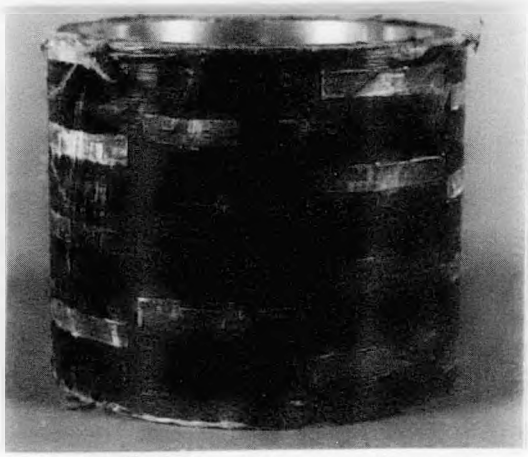

Figure 7-67. Closeup of hub, 0°.

CP267-7104

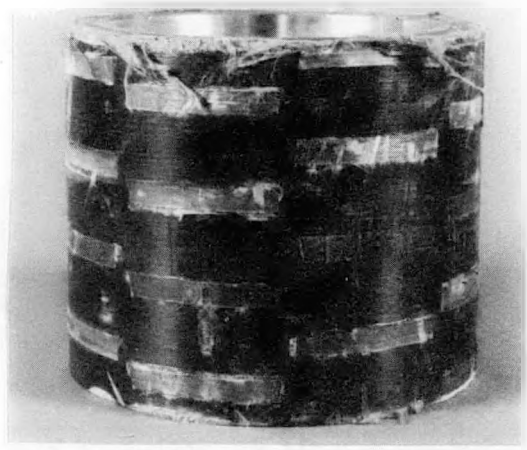

Figure 7-68. Closeup of hub, 90°.

CP267-7103

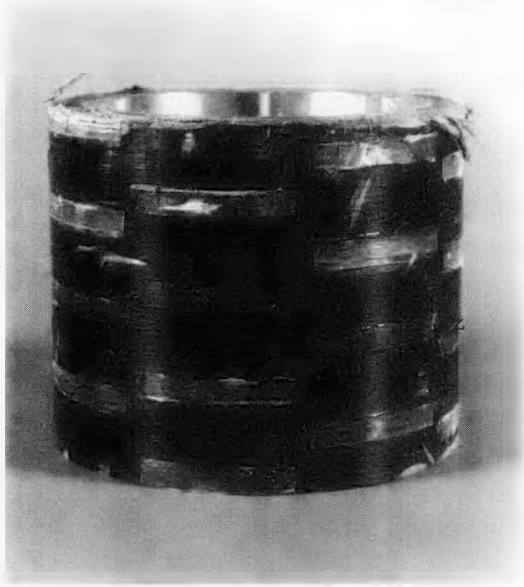

Figure 7-69. Closeup of hub, 180°.

CP267-7102

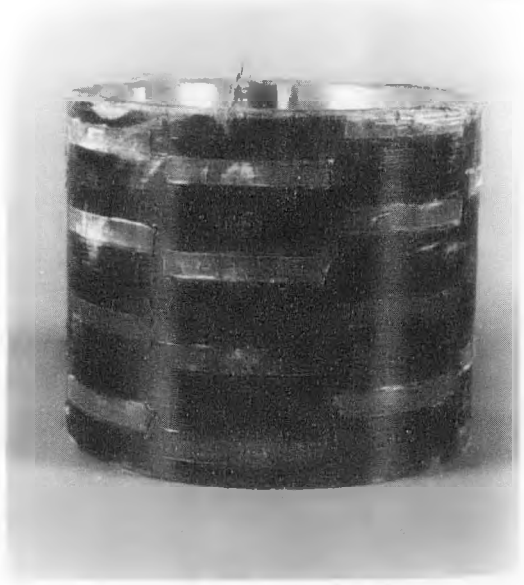

Figure 7-70. Closeup of hub, 270°.

CP267-7090

Figure 7-71. End of lower quill remnant.

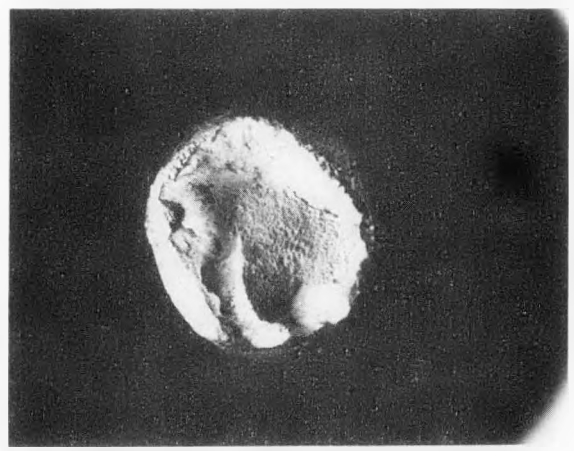

Figure 7-72. Closeup of lower quill remnant.

CP267-7088

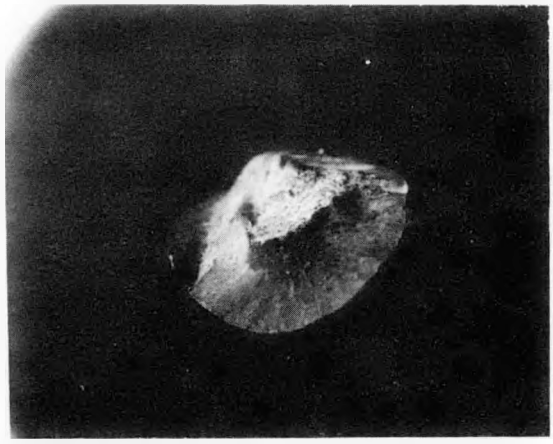

Figure 7-73. End of upper quill remnant.

CP267-7099

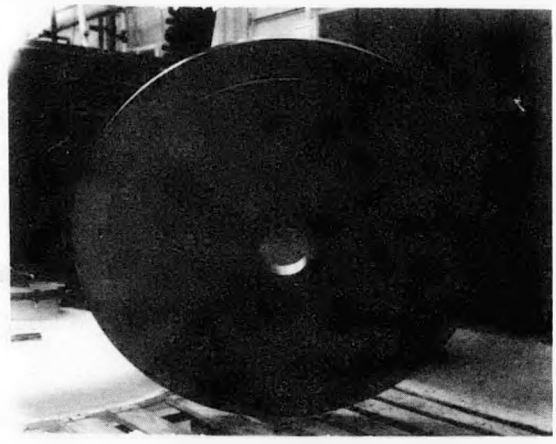

Figure 7-74. Underside of containment cover.

The instantaneous transition from a magnetically levitated position to one on mechanical touchdown bearings is believed to be due to a change in balance of the rotor. For reference, this was the first abrupt transition from magnetic suspension to have occurred in over 10,000 hours of testing. The possibility that transition occurred as a result of operating near or on a resonance was eliminated by earlier measurements which showed no reasonances within $\pm$1000 RPMs. Then, due to motions set up while on the mechanical touchdown bearings, the flywheel rim separated from the hub and fell to the bottom of the tank. The central hub and quill remained attached to the magnetic bearing shaft. The possibility that the broken quill, central hub and outer rim fell to the bottom of the tank as a unit was ruled out by several facts, including the final resting position of the central hub on top of the rim, the absence of scuff marks on the bottom face of the central hub, Fig. 7-6 , (that face showed no evidence that it had come in contact with the floor of the containment system), and the absence of circumferential scars on the outer surface of the central hub, Figs. 7-67 through 7-70. In fact, close examination of photographs, Fig. 7-67 through Fig. 7-70, shows rub marks in the vertical direction only and the surface areas between epoxy joints are unscarred. These features are compatible with a scenario in which the rotor rim separates from the hub and gently falls away to the bottom of the tank. Also, many of the epoxy joints are smooth with no attached Kevlar remnants, perhaps indicative of poor bonding in the epoxy joints.

Then either due to the flywheel rim bouncing up against the central hub and quill or due to the buildup of a whirl oscillation due to imbalance forces acting on the central hub, the quill bent and the edges of the hub struck the containment cover. Then the quill broke and the central hub fell on top of the rim. The key question remaining is why a change of imbalance occurred which led to the ultimate rotor failure. Several possibilities are plausible. Since the magnetic suspension system applies axial loads to the rotor unit during lift-off and operation, it is possible that one or more of the epoxy joints between the catenaries and hub failed due to fatigue. Another possibility is that undetected damage occurred to the rotor and that this weakness ultimately became magnified and resulted in larger and larger imbalances. Unfortunately, the exact reason could not be deduced from the available information.

7.3.4.5 Summary and Conclusions

The testing reported here for a GFE advanced composite rotor on magnetic suspension is the first attempted in the United States on a system with significant energy storage capability. This part of the Lincoln Laboratory flywheel project was exploratory in nature and was undertaken to develop an awareness of real and potential problems facing advanced magnetically suspended flywheel energy storage systems. A significant accomplishment during the test program was the fabrication and testing of a new, simplified, two-element magnetic bearing in conjunction with the advanced composite rotor. The new bearing design demonstrated a unit with lower parts count and potentially lower cost. Because of budgetary constraints, an existing advanced composite rotor, originally fabricated for a vehicular application, was tested rather than a rotor specifically designed and tailored for use on magnetic suspension. The GFE advanced composite rotor with tension-balanced catenary spokes was extremely flexible in the axial direction, the direction controlled by the magnetic servo loop, and it was probably the most challenging rotor design for use on magnetic suspension that could have been selected from among the available candidates. The presence of structural vibration frequencies of the

GFE advanced composite rotor in the operating region of the prototype system servo control loop interfered with control system performance and required that the control system be modified to attain lift-off and stable levitation. This was accomplished successfully.

The as-delivered GFE advanced composite rotor was found to be poorly balanced and it was necessary to rebalance the rotor by attaching balance weights to the inner rim surface, a situation that it is hoped will be eliminated in future "advanced" composite rotor designs. Also it was found that the composite rotor could not be balanced to the same low degree of imbalance achieved with a steel rotor. The advanced composite rotor also demonstrated significant outgassing effects during outgassing tests. The outgassing did not affect the present experiments because sufficient pumping capacity was available to maintain the desired test pressures but it would have significant effects, if not corrected on future designs, for terrestrial energy storage systems that are fielded with the hope of long periods between maintenance vacuum pump-downs. Selection of rotor construction materials that have low outgassing properties should be a prerequisite in future designs.

The rotor was actually tested to a maximum speed of 12,000 RPM, rather than to the goal of 15,000 RPM. The maximum attainable speed was limited by the development of an oscillation in the vertical (axial) direction which ultimately coupled to the radial direction causing radial oscillation amplitude buildup and finally touchdown on the mechanical touchdown bearings. The maximum operating speed did increase as the amount of external damping from mechanical dampers increased. However, it was found that significantly more damping is required for high-speed operation with the composite wheel than is required with the steel flywheel. The maximum speed of 12,000 RPM was achieved with two mechanical dampers in place.

Plans to complete the test series with a test of three-damper configuration were forestalled when problems were discovered in the magnetic bearing unit after the dual-damper test run. The lower magnetic bearing stator and rotor were found to require repair. The outer fringe ring of the stator had become partially unglued from the permanent magnets and the press-fit rotor had loosened on the shaft. The stator was restored to initial condition by mechanically

fastening the inner and outer fringe rings in place and the rotor was electron-beam-welded to the magnetic bearing shaft. The magnetic bearing was then reassembled and readied for testing.

After repair of the magnetic bearing unit, the system characteristics differed substantially from earlier test results and operating speeds of only 10,000 RPM or less could be achieved. Greater levels of imbalance were suspected of causing the degraded performance which manifested itself as an earlier onset of magnetic shaft oscillations. The precise reason for the new dynamic behavior could not be ascertained.

Subsequently, two-damper and single-damper tests were run to 9800 RPM and 10,000 RPMs, for the purposes of comparing performance to earlier runs and to obtain slow-down tare loss data. Slow-down tare losses for the two-element magnetic bearing system with dual damper and advanced composite rotor were found to be small from an absolute point of view, as had been observed in earlier prototype tests, but 50% larger than the prototype system. Slow-down tare losses for the single-damper case were found to be 30% higher than the prototype. Whether the increase in tare loss is due to higher internal damping losses in the composite rotor or due to larger losses in the new two-bearing design needs to be determined. While the rotor was being accelerated in the next test without damper, it inexplicably made a transition from magnetic suspension to mechanical touchdown bearings at a speed of 2,850 RPM. Normal rotor slow-down by power extraction was initiated. Attempts to relevitate the rotor on magnetic suspension were unsuccessful. Shortly thereafter, a failure of the rotor occurred at 1900 RPM.

The sequence of events during failure was reconstructed from examination of the evidence existing after failure. It was determined that the rotor separated from the central hub and fell to the bottom of the containment system. Subsequently, the quill was broken and the central hub with quill remnant fell on top of the rotor rim. A change in imbalance is suspected as the initiator of the failure. Whether the failure was due to fatigue of the epoxy bonds or was related to an intrinsic rotor weakness that amplified with time remains open.

The test series with the advanced composite rotor was an unqualified success though some difficulties were experienced during the tests. In addition to reaching a maximum speed of 12,000 RPM, much experience was gained. This experience has shown that the design of the magnetic suspension servo control system and the design of advanced composite rotors must be considered in concert rather than separately as has been the case to date. Much work still remains to be accomplished on structural vibration/control system coupling and on large magnetically suspended rotor systems capable of storing 20 kWh. The present advanced composite rotor stored less than one-twentieth of the energy that is required for a residential terrestrial PV storage application. Larger units should be constructed and tested.

REFERENCES

3-1 Millner, A. R., "Scaling Laws for Flywheel System Components," MIT Lincoln Laboratory Report No. COO-4094-63, 15 November 1979.

4-1 Millner, A. R., "Flywheel Components for Satellite Applications," MIT Lincoln Laboratory Technical Note 1978-4, MIT Lincoln Laboratory, Lexington, MA, 16 May 1978.

4-2 Millner, A. R., "A Low-Drag, Low-Power Magnetic Bearing," The Third International Workshop on Rare Earth-Cobalt Permanent Magnets and Their Applications, University of California, San Diego, CA, 27-30 June 1978.

4-3 J. Wolowit, et al, "A Theoretical and Experimental Investigation of the Magnetic Fields and Forces Arising in Magnetic Suspension Systems, NTIS AD/A-006109, January 1975, Mechanical Technology, Inc.

4-4 Standard Handbook for Electrical Engineers, A. E. Knowlton, Editor-in-Chief, Ninth Edition, pp. 660, McGraw-Hill Book Company, NY, 1957.

4-5 Britten, S. S., "Electromagnetic Field Analysis of a Magnetic Bearing Using New STRUDL Finite Elements," 21st ICES Users Group Conference, Dallas, TX, 1979.

4-6 ISES STRUDL--1, The Structural Design Language, Engineering User's Manual, MIT, Cambridge, MA 1968.

4-7 W. T. Thompson, F. C. Younger and H. S. Gordon, "Whirl Stability of Pendulously Supported Flywheel System," Transactions of ASME, June 1977.

4-8 T. L. C. Chen and C. W. Bert, "Whirling Response and Stability of Flexibly Mounted, Ring-Type Flywheel Systems," prepared for Sandia Labs under Contract No. 07-7843, SAND 78-7073, February 1979.

4-9 Bolotin, Non-Conservative Problems in the Theory of Elastic Stability, McMillan Company, NY, 1963, p. 139-198.

4-10 Wiegel, R. L., Earthquake Engineering, Coordinating Editor, Prentice-Hall, NY, 1970.

4-11 Neal, R. W., "Assessment of Distributed Photovoltaic Electric Power Systems," EPRI Solar Energy Program Review, 26-28 August 1980, Rockport, ME, RP 1192-1.

4-12 "American National Standard-Building Code Requirements for Minimum Design Loads in Buildings and Other Structures," ANSI A58.1-1972 American National Standards Institute, Inc., 1430 Broadway, New York, NY 10018.

4-13 Theodorsen, T. and Regier, A., "Experiments on Drag of Revolving Discs, Cylinders and Streamline Rods at High Speeds," NASA Report No. 793, 1945.

References (con'd)

7-1 W. H. Brauer, F. C. Younger, "Conceptual Design of a Flywheel Energy Storage System," 1980 Flywheel Technology Symposium, p. 287, Scottsdale.

7-2 "Evaluation of Bidirectional Weave Composite Flywheel Materials," Mechanical Energy Storage Technology Project Report for 1979, p. 86, UCRL-50056-79, May 1980.

7-3 Kern, E. C., "Gearing Up for Homeowners," Solar Age, March 1981.

7-4 Personal communication with Robert Steele, Oak Ridge, TN, August 1981.

Appendix 4-1

Maximum-Power-Point Computer Program

```
Tektronix  8080/8085 ASM V3.1                                    Page     1

00001                    ;MARKDOWN TRACKER
00002                    ;**********
00003                    ;INITIALIZATION ROUTINE
00004                    ;**********
00005       0000     >          ORG      0000H
00006 0000 F3            START  DI
00007 0001 3E01                 MVI      A,1       ;INITIALIZE PORT A OUTPUT AND
00008 0003 D300                 OUT      0         ;  PORTS B & C AS INPUTS
00009 0005 32F03F    >          STA      DIR       ;INIT DIRECTIPPN = UP
00010 0008 3E10                 MVI      A,10H
00011 000A 32F13F    >          STA      COUNT     ;INIT COUNT = 10000000
00012 000D 210000               LXI      H,0
00013 0010 22F23F    >          SHLD     OLD
00014 0013 22F43F    >          SHLD     NEW
00015 0016 3E40                 MVI      A,40H     ;OUTPUT A HIGH TO BLK & CONV
00016 0018 30                   SIM                ;TO END CONVERSION
00017                    ;**********
00018                    ;BEGINNING OF MAIN LOOP OF PROGRAM
00019                    ;**********
00020 0019 2AF23F    >  LOOP   LHLD     OLD
00021 001C 4D                   MOV      C,L
00022 001D 44                   MOV      B,H
00023 001E 2AF43F    >          LHLD     NEW
00024 0021 08                   BYTE       08      ;SUBTRACT BC FROM HL REGS
00025 0022 CA3400    >          JZ       EQUAL     ;IF NEW = OLD,DIR = NOT MSB OF COUNT
00026 0025 F24900    >          JP       NODIR     ;IF NEW > OLD,DIR = DIR
00027 0028 3AF03F    >  LESS   LDA      DIR       ;ELSE DIR = NOT DIR
00028 002B 1F                   RAR
00029 002C 3F                   CMC
00030 002D 17                   RAL
00031 002E 32F03F    >          STA      DIR
00032 0031 C34900    >          JMP      NODIR     ;AND GO CHANGE COUNT
00033 0034 3AF13F    >  EQUAL  LDA      COUNT
00034 0037 FEFA                 CPI      0FAH       ;NEAR DUTY 1
00035 0039 D24400    >          JNC      TBIG
00036 003C 3E01                 MVI      A,01H     ;SET DIR = UP
00037 003E 32F03F    >          STA      DIR
00038 0041 C34900    >          JMP      NODIR
00039 0044 3E00          TBIG   MVI      A,00H
00040 0046 32F03F    >          STA      DIR
00041 0049 3AF03F    >  NODIR  LDA      DIR
00042 004C FE00                 CPI      0         ;IF DIR = 0
00043 004E 3AF13F    >          LDA      COUNT
00044 0051 CA5E00    >          JZ       DECR      ;GO DECREMENT COUNT
00045 0054 FEFD                 CPI      0FDH      ;IF COUNT = FD DONT INCREMENT COUNT
00046 0056 D26500    >          JNC       OUTCN
00047 0059 C601                 ADI      1         ;ELSE INCREMENT COUNT
```

```
00048 005B C36500  >          JMP     OUTCN
00049 005E FE00       DECR    CPI     0       ;IF COUNT = 0 DONT DECREMENT COUNT
00050 0060 CA6500  >          JZ      OUTCN
00051 0063 C6FF               ADI     0FFH    ;COUNT = COUNT - 1
00052 0065 32F13F  >  OUTCN   STA     COUNT
00053 0068 D301               OUT     1
Tektronix  8080/8085 ASM V3.1                                   Page     2

00054 006A 2AF43F  >          LHLD    NEW
00055 006D 22F23F  >          SHLD    OLD     ;SAVE NEW IN OLD
00056                 ;DELAY FOR 50 MS
00057 0070 210000             LXI     H,0000H
00058 0073 2B         AGAIN   DCX     H
00059 0074 7D                 MOV     A,L
00060 0075 FE00               CPI     0
00061 0077 C27300  >          JNZ     AGAIN
00062 007A 7C                 MOV     A,H
00063 007B FE00               CPI     0
00064 007D C27300  >          JNZ     AGAIN
00065                 ;GET NEW INPUT AND AVERAGE 32 READINGS
00066 0080 210000             LXI     H,0     ;INIT HL REG AS ACCUMULATOR
00067 0083 1E20               MVI     E,20H   ;SET FOR 32 ADDITIONS
00068 0085 3EC0       LOOP2   MVI     A,0C0H
00069 0087 30                 SIM     ;OUTPUT A LOW TO START CONVERSION
00070 0088 DB03       LOOP1   IN      3       ;CHECK DATA READY
00071 008A E604               ANI     4       ;IF CONVERSION NOT DONE
00072 008C C28800  >          JNZ     LOOP1   ;LOOP BACK
00073                 ;CONVERSION DONE SO GET DIGITAL DATA
00074 008F DB02               IN      2       ;GET LSB 8 BITS
00075 0091 4F                 MOV     C,A
00076 0092 DB03               IN      3       ;GET MSB 2 BITS
00077 0094 E603               ANI     3       ;SAVE 2 BITS
00078 0096 47                 MOV     B,A
00079 0097 09                 DAD     B       ;ADD INTO ACCUMULATOR
00080 0098 3E40               MVI     A,40H   ;OUTPUT A HIGH TO STOP CONVERSION
00081 009A 30                 SIM
00082 009B 1D                 DCR     E
00083 009C C28500  >          JNZ     LOOP2   ;AVERAGE 32 READINGS
00084 009F 10                 BYTE    10H     ;SHIFT RIGHT
00085 00A0 10                 BYTE    10H
00086 00A1 10                 BYTE    10H
00087 00A2 22F43F  >          SHLD    NEW     ;SAVE NEW AND
00088 00A5 7C                 MOV     A,H
00089 00A6 FE0E               CPI     0EH
00090 00A8 DA1900  >          JC      LOOP
00091 00AB 3E00               MVI     A,00H
00092 00AD 32F03F  >          STA     DIR
00093 00B0 C34900  >          JMP     NODIR
00094 00B3 C31900  >          JMP     LOOP    ;LOOP BACK
00095                 ;***********
00096                 ;CONTANTS
```

```
00097                   ;************
00098      3FF0     >           ORG     3FF0H
00099 3FF0 00           DIR     BYTE      0
00100 3FF1 00           COUNT   BYTE      0
00101 3FF2 0000         OLD     WORD      0
00102 3FF4 0000         NEW     WORD      0
00103 3FF6 0000         SVHL    WORD    0
00104      0000     >           END     START
Tektronix  8080/8085 ASM V3.1                          Page     3


Scalars

   A ------ 0007          B ------ 0000          C ------ 0001          D ------ 0002          E ------ 0003
   H ------ 0004          L ------ 0005          M ------ 0006          PSW ---- 0006          SP ----- 0006

XFLYOB (default) Section (3FF8)

   AGAIN -- 0073          COUNT -- 3FF1          DECR --- 005E          DIR ---- 3FF0          EQUAL -- 0034
   LESS --- 0028          LOOP --- 0019          LOOP1 -- 0088          LOOP2 -- 0085          NEW ---- 3FF4
   NODIR -- 0049          OLD ---- 3FF2          OUTCN -- 0065          START -- 0000          SVHL --- 3FF6
   TBIG --- 0044


  104 Source Lines     104 Assembled Lines   14837 Bytes available

          >>> No assembly errors detected <<<
```

Appendix 6-1

FLYWHEEL STORAGE FOR PHOTOVOLTAICS:
AN ECONOMIC EVALUATION OF TWO APPLICATIONS

Thomas L. Dinwoodie

MIT Energy Laboratory Report No. MIT-EL-80-002

February 1980

ABSTRACT

A worth analysis is made for an advanced flywheel storage concept for tandem operation with photovoltaics currently being developed at MIT/Lincoln Laboratories. The applications examined here are a single-family residence and a multi-family load center, 8 kWp and 100 kWp, respectively. The objectives were to determine optimal flywheel sizing for the various operating environments and to determine the financial parameters that would affect market penetration. The operating modes included both utility interface and remote, stand-alone logics. All studies were performed by computer simulation.

The analysis concludes that flywheel systems are more attractive in residential applications, primarily because of differences in financing parameters and, in particular, the discount rate.

In all applications flywheel storage is seen to increase the optimum size of a photovoltaic system. For stand-alone environments, optimum configuration sizing is fairly insensitive to hardware cost of photovoltaics and flywheels for a given reliability when no diesel generator is included.

Overall, the worth analysis finds a high sensitivity in the areas of discount rate, PV capital cost, flywheel capital cost, and diesel fuel costs.

ACKNOWLEDGMENTS

The author gratefully acknowledges Dr. Alan Millner, Project Manager, for his assistance in preparing this document.

Also, a special thanks is extended to the Salt River Project, and specifically James Watkins and Marilyn George on their expedient handling of the institutional and technical barriers in supplying M.I.T. with the customer load profile data essential to the load center portion of this study.

Finally, many thanks to the members of the M.I.T. Energy Laboratory Photovoltaics Project, especially Dr. Richard Tabors, Project Manager, and Alan Cox. Where would the discount rate be without them?

This project was funded by the M.I.T. Lincoln Laboratory under contract 87861.

CONTENTS

CONTENTS (continued)

TABLE OF FIGURES

TABLE OF FIGURES (continued)

TABLE OF FIGURES (continued)

Chapter I. INTRODUCTION

This paper addresses economic issues that define the market environment for the advanced flywheel energy storage concept now being investigated by MIT/Lincoln Laboratories. The application is supplemental storage to photovoltaic energy conversion systems on the scale of 8-kWp and 100-kWp array sizes, as utilized by a residential and a multi-family load center, respectively.

Previous studies have indicated that total system energy capture by solar-electric conversion systems can be improved by 46-58 percent with the addition of a storage capacity roughly equivalent to an average one-day residence demand.[1] It has also been established that conventional flywheel energy storage is neither technically nor economically competitive with batteries.[2] However, for use in conjunction with photovoltaics in a residential configuration, it is suggested that flywheels can offer certain specific advantages over analogous battery functions. These advantages are obtainable only in a total system configuration, where the flywheel does not simply serve the single purpose of energy storage, but covers the function of power inversion and maximum power tracking as well. In addition, the new advanced concept incorporates magnetic bearing suspension, which cuts drag losses to levels previously unconsidered. Figure 1 illustrates where technical simplicity and cost savings find potential with this new concept in comparison with the battery/inverter and conventional flywheel/inverter systems. For a further account of design specifications, critical design areas, and development status, see [2].

---

*This project was funded by the MIT Lincoln Laboratory under contract 87861.

SOLAR PV SYSTEM COMPARISON

1. BATTERY SYSTEM

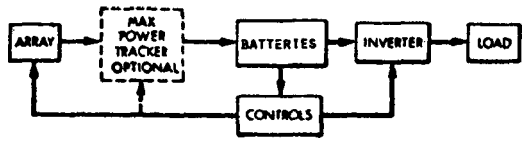

2. FLYWHEEL STORAGE PLUS INVERTER

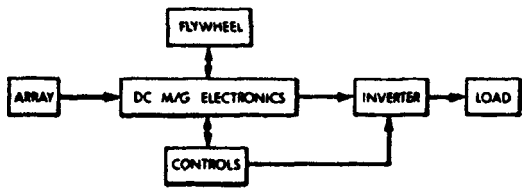

3. FLYWHEEL STORAGE AND CONDITIONING

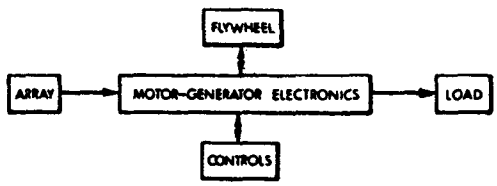

FIGURE 1

Chapter II. ORGANIZATION OF THE STUDY

II.1 Study Objectives

There were two objectives to this study. First, the appropriate sizing of a flywheel unit had to be determined for two application types: a single-family residence utilizing a PV array of roughly 8-kWp capacity, and a multi-family load center utilizing an array size of roughly 100 kWp. The second objective was to simulate a range of technical and economic environments to determine sensitive market parameters.

II.2 Environments

Figure 2 shows an outline of the technical operating environments that provided the basis for testing market sensitivities. The utility interface studies were aimed primarily at determining the significance of various utility policies, including utility purchase prices for excess PV electricity and the utility rate structure, on the effect of flywheel storage on overall system worth.

The stand-alone studies included remote, non-grid-connect applications where all electricity demands, at a required reliability, were assumed to be supplied by the PV and flywheel (or PV, flywheel and diesel) system alone. The effort here was directed toward the issues of optimum configuration sizing, the cost of supply at a specified level of reliability, and the determination of distances from the distribution grid at which such a stand-alone system represented an economically viable alternative to grid-connection.

ENVIRONMENTS

- UTILITY INTERFACE (FLAT RATE AND T·O·D)
  - PV FLYWHEEL
  - FLYWHEEL (T·O·D RATES)

- STAND-ALONE ANALYSIS
  - PV FLYWHEEL
  - PV FLYWHEEL DIESEL

FIGURE 2

II.3 Assumptions

Any study utilizing computer simulation with parametric variation is accompanied by a host of technical, logical, or economic modeling assumptions. The technical assumptions relate to the physical operational aspects of the hardware units employed; in this case, the flywheel and photovoltaics. Figure 3 summarizes these technical assumptions. Figure 4 lists methods for allocating and transferring watt-hours of energy within the simulation model, defined as program logic assumptions.

This study benefits from an economics routine with fairly broad capabilities for modeling the economic environment likely to exist over the operating life of the system. The assumptions defining this environment must be separated into several categories. First, the residence application must be separated from the larger load center application to reflect the difference in financing and construction characterizing these two types of projects (see Figures 5 and 6). Utility-interfaced operation requires assumptions as to the pricing environment for displaced utility electricity; these prices are listed in Figure 7. Finally, Figure 8 lists all hardware costs assumed in this study.

All figures in this paper are in 1980 dollars unless otherwise indicated.

Figure 3

Technical Assumptions

FLYWHEEL

- Efficiencies

fixed loss:	200 watts
charge proportional:	.3 percent/hour
input electronics:	8 percent full load
	7 percent half load
output electronics:	8 percent full load
	7 percent half load
motor-generator:	4 percent full load
	2 percent half load

- Maximum storage capacity set to vary.
- Minimum storage capacity set to .25 max.
- Maximum input electronics charge capacity (in kW) set to vary as .14 times the area of the collector in m^2.
- Maximum output electronics discharge capacity (in kW) set to vary as the peak demand divided by .9.

PV

Cell efficiency (at 28° C): .12
Cell efficiency temperature coefficient: .004
Average cell efficiency: .10
Tilt angle: latitude + 10°

DIESEL

Heat rate: 11,333 Btu/kWh

Figure 4

Logic Assumptions

Utility Interface

Distributed-dedicated storage logic modeled for operation of PV/flywheel system (flywheel is not charged by the utility)

Distributed-system storage logic modeled for operation of flywheel alone (with no PV, flywheel is charged by the utility).

Stand-Alone

Diesel generator rated to 2.33 times the average kWh demand level.

Diesel is not used to charge the flywheel but rather serves only as an instantaneous power backup.

Figure 5

Residence Application Initial Economic Assumptions

- 20-year system life
- 0 construction years
- 3-percent real discount rate
- Electricity price escalator: 3 percent/year
- Grid costs for single-phase line: $8,712/mile
- Diesel costs

  Diesel generator:
  Regression formula to fit current manufacturers costs

  Diesel fuel:
  Escalation rates vary given 55¢/gal wholesale, second quarter 1979 cost
  Escalation rate fixed at 6.6 percent/year after 1985

- Balance-of-system Costs

  -- High estimate:

  Array material and installation.....$14.3/m2
  Lightning protection.....$943.00
  Electrical equipment and installation....$522.00
  Operation and maintenance.....$70/yr.

  Figures include 15-percent distribution and 15-percent contractor mark-up

  Source: G.E./SANDIA Executive Summary (vol. 1) January 1979 (ref. 3).

  -- Low estimate:

  PV array size proportional: $20.80/$m^2$.

Figure 6

Multi-Family Load Center
Initial Economic Assumptions

- 20-year system life
- Balance of systems (BOS) costs of $20.80/m2
- 2-year construction period
- Sum-of-the-years digits depreciation

  No depreciation during construction
  40-percent debt/(debt + equity) ratio
- Investment tax credits of 10 percent
- Grid costs per mile:

  3 phase line $14,229/mile
- Diesel costs

  Diesel generator:

  Regression formula to fit current manufacturers costs

  Diesel fuel

  Escalation rates vary given 55¢/gal wholesale, second quarter 1979 start cost fixed at 6.6 percent/year thereafter

Figure 7

Utility Rate Structures

- Electric Rate Structures (1980 $)

Phoenix

Flat Rate	$.066/kWh
TOD Rate	
TOD season:	April 1 - November 1
Peak period:	10 A.M. - 8 A.M.
Peak price:	$.071/kWh
Base price:	$.061/kWh

Boston

Flat Rate	$.0523/kWh
TOD Rate	
TOD season:	April 15 - August 15
Peak period:	Noon - 3 P.M.
Peak price:	$.125/kWh
Base price:	$.0498/kWh

- Exogenous price inflation for electricity fixed at 3 percent/year.

FIGURE 8

COST ASSUMPTIONS

FLYWHEEL COSTS

ESTIMATED UNIT PRICE OF FLYWHEEL ENERGY STORAGE AND CONVERSION SYSTEM - 1985 (1980 $):

ITEM	LOW 1985 (LOW)	MEDIUM (1985 HIGH)	HIGH (CURRENT 1978)
ROTOR	$70/KWH	$140	$280
MOTOR-GENERATOR	105/KWAC	140	162
MAG. BEARING	14/KWH	28	105
VACUUM HOUSING	35/KWH	56	60
ELECTRONICS (GEN)	42/KWAC	140	140
ELECTRONICS (MOTOR)	42/KWAC	105	140
ENCLOSURE	34/KWH	45	45
SHAFT & HUB			34/KWH

PV COSTS

PV ARRAY ESTIMATES ARE DOE GOALS FOR 1985:

	1975 ($)	1980 ($)
LOW	$0.20/PK WATT	$0.28
MEDIUM	0.50	0.70
HIGH	0.65	0.91

II.4 Definitions

Breakeven Capital Cost

Throughout the analysis, the term Breakeven Capital Cost (BECC) is used in judging system or component worth. By standard definition, Breakeven Capital Cost is defined as:

$$BECC = \sum_{i=1}^{life} \frac{BENEFITS-COSTS}{(1+r)^i}$$

where:

BENEFITS = total dollar equivalent of utility electricity displaced by the PV-flywheel system; plus, for stand-alone applications, distribution-line costs otherwise incurred.

COSTS = All costs of the system not to be included in the BECC figure.

LIFE = Assumed lifetime of the system is 20 years.

r = discount rate.

In calculating System Breakeven Capital Cost, the COSTS figure includes none of the costs associated with any component of the system. It thereby defines the total benefits that accrue to the system over its lifetime. Hence, the system BECC must account for all costs associated with: (1) the flywheel storage unit, (2) the PV modules, and (3) all balance of system. This includes all maintenance over the lifetime of the system.

The flywheel Breakeven Capital Cost maintains the original definition for BENEFITS, but defines COSTS as the balance of PV system costs plus PV module prices at an assumed module cost. Hence, it is important to note that when PV prices are attached to curves in the BECC graphs, they serve only as labels to describe the cost assumption made on

the module component of the PV system, which is in addition to fixed BOS costs.

Flywheel Capacity

It is also necessary to define the term Flywheel Capacity. One characteristic of the flywheel is that its minimum state of charge be no less than 25 percent of its maximum charge capacity. The labels applied to the flywheel throughout specify this maximum charge capacity; hence, its real energy storage value is actually only 75 percent of this figure. Furthermore, losses are associated with the input and output electronics as well as the storage unit itself, the average storage capacity is reduced further. A rough approximation to the real storage capacity can be obtained by applying a factor of 0.62 to the labeled storage capacity figure (see [2]).

A Note on Analyzing System Value

One of the principal methods of worth analysis employed by this study is SYSTEM VALUE (or System BECC; see above). This has proven instrumental in comparing the effects of market parameters on total system operation. There are primarily two reasons why this has been important.

First, all studies to date have acknowledged that storage and photovoltaics are "competitive," in the sense that they each vie for displacing the first (and generally, most valuable) watt-hours of alternatively obtained electricity (either from the utility or from a diesel generator). The component that is capable of supplying energy coincident in time with a highly valued, closest alternative will render

the greatest increment in system benefits in return. However, there are obvious functional and logical contingencies in a dual flywheel and PV application that restrict their system performance below the additive value of each, defined if each were to operate (and be valued) independently of the other. Hence, whereas it is certainly useful to investigate the effect of one component technology upon the economics of another, the entire story cannot be told here. System operation is fundamentally different from the summation of component operation.

This leads directly to the second reason for analyzing system value. Worth provides a rather safe comparative tool when examining the effects of sizing and market parameter trade-offs. This is because system hardware costs, at this point, can only be described in terms of goals, and the system BECC definition maximizes information content about a system with minimum reliance on market uncertainties. In addition, when system value is defined in terms of the worth of conventional electricity displaced, it takes on a special significance as energy policy becomes directed away from reliance on conventional fuels.

II.5 The SOLIPS Model and Data Base

This analysis was performed on the basis of computer simulation studies performed with the Solar Interactive Photovoltaic Simulator (SOLIPS)*. This model was designed to provide full kilowatt-hour energy consumption accounting for use in photovoltaic applications analysis. An economics package is attached and is capable of translating energy transfer summations into net present worth and breakeven capital cost

---

*The SOLIPS model was developed by the author and the economics package was developed by Mr. Alan Cox, both of the M.I.T. Energy Laboratory.

figures, subject to specification of pertinent pricing, construction, and investment parameters. The model requires hourly energy demand profiles and solar weather data for the specific cases. Solar data for this study is provided by SOLMET. Load profile data was obtained by two means: The multi-family load center was represented by an actual demand tape for a master-metered apartment complex in Phoenix, Arizona; and the residence demand tape was created by the use of an existing model for residential energy consumption.

Chapter III. RESULTS

III.1 Single-Family Residence

III.1.a Utility Interface

Flat Rate

Solar and load profile data were obtained for sites in Boston and Phoenix, and are considered characteristic of the northeast and southwest geographic regions. Figure 9 outlines the issues crucial to this study and lists the simulation parameters that were varied. Figure 10 presents two graphs, which lay the groundwork for the utility-interface analysis. The case shown is for a Phoenix residence purchasing electricity from the grid at a flat rate; the utility does not purchase excess PV electricity.

The upper graph examines the effect of varying both PV array size and flywheel capacity on system breakeven capital cost. Note that the labels associated with flywheel capacity represent maximum charge capacity and that the real storage value is, in fact, roughly 0.62 times the labeled value (see "Definitions"). For 0-percent utility buyback, each configuration would be expected to reach an asymptotic benefit value as array size increased. In the zero flywheel case, for example, increasing the array size can at best serve only the solar-hour portion of the load, with no benefits accruing to electricity generated in excess of each hour's residence demand. As flywheel capacity is increased above zero, the displacement of utility electricity is extended beyond the solar fraction of the day. However, system benefits are again limited to an asymptote, since fixing the flywheel capacity restricts the number of watt-hours displaced by the system in the nonsolar hours.

This figure also reveals the diminishing returns that accrue to an increase in flywheel capacity. The finite demand of the residence over

FIGURE 9

UTILITY INTERFACE

PV + FW

ISSUES

- EFFECT OF FW ON SYSTEM WORTH
- SIGNIFICANCE OF UTILITY BUY-BACK RATE
- SIGNIFICANCE OF UTILITY RATE STRUCTURE

PARAMETERS VARIED

- UTILITY RATE STRUCTURE
- UTILITY BUY-BACK RATE
- COMPONENT SIZES

MEDIUM COST RANGE FOR HARDWARE COMPONENTS ASSUMED

FIGURE 10

UTILITY INTERFACE PV FLYWHEEL

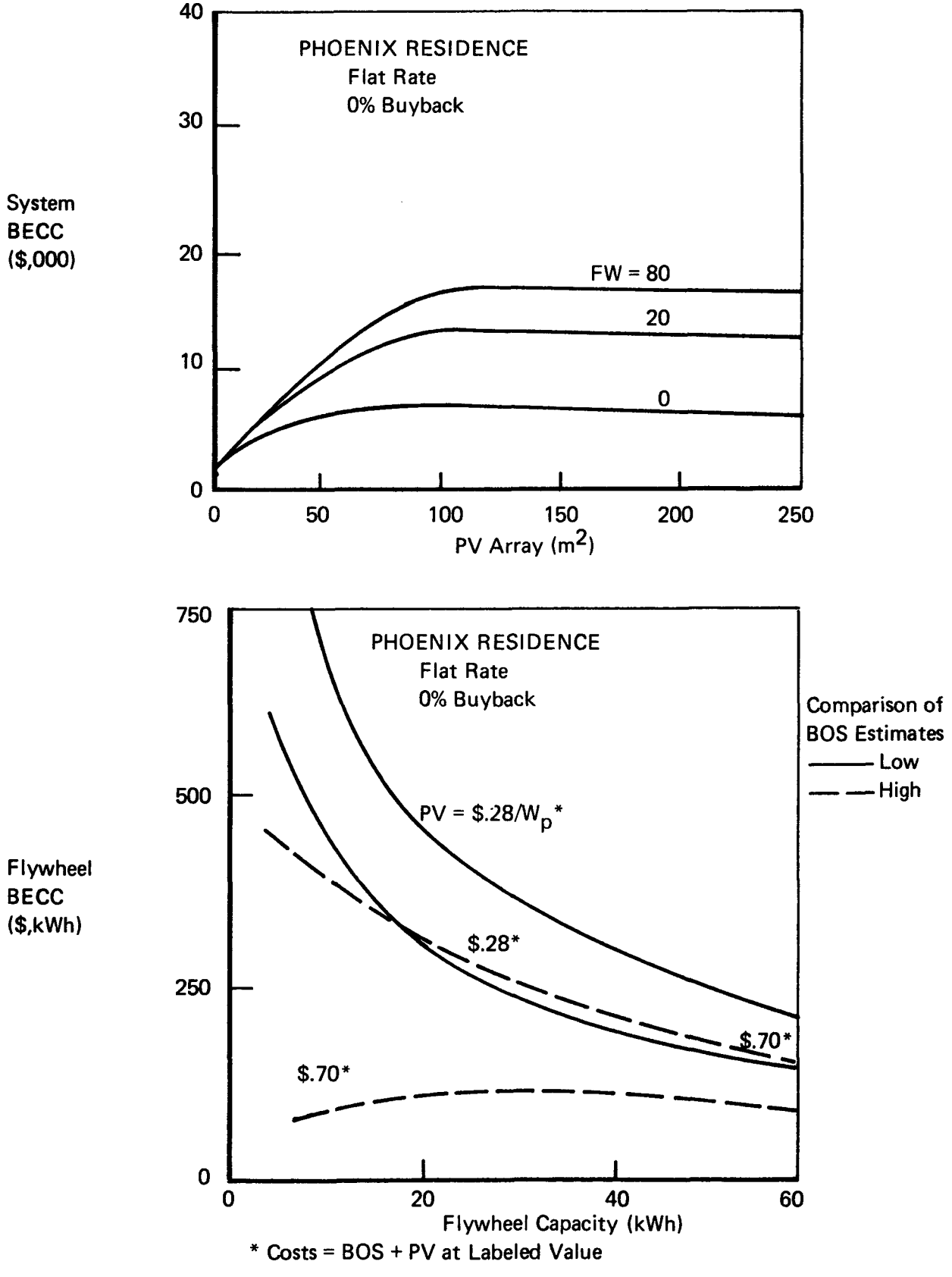

the year represents a maximum possible value for benefits when defined in terms of utility electricity displaced. Increasing flywheel capacity beyond what is necessary to service the nonsolar portions of the day leaves an increasing proportion of the storage capacity redundant and underutilized.

Accepting the shapes of the curves as reasonable, we can interpret the significance of the system dollar values. In this figure, any point along a given curve reveals the total dollar amount that could be afforded for the purchase of the correspondingly sized flywheel and PV array so the investor would break even in terms of total costs equaling total benefits. This sum includes all costs associated with all components of the alternative energy system, including operation and maintenance over an assumed 20-year system lifetime. If the summation of all costs to the investor lies below this curve, then there would be sufficient financial incentive to invest in the PV and flywheel system.

Another important feature of the flywheel as revealed by this graph has been found to be true of storage in general. This is the shifting of optimum PV array size to the right as storage capacity is increased. This is true since more PV electricity is required to justify an incremental addition of energy storage capacity.

The lower curve of Figure 10 maps out the total cost to which only the flywheel component of the system would have to decline before net positive benefits began to accrue. This dollar sum includes all costs associated with the flywheel, again including operation and maintenance over the 20-year system lifetime. To establish this figure it was necessary to estimate a cost for all nonflywheel components, including

the PV modules and balance of PV system. The estimates for Balance of System Costs were fixed at both the high and low values as defined in Figure 5. Flywheel breakeven costs are contrasted by the solid and dashed curves. For each BOS cost assumption, the cost of the PV module component was varied. Note again that the PV cost labels are merely indicative of the estimate used for the PV module component of the system. What follows directly from the figure is that the first kilowatt-hours of storage capacity are the most valuable to flywheel capacity, again revealing the phenomenon of diminishing returns. Taking the PV system costs as BOS + $ .70Wp, it is seen that a 40-kWh flywheel would have to sell for roughly $200/kWh total cost before adding any net value to the system when BOS costs are low, and just under $100/kWh for high cost BOS components.*

Figure 11 examines the case where the utility agrees upon a purchase price for excess PV electricity of 50 percent of its current (instantaneous) price to the customer. Under these conditions, benefits continue to accrue to the system for all electricity generated beyond that demanded by the residence. However, the incremental value of adding storage is seen to diminish over the no-buyback case.

For the lower set of curves involving flywheel BECC, it is necessary to label, in addition to module cost assumptions, the PV-array sizes, since the optimum configuration match (in terms of maximizing flywheel BECC) to any flywheel capacity always involves the addition of more PV. This is because the return on the PV investment, even when valued at 50

---

*The cost figures in the lower graph of Figure 10 are optimum in the sense that they result from finding the maximum flywheel BECC figure at each flywheel capacity over the range of PV array sizes. Hence this figure is established for optimum component (flywheel and PV) matches.

FIGURE 11

UTILITY INTERFACE PV AND FLYWHEEL SYSTEM

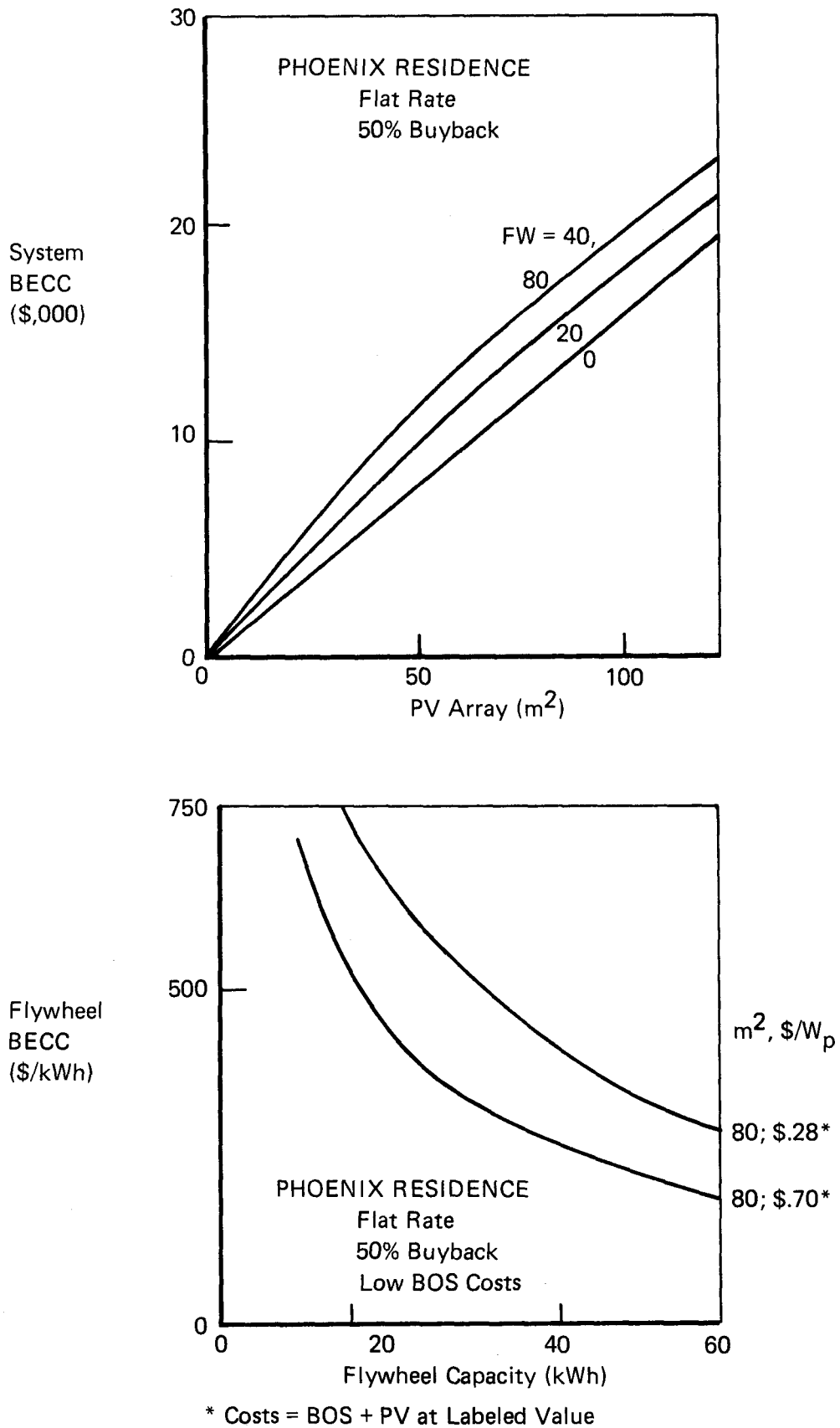

* Costs = BOS + PV at Labeled Value

percent of the price of utility electricity, totals a figure larger than the projected cost of the investment. These positive net benefits can then be applied to the purchase of a flywheel unit to yield the investment indifference values shown. Figure 12 depicts this relationship of PV array size to flywheel BECC.

By not fixing the PV cost assumption, but rather by assuming that PV costs are set at their non-storage-supplemented breakeven value at each buyback rate, the true relationship of just storage benefits (not "system" benefits) to buyback rate is exposed. This is shown in Figure 14. Two issues are readily apparent from this figure: First, storage looks best at the low buyback rates, and second, returns per kWh of flywheel capacity decrease as storage capacity is increased.

Time-of-Day-Rates

Figures 15 and 16 repeat the conditions of Figures 10 and 11 but assume that the utility adopts a time-of-day pricing scheme (outlined under "Cost Assumptions"). Comparison of Figures 15 and 16 indicates that a negligible increase in benefits accrues as a result of switching to the assumed time-of-day price structure. This cannot be regarded as revealing, however, since the differential rate structure used lasted for only a single season (summer), with only a 1.16/1 peak-to-base price ratio.

The sensitivity of cost figures to variations in time-of-day rates is explored in the Boston residential time-of-day study. Figure 17 presents the 50-percent buyback case for the rate structure described in Figure 19a, whereas Figure 18 presents the same case for the rate structure outlined in Figure 19b. Both sets of rates are within the range of reasonable utility policies. By extending the time-of-day

FIGURE 12

UTILITY INTERFACE:

EFFECT OF PV ARRAY SIZE ON

FLYWHEEL BREAKEVEN CAPITAL COST

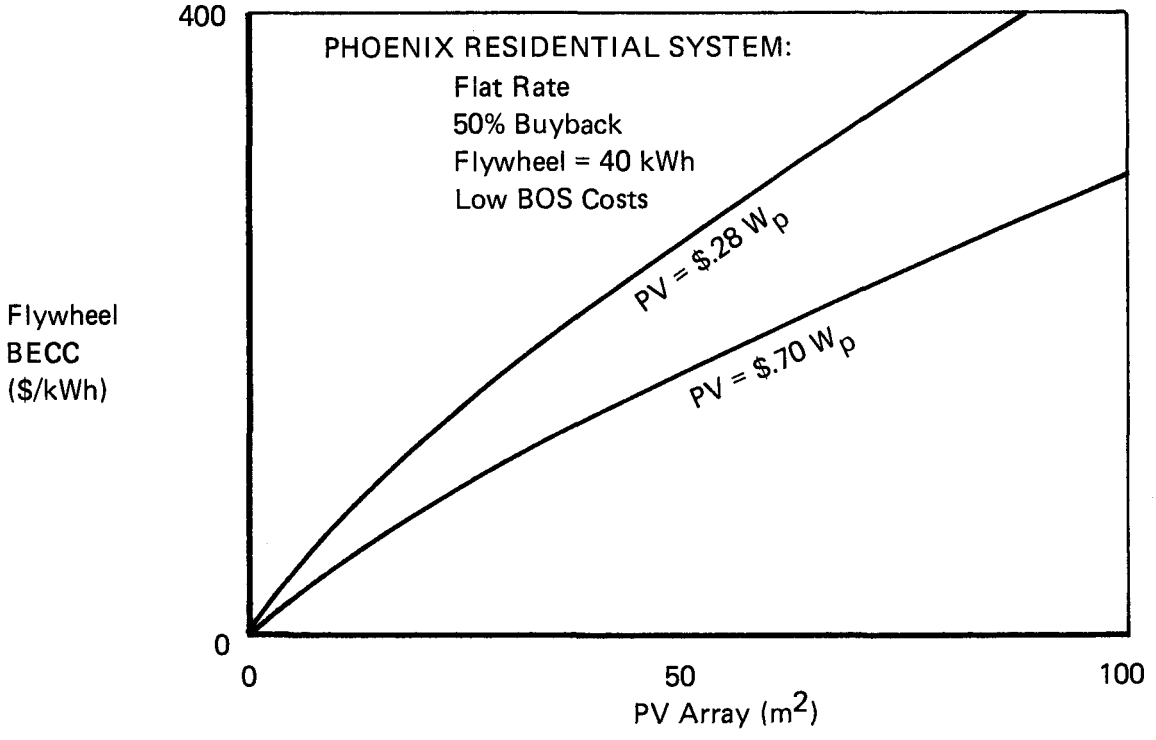

FIGURE 14

INFLUENCE OF UTILITY BUYBACK RATE ON FLYWHEEL WORTH

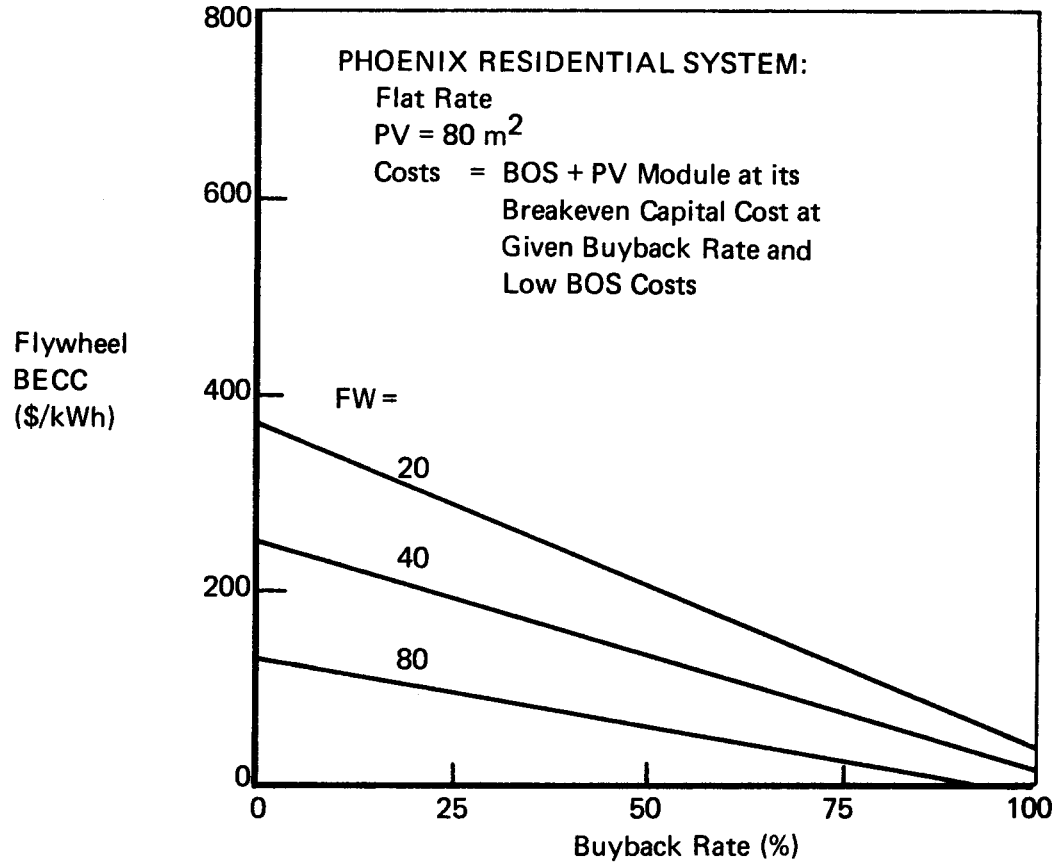

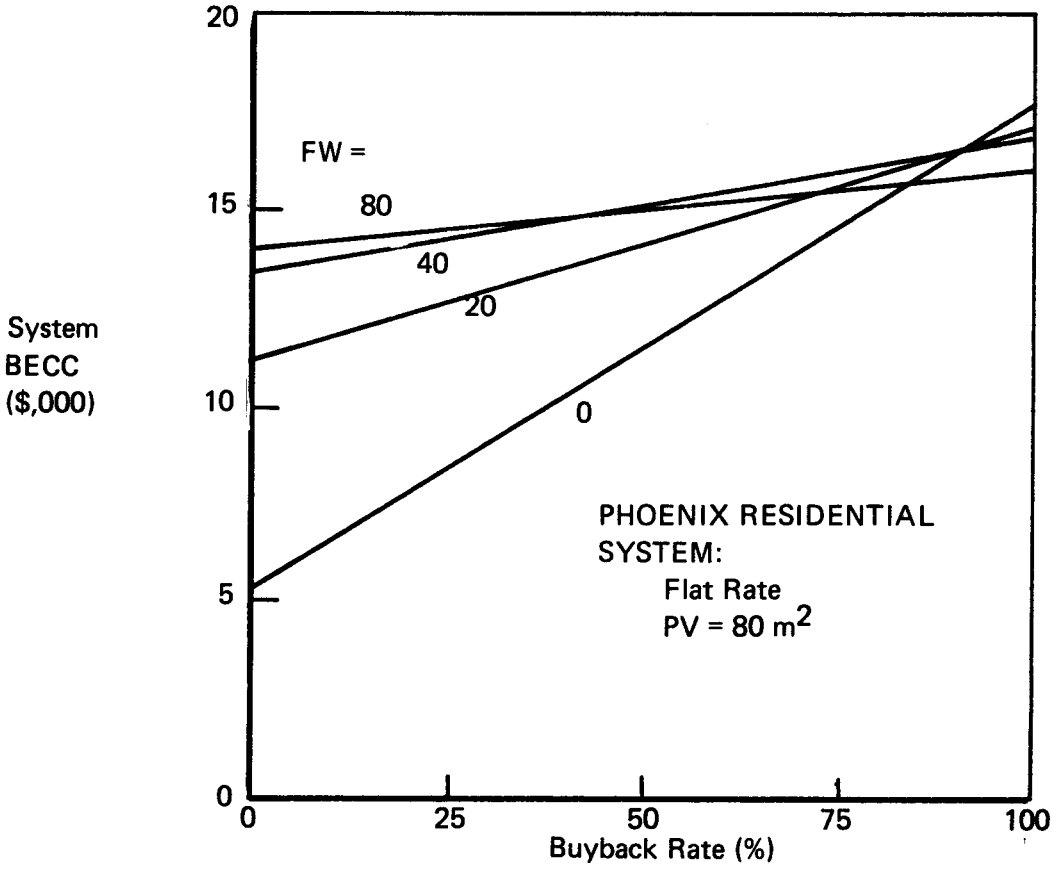

FIGURE 15

UTILITY INTERFACE/PV AND FLYWHEEL SYSTEM

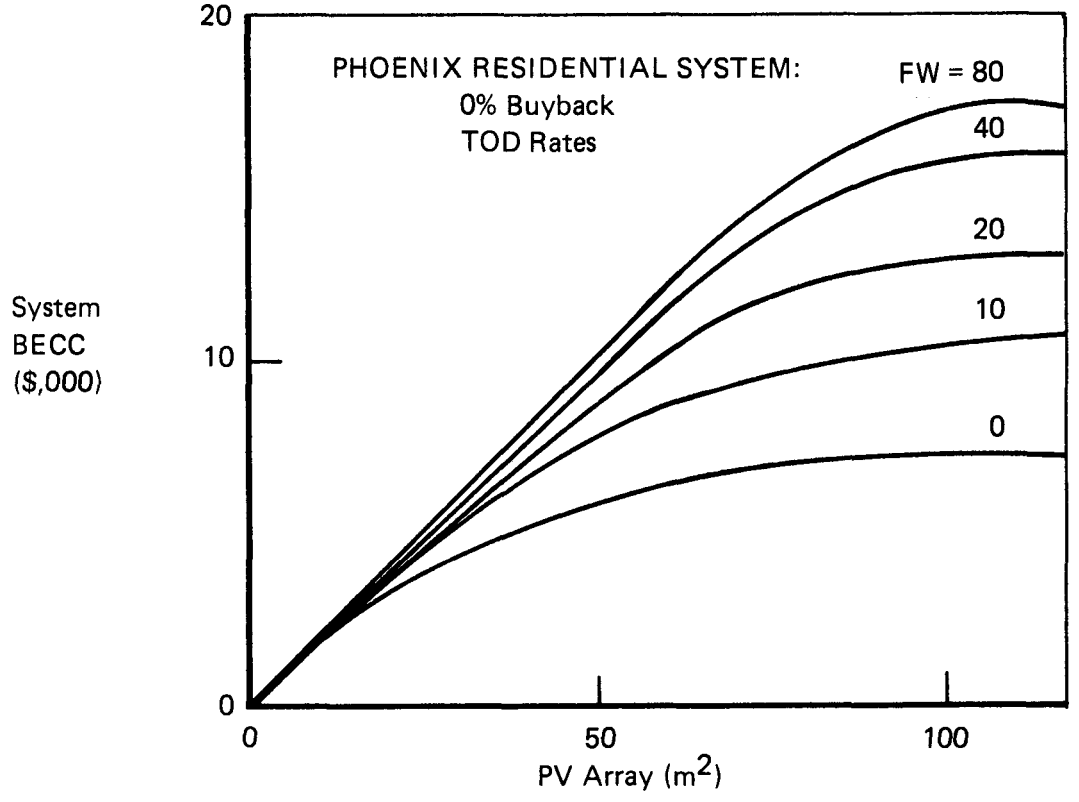

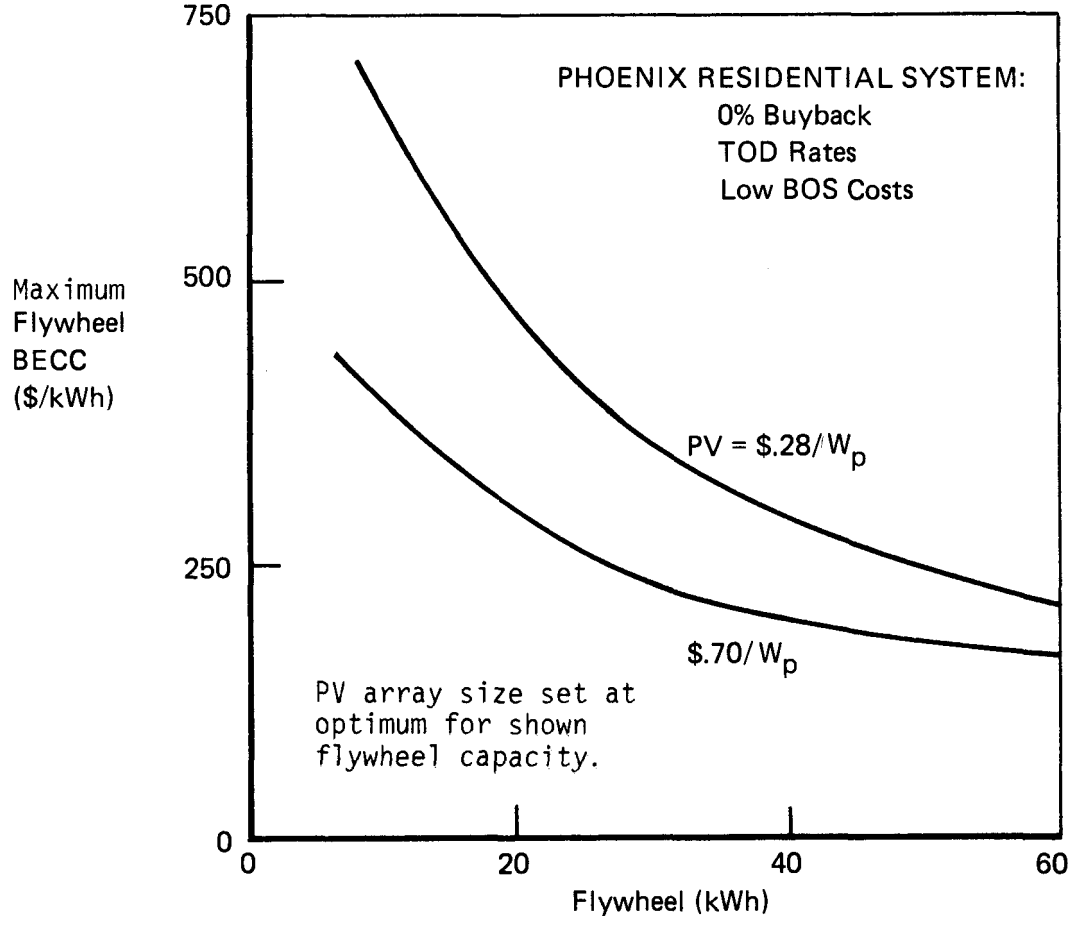

FIGURE 16

UTILITY INTERFACE/PV AND FLYWHEEL SYSTEM

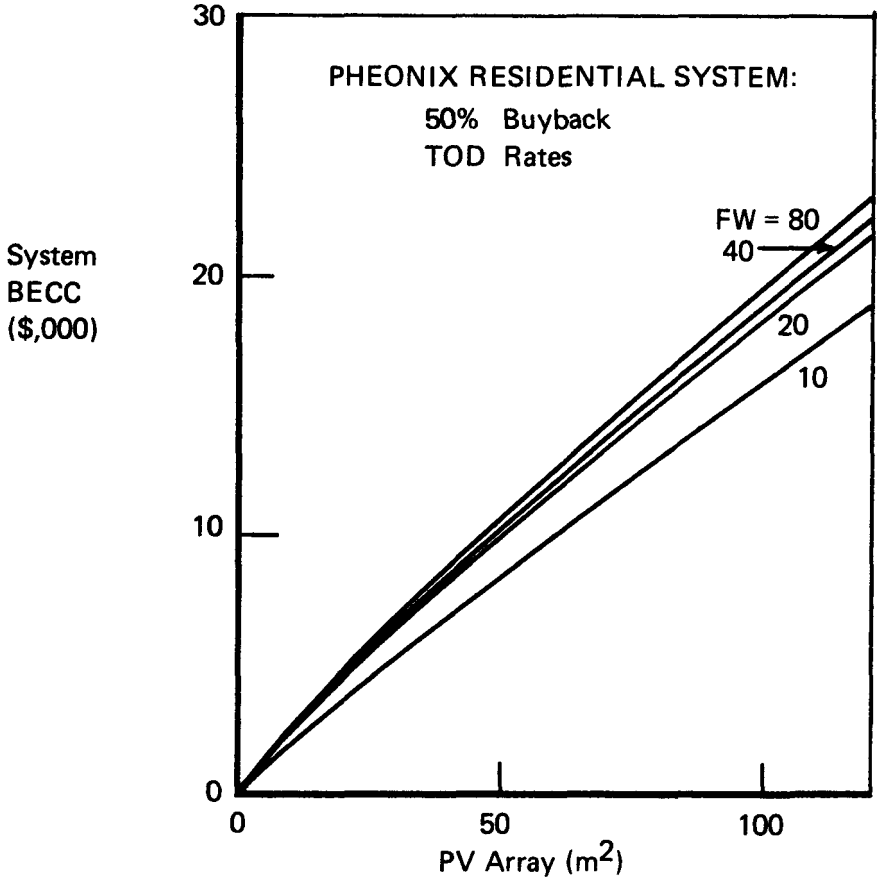

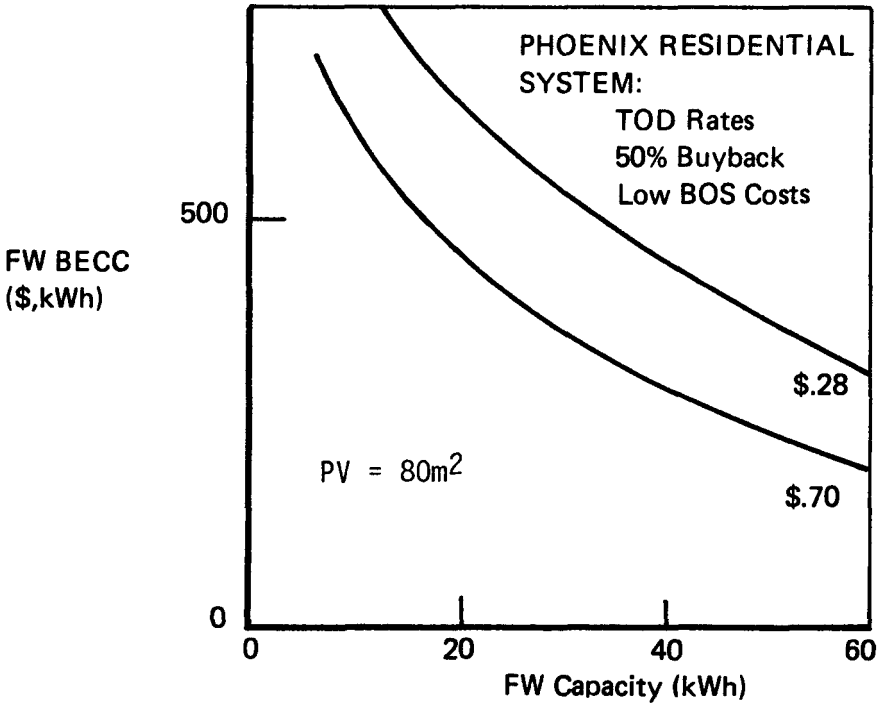

FIGURE 17

UTILITY INTERFACE/PV AND FLYWHEEL SYSTEM

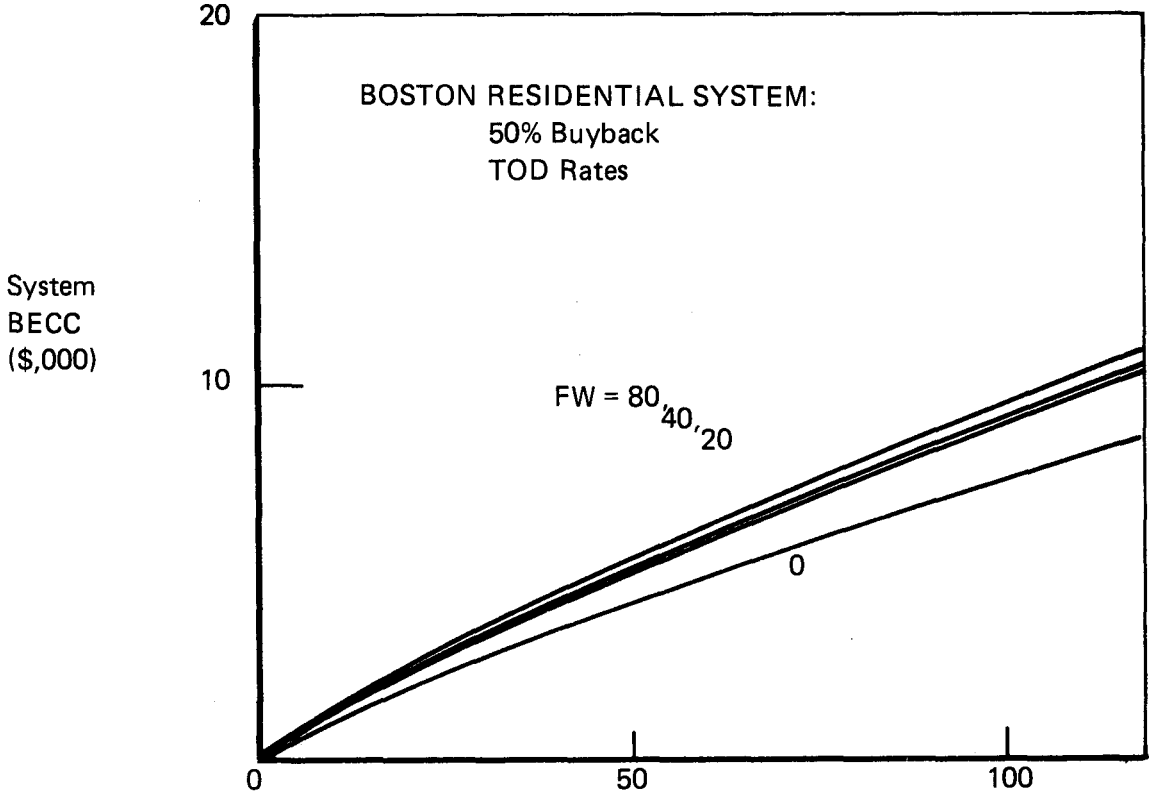

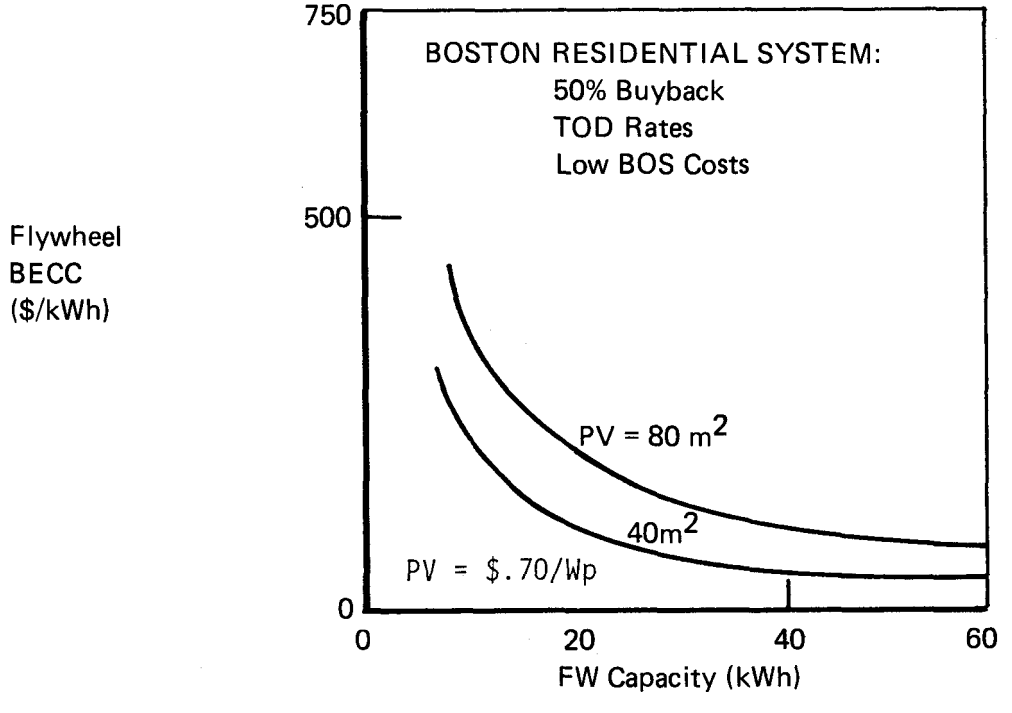

FIGURE 18

UTILITY INTERFACE/PV AND FLYWHEEL SYSTEM

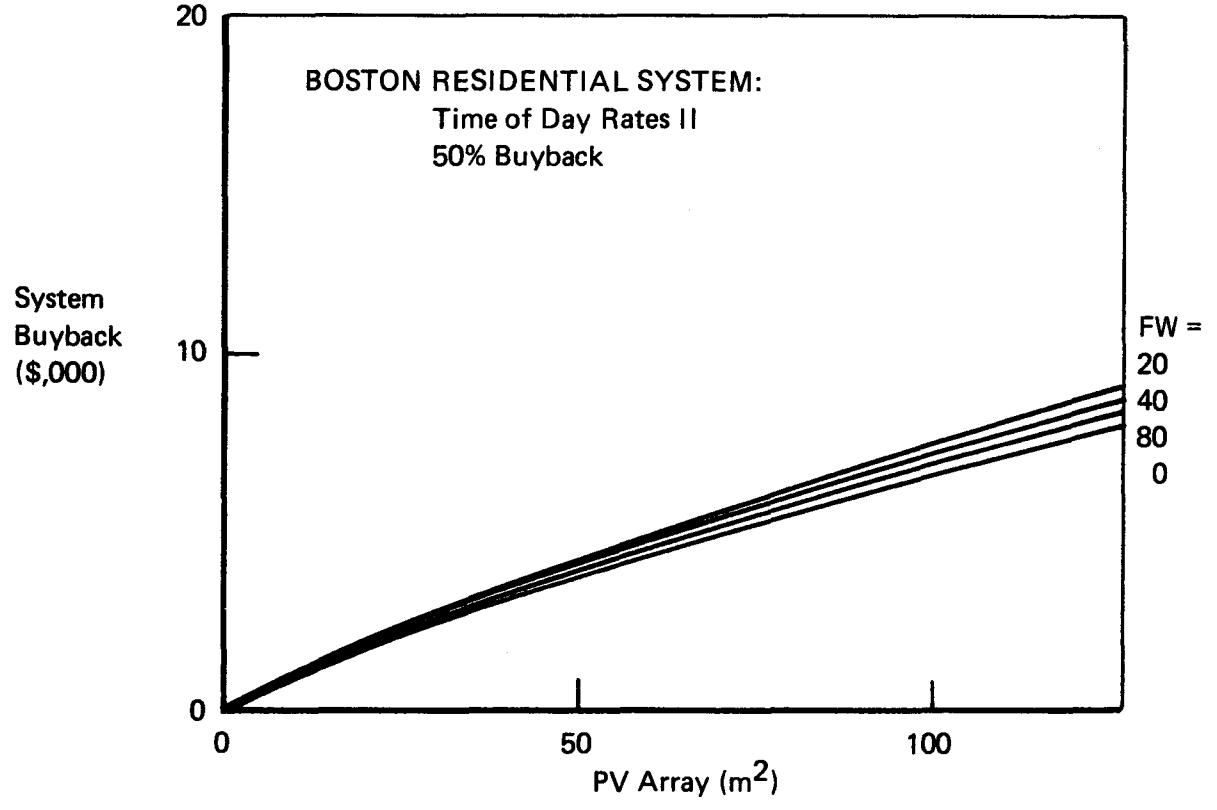

FIGURE 19

BOSTON T.O.D. RATES

(A)

RATE STRUCTURE I:

(1980 $)	AUG 15 - APRIL 15	APRIL 15 - AUG 15
PEAK HOURS	NONE	NOON - 3:00
PEAK PRICE		12.5¢/KWH
BASE PRICE	4.98¢/KWH	4.98¢/KWH

(B)

RATE STRUCTURE II:

(1980 $)	8 MOS WINTER PERIOD NOVEMBER - JUNE	4 MOS SUMMER PERIOD JULY - OCTOBER
PEAK HOURS	8:00 AM - 9:00 PM	8:00 AM - 9:00 PM
PEAK	6.175¢/KWH	6.977¢/KWH
BASE	1.264¢/KWH	1.264¢/KWH

season to include the full year and by broadening the price differentials between periods of the day, the effect of breakeven cost values is insignificant. In fact, for the pricing structures shown, the effects decrease system worth.

Comparing Boston and Phoenix

Figures 20, 21, and 22 repeat the analysis of Figures 15, 10, and 11, respectively, although with Boston data and parameters. The issues that prescribe curve shapes are the same for both geographic regions. However, taken in total, the different regions are defined by significantly contrasting results. All results for the Phoenix region are associated with consistently higher dollar breakeven values above the Boston cases. There are two primary reasons for this. First, both the flat rate and average time-of-day price figures for Boston are lower than the corresponding Phoenix prices. This yields a lesser total system value when the benefit is valued at utility-displaced electricity. Second, the sun shines brighter and longer in Phoenix than in Boston. This means not only that more electricity is supplied by the PV array, but also that with greater insolation intensities, PV generation is more likely beyond the instantaneous demand. This latter point is illustrated by the slightly lower optimum array sizes for given flywheel capacities in all Phoenix runs.

Sensitivity to the Cost of Electricity

An obvious question arises as to the sensitivity of investment indifference values to the cost of utility electricity, and to the role the latter plays as an incentive toward a PV-flywheel investment. Figure 23 explores these relationships for the Phoenix residential case. With no electricity buyback and with a flat-rate price structure, hardware

FIGURE 20

UTILITY INTERFACE/PV AND FLYWHEEL SYSTEM

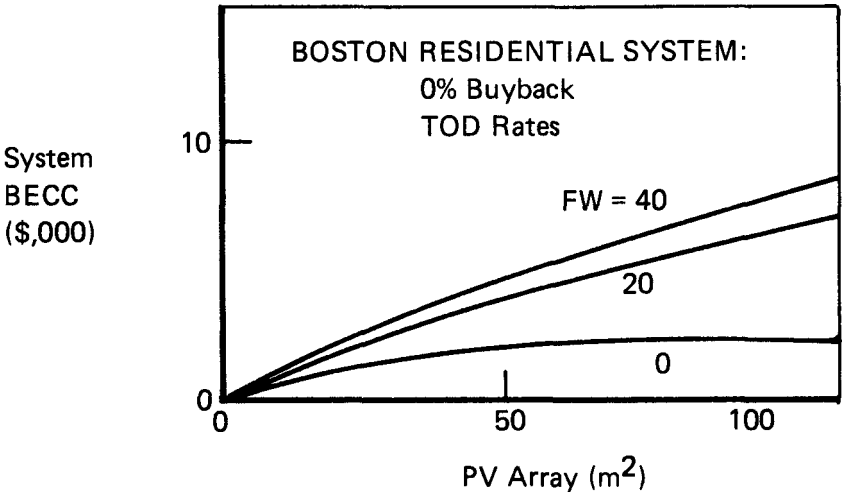

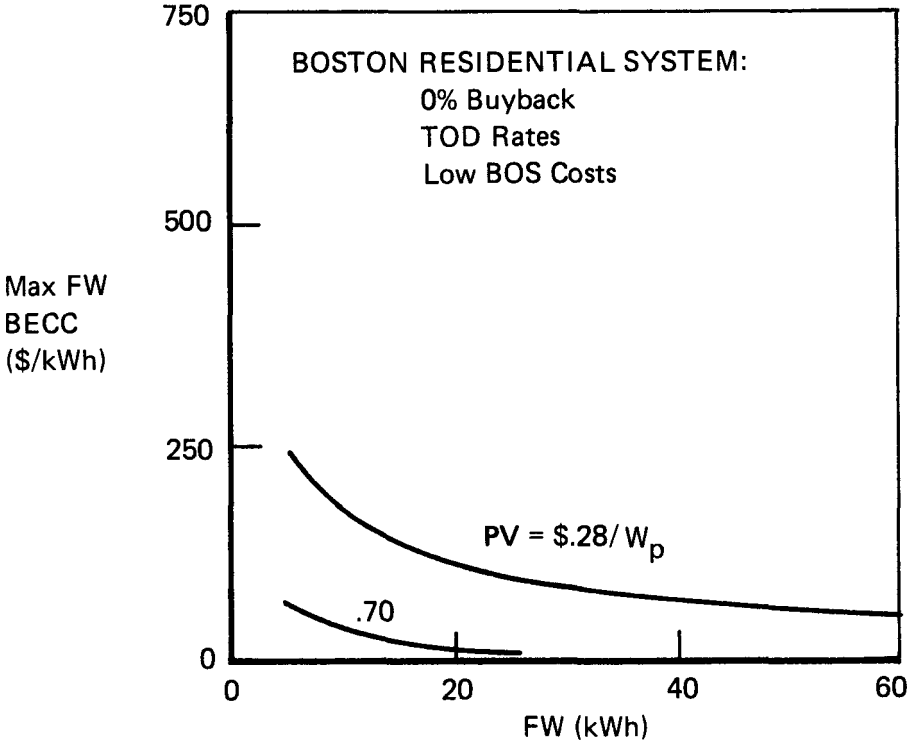

NOTE: Comparison of figures 17 and 20 suggest increasing flywheel BECC with utility buyback rate, contrary to the findings in figure 14. Figure 14 subtracts out PV costs at non-storage-supplemented PV breakeven values at each buyback rate whereas all other flywheel breakeven figures subtract out fixed PV costs at the labeled values. In this way, the PV portion of the system subsidizes the flywhe at low-to-medium PV cost estimates. Further explanation is given on pages 27-2. Also in the figures, "max FW BECC" refers to flywheel BECC when PV is optimally sized to attain maximum flywheel BECC.

FIGURE 21

UTILITY INTERFACE/PV AND FLYWHEEL SYSTEM

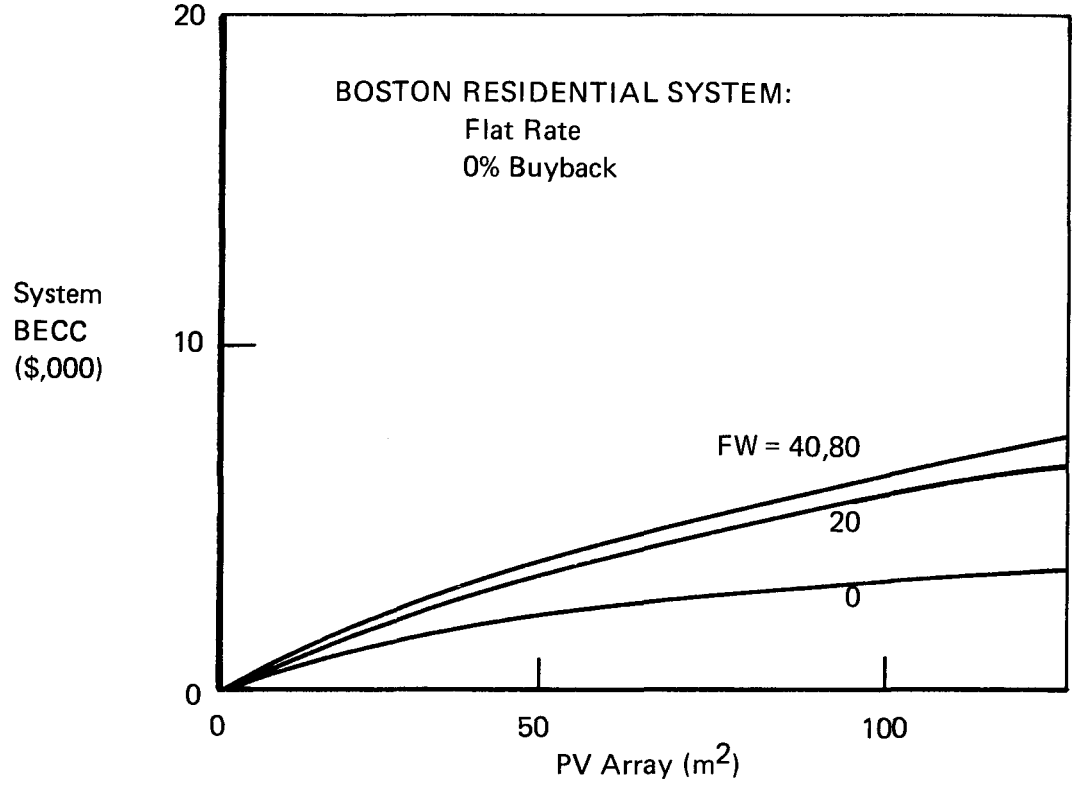

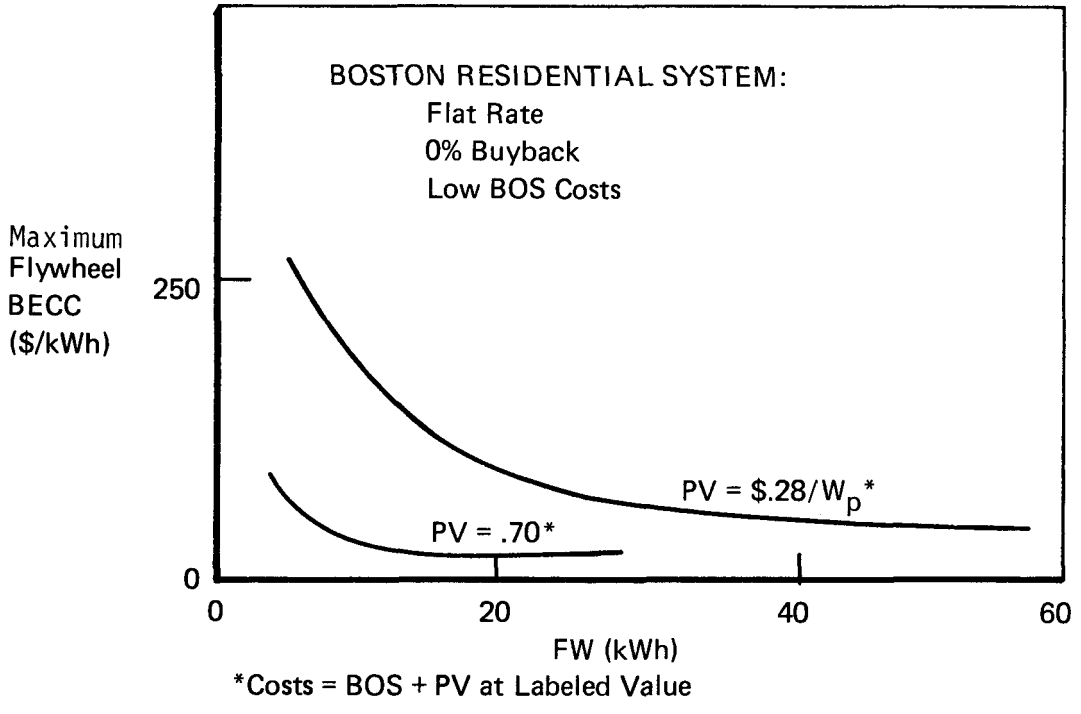

*Costs = BOS + PV at Labeled Value

FIGURE 22

UTILITY INTERFACE/PV AND FLYWHEEL SYSTEM

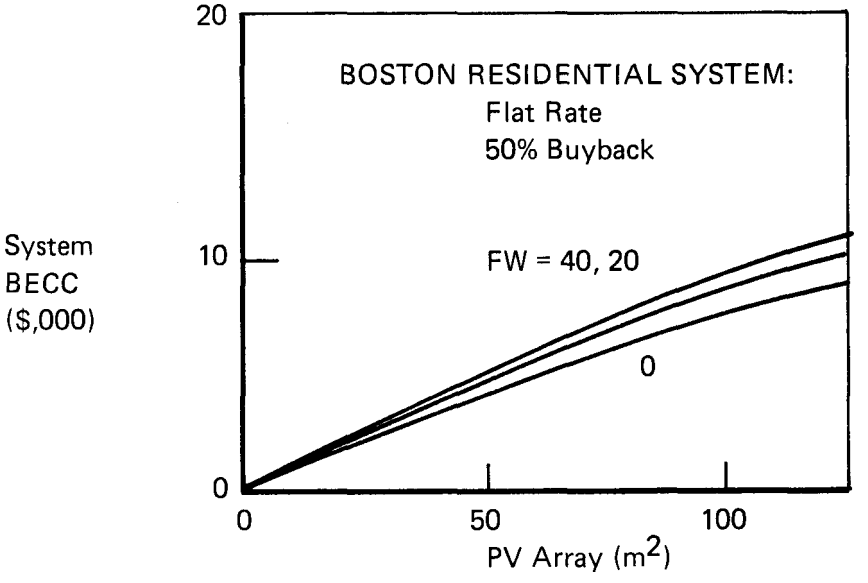

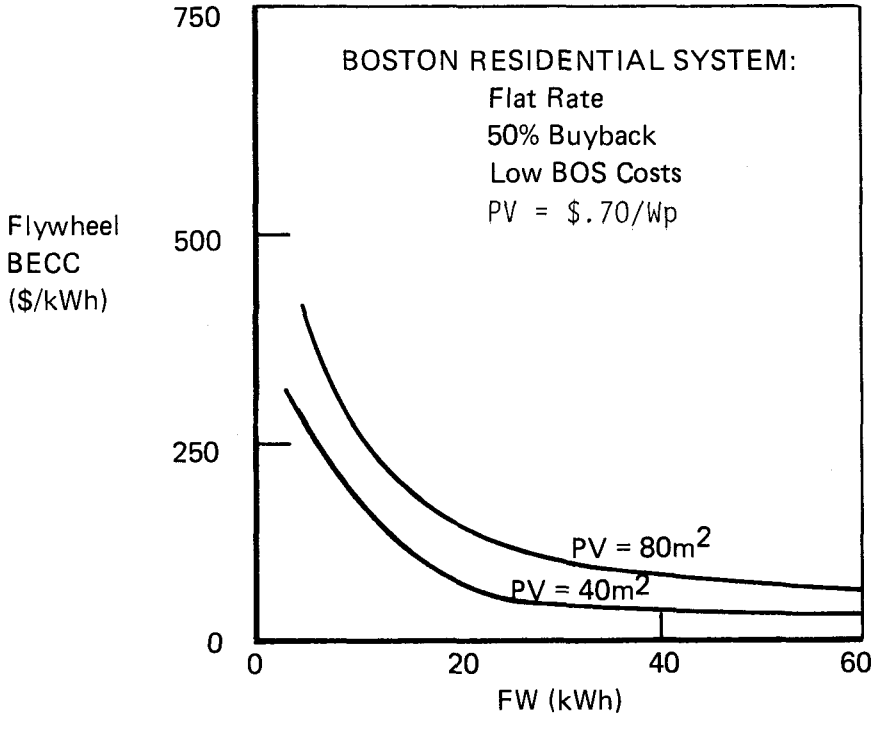

costs have been varied for the fixed configuration of 80 m^2 array with a 40-kWh flywheel to determine the relation of net benefits to cost of utility electricity at the start of the 20-year life of the system. The low-, medium-, and high-cost assumptions are again defined in Figure 24. Breakeven costs, defined by zero net benefits, are the indifference points for investment decisions. It is seen that a $.10/kWh differential in assumed start cost of electricity is required to absorb the uncertainty in configuration cost projections. The steepness of the curves indicates the rate at which net benefits accumulate for the investment once beyond the breakeven value.

As an additional exercise, the discount rate was varied from 1 percent to 5 percent for the assumed Medium Costs case. The results are indicated by the dashed lines in the figure. A mere 4-percent difference changes the breakeven start cost of electricity by roughly 4 cents per kWh. This result is explored later in the analysis as finance explanations are given for the difference in investment outlook for the residential over the load center scale of application. Figure 25 then goes on to relate the same criteria under a 50-percent buyback scheme.

Utility and Flywheel Alone--No PV

Under the assumption that future utility policy may include the option for residences to serve as distributed energy storage centers, a logic was formulated to handle flywheel kWh transfers (no PV) in a grid-connected environment. This logic seeks to maximize benefits given the high- and low-cost purchasing opportunities of a time-of-day rate structure. Figure 26 presents the results of this study. Shown here is the flywheel BECC subject to implementation of the price structures of Figures 19a and 19b. The low curve (rate I) is a result of flywheel

FIGURE 23

NET BENEFITS VS.COST OF ELECTRICITY

Phoenix Residence: 0% Buyback; Flat Rate

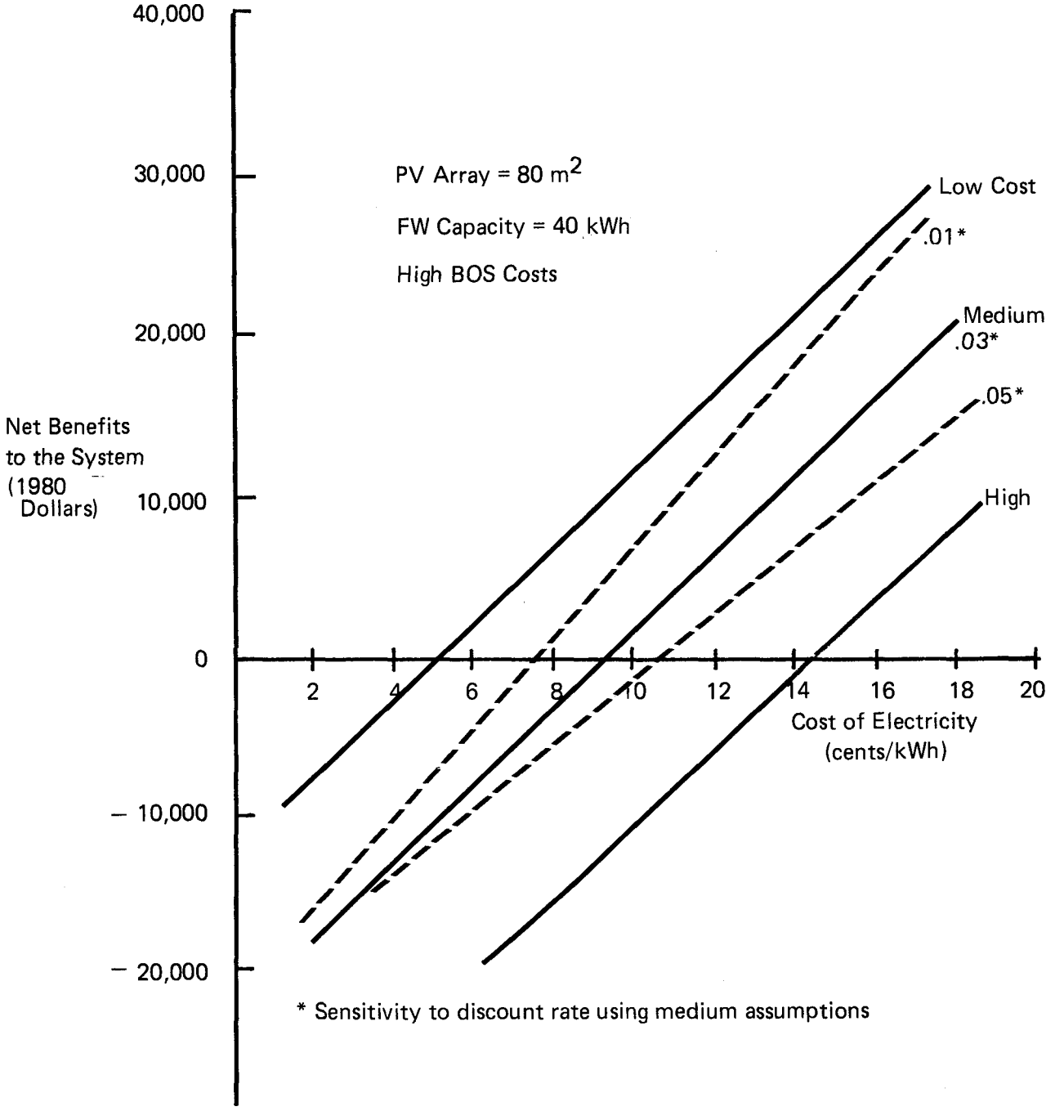

FIGURE 24

NET BENEFITS VS: COST OF ELECTRICITY

ASSUMPTIONS

PV ARRAY = 80 M^2

FW CAPACITY = 40 KWH

HARDWARE COSTS			DISCOUNT RATE
LOW:	$.28/$W_P$	PV	.01
	LOW	FW	
			.02
MED:	$.70/$W_P$	PV	
	MEDIUM	FW	.03
HIGH:	$.91/$W_P$	PV	
	HIGH	FW	

FIGURE 25

UTILITY INTERFACE PV AND FLYWHEEL SYSTEM
NET BENEFITS VERSUS COST OF ELECTRICITY

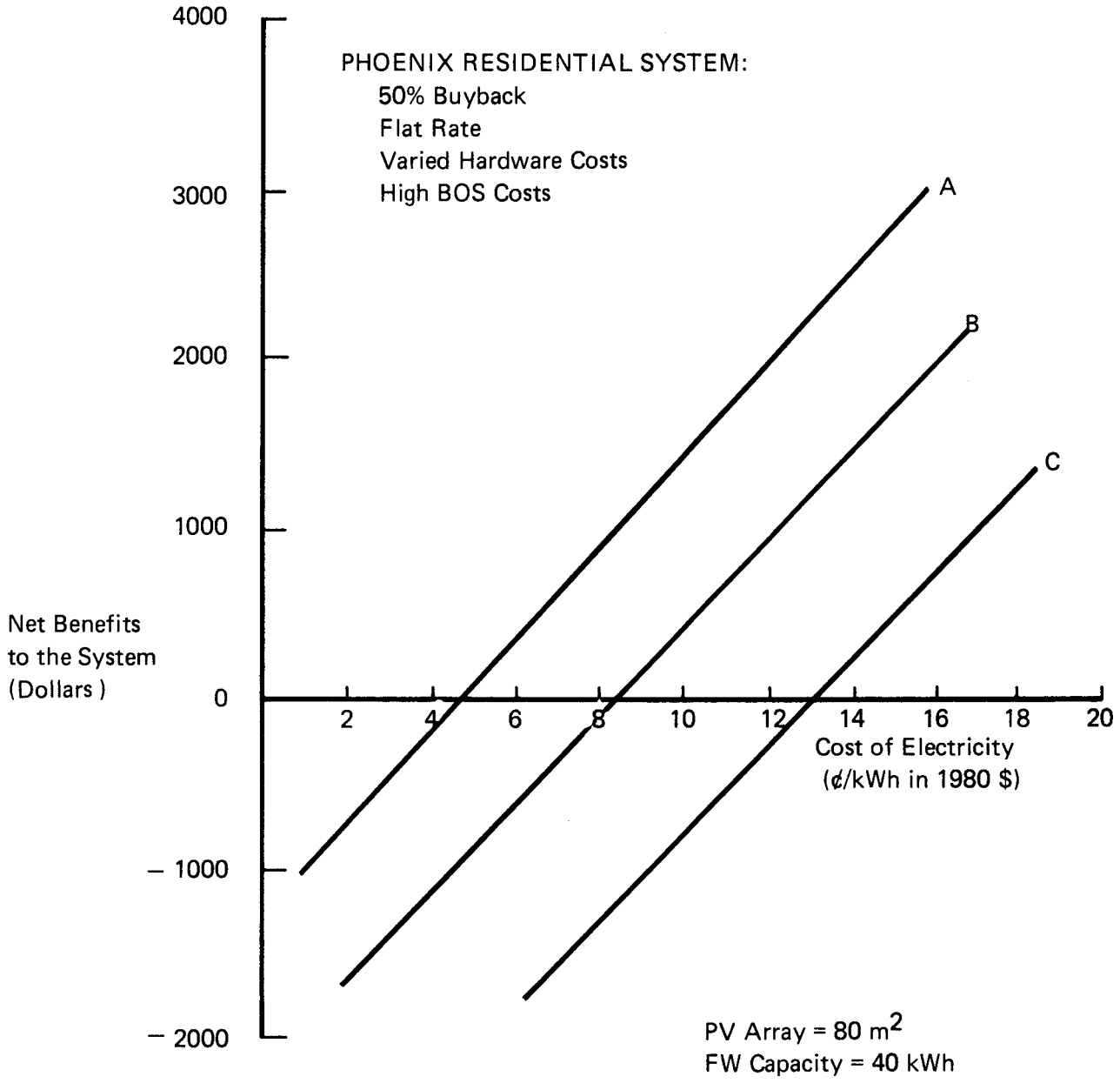

Hardware Costs

A: PV = $.28/Wp
FW = Low

B: PV = .70
FW = Medium

C: PV = .91
FW = High

FIGURE 26
UTILITY INTERFACE/FLYWHEEL ALONE

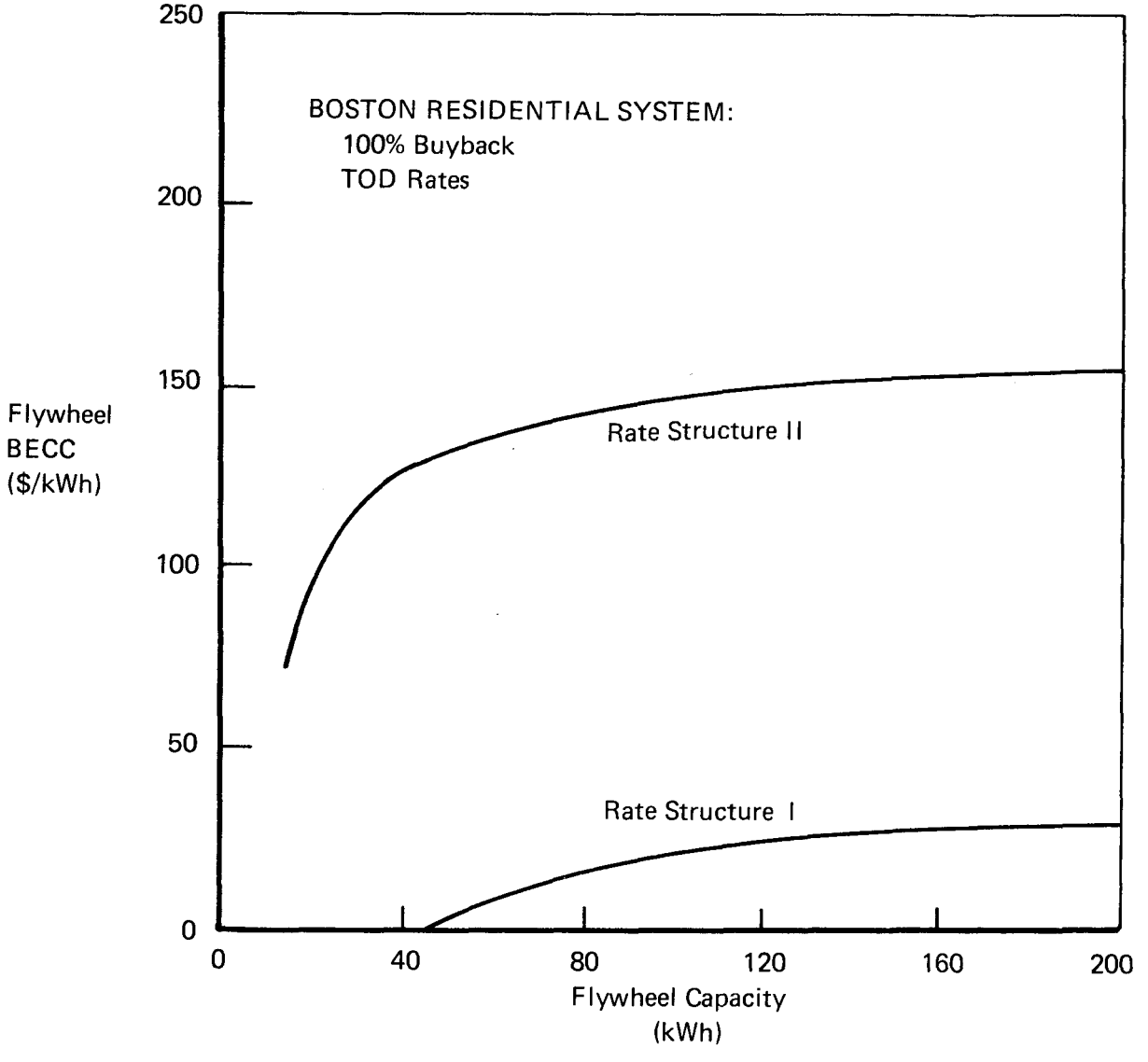

charging maintenance over that portion of the year where no time-of-day price differential exists. Conclusions drawn from this graph support the contention that storage cost economics are highly affected by differences in time-of-day rate-setting policy. Additional studies of storage utility interface in general will reflect more completely the worth of distributed storage used with time-variant rates.

III.1.b. Residential Stand-Alone Analysis

A remote applications analysis was performed for a single-family residence with a benefit analysis now including, in addition to utility-displaced electricity, the cost of a distribution line as a function of distance from the grid. Figure 27 outlines the issues that are pertinent here as well as parameters varied to affect the analysis. The "cost of reliability" issue applies principally to the first part of the stand-alone study, which is a comparison of a flywheel and PV system with the economics of a grid connect. The second part assumes that a utility-equivalent reliability is attained with the addition of a diesel generator backup unit; the issues of configuration sizing of the tri-component system become prevalent.

PV and the Flywheel Alone--The Issue of Reliability

In any energy demand scenario, coordination of energy supply requires some assumptions regarding basic resource inputs. For conventional electricity production these assumptions include a readily available marketplace for conventional fossil or nuclear fuels. In the U.S., this marketplace has reached a level of sophistication where resource supply reliability is virtually no longer an issue. However, it appears a revival of energy systems based on weather-dependent technologies is in the offing and thus the issue of supply reliability becomes of paramount concern.

FIGURE 27

STAND ALONE ANALYSIS
PV + FW
VS.
UTILITY GRID CONNECT

ISSUES

- CONFIGURATION SIZING
- COST OF RELIABILITY
- DISTANCE FROM GRID AS BENEFIT

PARAMETERS VARIED

- FW CAPACITY (KWH)
- PV ARRAY SIZE (M^2)
- HARDWARE COSTS
- DISTANCE FROM GRID

For a stand-alone configuration comprised of photovoltaics and a flywheel alone, it was necessary to analyze the issue of supply reliability and its implications for configuration sizing and system costs. Figure 28 begins this analysis. Here, iso-reliability lines are drawn over a range of component size combinations. Reliability in this case is defined as the Service Reliability Index (SRI), or the number of customer hours served over the number of customer hours demanded. The important difference here is that the utility definition of reliability applies to failure due to hardware outages, whereas the definition that applies to Figure 28 relates to interruptions resulting from insufficient array or storage sizing.

Figure 29 reveals the relationship between the SRI and Total Energy Not Met (TENM) for the first year of the simulated run life. As configuration size increases upward and to the right in the diagram, total energy not met by the system goes to zero. It is seen that the curve slopes in the two figures are nearly identical, indicating a high correlation and hence substitutability of the two measures.

The reason for the backward-bending vertical portions of the curves is inherent in the flywheel operating specifications. Each of the functional components of the flywheel has an associated loss; one of these is directly proportional to the flywheel's state of charge. The operating logic for the flywheel dictates that it shall never be drained below one quarter of its total kWh capacity and hence larger flywheels, requiring a higher minimum state of charge, will necessarily have higher proportional losses. Thus, as flywheel capacity is increased for any fixed array size, total usable kWh will decline since total kilowatt-hours captured does not change.

FIGURE 28

REMOTE STAND ALONE RESIDENTIAL SYSTEM: PV AND FLYWHEEL ONLY

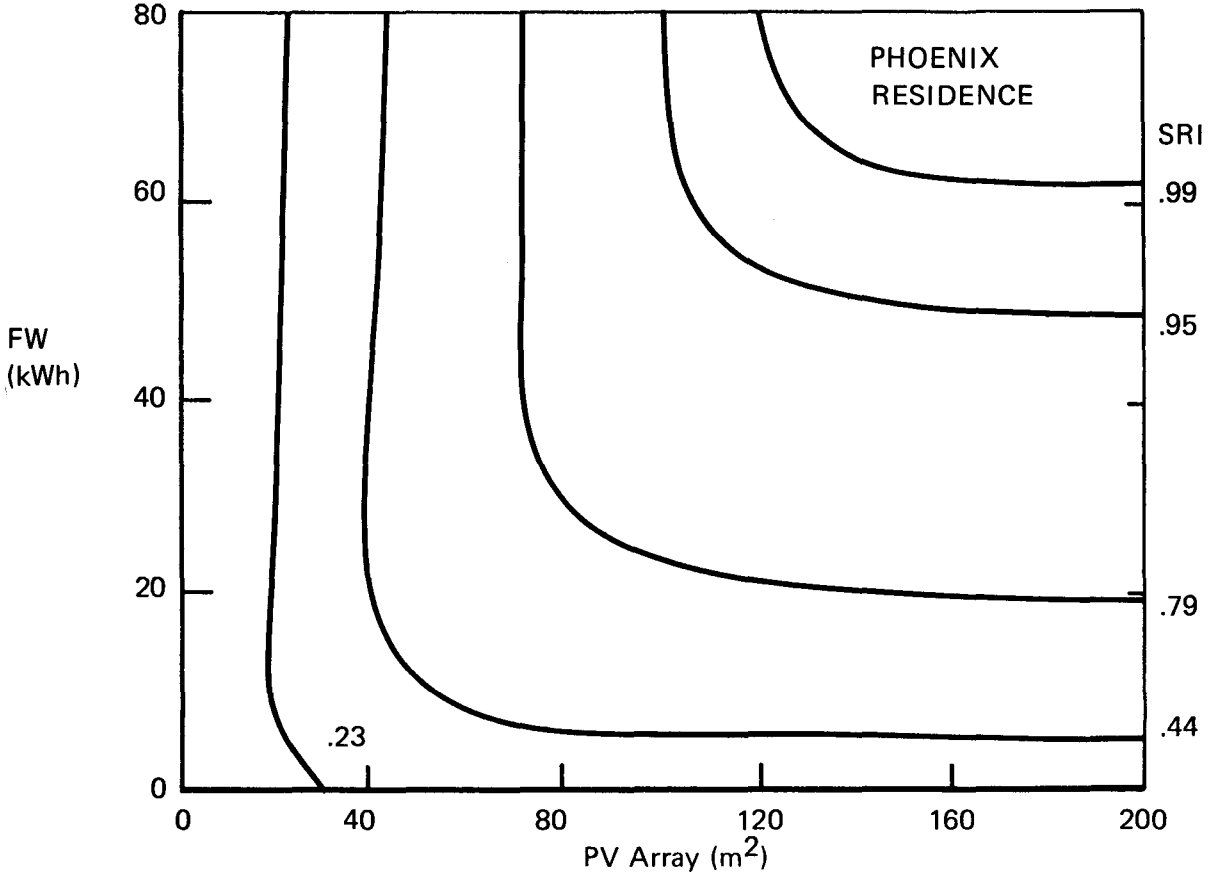

ISO - RELIABILITY CURVES
BY SERVICE RELIABILITY INDEX (SRI)
(Hours Served/Hours Demanded)

FIGURE 29

REMOTE STAND ALONE RESIDENTIAL SYSTEM: PV AND FLYWHEEL ONLY

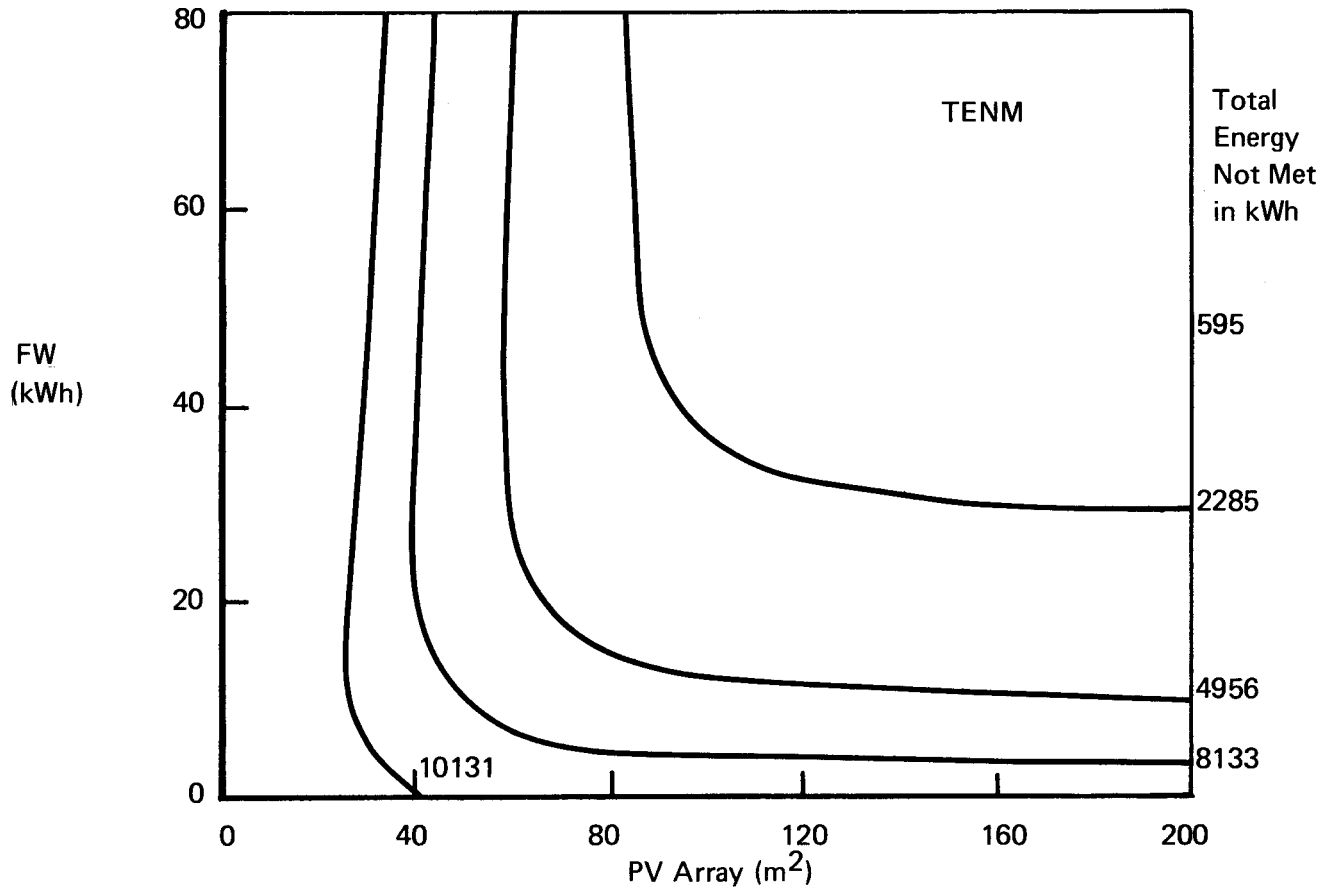

ISO -Total - Energy - Not - Met Curves

Fixing the PV module and balance-of-system costs, the flywheel cost projection is varied from its lowest to highest value to arrive at iso-total cost lines, as shown in Figures 30 and 31. As expected, those iso-cost lines with the lower flywheel cost assumption show a vertical shift toward greater flywheel dependence. What is most significant is revealed by the overlay of these lines on the iso-reliability curves. The sharp knee at each fixed reliability rules that optimum configuration sizing is quite insensitve to component costs. Note that sizing in the lower ranges of reliability requires a flywheel-(kWh) to-PV-array (kWp) ratio of roughly 2.5, whereas in the higher reliability ranges a ratio of 4 applies.

PV and Flywheel with Diesel Backup

When a diesel generator is added to the PV and flywheel system, the issue of supply reliability is eliminated, under the assumption of a ready means for obtaining the diesel fuel. Again, the issues of component reliability remain intact but were not modeled in this study. Figure 32 presents the directions for analysis under these conditions as well as the parameters varied to achieve these goals. The market parameters deemed important were the cost projections made for the system hardware as well as for the cost of diesel fuel.

Figure 33 represents a summary of the analysis for a remote residence application utilizing PV, a flywheel, and a diesel generator. With component size ranges set on each of the axes, and the TENM curves representing kilowatt hours of diesel energy, any point in the plane deterministically represents satisfaction of 100 percent of the total yearly application demand.

FIGURE 30

REMOTE STAND ALONE RESIDENTIAL SYSTEM: PV AND FLYWHEEL ONLY

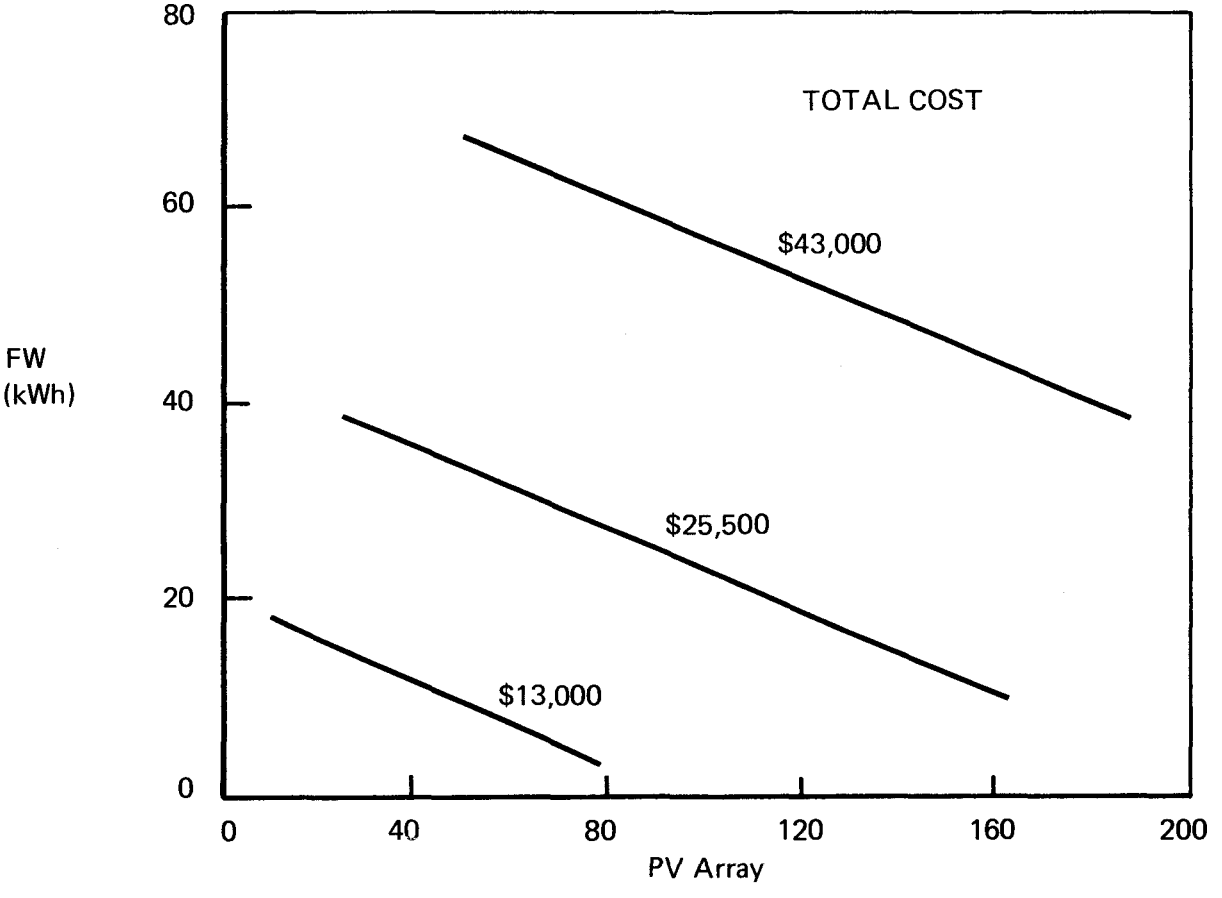

ISO – COST LINES

PV: $.70/PK WATT
FW: High Costs
Low BOS Costs

FIGURE 31

REMOTE STAND ALONE RESIDENTIAL SYSTEM: PV AND FLYWHEEL ONLY

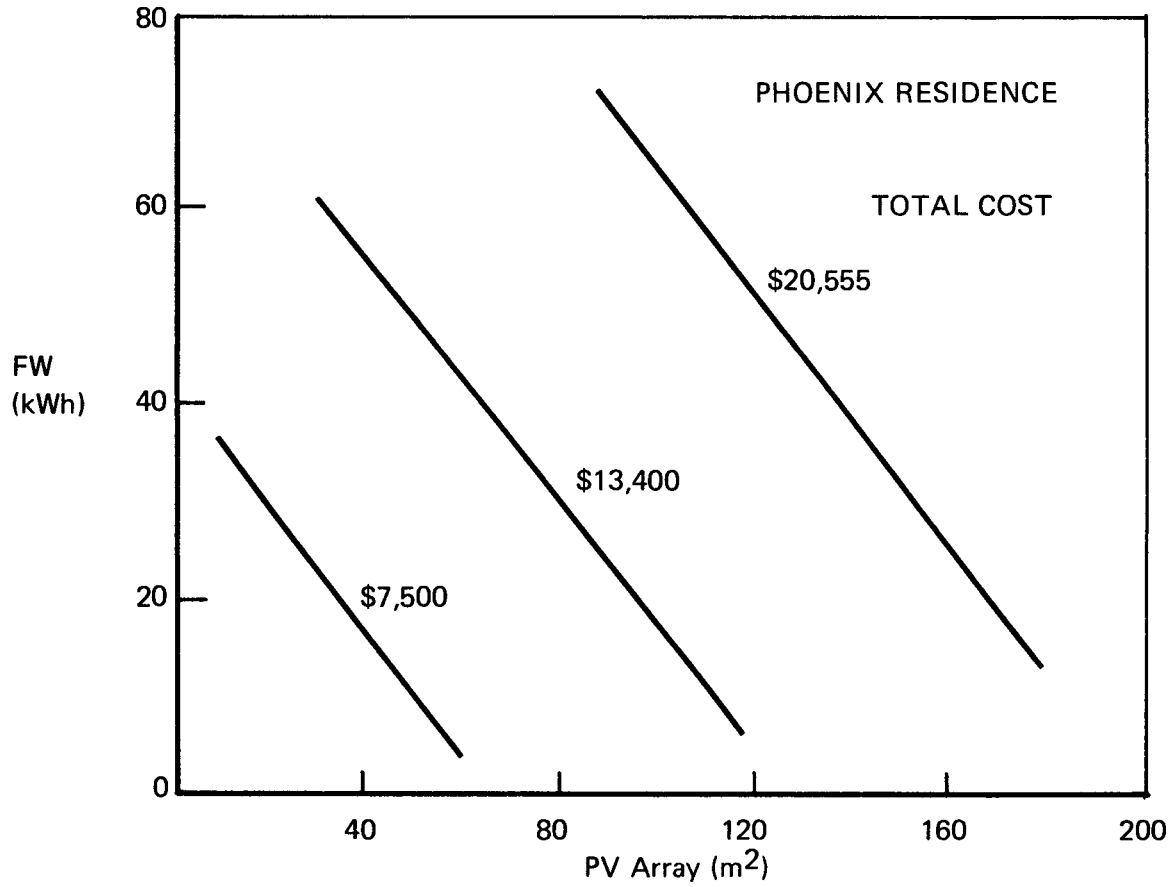

ISO Cost Lines
PV: $.70/pk Watt
FW: Low Costs
Low BOS Costs

FIGURE 32

STAND - ALONE ANALYSIS

PV + FW + DSL

VS:

UTILITY GRID CONNECT

ISSUES

- OPTIMUM CONFIGURATION SIZING
- SENSITIVITY TO MARKET PARAMETERS

PARAMETERS VARIED

- HARDWARE COSTS
- DIESEL FUEL START COSTS
- COMPONENT HARDWARE CAPACITIES

FIGURE 33
REMOTE STAND ALONE PV FLYWHEEL/DIESEL RESIDENTIAL SYSTEM

Sensitivity of Optimum Configuration Sizing to
– Diesel Start Costs in 1985
– Hardware Costs
– Low BOS Costs

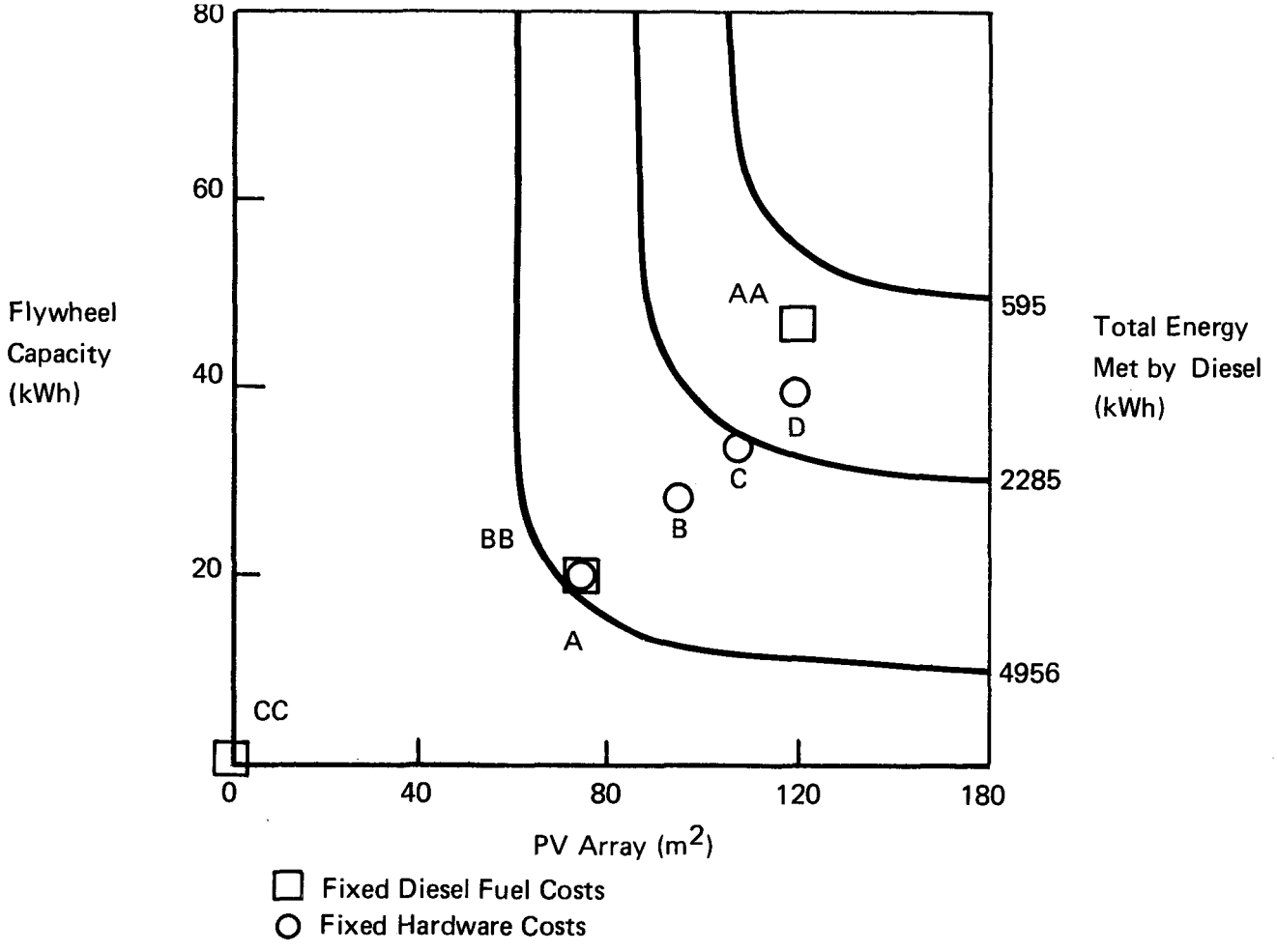

ASSUMPTIONS

Utility Tie in Costs as Benefits

- $ .066/kWh 3%/Year Real Price Escalator
- 30 Miles from Grid $8712/Mile

Diesel Fuel Costs Fixed at $ .07/kWh in 1985; Hardware Costs Varied

AA	PV = .28 FW = Low
BB	PV = .70 FW = Medium
CC	PV = .91 FW = High

Hardware Costs Fixed at PV = $.07/pk Watt FW = Middle; Diesel Fuel Costs in 1986

A	$ .07/kWh
B	.097
C	.133
D	.169

After 1986 Escalate at 6.6%/Annum

The boxes and squares represent economically optimal solutions. The boxes are a result of fixing diesel fuel costs at $.07/kWh in 1980, applying a fixed 6.6-percent/year fuel price escalation factor for the years thereafter, and examining the effects of varying component cost assumptions on the configuration sizing solution. The range of solutions here is dramatic, revealing that a low-cost assumption for the PV and flywheel dictates that fully 92 percent of the energy demand be satisfied by these components alone, whereas assuming the high cost range optimally yields an all-diesel system.

On the other hand, fixing hardware costs at the medium projection and varying diesel fuel start costs for 1985 over a broad range yields a relatively minor, although significant, change in optimum system sizing. Figures 35-38 summarize the maximum net benefit analysis used to arrive at the configuration optimums of Figure 33.

Taking the most likely configuration solution (i.e., reasonable diesel fuel and hardware cost assumptions shown by the boxed circle (BB-A) of Figure 33), the net benefits as a function of distance from the grid are charted in Figure 39, where miles of distribution line not built now serve the benefits side of the equation. At just over one mile from the utility line, benefits rapidly begin to accrue to such isolated, total energy configurations.

III.1.c Summary of Residential Results

The significant findings of the foregoing results are listed below:

Utility Interface

- Additional storage increases the optimum capacity of installed PV when hardware costs are in the low range.
- Storage has the greatest value at low buyback rates.

FIGURE 35

OPTIMUM CONFIGURATION SIZING APPROACH

$$\text{MIN. COST} = A \cdot KW_D + B \cdot KW_{PV} + C \cdot KW_F + D \cdot KWH_D + E \cdot KWH_{PV} + F \cdot KWH_F$$

$$\text{S.T.} \quad \Sigma\ KWH \geq \text{ANNUAL DEMAND}$$

$$KW_D \cdot 8760 \geq KWH_D$$

$$KW_{PV} \cdot 8760 \geq KWH_{PV}$$

$$KW_T \cdot 8760 \geq KWH_F$$

WHERE:

$A = \$/KW_D/YR$ $\quad$ $D = \$/KWH_D$

$B = \$/KW_{PV}/YR$ $\quad$ $E = \$/KWH_{PV}$

$C = \$/KW_{FW}/YR$ $\quad$ $F = \$/KWH_{FW}$

(CAPITAL COSTS) $\quad$ (FUEL COSTS)

FIGURE 36

STAND-ALONE/PV FLYWHEEL DIESEL

SYSTEM NET BENEFITS VERSUS: ARRAY SIZE AND FLYWHEEL CAPACITY

DIESEL FUEL COST OF $.07/kWh ASSUMED HARDWARE COSTS* VARIED

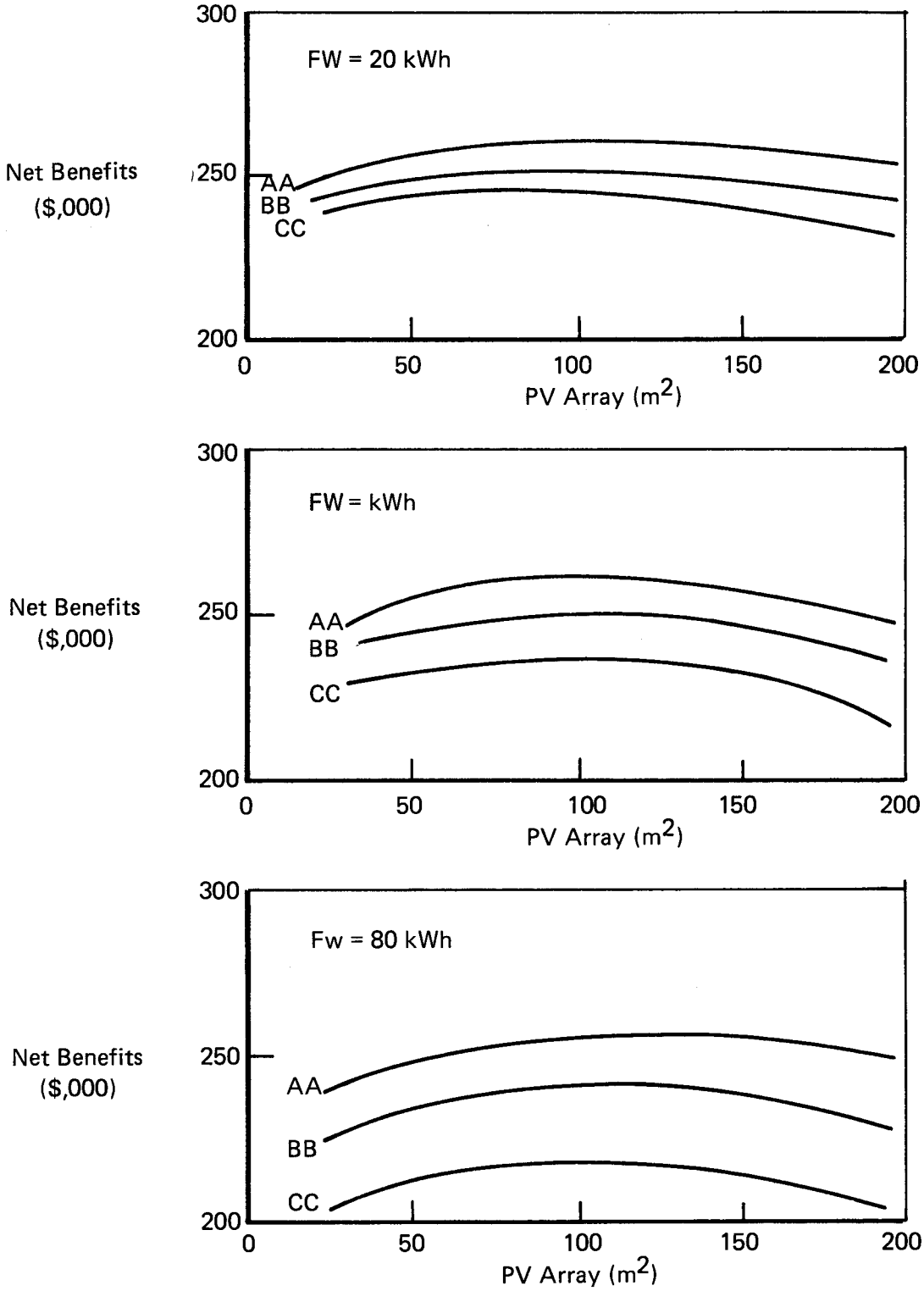

*Hardware Costs (1980):

AA: PV = $.28 FW = Low

BB: PV = $.70 FW = Middle

CC: PV = $.91 FW = High

FIGURE 37

STAND-ALONE PV FLYWHEEL DIESEL
SYSTEM NET BENEFITS VS ARRAY SIZE AND FLYWHEEL CAPACITY
MIDDLE HARDWARE COSTS ASSUMED
DIESEL FUEL START COSTS* IN 1985 VARIED
COST COMPARISON TO UTILITY TIE-IN 30 MILES FROM GRID

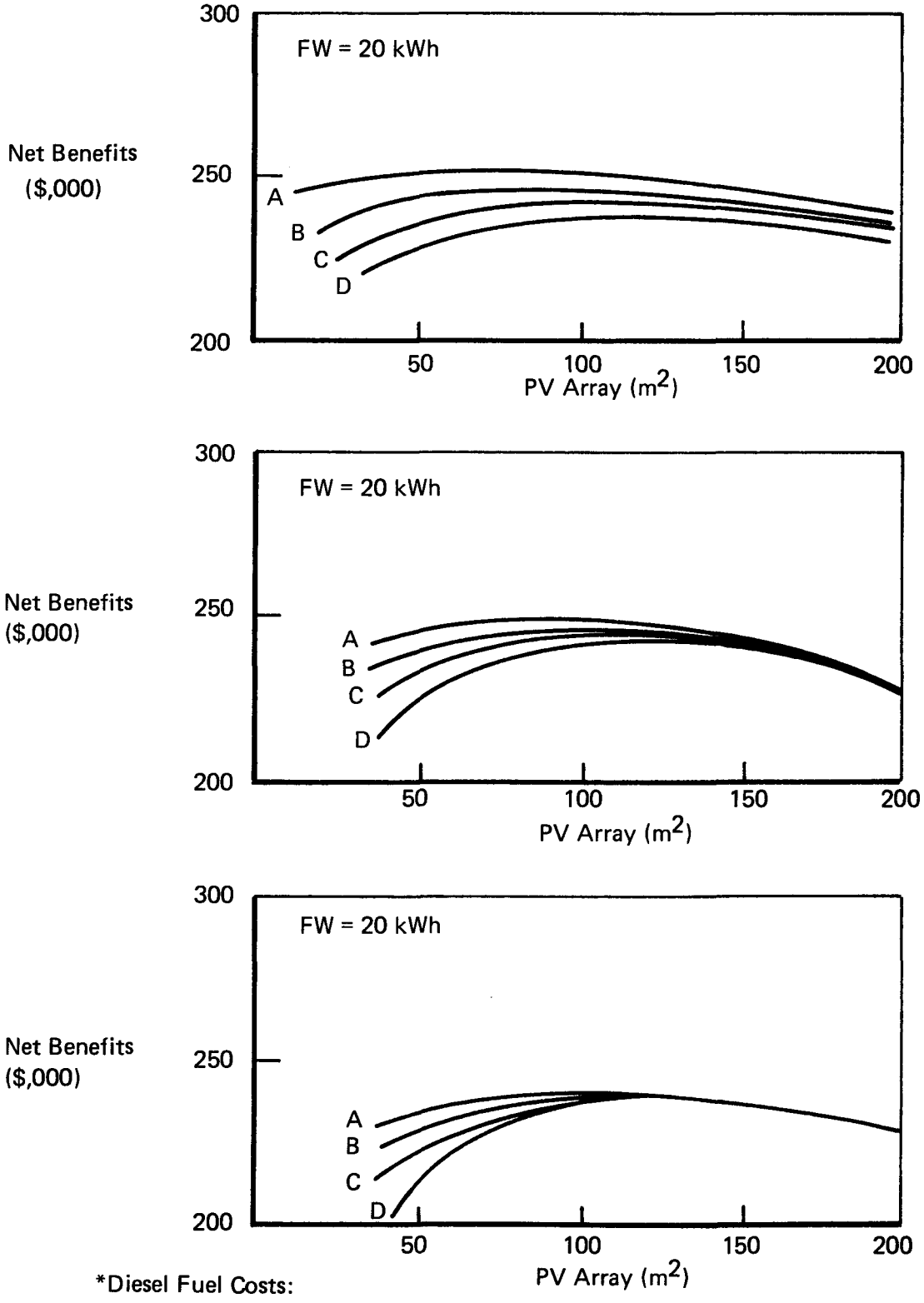

*Diesel Fuel Costs:
A = $.07/kWh; B = $.097/kWh; C = $.133/kWh; D = $.169/kWh

FIGURE 38A

STAND-ALONE PV FLYWHEEL DIESEL

MAXIMUM SYSTEM NET BENEFITS AT GIVEN FLYWHEEL CAPACITY

- Cost Compared to Utility Tie-In
  $.066/kWh
  30 Miles from Grid:
- Middle Hardware Costs Assumed
- Diesel Fuel Start Costs in 1985 Varied

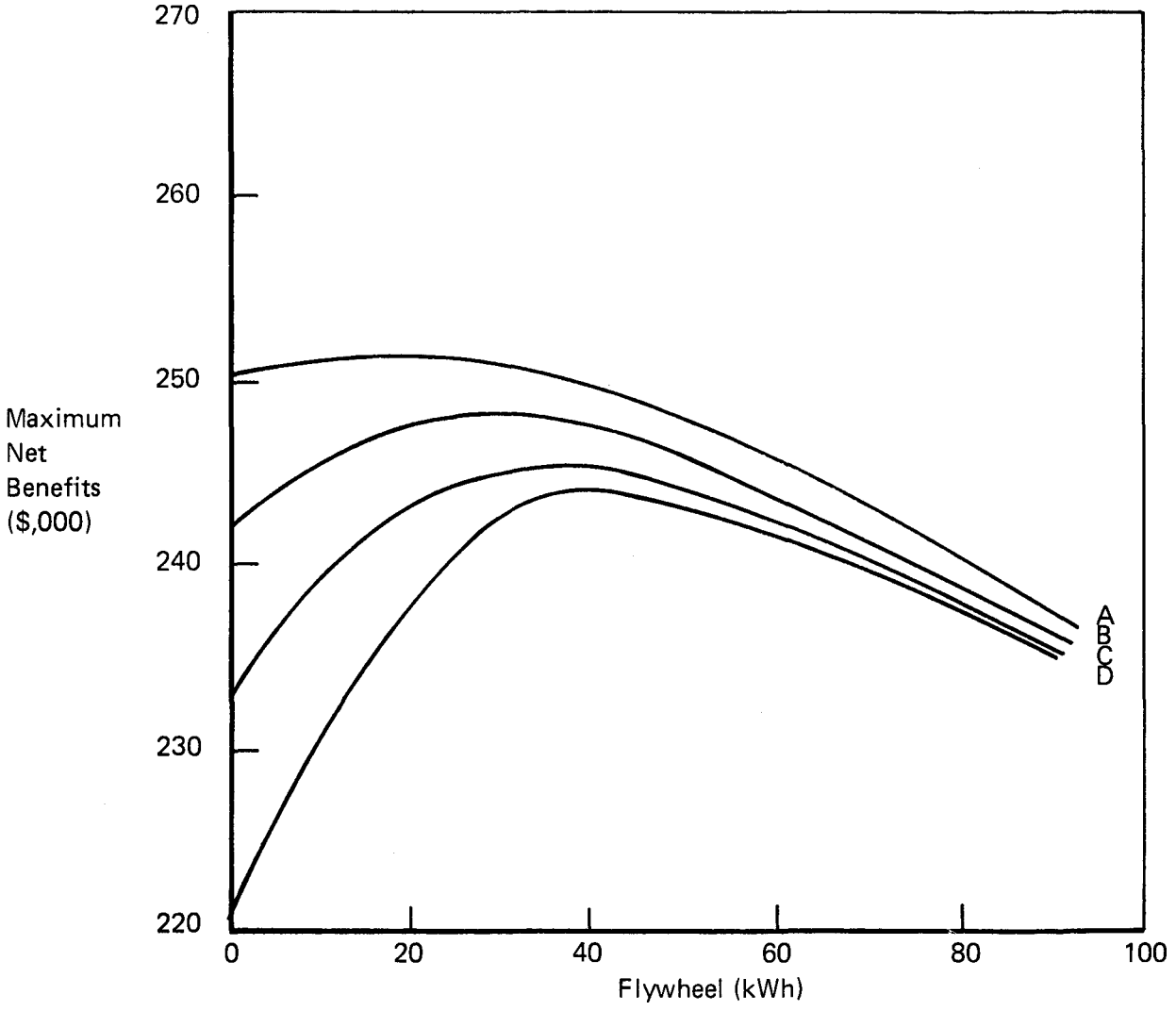

Diesel Fuel Start Costs in 1985

A = $.07/kWh
B = $.097/kWh
C = $.133/kWh
D = $.169/kWh

Hardware Costs Assumed

PV = $.70 W_p
FW = Middle

Benefits

$.066/kWh

FIGURE 38B

STAND-ALONE/PV FLYWHEEL DIESEL

Maximum System Net Benefits at Given Flywheel Capacity

Cost Compared to Utility Tie-In
$.066/kWh
30 Miles from grid at $8,712/mile
Hardware Costs Varied
Diesel Fuel Start Cost in 1955 Set at $.07/kWh

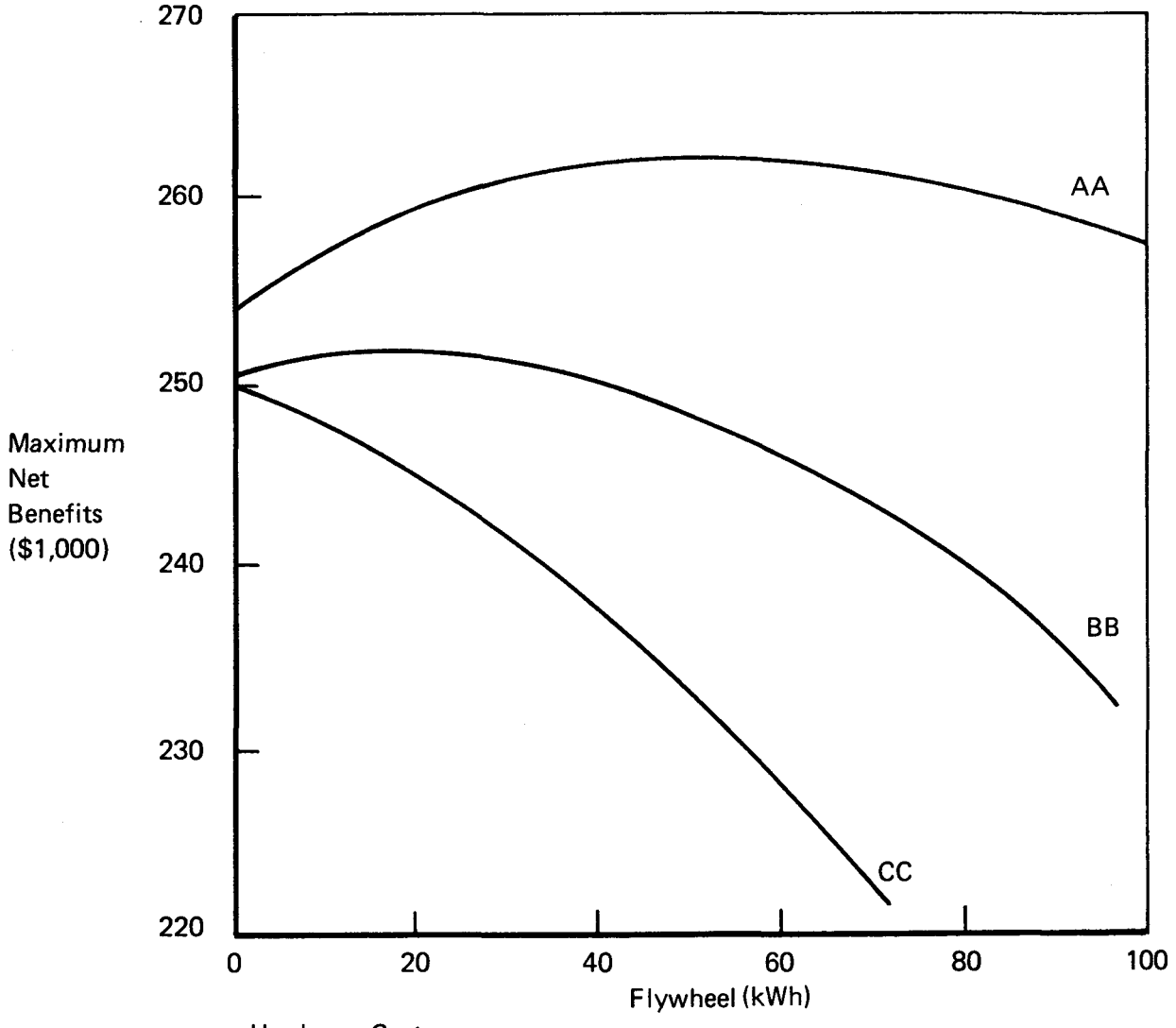

Hardware Costs

AA = PV : $.28/$W_p$ (1980)
FW : Low

BB = PV : $.70/$W_p$ (1980)
FW : Medium

CC = PV : $.91/$W_p$ (1980)
FW : High

FIGURE 39

PV + FW + DIESEL STAND ALONE COMPARED AGAINST UTILITY GRID CONNECT

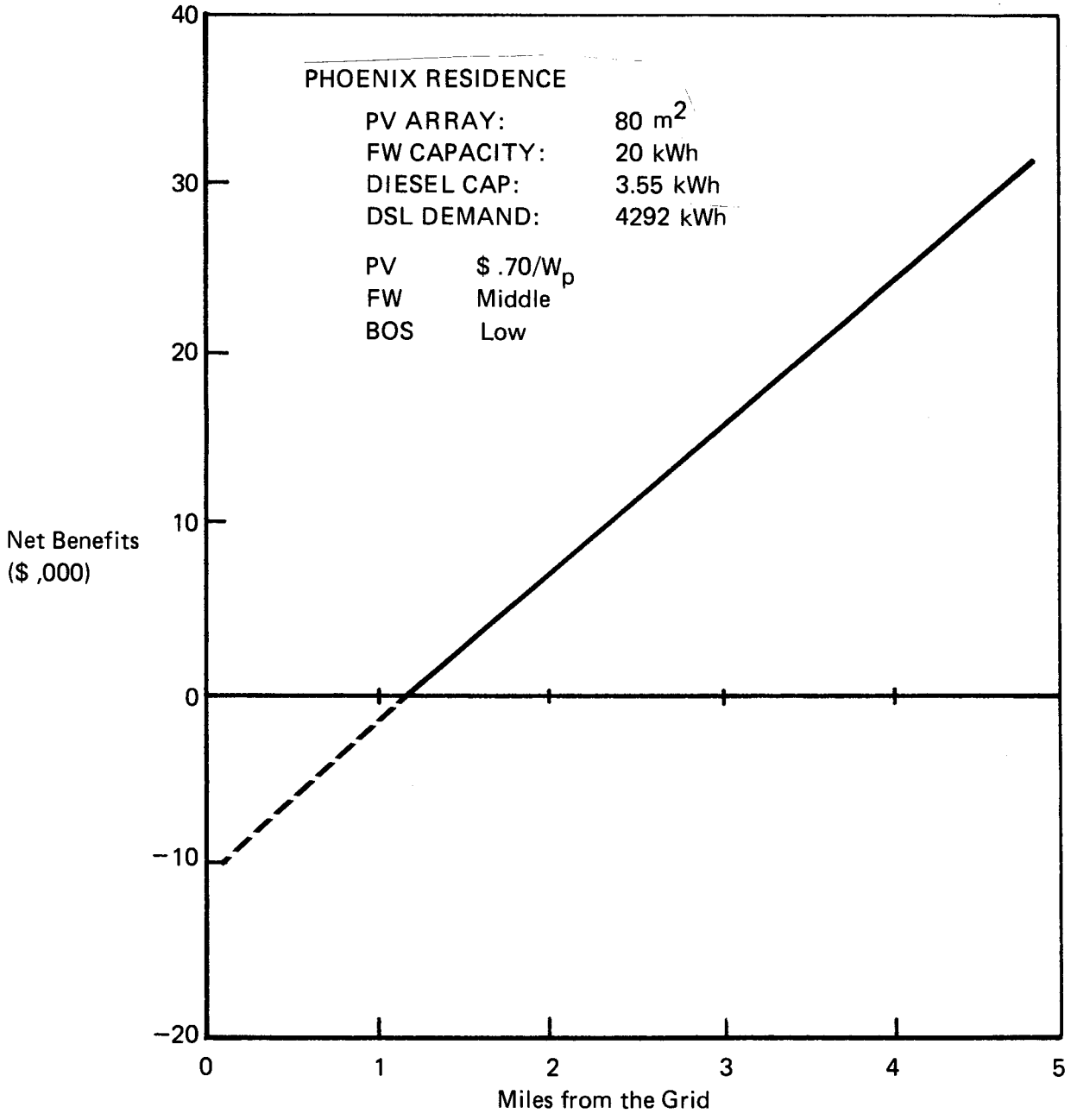

- o For a fixed storage capacity and PV array size, increasing utility buyback rates increases system worth when hardware costs are low. This is true since the marginal increase in benefits due to PV exceed the marginal decrease in benefits for the flywheel when buyback rate is increased.
- o There are diminishing returns to increasing flywheel capacity at a given array size.
- o Variations over the range of reasonable time of day rate structures have an insignificant impact on flywheel and system economics.
- o Ten cents per kilowatt hour differential in assumed start cost for electricity is required to absorb the uncertainty in configuration cost projections.
- o Using the most reasonable set of cost and financing projections for 1985, a PV-flywheel system will begin to look economically attractive when the cost of electricity exceeds 9¢/kWh (1980 $).
- o The discount rate applied to residential investments is significant in determining when penetration of PV systems is likely to occur.
- o Flywheel-Grid Connect (no PV) cost economics is highly affected by differences in time-of-day rate setting.

Remote/Stand-Alone

- o Optimum configuration sizing for PV and flywheel (no diesel) is quite sensitive to component costs, requiring that flywheel capacity (in kWh) be roughly 2.5 - 4.0 times the array size (in kWp).
- o Optimum size of a flywheel + PV system is highly sensitive to desired reliability.

- For a flywheel, PV, and diesel generator system, there is high sensitivity of optimum configuration size to the range of hardware cost projections when diesel fuel start costs are held fixed.
- For the same system, there is a medium sensitivity of optimum configuration size to diesel fuel costs when hardware costs are fixed.
- At just over one mile from the utility grid, positive net benefits begin to accrue to the operation of isolated total energy systems comprised of photovoltaics, a flywheel, and a diesel generator.

III.2 100-kWp Load Center

III.2.a. Utility Interface

Load profile data for a master-metered apartment complex in Phoenix were obtained from the Salt River Project and used as a representative of a large load center application for flywheels. The load tape shows a 36-kW average demand from September 1976 to August 1977, and an 84-kW peak demand. The studies performed are directly analogous to those of the residential analysis. Figures 40 and 41 reproduce the analytic environment of Figures 10 and 11 for the load center. All of the characteristics of the residential analysis are enforced, including diminishing returns to increasing storage capacity and the effects of storage in shifting optimum PV array capacity to the right. The most marked differences between the small-scale and large-scale applications to be noted here are the substantial reductions in flywheel breakeven capital cost over the range of flywheel capacities for the load center.

FIGURE 40

100 KW LOAD CENTER UTILITY INTERFACE

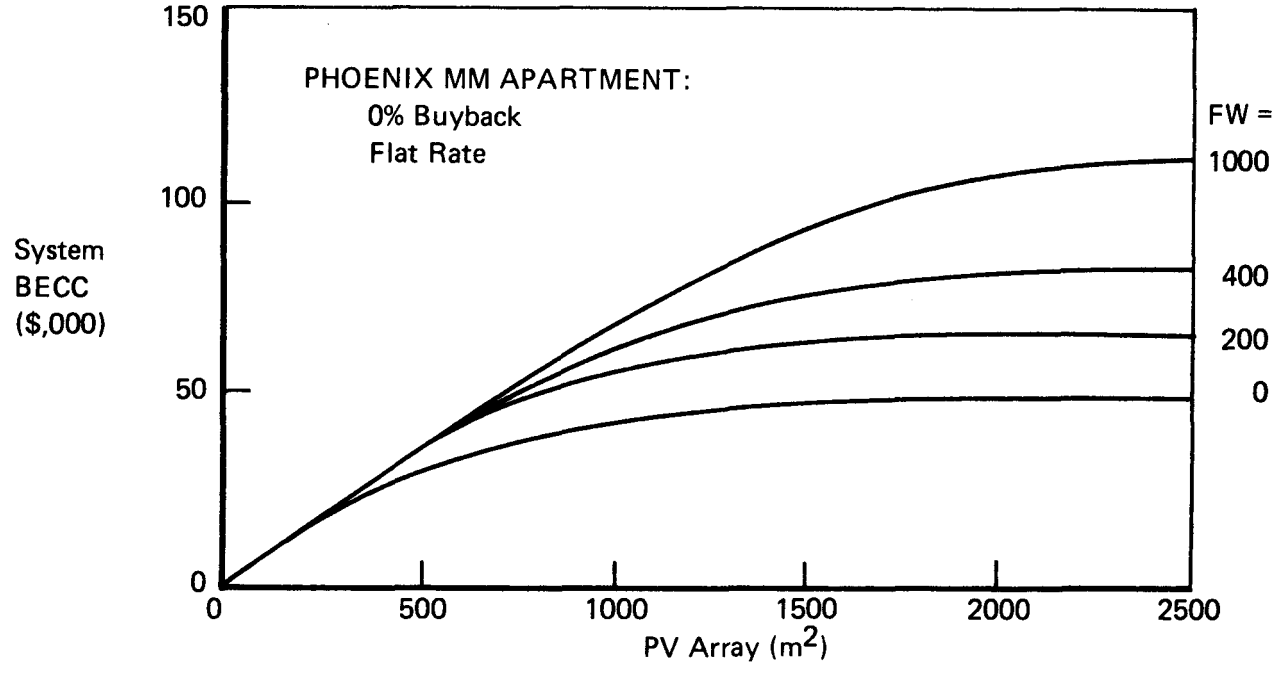

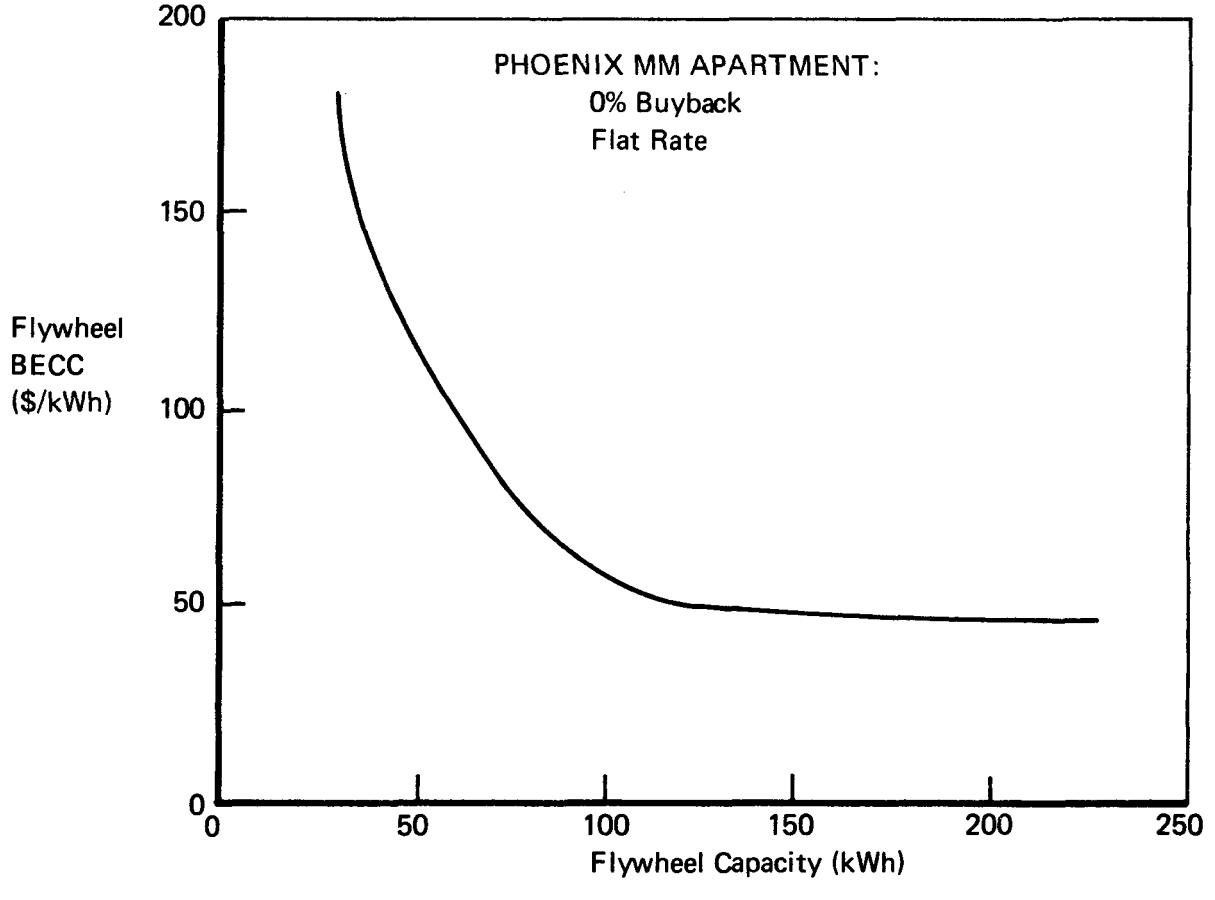

FIGURE 41

100 KW LOAD CENTER UTILITY INTERFACE

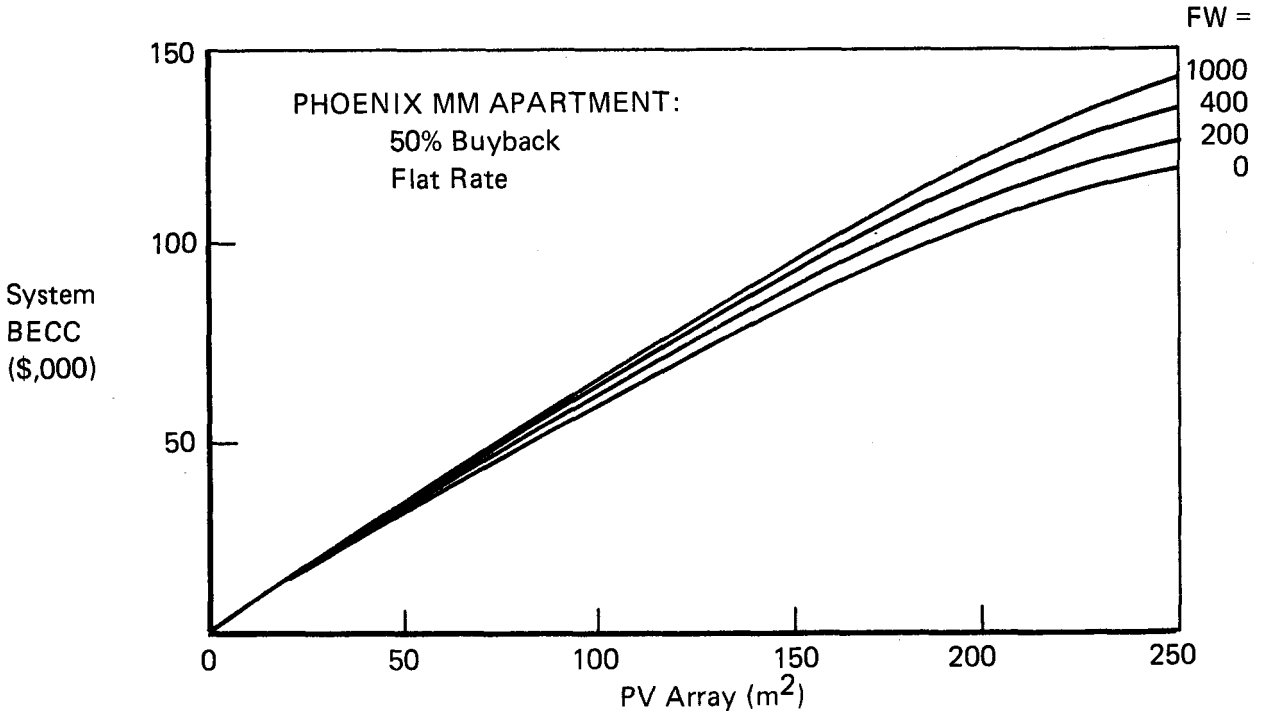

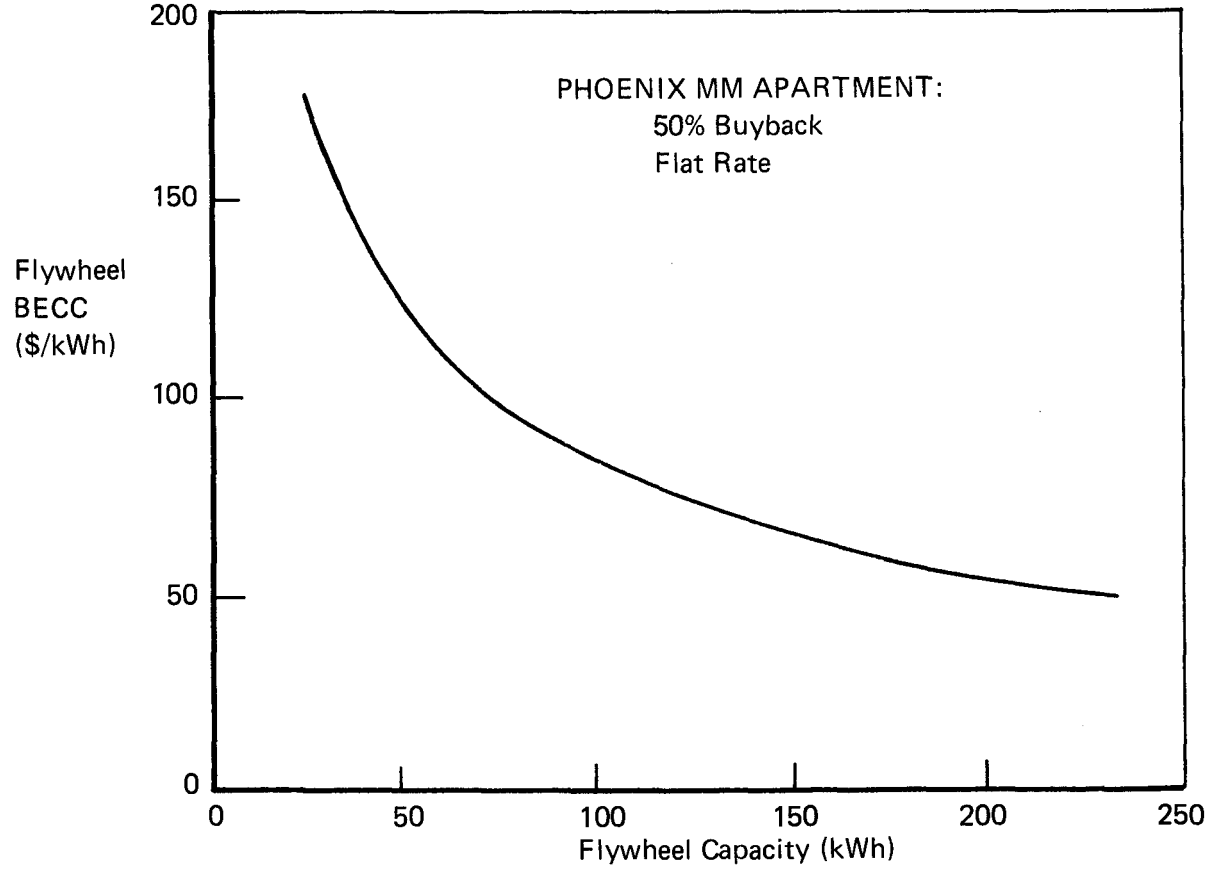

The parameter found to affect this difference most significantly is the discount rate, being set at 10 percent for the load center and 3 percent for the residence case.

III.2.b Remote Stand-Alone

PV and Flywheels/No Diesel

The studies conducted for the remote stand-alone residence were repeated for the 100-kWp load center. Figures 42 and 43 repeat the iso-reliability and iso-cost mappings, respectively, and again indicate the insensitivity of flywheel/array sizing to component hardware costs. Roughly the same rule applies as described in the single-residence analysis--that the optimum ratio of flywheel capacity (in kWh) to array size (in kWp) is roughly 2.5 in the lower ranges of reliability, rising to 4.0 in the higher ranges.

Figure 44 examines the total costs and benefits of such a system as a function of reliability. Reliability is defined here only in terms of resource sufficiency in meeting demand, not in terms of hardware outage. The total costs curve was established by assuming the hardware costs as shown; the total benefits are again defined in terms of the cost of kilowatt-hours of utility electricity not purchased. In a sense, the net benefits curve then maps out the cost of service reliability, however, it should be noted that the alternative electrical source against which the PV system is valued--the utility--generally provides power at 100-percent reliability (as reliability is defined here).

Figure 45 is a reflection of the previous figure with total benefits now including the advantage of not constructing a distribution line from distances of 10 and 20 miles from the grid. Net benefits under these conditions become positive, and intersection with the zero dollar line

FIGURE 42

ISO - RELIABILITY

(HOURS SERVED/HOURS DEMANDED)

100 KW LOAD CENTER

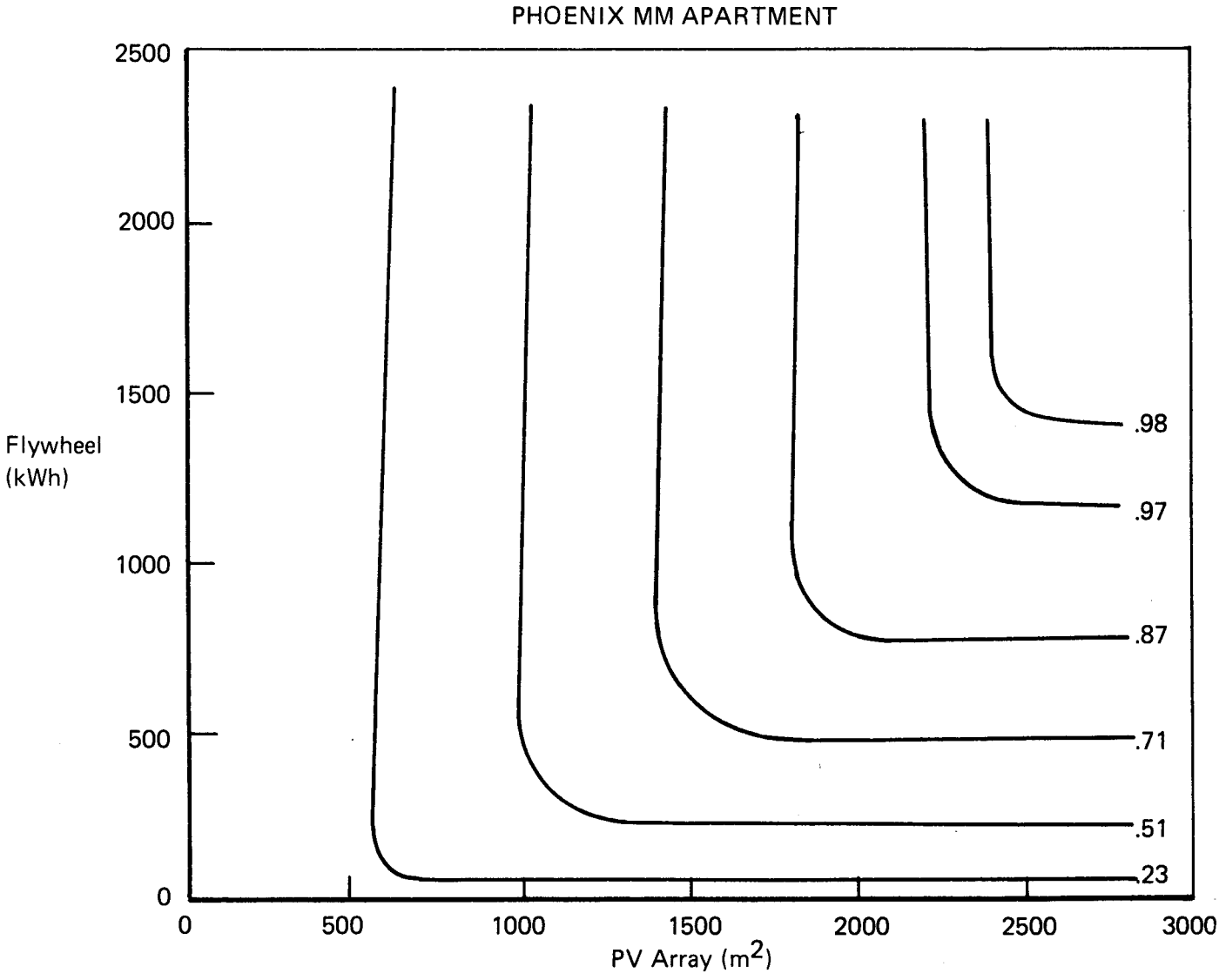

FIGURE 43

ISO - TOTAL COSTS

100 KW LOAD CENTER

PHOENIX MM APARTMENT

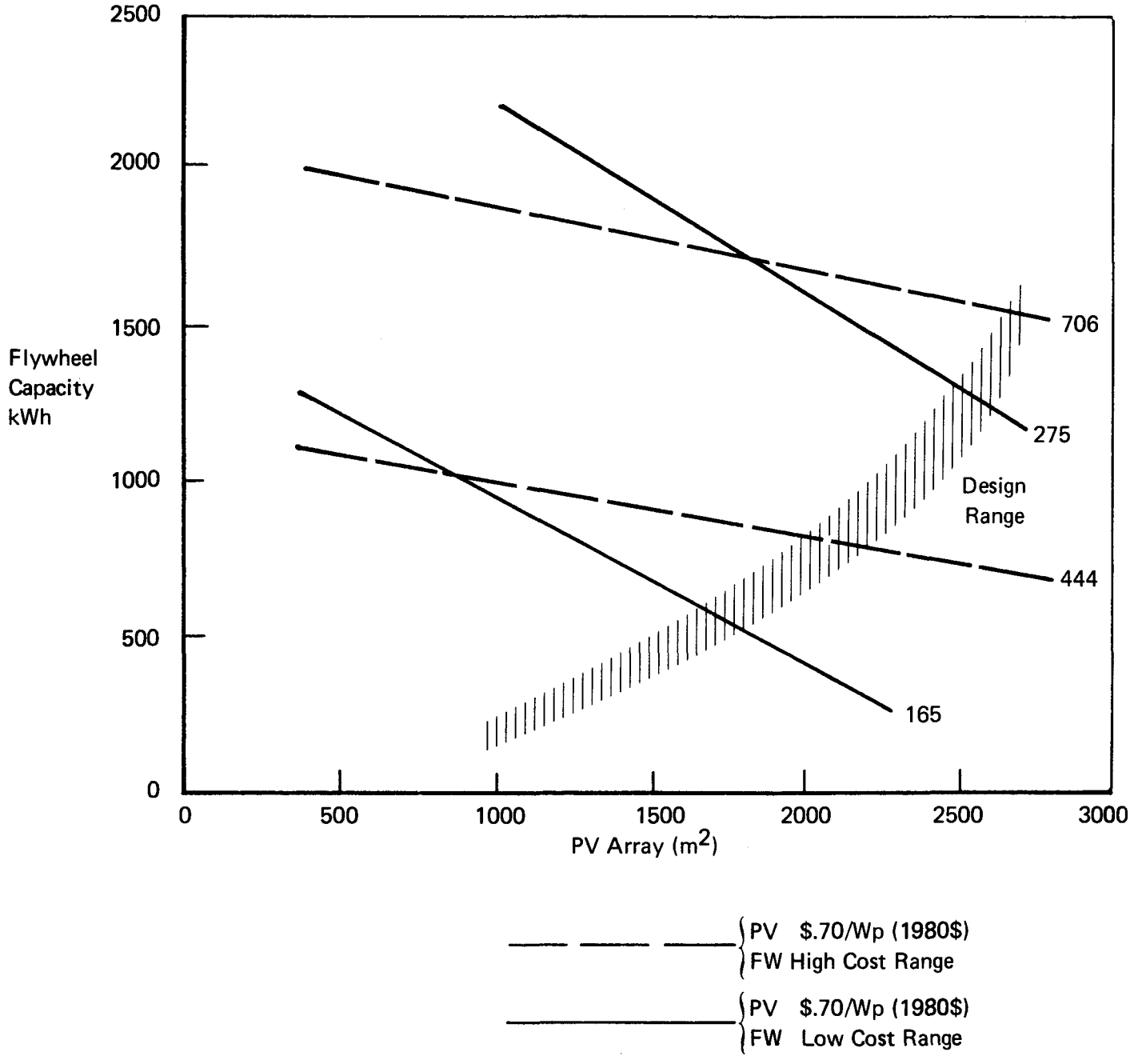

FIGURE 44

THE COSTS AND BENEFITS OF SERVICE RELIABILITY

(Benefits Equal Utility Electricity Displaced Where Utility Supplies at 100% Reliability)

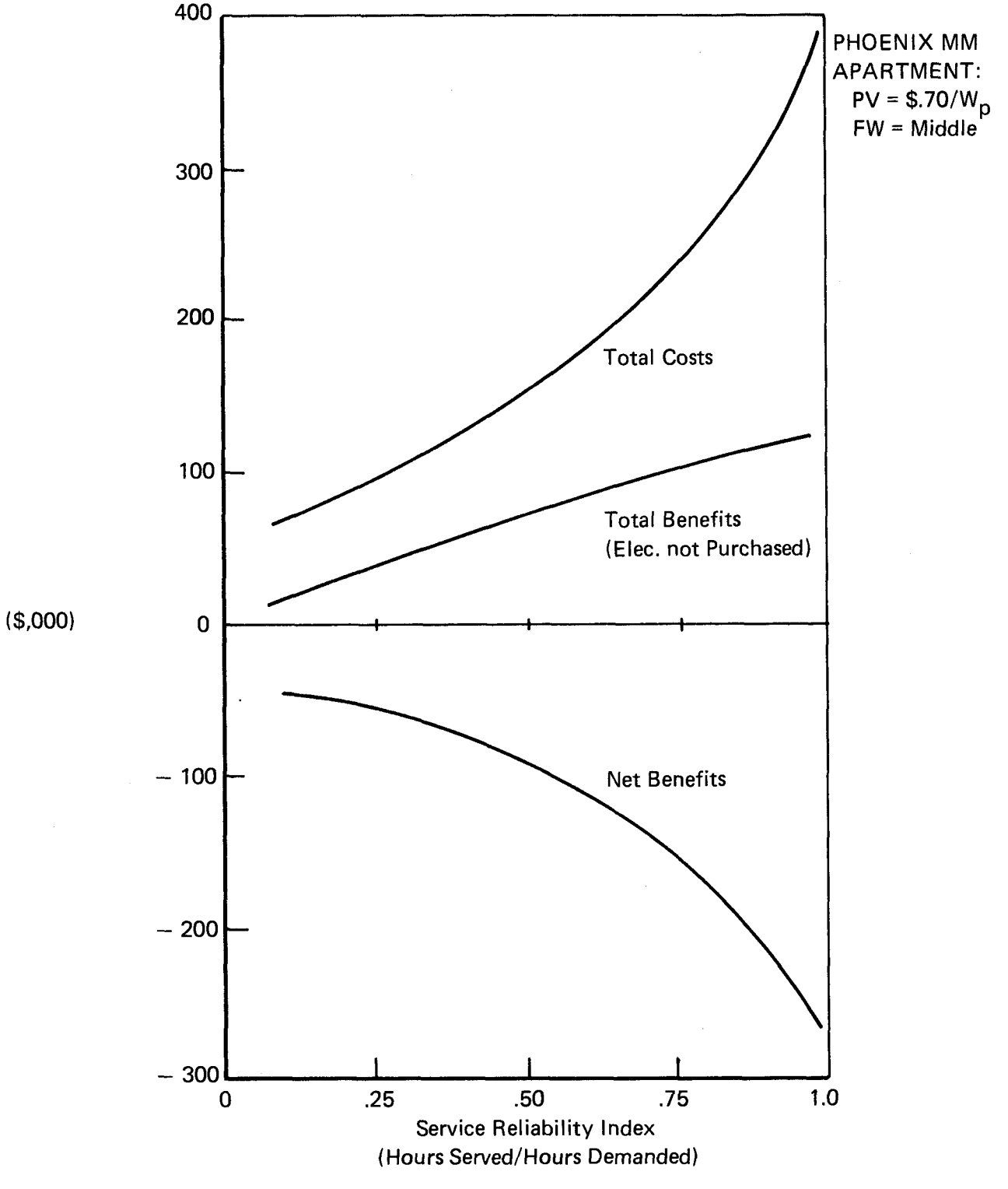

FIGURE 45

THE COSTS AND BENEFITS OF SERVICE RELIABILITY

(Benefits Equal Utility Electricity Displaced Plus
Distribution Line Benefit at 10 and 20 Miles from Grid)

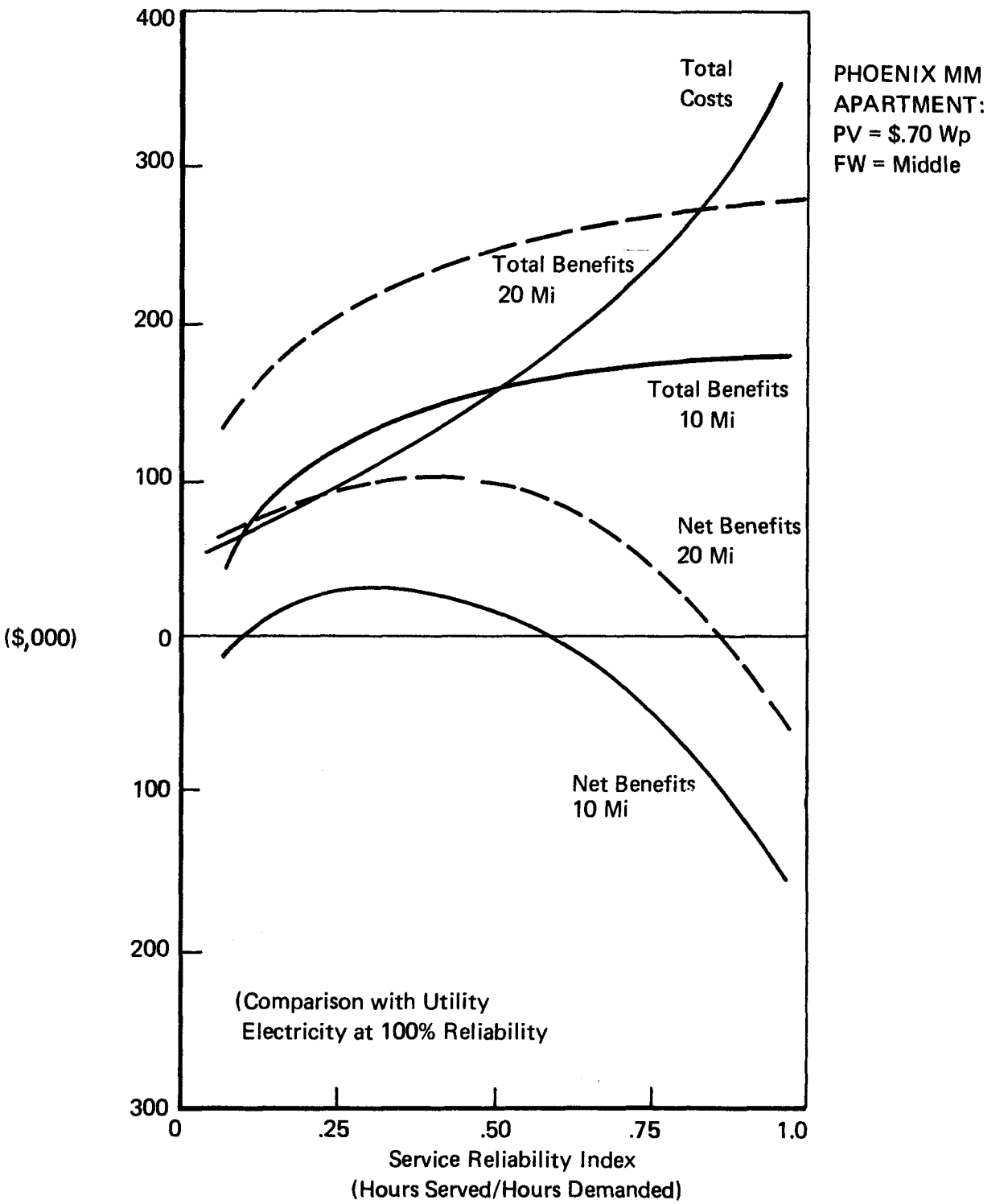

(vertical axis) discloses the reliability at which an investor would be indifferent toward a grid connect over constructing the PV/flywheel total (electric) energy system.

PV and Flywheel/Diesel Backup

The effect of large-project financing is perhaps revealed most strikingly by comparing Figures 46 and 33. Here the optimum configuration mix of flywheel, photovoltaics, and a diesel generator is sought. Whereas Figure 33 of the single-family residence study revealed large contributions by the flywheel and photovoltaics, the load center application finds that an all-diesel system is most practical under most economic conditions. Only when diesel fuel is expensive and hardware costs are at their lowest estimate do the new energy technologies enter the picture. These technologies represent large initial investments, and the high discount rate of 10 percent applied to such large-scale projects virtually eliminates all economic viability.

Figure 47 establishes the relationship of investment worth in terms of net benefits versus distance from the grid under the set of market conditions that prescribed the PV/flywheel/diesel system of box AA of Figure 46. Net positive benefits accrue to the system at a distance of only 10 miles from the distribution grid.

III.2.c Results of the 100-kWp Load Center Study

Utility Interface

- The addition of storage increases the optimum capacity of PV installed when hardware costs are in the low range.
- Storage serves the greatest increment in system value at the lower buyback rates.

FIGURE 46

OPTIMUM CONFIGURATION SIZING
REMOTE STAND ALONE 100 KW LOAD CENTER

PV FLYWHEEL DIESEL

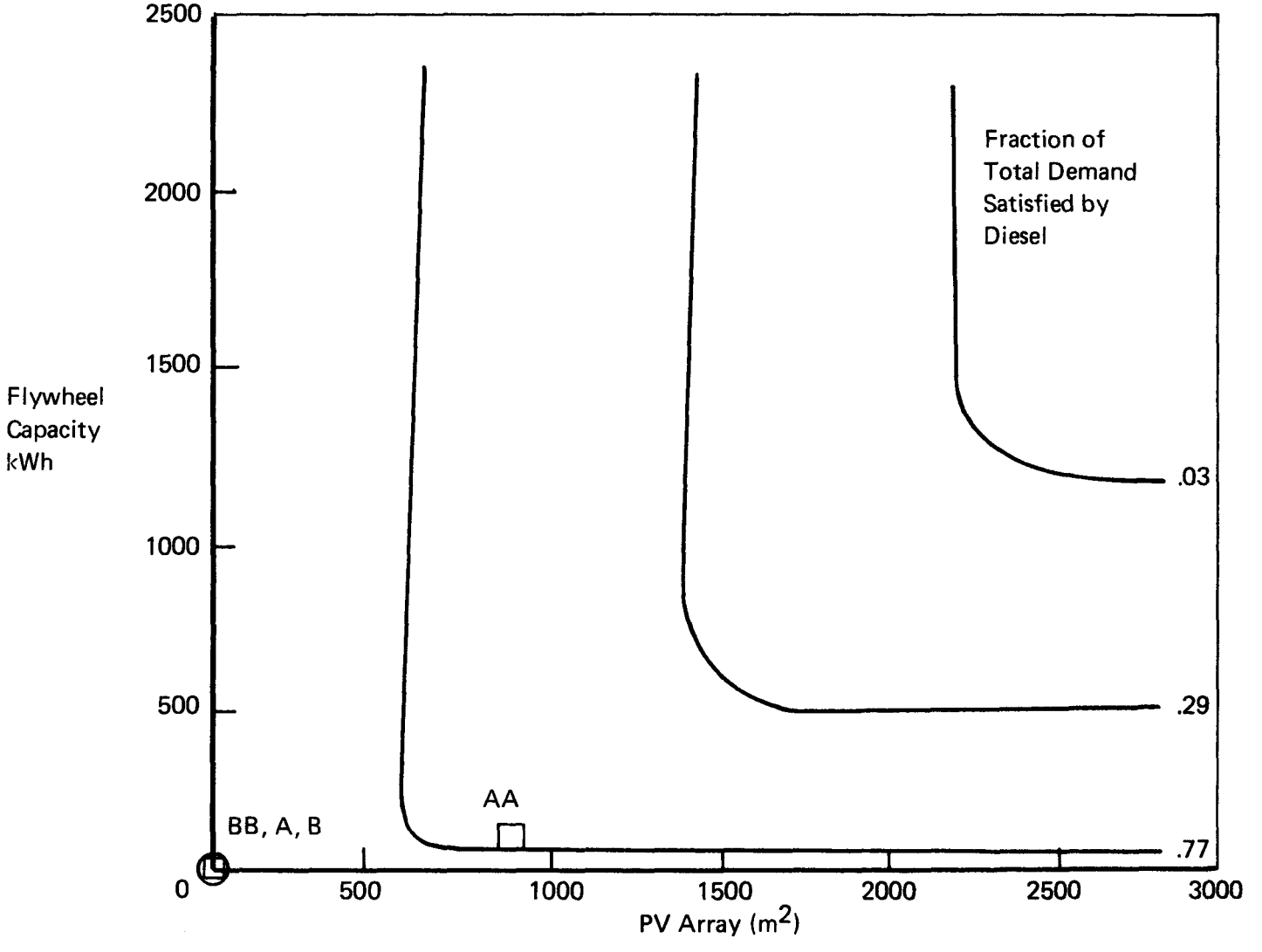

Summary:
Phoenix Master Metered Apartment
Avg. Load: 36Kw
Pk Load: 84Kw
Diesel Capacity: 84Kw

□ Fixed Diesel Fuel Start Cost
AA Low Hardware Cost
BB High Hardware Cost

○ Fixed (Medium) Hardware Cost
A High Diesel Fuel Start Cost
B Low Diesel Fuel Start Cost

- o Diminishing returns accrue to increased flywheel capacity.

Stand-Alone

- o Optimum configuration sizing for PV and flywheel with no diesel is quite insensitive to component costs, but is very sensitive to desired reliability.
- o Sizing of a PV, flywheel, and diesel system tends toward high diesel contribution due to effects of the discount rate applied to high capital outlays for the PV and flywheel.
- o Positive net benefits accrue to the larger total energy applications at about 10 miles from the distribution grid.

III.3 Additional Studies

III.3.a Sensitivity to Flywheel Component Efficiencies

A full-scale prototype of the advanced flywheel concept has not yet been constructed at Lincoln Laboratory. This has necessitated the use of "best estimates" for component operating efficiencies. The assumed loss rates were summarized under Technical Assumptions in Figure 3. By fixing all components at these efficiencies, it was then possible to vary component efficiencies one by one to effect an overall parametric sensitivity analysis. Figure 48 presents the results of this analysis; Figure 49 describes the manner in which component losses were varied from the base case. All input, output, motor, and generator losses were varied by 2 percent in either direction, whereas a somewhat arbitrary variation was placed on other components. The double set of efficiencies given for the electronics components in Figure 49 describes rate of charge/discharge proportional loss figures. The left figure represents losses from 0 to 0.5 the maximum rate of charge/discharge and the right figure is the loss for higher charge/discharge rates.

FIGURE 47

STAND-ALONE VERSUS GRID CONNECT

WHEN DISPLACED DISTRIBUTION LINE COSTS ARE ACCOUNTED FOR

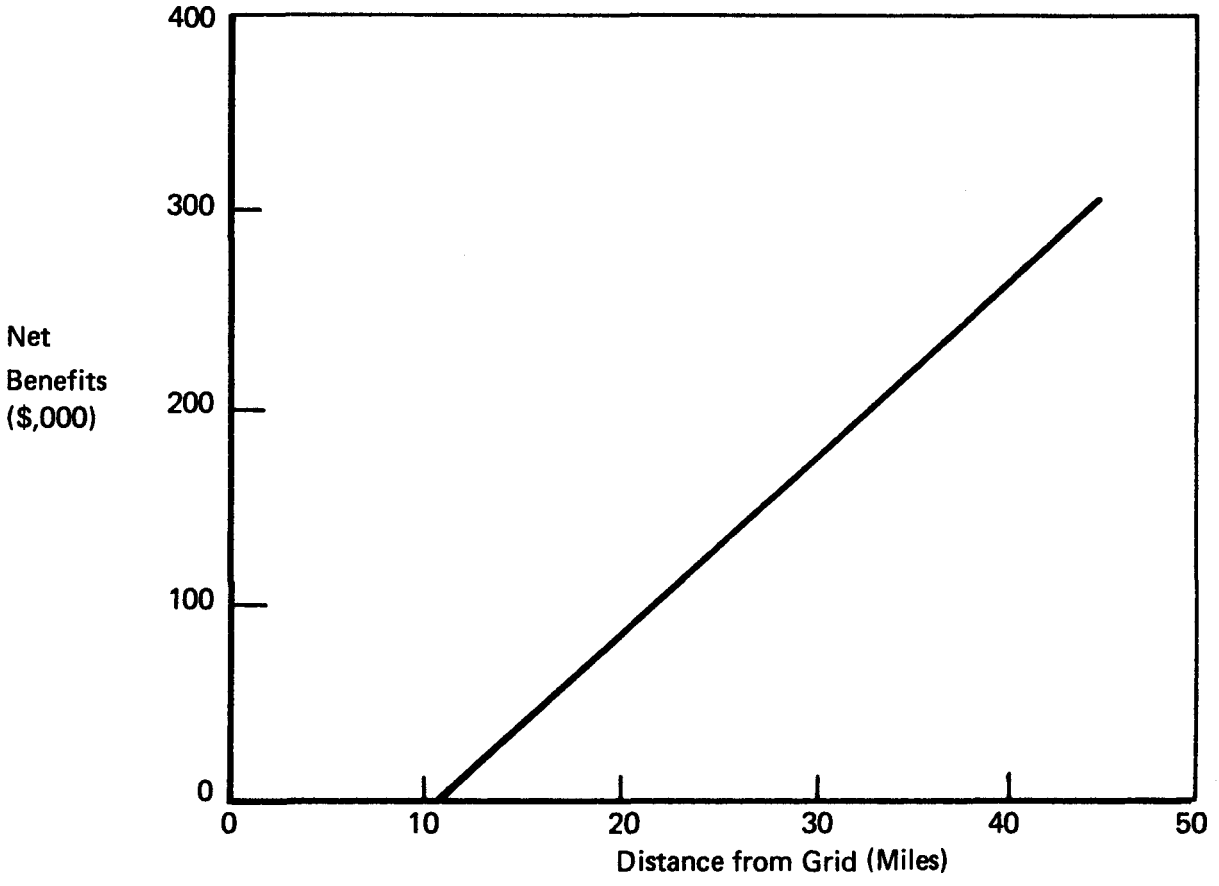

PV + FW + DSL Versus Grid-Connect

FIGURE 48

SENSITIVITY TO FLYWHEEL COMPONENT EFFICIENCIES

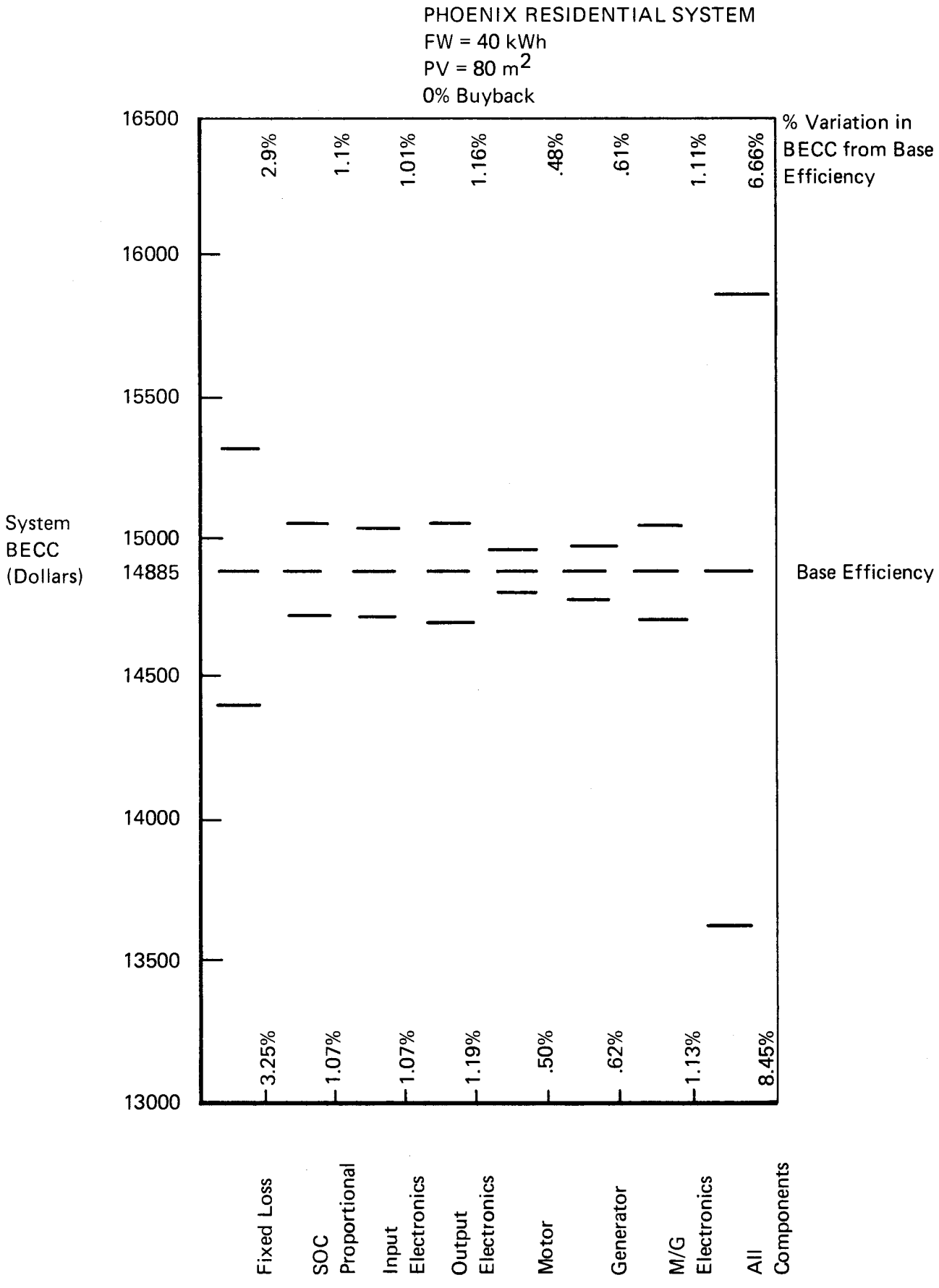

FIGURE 49

SENSITIVITY TO COMPONENT EFFICIENCIES

VARIATIONS PLACED ON EFFICIENCIES

PHOENIX RESIDENCE

PV = $80M^2$ FLYWHEEL = 40 KWH

0% UTILITY BUYBACK

COMPONENT	EFFICIENCY		
	BASE	HIGH	LOW
FIXED LOSS	200 WATTS	300 WATTS	100 WATTS
STATE-OF-CHARGE PROPORTIONAL	.003	.005	.001
INPUT ELECTRONICS	7%/3%	9%/10%	5%/6%
OUTPUT ELECTRONICS	7%/8%	9%/10%	5%/6%
GENERATOR ELECTRONICS	2%/4%	4%/6%	0%/2%
MOTOR ELECTRONICS	2%/4%	4%/6%	0%/2%
MOTOR/GENERATOR ELECTRONICS	PREVIOUS TWO	PREVIOUS TWO	PREVIOUS TWO
ALL COMPONENTS	ALL PREVIOUS	ALL PREVIOUS	ALL PREVIOUS

It is seen that input, output, and combined motor/generator electronics all yield roughly equivalent variations in system value for like changes in efficiency rating. That value is also similar to that produced by the shown change in state-of-charge proportional loss, and roughly one-third of the loss due to varying the fixed-loss rate.

III.3.b. Comparison to Battery Storage

Conceptually, both batteries and flywheels can be described in terms of a generalized storage function, including all component loss characteristics as listed in Figure 3. In actuality, however, this is far too simple. For example, the battery loss estimates are hindered by the imprecision with which estimates can be made of the battery state-of-charge. In fact, no standard means has yet been developed for making such estimates on actual batteries in operation. Millner [2] has already placed estimates of the overall flywheel operating efficiency at 73.3 percent, and has summarized the battery-based storage efficiency (including max power tracker and inverter) at 65.4 percent.

To maintain this overall efficiency advantage over batteries, one needs to look again at the sensitivity of component efficiencies of Figure 48. For example, if a large change were expected in fixed-loss rate, this would have fairly significant impact on overall flywheel efficiency, whereas an unexpected difference in merely the motor electronics component would have minimal impact on overall flywheel efficiency.

III.4 Comparison of Single-Family Residence with the 100-kWp Multi-Family Load Center

From the previous analysis, the following conclusions can be drawn in comparing the two application types of this study:

- Breakeven cost figures for flywheels are lower for the load center application due to:
  - higher discount rates
  - delay of benefits due to longer construction lags
- As a result, the issues most affected are:
- flywheel breakeven cost curves
- optimum component sizing
- distance from the grid at which positive net benefits accrue to the system (stand-alone analysis)

Chapter IV. DISCUSSION

IV.I Investment Decision Making

The question that must be answered in the flywheel worth analysis is whether the addition of energy storage to a photovoltaic system enhances the economic stature of that system. It has been shown that, looking at system benefits as whole, storage increase system value. However, this is only one side of the equation. The complete equation takes into account the costs of that system, and tests whether or not system benefits exceed these costs. The question with regard to flywheel storage is thus whether or not the expected cost of an increment in energy storage is greater or less than its marginal improvement upon system value. In other words, taking into account the expected cost of energy storage, do net benefits accrue as a result of its addition to system operation? Formulated in this manner, a criterion of maximizing net benefits explains under what conditions an investment would be made in energy storage as supplementing photovoltaics.

Evaluation of this figure is not so straightforward, however, for a number of reasons. First, the exact costs of all components and maintenance are unknown. We have, at best, estimates, usually in terms of manufacturers' prices and DOE price goals. In the flywheel study, a best estimate is assumed for costs, which are then varied in either direction to determine cost sensitivity. Second, there are various ways to value the benefits of any one project, depending upon the perspective of the investor. Here it is necessary to distinguish between a private investor's decision process versus that of a public decision-making body, or possibly, a public-minded consumer. Public investment decisions are

likely to involve issues of social cost in producing electricity, such as relative environmental hazards, as well as reliability, security, and psychological concerns. These issues are inherently controversial and therefore not subject to discussion here. Private investment decisions deal almost exclusively with normal market conditions and prices. These conditions are more easily dealt with.

The Private Investor

It is assumed that the private investor always seeks to maximize profits. Any homeowner with a fixed dollar budget will make the decision to invest based solely on issues of relative return and relative risk. To satisfy his energy demand, an investor will go with the option that offers the potential for maximum return on investment when compared against the most likely alternative. This should include the full range of investment opportunities, including the option to reduce demand through conservation. However, in this study benefits have been strictly defined as the total dollars otherwise spent on utility-supplied electricity, priced at the expected cost of electricity in that year.

Under these conditions, a net benefit study was performed for the Phoenix residence case utilizing an 8-kWp PV array with a varying flywheel storage capacity. For the medium-cost assumption (dashed line of Figure 3) net benefits would never accrue unless the utility were purchasing electricity at, minimally, a 60-percent buyback rate, in which case an investor would invest in PV alone with no storage (Figure 50). So except for the very low buyback rates, over the full range of flywheel capacities the costs assumed would always exceed the benefits as defined above.

FIGURE 50

NET BENEFITS STUDY OF OPTIMAL
FLYWHEEL CAPACITY

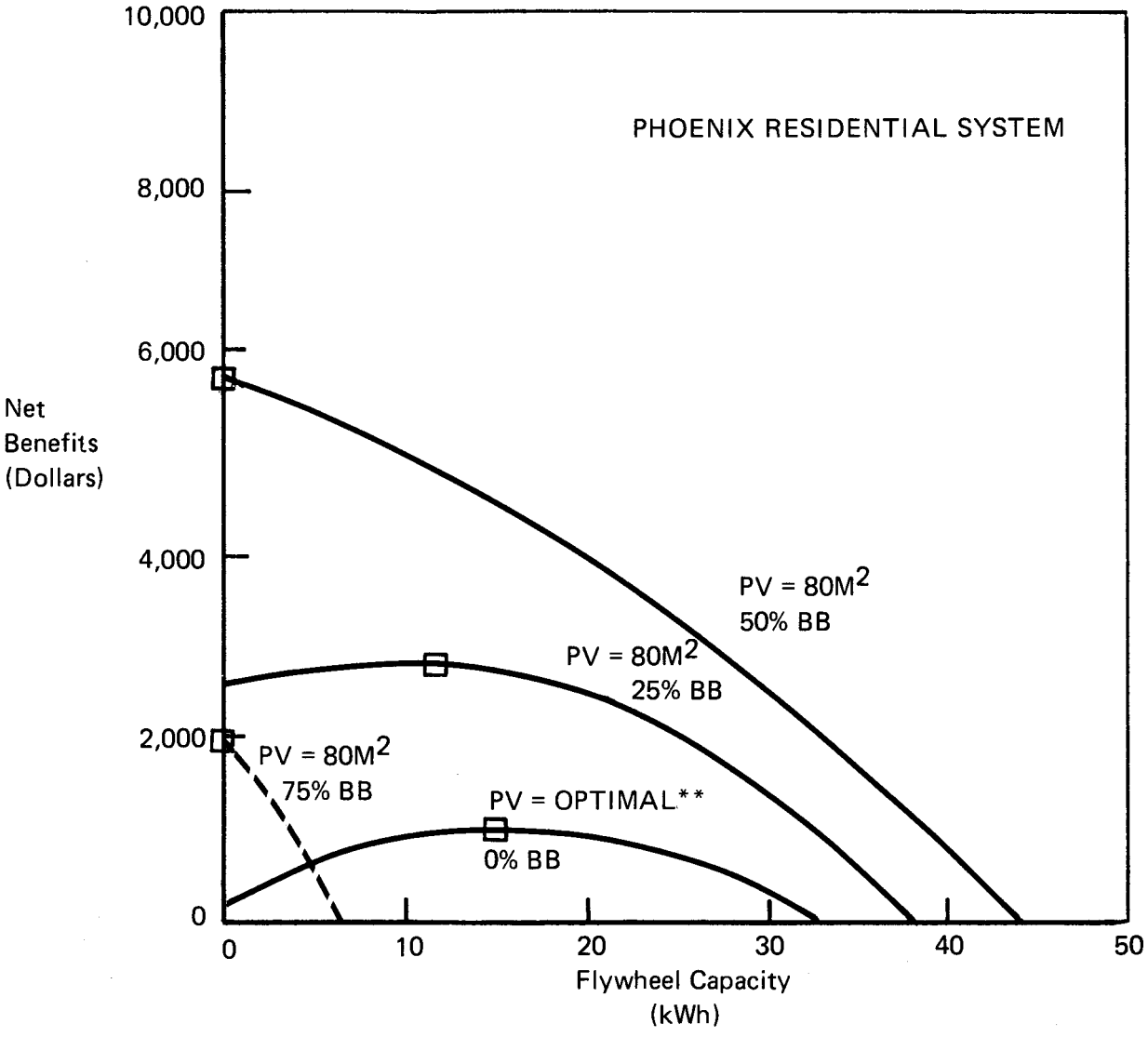

— — — Medium Costs Assumed

——— Low Costs Assumed

□ Indicates Economic Flywheel Sizing Choice

** PV Array Size Corresponds to Optimal at Given Flywheel Capacity

* High BOS Assumptions

For purposes of carrying the description further, the low-costs assumption was used for system components. Figure 50 reveals that under these conditions storage does enhance system economics to the point where incentive for the investment would actually exist. For the 0-percent buyback case shown, little net benefits accure to PV alone, whereas adding of 20 kilowatt hours of storage capacity forces a peak in net benefits accumulated over the 20-year life of the system. The reason for this is as follows. The initial (infrastructure) costs of a photovoltaic system are significant, so substantial benefits must accrue before net benefits become positive. With a fixed household demand and low utility buyback, there are diminishing returns to increasing PV array size beyond roughly 35 m^2 with no storage. Energy storage captures excess PV electricity and so has the effect of "smoothing" the array output to precisely match the load, thus stalling the effect of diminishing returns to increasing array size. As the buyback rate increases, the utility purchase of excess PV serves the same purpose of storage in smoothing array output, and hence energy storage (and its associated cost) is merely redundant.

IV.2 The Need for Flywheel Research

Further research into the advanced flywheel storage concept is needed in many areas, most of which apply to storage systems in general. However, given that the flywheel concept does offer certain specific advantages over any other means of energy storage tested to date, and given the need to ensure a diversified competitive future market in energy storage devices, the reasons outlined here apply to flywheels in particular.

Alan Cox of the MIT Energy Laboratory has quantified some of the implications of storage availability based on the results of this study. A summary of his work is provided below, and his methodology is included as Appendix A.

- o REMOTE LOCATIONS
  - Savings of $8,712/mi in transmission costs for residential standalone systems.
  - Storage economically preferable at locations 1-20 miles from grid (residential).
  - Present-valued savings in diesel-fuel backup are $4,165 at remote residence (3-percent discount rate, 20-year life).
- o PEAK SHAVING
  - 50 kWh shifted per day will result in $5,000 in BOE savings (discounted)
- o DECREASED UNCERTAINTY in electricity supply from PV decreases discount rate applied to PV investment decisions.
- o DEMAND FOR STORAGE AS PV PRICES FALL
  - For users with PV BECC greater than future PV prices, optimal array size will increase (until MC = MB) with storage.
  - With storage at residence, optimum array size increases from 60 m^2 to 110 m^2. Electricity savings will be 15/BOE/year at residence.
  - Increased penetration. If Phoenix residential penetration is 5 percent without storage, increased optimum array size will result in 840,820/BOE/year savings.
- o NEED FOR DIVERSIFIED RESEARCH EFFORT to ensure a competitive future market in storage devices.

Chapter V. CONCLUSIONS

The following conclusions can be drawn from this study:

- Flywheel systems are more attractive in smaller distributed applications that have small construction period lags and where low discount rates are applicable. These include residential applications as well as applications in developing countries.
- For low expected costs for PV and flywheels, the flywheel increases the size of an optimal photovoltaic system.
- Flywheel storage serves the greatest increment in system value at the lower buyback rates.
- Variations over the range of reasonable time-of-day rate structures have an insignificant impact on flywheel economics unless the flywheel is allowed to serve in a dispersed/system storage mode (as opposed to dispersed-dedicated).
- PV/flywheel/diesel total energy systems are competitive with a utility grid connect at distances starting one mile from the utility grid.
- For PV and flywheel remote stand-alone applications utilizing no diesel, optimum component sizing is insensitive to hardware cost.

APPENDIX A

THE NEED FOR FLYWHEELS

Alan J. Cox

MIT Energy Laboratory

This memo represents a brief attempt to set down a concise rationale for a well-funded flywheel storage and power conditioning project. The list of points is by no means complete.

The first point to be made is that flywheels should be evaluated on their capacity for penetrating the future market for electricity storage, in the same manner and order as PV arrays themselves are being evaluated.

The PV marketing plan is to introduce this technology in remote locations, and in developing countries, allowing the industry to build up production in anticipation of the market opening up for such low discount-rate users as government installations and electric utilities, or users who are experiencing high electricity costs, such as those already found in the Northeast residential-commercial rate classes. As the industry continues to enjoy the benefits of economies of scale and to develop new lower-cost technologies, the PV systems should penetrate deeply into the remaining residential market and enjoy considerable use in the industrial sector.

This study shows that there are clear advantages to using flywheels as backup storage in remote locations over diesel fuel use or construction of electricity transmission facilities. The benefits arising from investment savings in 69-kV transmission lines are $8,712/mile (1980 $). For an Arizona location, using reasonable estimates of 1985 flywheel costs, this makes flywheel storage an economically preferable option (over transmission line construction) at

distances greater than 1 to 20 miles, depending on whether the load is residential or commercial and depending on other economic assumptions. The benefits in terms of diesel fuel saved would be $4,200 in 1985, over 20 years, discounted at 3 percent and assuming a 1985 diesel fuel price of $0.97/gallon. These figures, supplemented with the more extensive analysis of such factors as reliability, clearly indicate an early market for storage devices.

Another relatively short-term market at which the flywheel technology should be aimed is that arising out of attempts to shave peaking electricity requirements. Assuming heat rates of 8.5 mBtu/kWh for a base oil, coal, or synfuel plant, 10.0 mBtu/kWh for nuclear plant and 14.0 mBtu/kWh for a peaking gas turbine, 50 kWh shifted each day from peak to base plants will result in savings of 12.2 barrels of oil equivalent per year shifting to a nuclear base and 16.7 bbl/year for shifting to oil-synfuel base. Assuming a $20.00/bbl for oil, a 20-year life for the project, no operating and maintenance costs, no inflation and a 3-percent discount rate, the shift to oil-coal-synfuel base would have a discounted present value of almost $5,000. That figure is what could be afforded for a suitable flywheel within the reasonable future if required rates of return can be brought down through reduced interest loans and other incentives.

It may be worthwhile to note that anything which increases the reliability of the supply of electricity from a new technology is certain to reduce the discount rate that individuals and firms apply to it. The uncertainty and risk associated with PV will be reduced, to some extent, bringing individual discount rates with it.

As PV arrays continue to fall in price, users in situations that had experienced high breakeven capital costs will find themselves able to buy PV systems that will provide them larger savings in their electricity bills, provided, of course, a suitable storage system can be bought. For instance, in situations in which the original BECC peaked at $1.00/Wp, a PV user will experience considerable savings when array costs fall to $0.50/Wp. A PV consumer would be willing to expand his/her PV investment until the marginal benefit of increasing that investment reaches $0.50/Wp. The resulting savings could offset the cost of a flywheel since only with a storage device will the expanded electricity production be useful, once all desired load-shifting has taken place.

With such a system, and with falling array costs, more and more electricity consumers will correctly ascertain that their optimal PV array size is larger than that with no storage. Again, this is a clear result of the current study. These results indicate that, for a buyback rate equal to 0 percent, the optimum array size shifts from 60 m^2 to 110 m^2 for a Phoenix residence. This difference converts to annual electricity production of 10,624 kWh at the residence, or barrel of oil equivalent savings of 15.0 bbl/year, assuming the oil baseload heat rates. At a 5-percent penetration within the Phoenix synthetic utility, without storage, the increase in optimal sizing would increase the installed PV with storage from 400 MW to 733 MW. The increase in energy savings would be 840,820 barrels of oil equivalent per year.

A final argument to be made in favor of a strong flywheel-power-conditioning research program is to develop alternative storage devices which may maintain some competition in the future storage devices market, and which will have certain features that will make it a more appropriate storage device for some uses.

FOOTNOTES

1. General Electric Space Division, Applied Research on Energy Storage and Conversion for Photovoltaic and Wind Energy Systems, Final Report, Volume I: Study Summary and Concept Screening and Volume II: Photovoltaic Systems with Energy Storage, January 1978.

2. Ibid.

3. Alan R. Millner, "A Flywheel Energy Storage and Conversion System for Photovoltaic Applications," M.I.T./Lincoln Laboratory, paper presented at the international Assembly on Energy Storage, Dubrovnik, May 28-June 1.

4. From Alan J. Cox, "The Need for Flywheels," internal M.I.T. Energy Laboratory Memorandum, August 15, 1979. This memorandum is based on calculations using the results of this report and is enclosed as Appendix A.

BIBLIOGRAPHY

1. General Electric Space Division, Applied Research on Energy Storage and Conversion for Photovoltaic and Wind Energy Systems, Final Report, Volume I: Study Summary and Concept Screening and Volume II: Photovoltaic Systems with Energy Storage, January 1978.

2. Millner, Alan R. A Flywheel Energy Storage and Conversion System for Photovoltaic Applications, M.I.T./Lincoln Laboratory, paper presented at the International Assembly on Energy Storage, Dubrovnik, May 28-June 1, 1979.

3. General Electric Space Division, Regional Conceptual Design and Analysis Studies for Residential Photovoltaic Systems, Volume I: Executive Summary, January 1979.

☆ U. S. GOVERNMENT PRINTING OFFICE: 1982--500-000--54